Technische Universität München

Lehrstuhl für Aerodynamik

Implicit Turbulence Modeling for Large-Eddy Simulation

Stefan Hickel

Vollständiger Abdruck der von der Fakultät für Maschinenwesen der Technischen Universität München zur Erlangung des akademischen Grades eines

Doktor-Ingenieurs

genehmigten Dissertation.

Vorsitzender:		Univ.-Prof. Dr.-Ing. Thomas Sattelmayer
Prüfer der Dissertation:	1.	Univ.-Prof. Dr.-Ing. habil. Nikolaus A. Adams
	2.	Univ.-Prof. Dr.-Ing. Leonhard Kleiser,
		Eidgenössische Technische Hochschule Zürich

Die Dissertation wurde am 14.01.2008 bei der Technischen Universität München eingereicht und durch die Fakultät für Maschinenwesen am 16.06.2008 angenommen.

STEFAN HICKEL

Gerichtstrasse 41a

15806 Zossen

Germany

sh@tum.de

Released   December 20, 2007

Typesetting   LaTeX

ABSTRACT

The subgrid-scale (SGS) model in a large-eddy simulation (LES) generally operates on a range of scales that is marginally resolved by discretization schemes. Consequently, the discretization scheme's truncation error and the subgrid-scale model are linked, which raises the question of how accurate the computational results are. The link between the SGS model and truncation error can be beneficially exploited by developing discretization methods for subgrid-scale modeling, or vice versa. Approaches where the SGS model and the numerical discretization scheme are fully merged are called implicit LES (ILES) methods.

In order to improve on modeling uncertainties, a systematic framework is proposed for design, analysis, and optimization of nonlinear discretization schemes for implicit LES. The resulting adaptive local deconvolution method (ALDM) for implicit LES is a finite volume method based on a nonlinear deconvolution operator and a numerical flux function. Free parameters inherent to the discretization allow to control the truncation error. They are calibrated in such a way that the truncation error acts as a physically motivated SGS model. An automatic optimization based on an evolutionary algorithm is employed to obtain a set of parameters that results in an optimum match between the spectral numerical viscosity and theoretical predictions of the spectral eddy viscosity for isotropic turbulence. The method is formulated for LES of turbulent flows governed by the incompressible NAVIER-STOKES equations and for passive-scalar mixing.

ALDM has shown the potential for providing a reliable, accurate, and efficient method for LES. Various applications, such as three-dimensional homogeneous isotropic turbulence, transitional and turbulent plane channel flow, and turbulent boundary-layer separation, demonstrate the good performance of the implicit model. Computational results agree well with theory and experimental data and show that the implicit SGS model performs at least as well as established explicit models, for most considered applications the performance is even better. This is possible because physical reasoning is incorporated into the design of the discretization scheme and discretization effects are fully taken into account within the SGS model formulation.

CONTENTS

LIST OF TABLES

NOMENCLATURE

Roman Symbols

$\boldsymbol{a}$	REYNOLDS stress anisotropy tensor
c	passive scalar
$\boldsymbol{C}$	coefficient matrix
C_B	BATCHELOR constant
C_f	friction coefficient
C_K	KOLMOGOROV constant
C_{OC}	OBUKHOV–CORRSIN constant
C_S	SMAGORINSKY constant
C_τ	mean friction concentration
C_W	mean concentration at the wall
$\widehat{E}$	turbulent kinetic energy spectrum
$\widehat{E}_c$	scalar variance spectrum
F	flux
$\boldsymbol{f}$	flux vector, one column of $\boldsymbol{F}$
$\boldsymbol{F}$	flux tensor
G	filter kernel
$\mathcal{G}$	general error or residual
h	grid spacing
$hx,\ hy,\ hz$	directional grid spacing
H	channel half width
H_{12}	shape parameter based on δ_1 and δ_2
H_{32}	shape parameter based on δ_3 and δ_2
i	imaginary unit
I	tensor invariant
k	turbulent kinetic energy

k	order of reconstruction polynomial
K	maximum order of reconstruction polynomials
K	acceleration parameter
K^+	non-dimensional mass-transfer coefficient
l^+	viscous length scale
L	integral length scale
N	number of grid points
$\boldsymbol{N}$	flux tensor
p	pressure
Pe	PÉCLET number
r	shift (of leftmost stencil point)
Re	REYNOLDS number
Re_δ	REYNOLDS number based on boundary-layer thickness
Re_{δ_1}	REYNOLDS number based on displacement thickness
Re_{δ_2}	REYNOLDS number based on momentum thickness
Re_{δ_3}	REYNOLDS number based on energy thickness
Re_λ	TAYLOR scale REYNOLDS number
Re_τ	wall-friction REYNOLDS number
Sc	SCHMIDT number
t	time
$\widehat{T}$	nonlinear energy transfer
$u \equiv u_1$	first velocity component (streamwise)
$\boldsymbol{u}$	velocity vector
U_τ	mean wall-friction velocity
$v \equiv u_2$	second velocity component (wall-normal)
$w \equiv u_3$	third velocity component (spanwise)
$x \equiv x_1$	first coordinate (streamwise)
$\boldsymbol{x}$	coordinate vector
$y \equiv x_2$	second coordinate (wall-normal)
$z \equiv x_3$	third coordinate (spanwise)

Greek Symbols

$\alpha_{k,r,l}$	coefficients of reconstruction polynomials

β	smoothness measure
β	CLAUSER pressure parameter
γ	model parameter of ALDM
γ_1	skewness
γ_2	excess kurtosis
δ	boundary-layer thickness
δ_1	displacement thickness
δ_2	momentum thickness
δ_3	energy thickness
δ_{ij}	KRONECKER's delta
Δt	time step
Δ_P	PATEL pressure gradient
Δ_{RC}	ROTTA–CLAUSER length
ε	dissipation
η_K	KOLMOGOROV length
η_B	BATCHELOR wavenumber
κ	VON KÁRMÁN constant
κ	scalar diffusivity
λ	shift
Λ	pressure gradient parameter of CASTILLO and GEORGE [19]
λ_T	TAYLOR micro scale
ν	kinematic viscosity
ν^+	viscosity normalized with $(\widehat{E}(\xi_C)/\xi_C)^{1/2}$
ξ	wavenumber
$\boldsymbol{\xi}$	wavenumber vector
ξ_B	BATCHELOR wavenumber
ξ_C	cut-off wavenumber
ξ_D	diffusive cut-off wavenumber
ξ_N	NYQUIST wavenumber
ξ_K	KOLMOGOROV wavenumber
ξ_S	threshold wavenumber of large-scale forcing
ρ	density
σ	model parameter of ALDM
τ	shear stress

φ	generic variable
Φ	primitive function of φ
χ	scalar diffusion
χ	reverse-flow parameter
$\mathcal{X}$	1-D deconvolution operator
$\boldsymbol{\mathcal{X}}$	3-D deconvolution operator
ω	weight functional
$\Omega_{i,j,k}$	cell of CARTESian computational mesh

Other Symbols

$\bar{\cdot}$	spatially filtered quantity
$\tilde{\cdot}$	numerical (discrete) approximation
$\breve{\cdot}$	analytical (continuous) approximation
$\hat{\cdot}$	FOURIER transform
$\langle\cdot\rangle$	mean value (REYNOLDS filter)
$\cdot'$	fluctuation

Subscripts

0	reference state
∞	free-stream property
δ	property at the boundary-layer edge or based on the length δ
$bulk$	bulk property
c	related to passive scalar c
C	truncated at cut-off wavenumber
N	grid function obtained by projecting a continuous function onto a numerical grid
num	numerical
p	based on pressure or pressure gradient
ref	reference value
vD	VAN DRIEST
w	property at the wall
θ	based on δ_θ

τ	based on wall friction

Superscripts

+	normalized , frequently for scaling in wall units
B	backward
D	downward
F	forward
L	left / leftward
R	right / rightward
U	upward

Frequently Used Abbreviations

1-D	one-dimensional
2-D	two-dimensional
3-D	three-dimensional
ADM	approximate deconvolution model
ALDM	adaptive local deconvolution method
APG	adverse pressure gradient
BiCGstab	stabilized bi-conjugate gradient method
CBC	COMTE-BELLOT and CORRSIN [27]
CFL	COURANT–FRIEDRICHS–LEWY ; COURANT number
CL	CHOLLET–LESIEUR
CPU	central processing unit
D	detachment
DIA	direct interaction approximation
DNS	direct numerical simulation
DSM	dynamic SMAGORINSKY model
EDQNM	eddy-damped quasi-normal MARKOVian
ENO	essentially non-oscillatory
FCT	flux-corrected transport
FD	finite difference
FFT	fast FOURIER transform

FV	finite volume
ID	incipient detachment
ILES	implicit large-eddy simulation
ITD	intermittent transitory detachment
LASER	light amplification by stimulated emission of radiation
LDA	LASER Doppler anemometry
LHDI	Lagrangean-history direct-interaction
LES	large-eddy simulation
MDE	modified differential equation
MDEA	modified-differential-equation analysis
MILES	monotonically integrated large-eddy simulation
MPDATA	multidimensional positive definite advection transport algorithm
MPI	message passing interface
MUSCL	monotonic upstream-centered scheme for conservation laws
PIV	particle-image velocimetry
PPM	piecewise parabolic method
RANS	Reynolds-averaged Navier–Stokes
rms	root of mean square
SFS	subfilter scale
SGS	subgrid scale
SI	international metric system (*Le Système international d'unités*)
SVV	spectral vanishing viscosity
TBL	turbulent boundary layer
TD	transitory detachment
TFM	test field model
TGV	Taylor–Green vortex
TV	total variation
TVB	total-variation bounded
TVD	total-variation diminishing
WENO	weighted ENO
ZPG	zero pressure gradient
ZS	Zagarola and Smits [187]

INTRODUCTION

1.1 Motivation

Large Eddy Simulation (LES) is becoming a more and more widely used simulation tool for the time-accurate prediction of unsteady flows at high REYNOLDS numbers. In contrast to Direct Numerical Simulation (DNS) the KOLMOGOROV dissipation scale is not resolved with LES, making the computational cost of LES largely independent of the REYNOLDS number[1]. The level of abstraction is lower than with statistical approaches based on the REYNOLDS-averaged NAVIER-STOKES (RANS) equations. Thus the scope of LES extends to unsteady turbulent flows with a broad range of spatial and temporal scales.

With LES the NAVIER–STOKES equations are numerically solved on a grid that is too coarse to represent the entire range of turbulent flow scales. The large resolved scales provide a direct representation of the energy-containing flow structures. This representation is adequate for most practical purposes in engineering and in geophysical sciences, i.e., where the unrepresented small-scale, high-frequency fluctuations are of minor interest. From a mathematical point of view, however, there are nonlinear interactions between all turbulent flow scales, with the truncated small-scale information being crucial for the proper evolution of large-scale structures in the flow. The purpose of a subgrid-scale (SGS) model is to close the resolved-scale equations by representing the *effect* of their nonlinear interaction with unrepresented scales.

The development of efficient and accurate SGS models constitutes a major research challenge. First attempts on LES and SGS modeling date back to the 1960s. Motivated by meteorological applications, the first SGS model was proposed by SMAGORINSKY [161] and analyzed in depth by LILLY [100]. First successful applications to turbulent channel flow were reported by DEARDORFF [31]. Years of intense research have further allowed for a consensus on the limitations of the eddy-viscosity concept - the basis of SMAGORINSKY's model - to be reached: First, that the model parameter is not universal,

---

[1] With wall boundary layers are a prominent exception. The computational cost of resolving the viscous sublayer scales like $Re^{2.4}$, unless wall models are used. [21, 134].

and second, that the subgrid-stress tensor and the strain tensor involved in the model are only weakly correlated. Eddy-viscosity models that improve on the first point can be constructed, e.g., by incorporating an algebraic rule that adapts the model constant [46, 101, 117] or high-pass filtering that eliminates the effect of mean-flow gradients [145, 171, 179]. An alternative to eddy-viscosity models are approaches that replace modeling by an ad hoc mathematical procedure based on a similarity assumption between the smallest represented scales and the largest non-represented scales. With BARDINA's scale-similarity model [5] the SGS stress is computed directly from its definition, while using the filtered solution as approximation of the unfiltered solution. Deconvolution-type models, such as the approximate deconvolution model of STOLZ and ADAMS [168], can be interpreted as a generalization of this approach. Based on more sophisticated approximations, they extract as much information as possible from the represented range of scales. Mixed models which combine deconvolution with a dissipative component [170, 181, 190] show significantly improved correlations with true SGS stresses[2]. The numerous SGS models that were developed over the last four decades can be classified in various ways. However, a common distinction is made between eddy-viscosity models, scale-similarity models, and mixed models. Valuable reviews on recent developments, their historical aspects, as well as related mathematical and physical theories are given by PIOMELLI [133], LESIEUR *et al.* [94], MENEVEAU and KATZ [116], and DOMARADZKI and ADAMS [34]. Several textbooks providing a good introduction to LES are also available (Refs. [93, 136, 144]).

We refer to all these approaches as *explicit SGS models*, as they rely on beforehand defined approximations or estimates for the unclosed SGS terms which have to be computed during time advancement. Theoretical development of explicit SGS models is mainly based on the filtering concept of LEONARD [92], where deriving the resolved-scale equations and SGS modeling are considered separately from numerical aspects of solving the equations. That is, SGS are modeled explicitly if the conservation law has been modified and subsequently discretized.

The conceptual separation of explicit SGS model and discretization implies the assumption that the numerical method provides an accurate solution to the resolved-scale equations. SGS models for LES operate mainly on the smallest represented scales, i.e., on the range of scales that is only marginally resolved by the underlying numerical method. This fact requires the numerical truncation error to be small. Otherwise the subgrid-scale model will unpredictably interfere with the discretization scheme. First theoretical

---

[2] A priori analysis showed superior correlations for deconvolution models without regularization. In practice, however, a dissipative component is needed for numerical stability.

analyses by GHOSAL [48] led to the conclusion that even the truncation error of a fourth-order accurate central-difference discretization can be of the same order of magnitude as the SGS stress. Comparative numerical studies [47, 89, 180, e.g.] corroborate these analytical results.

The reciprocal interference of the numerical truncation error and the SGS model brings the accuracy of the resolved-scale solution into question and therefore constitutes a major hindrance for the further development of LES. In order to reduce this coupling, one could resort to higher-order discretizations or to explicit filtering [48]. For LES of flows in or about complex geometries the use of higher-order schemes leads to complications concerning the implementation and increases the computational cost substantially. The modified-wavenumber concept of discretizations (see VICHNEVETSKY and BOWLES [176]) implies a distinction between *resolved scales* (accurately represented scales for which the modified wavenumber of the discretization is close to the exact wavenumber) and *represented scales* (scales larger than the grid cut-off). With explicit filtering the filter cutoff can be chosen according to the accuracy of the particular numerical method [169]. For a given discretization an explicit filter reduces the error caused by the band of non-resolved scales. On the other hand, filtering increases the required overall grid resolution and computational cost for a given smallest resolved flow-scale.

Recent studies indicate that the interference between the explicit SGS model and the truncation error can be exploited. The truncation error from the unmodified conservation law's discretization can itself be employed to model the effects of unresolved scales, thus functioning as an *implicit SGS model* that is directly contained within the discretization scheme. An explicit computation of the subgrid-stress tensor becomes unnecessary. Such an approach is referred to as *implicit LES* (ILES). With ILES under-resolution is treated as a primarily numerical problem which can be tackled by employing an appropriate discretization scheme. This approach is particularly convenient in flow regimes for which the derivation or the accurate computation of explicit SGS models is cumbersome. Many authors emphasize the potential of implicit LES for physically complex flows and for flows in complex geometries [52, 130, e.g.].

It is worthwhile to note that the original intention of subgrid-scale modeling was to stabilize under-resolved flow simulations while preserving reasonable accuracy of the resolved scales [162]. Rather than a deep reasoning about the physical correctness of the model assumptions, it actually was the artificial numerical dissipation of VON NEUMANN and RICHTMYER [178] that motivated SMAGORINSKY to propose his SGS model. KAWA-MURA and KUWAHARA [85] first reported indications that the truncation error of an upwind scheme may function as an SGS model in some cases. More generally, the use

of nonlinearly stable schemes for ILES was proposed by BORIS *et al.* [14]. Originating from the use of monotone schemes this approach has been dubbed MILES for monotonically integrated LES, although more accurate schemes satisfying less restrictive stability constraints are used in practice. For this reason the designation implicit LES, i.e. LES with an implicit SGS model, is considered to be a more appropriate for approaches that merge the numerical discretization with the SGS model.

Implicit LES can be approached in many ways; a comprehensive review is presented by GRINSTEIN *et al.* [51]. Mostly, 2nd-order-accurate schemes with a nonlinear regularization to maintain stability are used. Relevant discretizations are, e.g., the Flux-Corrected Transport (FCT) method of BORIS and BROOK [13], ZALESAK [188], the so-called Monotonic Upstream-Centered Scheme for Conservation Laws (MUSCL) of VAN LEER [175], the Multidimensional Positive Definite Advection Transport Algorithm (MPDATA) of SMOLARKIEWICZ [163], the Piecewise Parabolic Method (PPM) of COLELLA and WOODWARD [26], the entire family of Essentially Non-Oscillatory (ENO) schemes (see HARTEN *et al.* [57], SHU and OSHER [155]), and the Spectral Vanishing Viscosity (SVV) method of TADMOR [172].

As reported by GARNIER *et al.* [44], the application of robust discretization schemes to turbulence simulations is less straightforward: Even though the artificial dissipation introduced by second and higher order dissipative truncation errors indeed stabilizes under-resolved turbulence simulations, small flow scales may either behave unrealistically or suffer from excessive numerical damping. This causes probability-density functions of velocity increments and pressure to exhibit the typical behavior of low REYNOLDS-number turbulent flows, rather than that of high REYNOLDS-number ones. In particular, monotonic and total-variation diminishing (TVD) schemes, such as MUSCL, appear to be poorly suited for ILES. For implicit SGS models total-variation bounded (TVB) discretization schemes that allow for finite oscillations are have been used most successfully so far. The conclusions drawn by GARNIER *et al.* [44] are highly controversial and have stimulated a deeper analysis of ILES discretizations [42, 111–113, 143]. Recent studies report considerable success in predicting canonical turbulence and complex flows with ILES. In particular successful applications to wall-bounded turbulence, reported for the FCT method by FUREBY and GRINSTEIN [42] and for SVV by KARAMANOS and KARNIADAKIS [84] and SEVERAC and SERRE [151], are noteworthy. A successful application of PPM to decaying compressible turbulence is given by PORTER *et al.* [137, 138]. More recently the FCT method has been applied for complex engineering applications [52] and MPDATA is becoming a standard tool in geophysical sciences [114, 164, 165].

1.2 Contribution of this Work

Previous approaches to implicit SGS modeling rely on the application of preexisting discretization schemes, which have been developed for other purposes, to fluid-flow turbulence. Consequently, methods with suitable implicit SGS model are usually found by trial and error. Recent analyses have shown that stabilizing an under-resolved simulations by upwind or non-oscillatory schemes is insufficient for accurately representing SGS turbulence, although some general trends can be reproduced [36, 38, 44]. Employing implicit LES for prediction, however, requires numerical methods that are specially designed, optimized, and validated for the physical problem to be considered. A full coupling of SGS model and discretization scheme cannot be achieved without incorporating physical reasoning into the design of the implicit SGS model.

The objective of this work is to improve on the aforementioned modeling uncertainties. The starting point is to explore how implicit subgrid-scale modeling can be approached systematically. For this purpose, methods of design, analysis, and optimization of nonlinear discretizations for implicit LES are devised. Previous approaches to implicit modeling have frequently led to the belief that an implicit subgrid-scale model is generally inferred by the choice of discretization. This is not necessarily the case. In fact, implicit subgrid-scale models can be designed deliberately. The following systematic procedure for implicit SGS modeling is proposed:

1) Discretization design: First, a general nonlinear discretization scheme is developed on the basis of standard approaches. These, however, are modified in such a way that the resulting truncation error can be controlled. The resulting scheme should be as simple as possible to facilitate computation at reasonable cost, and as complex as necessary to allow for implicit modeling. A suitable framework is available by the finite-volume method, implying reconstruction or deconvolution of the unfiltered solution at cell faces and the approximation of the physical flux function by a numerical one.

2) Modified-differential-equation analysis: The general discretization method is analyzed with respect to its implicit SGS modeling capabilities. A suitable tool is an analysis of the modified-differential equation (MDEA) [98]. Based on TAYLOR-series expansions of the solution, such an analysis allows to determine the relation between the implicit model and any given explicit SGS model. With this method the MPDATA and the FCT were analyzed by MARGOLIN and RIDER [112] and FUREBY *et al.* [43], respectively. However, MDEA of more complex nonlinear discretization schemes for nonlinear three-dimensional differential equations is practically impossible. An alternative approach follows the method of DOMARADZKI [38, 69], where the spectral numerical dissipation is considered in an a-posteriori analysis.

3) SGS-model calibration: In the final step, appropriate values of the parameters inherent to the discretization scheme are determined. In classical numerical analysis, discretization coefficients are usually chosen in such a way that the formal order of accuracy of a discretization is maximum. This approach holds for direct numerical simulation but not for LES, where the chosen grid resolution essentially defines the range of represented scales. At a finite grid size, truncation errors interfere with the turbulence models. Thus, free discretization coefficients should be selected in such a way that the superposition of all contributions (truncation errors, SGS modeling terms, and modeling errors) is optimal. With implicit LES we do not aim at formally highest order of accuracy. Instead, discretization coefficients are optimized in such a way that the truncation error acts as a physically motivated SGS model in regions where the flow is turbulent, while maintaining a second-order accurate central discretization in regions where the flow is laminar.

The main achievement of this work is a novel nonlinear discretization for implicit LES based on a finite-volume method. Finite-volume methods imply cell-averaging and re-construction steps which - with respect to classical LES - can be interpreted as filtering and deconvolution. The resulting method is called the *Adaptive Local Deconvolution Method* (ALDM). It involves locality through the use of local approximation polynomials, nonlinear adaptivity through the use of a smoothness measure, and deconvolution through an approximate inversion of the finite-volume top-hat filtering. The truncation error of finite-volume methods readily appears as a divergence of a tensor. This form is advantageous with respect to physically motivated implicit modeling. The implicit model provided by the ALDM discretization can be interpreted as a combination of eddy-viscosity and scale similarity modeling. Model parameters are determined by a spectral-space analysis of the effective eddy viscosity for isotropic turbulence in the REYNOLDS number's infinite limit. We will show that implicit large-eddy simulation can be made rigorous by requiring that the numerical dissipation approximates the physical SGS dissipation obtained from the analysis of nonlinear interactions in turbulence. The good performance of the implicit model is demonstrated in various applications, e.g., three-dimensional homogeneous isotropic turbulence, plane channel flow, laminar-turbulent transition, and turbulent boundary-layer separation. Representing a full merger of numerical discretization and SGS model, ALDM has the potential to be a reliable, accurate, and efficient method for LES. Predictions of ALDM agree well with theory and experimental data. The implicit SGS model performs at least as well as established explicit models. This is possible because physical reasoning is incorporated into the design of the discretization scheme and discretization effects are fully taken into account within the SGS model formulation.

1.3 Mathematical Formulation

In LES the evolution of non-universal larger scales is computed whereas their interaction with universal smaller scales is modeled. The precise definition of large resolved scales varies from one approach to another. For the purpose of eliminating small scales, a spatial low-pass filter operation was suggested by LEONARD [92]. It is based on the convolution

$$\overline{\varphi}(\boldsymbol{x}, t) = G * \varphi = \int G(\boldsymbol{x} - \boldsymbol{x}')\varphi(\boldsymbol{x}', t)d\boldsymbol{x}' \ , \tag{1.1}$$

where G is a homogeneous filter kernel with normalization

$$\int G(\boldsymbol{x})d\boldsymbol{x} = 1 \ . \tag{1.2}$$

An overbar denotes the resolved-scale component of a function φ. The unresolved subfilter-scale (SFS) component results from

$$\varphi_{SFS}(\boldsymbol{x}, t) = \varphi(\boldsymbol{x}, t) - \overline{\varphi}(\boldsymbol{x}, t) \ . \tag{1.3}$$

LEONARD's concept is commonly employed for deriving model closures without reference to a computational grid. Therefore the term *subfilter scale* appears to be more appropriate than subgrid scale. More generally, a spatial and temporal filter can be considered, see ALDAMA [3] and DAKHOUL and BEDFORD [30]. Since spatial and temporal scales are coupled through the underlying transport equation it is common practice to consider spatial filtering only. This assumes that all relevant temporal scales are resolved by a time-step of small enough size. A converse approach as well as recent developments on temporal filtering can be found in PRUETT *et al.* [139, 140].

The initial-value problem for a generic transport equation with a nonlinear flux function $\boldsymbol{F}(\varphi)$ is considered,

$$\partial_t \varphi + \boldsymbol{\nabla} \cdot \boldsymbol{F}(\varphi) = 0 \ , \tag{1.4}$$

which yields the Modified Differential Equation (MDE)

$$\partial_t \overline{\varphi} + \boldsymbol{\nabla} \cdot \boldsymbol{F}(\overline{\varphi}) = \boldsymbol{\mathcal{G}}_G \ . \tag{1.5}$$

for the large-scale component $\overline{\varphi}$. The solution of Eq. (1.5) would be identical to the filtered solution of Eq. (1.4) if the residual $\boldsymbol{\mathcal{G}}_G$ could be computed exactly.

Using filtering as an analytical tool, the residual

$$\boldsymbol{\mathcal{G}}_G = \boldsymbol{\nabla} \cdot \boldsymbol{F}(\overline{\varphi}) - G * \boldsymbol{\nabla} \cdot \boldsymbol{F}(\varphi) \tag{1.6}$$

is obtained by subtracting the exact filtered transport equation

$$\partial_t \overline{\varphi} + G * \boldsymbol{\nabla} \cdot \boldsymbol{F}(\varphi) = 0 \tag{1.7}$$

from the modified differential equation (1.5). LEONARD [92] proposed a distinction between two contributions to $\boldsymbol{\mathcal{G}}_G$: The first component

$$\boldsymbol{\mathcal{G}}_L = \boldsymbol{\nabla} \cdot \boldsymbol{F}(\overline{\varphi}) - G * \boldsymbol{\nabla} \cdot \boldsymbol{F}(\overline{\varphi}) \tag{1.8}$$

is commonly known as the divergence of the LEONARD stress tensor and can be computed directly from the known filtered solution. The second contribution

$$\boldsymbol{\mathcal{G}}_{SFS} = G * \boldsymbol{\nabla} \cdot \boldsymbol{F}(\overline{\varphi}) - G * \boldsymbol{\nabla} \cdot \boldsymbol{F}(\varphi) \ . \tag{1.9}$$

arises from the subfilter scales. Reflecting the nonlinearity of $\boldsymbol{F}$, it encompasses both backscatter and dissipation due to autocorrelations between subfilter scales (the unresolved REYNOLDS stress) and semi-local cross correlations between SFS and resolved scales (so-called cross stress). In contrast to REYNOLDS' averaging [142], LEONARD's filtering is based on non-projective kernels, that is, $\overline{\overline{\varphi}} \neq \overline{\varphi}$ and $\overline{\overline{\varphi} \varphi_{SFS}} \neq 0$.

LEONARD showed that $\boldsymbol{\mathcal{G}}_L$ removes significant energy from the resolved scales and argued that better results are obtained when $\boldsymbol{\mathcal{G}}_L$ is not lumped together with the SFS model. He proposed the alternative MDE

$$\partial_t \overline{\varphi} + G * \boldsymbol{\nabla} \cdot \boldsymbol{F}(\overline{\varphi}) = \boldsymbol{\mathcal{G}}_{SFS} \ , \tag{1.10}$$

where the LEONARD stress merges with the nonlinear term. The right-hand side $\boldsymbol{\mathcal{G}}_{SFS} = -G * \boldsymbol{\nabla} \cdot \boldsymbol{\tau}_{SFS}$ has to be closed by an explicit model for the stress tensor

$$\boldsymbol{\tau}_{SFS} = \boldsymbol{F}(\varphi) - \boldsymbol{F}(\overline{\varphi}) \ . \tag{1.11}$$

Filtering and subfilter modeling are considered separately from numerical aspects of the subsequent discretization of the filtered equations. This implies that the numerical method has to provide an accurate solution to the resolved-scale equations.

An alternative derivation of the resolved-scale equations follows from the volume-balance procedure proposed by SCHUMANN [147, 148]. SCHUMANN starts from a given mesh for which the cell-averaged solution, denoted by $\overset{V-}{\varphi}$, is considered. Averaging and GAUSS' theorem lead directly to an integral equation form

$$\partial_t \overset{V-}{\varphi} + \oint \boldsymbol{n} \cdot \boldsymbol{F}(\varphi) dS = \partial_t \overset{V-}{\varphi} + \sum_l \overset{l-}{f} = 0 \tag{1.12}$$

for the time evolution of the finite-volume average $\overset{V}{\overline{\varphi}}$ of the quantity φ. Eq. (1.12) relates the finite-volume average to the transport across the surface of that volume by the cell-surface-averaged flux $\overset{l}{\overline{f}}$. The numerical method has to provide surface averages reconstructed from volume averages, which is accomplished through TAYLOR series expansion. Both surface average and volume average are discrete grid functions. The continuous solution is not reconstructed. With SCHUMANN's approach, scale separation, discretization, and SGS modeling are not separated. Discretization and splitting of resolved and unresolved scales is implied by the cell-averaging for a given mesh. A SGS model has to account for the transport by unresolved scales and for approximations involved in the reconstruction of surface averages. Accordingly, SCHUMANN's SGS model represents unresolved surface-averaged stresses, whereas LILLY [100], DEARDORFF [31], and LEONARD [92] consider filtered subgrid stresses corresponding to a volume average. A clear advantage of SCHUMANN's finite-volume method, which has been intensely used by GRÖTZBACH *et al.* [53–55], e.g., is that grid inhomogeneity and anisotropy are readily incorporated. The drawback - an unusual notation notwithstanding - lies in the strong influence of the underlying numerical method on the subgrid closure's character.

A link between the volume-balance procedure and the filtering approach can be constructed by evaluating the filtered conservation law (1.7) with the top-hat filter kernel. Top-hat filtering returns the cell-average of a function. An inverse-filter operation $\varphi = G^{-1} * \overline{\varphi}$ is used for the reconstruction of the unfiltered solution φ in (1.7) from the filtered solution $\overline{\varphi}$. At this point it should be noted that LEONARD's ansatz implies a *subsequent* discretization of the filtered equations, where the discrete grid function $\overline{\varphi}_N$ is obtained by projecting the filtered continuous function $\overline{\varphi}$ onto the numerical grid. This projection corresponds to an additional filtering in FOURIER space with cut-off at the NYQUIST wavenumber $\xi_N = \pi/h$, where h is a constant grid spacing. Exact deconvolution is ill-posed since non-represented scales cannot be recovered, that is, $G^{-1} * \overline{\varphi}_N = \varphi_N \neq \varphi$. The discrete filtered conservation law reads

$$\partial_t \overline{\varphi}_N + G * \boldsymbol{\nabla} \cdot \boldsymbol{F}_N(\varphi_N) = \boldsymbol{\mathcal{G}}_R \ . \tag{1.13}$$

The approximation of φ_N in terms of $\overline{\varphi}_N$ is called the *soft deconvolution problem* which can be handled numerically by an inverse filter operation G^{-1} on the represented scales. The computation of

$$\boldsymbol{\mathcal{G}}_R \ = G * \boldsymbol{\nabla} \cdot \boldsymbol{F}_N(\varphi_N) - G * \boldsymbol{\nabla} \cdot \boldsymbol{F}(\varphi) \ = -G * \boldsymbol{\nabla} \cdot \boldsymbol{\tau}_{SGS} \tag{1.14}$$

involves unavailable information on subgrid-scales $\varphi_{SGS} = \varphi - \varphi_N$ and therefore constitutes the *hard deconvolution problem* that requires modeling. Approximating the SGS stress tensor

$$\boldsymbol{\tau}_{SGS} = \boldsymbol{F}(\varphi) - \boldsymbol{F}_N(\varphi_N) \tag{1.15}$$

by an explicit model obviously cannot be accomplished in terms of local error norms. Rather the model should closely approximate the effect of $\boldsymbol{\mathcal{G}}_{SGS}$ on the resolved scales.

With implicit LES the truncation error of the discretization scheme itself is employed to model the SGS energy transfer instead of an explicit computation of the SGS stress. Due to numerical approximations the exact solution of the discrete equations does not satisfy Eq. (1.13) with $\boldsymbol{\tau}_{SGS} = \boldsymbol{0}$, but does satisfy the MDE

$$\partial_t \overline{\varphi}_N + G * \boldsymbol{\nabla} \cdot \boldsymbol{F}_N(\varphi_N) = \boldsymbol{\mathcal{G}}_N \ . \tag{1.16}$$

A spatial semi-discretization has the generic truncation error

$$\boldsymbol{\mathcal{G}}_N = G * \boldsymbol{\nabla} \cdot \boldsymbol{F}_N(\varphi_N) - \widetilde{G * \boldsymbol{\nabla} \cdot} \widetilde{\boldsymbol{F}}_N(\widetilde{\varphi}_N) \ , \tag{1.17}$$

where a tilde now indicates the respective numerical approximation. For example, the unfiltered continuous solution φ is unknown in an LES. However, an approximation $\widetilde{\varphi}_N$ of the grid function φ_N can be obtained from $\overline{\varphi}_N$ by regularized deconvolution $\widetilde{\varphi}_N = \widetilde{G}^{-1} * \overline{\varphi}_N$ [34, 168].

The truncation error, Eq. (1.17), can act as an implicit SGS model. Particularly, an explicit SGS model can be reproduced, if the filtered divergence of the model SGS tensor is approximated as

$$\boldsymbol{\mathcal{G}}_N \approx -G * \boldsymbol{\nabla} \cdot \boldsymbol{\tau}_{SGS} \ . \tag{1.18}$$

This can be achieved either by representing a given explicit SGS model for $\boldsymbol{\mathcal{G}}_{SGS}$ by the implicit model $\boldsymbol{\mathcal{G}}_N$, or by direct identification of discretization parameters from theoretical, experimental or empirical data.

1.4 Outline

In Chapter 2 ALDM is introduced as a new nonlinear discretization of the NAVIER–STOKES equations. In Chapter 3 the modified differential equation of ALDM is analyzed. Optimum values of free discretization parameters are determined in such a way that the truncation error of the discretization method acts as a physically motivated SGS model in developed NAVIER–STOKES turbulence. This parameter selection is then validated in Chapter 4 for large-scale forced and decaying three-dimensional homogeneous isotropic turbulence as well as for instability and breakdown of the 3-D Taylor-Green vortex. The response of the implicit SGS model to flow anisotropy and wall-bounded turbulence is analyzed in Chapter 5. A simple modification is proposed and assessed for turbulent channel flow at various REYNOLDS numbers. For further validation, zero-pressure-gradient boundary layer flow is considered that undergoes transition from the laminar

to the turbulent regime. In Chapter 5, the implicit SGS modeling is extended to LES of passive-scalar mixing. An adaptive advection algorithm is developed and discussed with respect to its numerical and turbulence-theoretical background. Computational results are presented for the turbulent transport of passive scalars in isotropic turbulence and in turbulent channel flow for a wide range of SCHMIDT numbers. For a final validation of ALDM, an LES of incompressible fully-turbulent flat-plate boundary-layer flow subjected to a constant adverse pressure gradient is presented in Chapter 7. REYNOLDS number and pressure-gradient parameters adapted to an experimental setup. Chapter 8 summarizes this study.

DISCRETIZATION-SCHEME DESIGN

In the following we develop a general nonlinear discretization scheme for the three-dimensional NAVIER-STOKES equations. Preliminary investigations on the example of the one-dimensional viscous BURGERS equation are summarized in Appendix A. The resulting method is based on standard approaches which, however, are modified in such a way that the resulting truncation error can function as implicit SGS model.

2.1 The incompressible NAVIER-STOKES Equations

We consider incompressible turbulent flows which are governed by the NAVIER-STOKES equations in non-dimensional form

$$\partial_t \boldsymbol{u} + \boldsymbol{\nabla} \cdot \boldsymbol{F} + \boldsymbol{\nabla}\, p - \nu\, \boldsymbol{\nabla} \cdot \boldsymbol{\nabla} \boldsymbol{u} = \boldsymbol{0} \ , \tag{2.1}$$

where $\boldsymbol{u} = [u, v, w]$ is the velocity, $\boldsymbol{F} = \boldsymbol{u}\boldsymbol{u}$ is the nonlinear convection term, and ν is the molecular viscosity. The pressure p serves as a scalar field to satisfy the incompressible continuity equation

$$\boldsymbol{\nabla} \cdot \boldsymbol{u} = 0 \ . \tag{2.2}$$

The nonlinearity enters the pressure through the POISSON equation

$$\boldsymbol{\nabla} \cdot \boldsymbol{\nabla} p = -\boldsymbol{\nabla} \cdot \boldsymbol{\nabla} \cdot \boldsymbol{F} \ , \tag{2.3}$$

which has to be accounted for in subgrid-scale (SGS) modeling. We collect all nonlinear terms in

$$\boldsymbol{\nabla} \cdot \boldsymbol{N}(\boldsymbol{u}) = \boldsymbol{\nabla} \cdot \boldsymbol{F}(\boldsymbol{u}) + \boldsymbol{\nabla}\, p \ . \tag{2.4}$$

The differential equations for the resolved scales are obtained by applying the filter (1.1) to Eqs. (2.1) and (2.2)

$$\partial_t \overline{\boldsymbol{u}}_N + \boldsymbol{G} * \boldsymbol{\nabla} \cdot \boldsymbol{N}_N(\boldsymbol{u}_N) - \nu\, \boldsymbol{\nabla} \cdot \boldsymbol{\nabla}\overline{\boldsymbol{u}}_N = -\boldsymbol{G} * \boldsymbol{\nabla} \cdot \boldsymbol{\tau}_{SGS} \ , \tag{2.5a}$$

$$\boldsymbol{\nabla} \cdot \overline{\boldsymbol{u}}_N = 0 \ . \tag{2.5b}$$

The subscript N indicates the grid functions obtained by projecting continuous functions onto the numerical grid.

In Eq. (2.5) the represented-scale part of the unfiltered field is reconstructed for computing the nonlinear term [34]. This can be accomplished by an inverse-filter operation $\boldsymbol{u}_N = \boldsymbol{G}^{-1} * \overline{\boldsymbol{u}}_N$ applied to represented scales. Since non-represented scales cannot be recovered it is $\boldsymbol{u}_N \neq \boldsymbol{u}$, which results in the subgrid-stress tensor

$$\boldsymbol{\tau}_{SGS} = \boldsymbol{N}(\boldsymbol{u}) - \boldsymbol{N}_N(\boldsymbol{u}_N) \ . \tag{2.6}$$

For uniform viscosity the diffusive term is linear in terms of $\boldsymbol{u}_N$ and does not contribute to the SGS tensor. For a closure of Eq. (2.5) the subgrid-stress tensor (2.6) has to be approximated by a model.

Instead of an explicit computation of the SGS stress, the truncation error of the discretization scheme itself is employed to model the effects of unresolved scales. Due to numerical approximations the exact solution of the discrete equations does not satisfy Eq. (2.5) with $\boldsymbol{\tau}_{SGS} = \boldsymbol{0}$, but rather a Modified Differential Equation (MDE). For a general implicit SGS model, as implied by a general LES discretization scheme, this MDE is given by

$$\partial_t \overline{\boldsymbol{u}}_N + \widetilde{\boldsymbol{G}} * \widetilde{\boldsymbol{\nabla}} \cdot \widetilde{\boldsymbol{N}}_N(\widetilde{\boldsymbol{u}}_N) - \nu \, \boldsymbol{\nabla} \cdot \boldsymbol{\nabla} \overline{\boldsymbol{u}}_N = \boldsymbol{0} \ , \tag{2.7a}$$

$$\boldsymbol{\nabla} \cdot \overline{\boldsymbol{u}}_N = 0 \ . \tag{2.7b}$$

In the following we consider a top-hat filter-kernel $\boldsymbol{G}$, see Eq. (2.10). For this filter kernel the LES equations (2.5) evaluated on a grid correspond to a finite-volume discretization, and $\widetilde{\boldsymbol{u}}_N$ denotes an approximant of the velocity $\boldsymbol{u}_N$. The local RIEMANN problem is approximated by a consistent numerical flux function $\widetilde{\boldsymbol{F}}_N$ which yields the divergence-free nonlinear term $\widetilde{\boldsymbol{N}}_N$. The symbols $\widetilde{\boldsymbol{G}} * \widetilde{\boldsymbol{\nabla}}$ indicate that $\boldsymbol{G}$ and $\boldsymbol{\nabla}$ are replaced by their respective numerical approximations. In fact $\widetilde{\boldsymbol{G}} * \widetilde{\boldsymbol{\nabla}}$ can be a nonlinear operator. The truncation error due to the discretization of the convective term is accordingly

$$\boldsymbol{\mathcal{G}}_N = \boldsymbol{G} * \boldsymbol{\nabla} \cdot \boldsymbol{N}_N(\boldsymbol{u}_N) - \widetilde{\boldsymbol{G}} * \widetilde{\boldsymbol{\nabla}} \cdot \widetilde{\boldsymbol{N}}_N(\widetilde{\boldsymbol{u}}_N) \ . \tag{2.8}$$

We point out that the effect of the truncation error on the diffusive flux could also be considered, as was done by ZANDONADE et al. [189] for finite-volume optimal LES. This approach, however, can lead to REYNOLDS-number dependent model coefficients and is therefore undesirable. We employ standard high-order centered schemes for discretizing

the diffusive flux. Their contribution to the implicit model is negligible even for rather small REYNOLDS numbers as will be shown below.

The numerical truncation error, i.e. the implicit SGS model, resembles an explicit SGS model if the filtered divergence of the model SGS tensor in Eq. (2.5) is approximated

$$\boldsymbol{\mathcal{G}}_N \approx -\boldsymbol{G} * \boldsymbol{\nabla} \cdot \boldsymbol{\tau}_{SGS} \ . \tag{2.9}$$

In the following we develop a general nonlinear discretization scheme for the NAVIER-STOKES equations, which is as simple as possible to facilitate computation and as complex as necessary to allow for implicit modeling. The essential building blocks are:

(1) a numerical integration and differentiation scheme based on the finite-volume method,

(2) an adaptive local reconstruction operator that returns the approximately deconvolved solution at the cell faces,

(3) a numerical flux function which approximates the physical convective flux.

2.2 Finite-Volume Filter and Differentiation Operator

With ALDM we consider the discretized equations directly as proposed by SCHUMANN [148]. Although filtering is not performed explicitly we can use the filter formulation of LEONARD as analytical tool when designing and analyzing the discrete operators. The framework is a finite-volume discretization with the top-hat filter

$$\boldsymbol{G}(\boldsymbol{x}_{i,j,k}, \boldsymbol{x}) = \frac{1}{hx_i \ hy_j \ hz_k} \begin{cases} 1 & , (\boldsymbol{x}_{i,j,k} + \boldsymbol{x}) \in \Omega_{i,j,k} \\ 0 & , \text{ otherwise} \end{cases} , \tag{2.10}$$

which returns the cell average of a function

$$\overline{\varphi}(\boldsymbol{x}_{i,j,k}, t) = \frac{1}{hx_i \ hy_j \ hz_k} \iiint\limits_{\Omega_{i,j,k}} \varphi(\boldsymbol{x}_{i,j,k} - \boldsymbol{x}', t) \ d\boldsymbol{x}' \ . \tag{2.11}$$

The integration domain

$$\Omega_{i,j,k} = \left[x_{i-\frac{1}{2}}, x_{i+\frac{1}{2}} \right] \times \left[y_{j-\frac{1}{2}}, y_{j+\frac{1}{2}} \right] \times \left[z_{k-\frac{1}{2}}, z_{k+\frac{1}{2}} \right] \tag{2.12}$$

is equivalent to a cell of the underlying CARTESian computational grid so that the filter width corresponds to the local grid size

$$
\boldsymbol{h}_{i,j,k} = \begin{bmatrix} hx_i \\ hy_j \\ hz_k \end{bmatrix} = \begin{bmatrix} x_{i+1/2} - x_{i-1/2} \\ y_{j+1/2} - y_{j-1/2} \\ z_{k+1/2} - z_{k-1/2} \end{bmatrix} .
\tag{2.13}
$$

Here and in the following half-integer indices denote cell faces.

For implicit SGS modeling we only consider the nonlinear term $\boldsymbol{N}(\boldsymbol{u})$ in the momentum equation (2.1), whereas the linear terms, i.e. the diffusive flux, are approximated by a standard centered discretization. By GAUSS' and GREEN's theorems filtering applied to the flux divergence $\boldsymbol{\nabla} \cdot \boldsymbol{N}(\boldsymbol{u})$ returns the flux through the surface $S_{i,j,k}$ of cell $I_{i,j,k}$

$$
[\boldsymbol{G} * \boldsymbol{\nabla} \cdot \boldsymbol{N}(\boldsymbol{u})]_{i,j,k} = \frac{1}{hx_i \, hy_j \, hz_k} \iint\limits_{S_{i,j,k}} \boldsymbol{n} \cdot \boldsymbol{F} \, dS + \frac{1}{hx_i \, hy_j \, hz_k} \iint\limits_{S_{i,j,k}} \boldsymbol{n} p \, dS , \tag{2.14}
$$

where $\boldsymbol{n}$ is the unit normal vector on the cell faces. ALDM applies to the convective flux $\boldsymbol{F} = \boldsymbol{u}\boldsymbol{u}$. For incompressible flows the normal stresses due to the pressure p are subsequently computed by solving a POISSON equation (2.3). Evaluating the convective integral in Eq. (2.14) we obtain

$$
\begin{aligned}
\frac{1}{hx_i \, hy_j \, hz_k} \iint\limits_{S_{i,j,k}} \boldsymbol{n} \cdot \boldsymbol{F} \, dS \;=\; & \frac{1}{hx_i} \left(\overset{1-}{\boldsymbol{f}}(x_{i+\frac{1}{2}}, y_j, z_k) - \overset{1-}{\boldsymbol{f}}(x_{i-\frac{1}{2}}, y_j, z_k) \right) \\
& + \frac{1}{hy_j} \left(\overset{2-}{\boldsymbol{f}}(x_i, y_{j+\frac{1}{2}}, z_k) - \overset{2-}{\boldsymbol{f}}(x_i, y_{j-\frac{1}{2}}, z_k) \right) \\
& + \frac{1}{hz_k} \left(\overset{3-}{\boldsymbol{f}}(x_i, y_j, z_{k+\frac{1}{2}}) - \overset{3-}{\boldsymbol{f}}(x_i, y_j, z_{k-\frac{1}{2}}) \right) .
\end{aligned}
\tag{2.15}
$$

The flux vector $\overset{l}{\boldsymbol{f}} = u_l \boldsymbol{u}$ denotes the l-direction component of $\boldsymbol{F}$ and $\overset{l-}{\boldsymbol{f}}$ is the spatial average of $\overset{l}{\boldsymbol{f}}$ over the cell face with $n_l = \pm 1$. Here and in the following the coordinate system $\{ x , y , z \}$ is synonymous with $\{ x_1 , x_2 , x_3 \}$.

The numerical computation of $\overset{l-}{\boldsymbol{f}}$ involves approximations which we explain now on the example of the flux in z-direction

$$
\overset{3-}{\boldsymbol{f}}(x_i, y_j, z_{k+\frac{1}{2}}) = \frac{1}{hx_i \, hy_j} \int\limits_{x_{i-\frac{1}{2}}}^{x_{i+\frac{1}{2}}} \int\limits_{y_{j-\frac{1}{2}}}^{y_{j+\frac{1}{2}}} \overset{3}{\boldsymbol{f}}(x, y, z_{k+\frac{1}{2}}) dx dy .
\tag{2.16}
$$

A GAUSSian quadrature rule with $(2m+1)^2$ numerical integration points returns

$$\overset{3-}{\boldsymbol{f}}(x_i, y_j, z_{k+\frac{1}{2}}) \doteq \sum_{\alpha=1}^{2m+1} \sum_{\beta=1}^{2m+1} C_{\alpha\beta} \overset{3}{\boldsymbol{f}}(x_{i+\alpha-m}, y_{j+\beta-m}, z_{k+\frac{1}{2}}) \ . \tag{2.17}$$

Our present computational implementation allows for two different integration schemes with 3^2 nodes, given by

$$\boldsymbol{C}_2 = \begin{bmatrix} 0 & 0 & 0 \\ 0 & 1 & 0 \\ 0 & 0 & 0 \end{bmatrix} \quad \text{and} \quad \boldsymbol{C}_4 = \frac{1}{24} \begin{bmatrix} 0 & 1 & 0 \\ 1 & 20 & 1 \\ 0 & 1 & 0 \end{bmatrix} \ . \tag{2.18}$$

The coefficient matrix $\boldsymbol{C}_2$ of the first scheme yields a second-order accurate solution on equidistant grids. A fourth-order integration scheme is obtained with $\boldsymbol{C}_4$. Preliminary tests, see Appendix B, showed that the difference between these operators has negligible effect on the computed energy and dissipation spectra. Therefore, we use the simple second-order integration $\boldsymbol{C}_2$ throughout this work.

A remark on the discretization of the POISSON equation (2.3) is in order. LANGFORD and MOSER [90] have pointed out that, given a divergence-free continuous turbulence field, for the corresponding filtered field a divergence residual arises. They propose to adjust the discrete divergence operator appropriately. A similar issue is faced with ALDM where an adaptive reconstruction could also be used for the discrete divergence operator. However, in doing so the implicit model would become significantly more complex. ZANDONADE *et al.* [189] come to the conclusion that the accuracy gained by the adjusted discrete divergence operator does not justify the increased complexity. We follow this conclusion and employ standard discrete operators for the POISSON equation. Parameters of ALDM, as will be shown below, enter the discrete Poisson equation by the discretization of the convective fluxes. Since energy redistribution due to pressure thus also contains the adaptive deconvolution through the discrete divergence of the convective fluxes the model parameters which will be determined in Section 3.3 reflect both contributions to the energy transfer.

2.3 Solution-Adaptive Local Deconvolution

As a consequence of identity (2.15), finite-volume schemes require a reconstruction of data at the faces of the computational volumes which corresponds to approximate deconvolution [1]. The three-dimensional (3-D) filter operation is defined in Eq. (2.11). The

3-D top-hat filter kernel can be factorized into three one-dimensional (1-D) operators

$$\boldsymbol{G}(\boldsymbol{x}) = \boldsymbol{G}_x(x) \cdot \boldsymbol{G}_y(y) \cdot \boldsymbol{G}_z(z) \ . \tag{2.19}$$

An inverse-filter operation can be defined as a convolution with the inverse kernel

$$\boldsymbol{G}^{-1}(\boldsymbol{x}) = \boldsymbol{G}_x^{-1}(x) \cdot \boldsymbol{G}_y^{-1}(y) \cdot \boldsymbol{G}_z^{-1}(z) \ , \tag{2.20}$$

factorized into three 1-D operators. An exact inverse filter operation is ill-posed, however, the de-filtered solution can be computed approximately by regularized deconvolution [34]. Following Eq. (2.20), the numerical scheme for performing approximate deconvolution with ALDM is assembled from 1-D operators.

The 1-D reconstruction (i.e. deconvolution and interpolation) operator is denoted by $\mathcal{X}_x^\lambda$. It is defined on a grid $x_N = \{x_i\}$ with cell size $h_i = x_{i+\frac{1}{2}} - x_{i-\frac{1}{2}}$. Applied to the filtered grid function $\overline{\varphi}_N = \{\overline{\varphi}(x_i)\}$ the reconstruction operator returns the approximately deconvolved grid function $\widetilde{\varphi}_N^\lambda \doteq \{\varphi(x_{i+\lambda})\}$ on the shifted grid $x_N^\lambda = \{x_{i+\lambda}\}$

$$\mathcal{X}_x^\lambda \overline{\varphi}_N = \{\varphi\left(\widetilde{\varphi}, x_{i+\lambda}\right) + \mathcal{O}\left(h_i^\kappa\right)\} = \widetilde{\varphi}_N^\lambda \ . \tag{2.21}$$

The filtered data are given at the cell centers $\{x_i\}$. Reconstruction at the left cell faces $\{x_{i-\frac{1}{2}}\}$ is indicated by $\lambda = -1/2$ and at the right faces by $\lambda = +1/2$. For obtaining a 3-D reconstruction by successive 1-D operations yet another approximation of the partially deconvolved solution is required at the cell centers. The respective operator is indicated by $\lambda = 0$.

Deconvolution and interpolation are done simultaneously. The unfiltered solution at the cell faces is obtained from a primitive-function reconstruction as proposed by HARTEN *et al.* [57]. Given the cell-averaged grid function $\overline{\varphi}_N$, point values of the primitive function

$$\Phi(x) = \int\limits_{x_0}^{x} \varphi(x')dx' \tag{2.22}$$

can be expressed by the cell averages $\overline{\varphi}_N$ as

$$\Phi(x_{i+\frac{1}{2}}) = \sum_{j=i_0}^{i} h_j \overline{\varphi}_j \ . \tag{2.23}$$

We now apply interpolation to the point values of the primitive function. Given a generic k-cell stencil (spanning $(k+1)$ cell faces) with shift r of the left-most stencil point with

respect to x_i the interpolation polynomial in LAGRANGE form is

$$\check{\Phi}_{k,r}(x) = \sum_{m=0}^{k} \Phi(x_{i-r+m-\frac{1}{2}}) \prod_{\substack{n=0 \\ n \neq m}}^{k} \frac{x - x_{i-r+n-\frac{1}{2}}}{x_{i-r+m-\frac{1}{2}} - x_{i-r+n-\frac{1}{2}}} \quad . \tag{2.24}$$

Standard approximation theory gives

$$\check{\Phi}_{k,r}(x) = \Phi(x) + \mathcal{O}\left(h_i^{k+1}\right) \quad , \tag{2.25}$$

provided the function $\varphi(x)$ is piecewise smooth on the interpolation stencil. Note that $\Phi(x)$ is one derivative smoother than $\varphi(x)$. We define

$$\check{\varphi}_{k,r}(x) = \frac{\partial}{\partial x}\check{\Phi}_{k,r}(x) \quad , \tag{2.26}$$

where the dependence on the lower limit x_0 in (2.22) cancels out. From (2.25) follows immediately

$$\check{\varphi}_{k,r}(x) = \varphi(x) + \mathcal{O}\left(h_i^{k}\right) \quad . \tag{2.27}$$

Taking the derivative on both sides of (2.24), we finally obtain

$$\check{\varphi}_{k,r}(x_{i+\lambda}) = \sum_{l=0}^{k-1} \alpha_{k,r,l}^{\lambda}(x_i)\overline{\varphi}_{i-r+l} \quad , \tag{2.28}$$

where

$$\alpha_{k,r,l}^{\lambda}(x_i) = \left(x_{i-r+l+\frac{1}{2}} - x_{i-r+l-\frac{1}{2}}\right) \sum_{m=l+1}^{k} \frac{\sum\limits_{\substack{p=0 \\ p \neq m}}^{k} \prod\limits_{\substack{n=0 \\ n \neq p,m}}^{k} x_{i+\lambda} - x_{i-r+n-\frac{1}{2}}}{\prod\limits_{\substack{n=0 \\ n \neq m}}^{k} x_{i-r+m-\frac{1}{2}} - x_{i-r+n-\frac{1}{2}}} \tag{2.29}$$

is found after some algebra, see also SHU [154], where a more detailed derivation is given. The grid-dependent coefficients $\alpha_{k,r,l}^{\lambda}(x_i)$ contain the deconvolution, i.e. the inversion of the top-hat filter on the space of admissible local interpolation polynomials, and the interpolation from x_i to $x_{i+\lambda}$. As indicated, this rule applies for grids with variable mesh width and for arbitrary target positions $x_{i+\lambda}$. In case of a staggered grid the values of x_i are different for each velocity component and the coefficients $\alpha_{k,r,l}^{\lambda}$ have to be specified accordingly.

Selecting a particular interpolation stencil (k, r) would return a linear discretization

$$\widetilde{\varphi}_N^\lambda(x_{i+\lambda}) = \sum_{l=0}^{k-1} \alpha_{k,r,l}^\lambda(x_i)\overline{\varphi}_N(x_{i-r+l}) = \varphi(x_{i+\lambda}) + \mathcal{O}\left(h_i{}^k\right)$$

with a fixed, solution independent functional expression of the k-th order truncation error.

HARTEN *et al.* [57] have combined reconstruction with an interpolation-stencil selection, leading to the essentially non-oscillatory (ENO) property of the reconstructed solution. This procedure constitutes a nonlinear approximation or regularized deconvolution of the filtered solution since the stencil selection depends on the local properties of the actual computed solution. ALDM adopts the idea of the Weighted-Essentially-Non-Oscillatory (WENO) scheme of SHU [154] where interpolation polynomials of order $k \equiv K$ are selected and combined nonlinearly. The essential difference between ALDM and WENO is that we superpose all interpolants of order $k = 1, \ldots, K$

$$\widetilde{\varphi}_N^\lambda(x_{i+\lambda}) = \sum_{k=1}^{K}\sum_{r=0}^{k-1} \omega_{k,r}^\lambda(\overline{\varphi}_N, x_i) \ \sum_{l=0}^{k-1} \alpha_{k,r,l}^\lambda(x_i) \ \overline{\varphi}_N(x_{i-r+l}) \qquad (2.30)$$

to allow for lower-order contributions to the truncation error for implicit SGS modeling. The restriction on the local approximation polynomials is that their stencils interpolate at the cell faces $x_{i+\lambda}$, extrapolating stencils are excluded. Admissible stencils range from x_{i-r} to $x_{i-r+k-1}$ with $r = 0, \ldots, k-1$.

The weights $\omega_{k,r}^\lambda(\overline{\varphi}_N, x_i)$ can be constructed as to yield an accurate approximation of order $2K-1$ in smooth regions [154]. For our purpose, however, we do not need highest possible order of accuracy. Rather the superposition (2.30) introduces free discretization parameters which allow to control error cancelations. The sum of all weights is constrained to be unity for consistency. More restrictively we require

$$\sum_{r=0}^{k-1} \omega_{k,r}^\lambda = \frac{1}{K} , \qquad (2.31)$$

with $k = 1, \ldots, K$, and compute each weight from

$$\omega_{k,r}^\lambda(\overline{\varphi}_N, x_i) = \frac{1}{K}\frac{\gamma_{k,r}^\lambda \beta_{k,r}\left(\overline{\varphi}_N, x_i\right)}{\sum\limits_{s=0}^{k-1} \gamma_{k,s}^\lambda \beta_{k,s}\left(\overline{\varphi}_N, x_i\right)} , \qquad (2.32)$$

with $r = 0, \ldots, k - 1$ for each $k = 1, \ldots, K$. The solution-adaptive behavior of ALDM is controlled by the functional

$$\beta_{k,r} \left(\overline{\varphi}_N, x_i \right) = \left(\varepsilon_\beta + \sum_{l=-r}^{k-r-2} \left(\overline{\varphi}_{i+l+1} - \overline{\varphi}_{i+l} \right)^2 \right)^{-2} , \qquad (2.33)$$

where $\varepsilon_\beta = 10^{-10}$ is a small number to prevent division by zero. $\beta_{k,r}$ measure the smoothness of the grid function on the respective stencil to obtain a non-linear adaptation of the deconvolution. LIU *et al.* [102] and by JIANG and SHU [80] proposed alternative smoothness measures for WENO schemes. Their use for ALDM is evaluated for the 1-D BURGERS equation in Appendix A. It is worth mentioning that an advantage of the total-variation smoothness measure, definition (2.33) is that

$$\beta_{k,r} \left(\overline{\varphi}_N, x_i \right) = \beta_{k,r-1} \left(\overline{\varphi}_N, x_{i-1} \right) \qquad (2.34)$$

can be exploited to improve computational efficiency.

The parameters $\gamma_{k,r}^{+1/2}$, $\gamma_{k,r}^{-1/2}$, and $\gamma_{k,r}^0$ represent a stencil-selection preference that would become effective in the statistically homogeneous case. The requirement of an isotropic discretization for this case implies symmetries on the parameters

$$\gamma_{k,r}^{-1/2} = \gamma_{k,k-1-r}^{+1/2} \qquad \text{and} \qquad \gamma_{k,r}^0 = \gamma_{k,k-1-r}^0 . \qquad (2.35)$$

As consequence of Eq. (2.31) the number of independent parameters is further reduced by

$$\sum_{r=0}^{k-1} \gamma_{k,r}^{+1/2} = 1 \qquad \text{and} \qquad \sum_{r=0}^{k-1} \gamma_{k,r}^0 = 1 . \qquad (2.36)$$

In the present implementation of ALDM we use $K = 3$, which is a compromise between computational complexity and modeling. Hence, four parameters $\{ \gamma_{2,0}^{+1/2} , \gamma_{3,0}^{+1/2} , \gamma_{3,1}^{+1/2} , \gamma_{3,1}^0 \}$ are available for modeling.

We assemble now the 3-D adaptive local deconvolution operator $\boldsymbol{\mathcal{X}}^{\boldsymbol{\lambda}}$ from 1-D operators of the kind of $\mathcal{X}_x^{\lambda}$. Following Eq. (2.20) we obtain

$$\widetilde{\varphi}_N^{\boldsymbol{\lambda}} = \boldsymbol{\mathcal{X}}^{\boldsymbol{\lambda}} \, \overline{\varphi}_N = \mathcal{X}_z^{\lambda_3} \left(\mathcal{X}_y^{\lambda_2} \left(\mathcal{X}_x^{\lambda_1} \, \overline{\varphi}_N \right) \right) . \qquad (2.37)$$

Analogous to the procedure in 1-D the vector $\boldsymbol{\lambda} = [\lambda_1 , \lambda_2 , \lambda_3]$ indicates the relative target position. Required operations are summarized in Table 2.1. Theoretically, the sequence of these 1-D operators is arbitrary. However, there is a certain preferred choice which minimizes computational cost. Since each operator in Table 2.1 consists

Direction	relative target index λ	Example
(R) rightward	$[+\frac{1}{2},\ 0\ ,\ 0\ ]$	$\widetilde{\boldsymbol{u}}^R_{i,j,k} \approx \boldsymbol{u}(x_{i+\frac{1}{2}}, y_j, z_k)$
(L) leftward	$[-\frac{1}{2},\ 0\ ,\ 0\ ]$	$\widetilde{\boldsymbol{u}}^L_{i,j,k} \approx \boldsymbol{u}(x_{i-\frac{1}{2}}, y_j, z_k)$
(F) forward	$[\ 0\ ,+\frac{1}{2},\ 0\ ]$	$\widetilde{\boldsymbol{u}}^F_{i,j,k} \approx \boldsymbol{u}(x_i, y_{j+\frac{1}{2}}, z_k)$
(B) backward	$[\ 0\ ,-\frac{1}{2},\ 0\ ]$	$\widetilde{\boldsymbol{u}}^B_{i,j,k} \approx \boldsymbol{u}(x_i, y_{j-\frac{1}{2}}, z_k)$
(U) upward	$[\ 0\ ,\ 0\ ,+\frac{1}{2}]$	$\widetilde{\boldsymbol{u}}^U_{i,j,k} \approx \boldsymbol{u}(x_i, y_j, z_{k+\frac{1}{2}})$
(D) downward	$[\ 0\ ,\ 0\ ,-\frac{1}{2}]$	$\widetilde{\boldsymbol{u}}^D_{i,j,k} \approx \boldsymbol{u}(x_i, y_j, z_{k-\frac{1}{2}})$

Table 2.1: Interpolation directions for 3-D reconstruction.

of two centered and one shift step, operations with $\lambda = \pm 1/2$ should be performed last. Furthermore, the order should be chosen by cyclic permutation to achieve rotational invariance of the implicit model. For example, to compute the approximately deconvolved solution $\widetilde{\boldsymbol{u}}^L_{ijk}$ at the left cell face $\boldsymbol{\lambda} = [-1/2,\, 0\,,\, 0\,]$ we first perform a 1-D deconvolution in y-direction using the central operator $\mathcal{X}^0_y$. Then, another 1-D operator $\mathcal{X}^0_z$ is applied to the partially deconvolved solution. Only in the final step the deconvolved solution is interpolated to the target position by $\mathcal{X}^{-1/2}_x$. For computational efficiency we simultaneously compute $\widetilde{\boldsymbol{u}}^R_{ijk}$ by applying $\mathcal{X}^{+1/2}_x$ in the final step. Note that $\widetilde{\boldsymbol{u}}^R_{i-1\,jk}$ stands for a second approximation at the same cell face as $\widetilde{\boldsymbol{u}}^L_{ijk}$ but with the neighbor cell $I_{i-1\,jk}$ as reference. For further details on the efficient implementation of ALDM refer to Appendix B where also possible simplifications are discussed.

2.4 Numerical Flux Function

Another tool exploited is the choice of an appropriate and consistent numerical flux function $\widetilde{\boldsymbol{F}}_N = \left[\overset{1}{\widetilde{\boldsymbol{f}}},\, \overset{2}{\widetilde{\boldsymbol{f}}},\, \overset{3}{\widetilde{\boldsymbol{f}}} \right]$ that operates on the reconstruction of the unfiltered solution at the cell faces and approximates the physical flux function, i.e.,

$$\widetilde{\boldsymbol{F}}_N \approx \boldsymbol{F} = \boldsymbol{u}\boldsymbol{u} \qquad \text{and} \qquad \overset{l}{\widetilde{\boldsymbol{f}}} \approx \overset{l}{\boldsymbol{f}} = u_l\boldsymbol{u}\ . \tag{2.38}$$

A review of common numerical flux functions can be found, e.g., in LeVeque's textbook [98]. During construction of the one-dimensional ALDM scheme for Burgers equation, see Appendix A, various flux functions were analyzed by MDEA. Based on these findings

we propose the following modification of a LAX-FRIEDRICHS flux function

$$
\begin{aligned}
{}^{1}\widetilde{\boldsymbol{f}}_{i+\frac{1}{2},j,k} &= \frac{1}{4} \left(\widetilde{u}^{L}_{i+1,j,k} + \widetilde{u}^{R}_{i,j,k}\right)\left(\widetilde{\boldsymbol{u}}^{L}_{i+1,j,k} + \widetilde{\boldsymbol{u}}^{R}_{i,j,k}\right) \\
&\quad - {}^{1}\sigma_{i,j,k} \begin{bmatrix} |\overline{u}_{i+1,j,k} - \overline{u}_{i,j,k}|\,(\widetilde{u}^{L}_{i+1,j,k} - \widetilde{u}^{R}_{i,j,k}) \\ |\overline{v}_{i+1,j,k} - \overline{v}_{i,j,k}|\,(\widetilde{v}^{L}_{i+1,j,k} - \widetilde{v}^{R}_{i,j,k}) \\ |\overline{w}_{i+1,j,k} - \overline{w}_{i,j,k}|\,(\widetilde{w}^{L}_{i+1,j,k} - \widetilde{w}^{R}_{i,j,k}) \end{bmatrix} ,
\end{aligned}
\tag{2.39a}
$$

$$
\begin{aligned}
{}^{2}\widetilde{\boldsymbol{f}}_{i,j+\frac{1}{2},k} &= \frac{1}{4} \left(\widetilde{v}^{B}_{i,j+1,k} + \widetilde{v}^{F}_{i,j,k}\right)\left(\widetilde{\boldsymbol{u}}^{B}_{i,j+1,k} + \widetilde{\boldsymbol{u}}^{F}_{i,j,k}\right) \\
&\quad - {}^{2}\sigma_{i,j,k} \begin{bmatrix} |\overline{u}_{i,j+1,k} - \overline{u}_{i,j,k}|\,(\widetilde{u}^{B}_{i,j+1,k} - \widetilde{u}^{F}_{i,j,k}) \\ |\overline{v}_{i,j+1,k} - \overline{v}_{i,j,k}|\,(\widetilde{v}^{B}_{i,j+1,k} - \widetilde{v}^{F}_{i,j,k}) \\ |\overline{w}_{i,j+1,k} - \overline{w}_{i,j,k}|\,(\widetilde{w}^{B}_{i,j+1,k} - \widetilde{w}^{F}_{i,j,k}) \end{bmatrix} ,
\end{aligned}
\tag{2.39b}
$$

$$
\begin{aligned}
{}^{3}\widetilde{\boldsymbol{f}}_{i,j,k+\frac{1}{2}} &= \frac{1}{4} \left(\widetilde{w}^{D}_{i,j,k+1} + \widetilde{w}^{U}_{i,j,k}\right)\left(\widetilde{\boldsymbol{u}}^{D}_{i,j,k+1} + \widetilde{\boldsymbol{u}}^{U}_{i,j,k}\right) \\
&\quad - {}^{3}\sigma_{i,j,k} \begin{bmatrix} |\overline{u}_{i,j,k+1} - \overline{u}_{i,j,k}|\,(\widetilde{u}^{D}_{i,j,k+1} - \widetilde{u}^{U}_{i,j,k}) \\ |\overline{v}_{i,j,k+1} - \overline{v}_{i,j,k}|\,(\widetilde{v}^{D}_{i,j,k+1} - \widetilde{v}^{U}_{i,j,k}) \\ |\overline{w}_{i,j,k+1} - \overline{w}_{i,j,k}|\,(\widetilde{w}^{D}_{i,j,k+1} - \widetilde{w}^{U}_{i,j,k}) \end{bmatrix}
\end{aligned}
\tag{2.39c}
$$

for the three-dimensional NAVIER-STOKES equations and collocated grids. The extension to a staggered grid arrangement is straight forward and leads to

$$
\begin{aligned}
{}^{1}\widetilde{\boldsymbol{f}}_{i+\frac{1}{2},j,k} &= \frac{1}{4} \begin{bmatrix} (\widetilde{u}^{L}_{i+1,j,k} + \widetilde{u}^{R}_{i,j,k})\,(\widetilde{u}^{L}_{i+1,j,k} + \widetilde{u}^{R}_{i,j,k}) \\ (\widetilde{u}^{B}_{i,j+1,k} + \widetilde{u}^{F}_{i,j,k})\,(\widetilde{v}^{L}_{i+1,j,k} + \widetilde{v}^{R}_{i,j,k}) \\ (\widetilde{u}^{D}_{i,j,k+1} + \widetilde{u}^{U}_{i,j,k})\,(\widetilde{w}^{L}_{i+1,j,k} + \widetilde{w}^{R}_{i,j,k}) \end{bmatrix} \\
&\quad - {}^{1}\sigma_{i,j,k} \begin{bmatrix} |\overline{u}_{i+1,j,k} - \overline{u}_{i,j,k}|\,(\widetilde{u}^{L}_{i+1,j,k} - \widetilde{u}^{R}_{i,j,k}) \\ |\overline{v}_{i+1,j,k} - \overline{v}_{i,j,k}|\,(\widetilde{v}^{L}_{i+1,j,k} - \widetilde{v}^{R}_{i,j,k}) \\ |\overline{w}_{i+1,j,k} - \overline{w}_{i,j,k}|\,(\widetilde{w}^{L}_{i+1,j,k} - \widetilde{w}^{R}_{i,j,k}) \end{bmatrix} ,
\end{aligned}
\tag{2.40a}
$$

$$
\begin{aligned}
{}^{2}\widetilde{\boldsymbol{f}}_{i,j+\frac{1}{2},k} &= \frac{1}{4} \begin{bmatrix} (\widetilde{v}^{L}_{i+1,j,k} + \widetilde{u}^{R}_{i,j,k})\,(\widetilde{u}^{B}_{i,j+1,k} + \widetilde{u}^{F}_{i,j,k}) \\ (\widetilde{v}^{B}_{i,j+1,k} + \widetilde{v}^{F}_{i,j,k})\,(\widetilde{v}^{B}_{i,j+1,k} + \widetilde{v}^{F}_{i,j,k}) \\ (\widetilde{v}^{D}_{i,j,k+1} + \widetilde{v}^{U}_{i,j,k})\,(\widetilde{w}^{B}_{i,j+1,k} + \widetilde{w}^{F}_{i,j,k}) \end{bmatrix} \\
&\quad - {}^{2}\sigma_{i,j,k} \begin{bmatrix} |\overline{u}_{i,j+1,k} - \overline{u}_{i,j,k}|\,(\widetilde{u}^{B}_{i,j+1,k} - \widetilde{u}^{F}_{i,j,k}) \\ |\overline{v}_{i,j+1,k} - \overline{v}_{i,j,k}|\,(\widetilde{v}^{B}_{i,j+1,k} - \widetilde{v}^{F}_{i,j,k}) \\ |\overline{w}_{i,j+1,k} - \overline{w}_{i,j,k}|\,(\widetilde{w}^{B}_{i,j+1,k} - \widetilde{w}^{F}_{i,j,k}) \end{bmatrix} ,
\end{aligned}
\tag{2.40b}
$$

$$
{}^{3}\widetilde{\boldsymbol{f}}_{i,j,k+\frac{1}{2}} = \frac{1}{4} \begin{bmatrix} (\widetilde{w}^{L}_{i+1,j,k} + \widetilde{w}^{R}_{i,j,k}) \, (\widetilde{u}^{D}_{i,j,k+1} + \widetilde{u}^{U}_{i,j,k}) \\ (\widetilde{w}^{B}_{i,j+1,k} + \widetilde{w}^{F}_{i,j,k}) \, (\widetilde{v}^{D}_{i,j,k+1} + \widetilde{v}^{U}_{i,j,k}) \\ (\widetilde{w}^{D}_{i,j,k+1} + \widetilde{w}^{U}_{i,j,k}) \, (\widetilde{w}^{D}_{i,j,k+1} + \widetilde{w}^{U}_{i,j,k}) \end{bmatrix}
$$

$$
- \; {}^{3}\sigma_{i,j,k} \begin{bmatrix} |\overline{u}_{i,j,k+1} - \overline{u}_{i,j,k}| \, (\widetilde{u}^{D}_{i,j,k+1} - \widetilde{u}^{U}_{i,j,k}) \\ |\overline{v}_{i,j,k+1} - \overline{v}_{i,j,k}| \, (\widetilde{v}^{D}_{i,j,k+1} - \widetilde{v}^{U}_{i,j,k}) \\ |\overline{w}_{i,j,k+1} - \overline{w}_{i,j,k}| \, (\widetilde{w}^{D}_{i,j,k+1} - \widetilde{w}^{U}_{i,j,k}) \end{bmatrix} \; . \tag{2.40c}
$$

Note that in the latter equation the indices are defined using the specific (staggered) coordinate system of the respective velocity component.

The first term on the right-hand side corresponds to the physical NAVIER-STOKES flux. For maximum order of consistency it is computed from the mean of both interpolants of the deconvolved velocity at the considered cell face. The difference between them is exploited as an estimate of the local truncation error. In the second term on the right-hand side it is multiplied with the magnitude of a filtered velocity increment which corresponds to the first-order structure function. For developed turbulence the KOL-MOGOROV theory predicts a scaling with a $1/3$ power of the two-point separation [41]. The coefficients

$$
{}^{1}\sigma_{i,j,k} = \sigma \left(\frac{L_0}{h_0} \frac{x_{i+1,j,k} - x_{i,j,k}}{L_{i,j,k}} \right)^{-s} , \tag{2.41a}
$$

$$
{}^{2}\sigma_{i,j,k} = \sigma \left(\frac{L_0}{h_0} \frac{y_{i,j+1,k} - y_{i,j,k}}{L_{i,j,k}} \right)^{-s} , \tag{2.41b}
$$

$$
{}^{3}\sigma_{i,j,k} = \sigma \left(\frac{L_0}{h_0} \frac{z_{i,j,k+1} - z_{i,j,k}}{L_{i,j,k}} \right)^{-s} , \tag{2.41c}
$$

were introduced to compensate for effects of varying grid-size. It was found that $s = 1/3$ ensures a correct scaling of the numerical viscosity in simulations of isotropic turbulence, as long as the numerical cutoff wavenumber is located within the inertial range of the turbulent kinetic energy spectrum. The length $L_{i,j,k}$ is a local estimate of the current integral flow scale and the scalar factor σ is another free parameter of the discretization scheme, see Tab. 3.1. It is interesting to note that with this kind of grid-width compensation the truncation error of ALDM, when formally determined by TAYLOR series expansion, is less than second order in terms of the mesh width. As a result of the parameter optimization process, see Section 3.3, the ratio of reference integral length and reference grid size is $L_0/h_0 = 32$.

2.5 Summary

The concept of a solution-adaptive deconvolution method based on a convex combination of HARTEN-type approximation polynomials is developed for the incompressible 3-D NAVIER-STOKES equations. Instead of maximizing the order of accuracy, here deconvolution is regularized by limiting the degree of local interpolation polynomials and by permitting lower-order polynomials to contribute to the truncation error. Adaptivity of the deconvolution operator is achieved by weighting the respective contributions by an adaptation of WENO smoothness measures. The approximately deconvolved field is inserted into a consistent numerical flux function. Flux function and nonlinear weights introduce five independent model parameters, namely σ, $\gamma_{2,0}^{+1/2}$, $\gamma_{3,0}^{+1/2}$, $\gamma_{3,1}^{+1/2}$ and $\gamma_{3,1}^{0}$. These parameters allow to control the truncation error and constitute the implicit SGS model.

IMPLICIT SGS MODELING

Discretization coefficients are usually chosen in such a way that the formal order of accuracy of a discretization is maximum. This approach holds for direct numerical simulation but not for LES, where the chosen grid resolution essentially defines the range of represented scales. At a finite grid size, truncation errors interfere with the turbulence models. Thus, free discretization coefficients should be selected in such a way that the superposition of all contributions (truncation errors, SGS modeling terms, as well as modeling errors) is optimal. With implicit LES, numerical discretization and turbulence model are indistinguishable and free discretization parameters have to be determined in such a way that the truncation error acts as a physically motivated SGS model.

By an analysis of the modified differential equation of a discretization scheme an implicit SGS model can be determined analytically. It can be observed that the TAYLOR-series expansion of the truncation error of nonlinear discretization schemes contains functional expressions which are similar to that of explicit SGS models [42, 113, 143]. For some discretizations a given explicit SGS model can be matched by adjusting parameters of the generic implicit SGS model.

As alternative to adjusting the model parameters for a given explicit SGS model one can try to find systematically the SGS model that gives the best statistical representation of the SGS effects on the filtered scales. Provided that the grid resolution is sufficient, turbulent subgrid scales are believed to obey general properties such as a KOLMOGOROV scaling in the inertial wavenumber range. This is exploited for determining optimal model parameters. Optimization target is a canonical reference flow configuration that represents the essential properties of 3-D NAVIER–STOKES turbulence.

3.1 Modified-Differential-Equation Analysis in Real Space

The modified-differential-equation analysis is based on the assumption that the discrete unfiltered solution in a neighborhood of x_i can be represented by local approximation

polynomials of degree K up to $K \leq L$. The polynomial approximation of the filtered solution is

$$\overline{\varphi}_i \doteq \sum_{\mu=0}^{L-1} \check{\varphi}_i^{(\mu)} \frac{M_\mu(x_i)}{(\mu)!} \ , \tag{3.1}$$

where $\check{\varphi}_i^{(\mu)}$ stand for the order μ derivatives of the approximation polynomial $\check{\varphi}$ of φ at x_i. M_μ is the μ-th moment of the filter kernel

$$M_\mu(x_i) = \int_{-\infty}^{+\infty} (x - x_i)^\mu G(x - x_i) dx \ . \tag{3.2}$$

The top-hat filter kernel gives

$$M_\mu(x_i) = \begin{cases} 0 & , \mu \ \ \text{odd} \\ \dfrac{h_i^\mu}{2^\mu(\mu + 1)} & , \mu \ \ \text{even.} \end{cases} \tag{3.3}$$

Taking the order ν derivatives on both sides of Eq. (3.1), we obtain

$$\overline{\varphi}_i^{(\nu)} \doteq \sum_{\mu=\nu}^{L-1} \check{\varphi}_i^{(\mu)} \frac{M_{(\mu-\nu)}(x_i)}{(\mu - \nu)!} \ , \tag{3.4}$$

for $\nu = 0, \ldots, L - 1$. The set of equations (3.4) can be written in matrix form

$$\begin{bmatrix} \overline{\varphi}_i \\ \overline{\varphi}_i' \\ \overline{\varphi}_i'' \\ \vdots \\ \overline{\varphi}_i^{(L-1)} \end{bmatrix} = \boldsymbol{C} \cdot \begin{bmatrix} \check{\varphi}_i \\ \check{\varphi}_i' \\ \check{\varphi}_i'' \\ \vdots \\ \check{\varphi}_i^{(L-1)} \end{bmatrix} \ , \tag{3.5}$$

where the coefficient matrix $\boldsymbol{C}$ is upper triangular and diagonally dominant [58]. Solving (3.5) for $\check{\varphi}_i^{(\nu)}$, $\check{\varphi}_N$ is obtained in terms of the first $L - 1$ derivatives of $\overline{\varphi}_N$. This series expansion for $\check{\varphi}_N$ can be inserted as approximation for φ_N when evaluating the truncation error of a numerical method.

For clarity it is common to restrict the analysis of the MDE (2.7) to the spatial semi-discretization and a uniform grid size. Consistent with the spatial-filtering concept the

time step is assumed to be sufficiently small so that all relevant time scales are well resolved. Under these assumptions, the truncation error $\boldsymbol{\mathcal{G}}_N$ is given by

$$
\begin{aligned}
\boldsymbol{\mathcal{G}}_N &= \boldsymbol{G} * \boldsymbol{\nabla} \cdot \boldsymbol{N}_N(\boldsymbol{u}_N) - \widetilde{\boldsymbol{G}} * \widetilde{\boldsymbol{\nabla}} \cdot \widetilde{\boldsymbol{N}}_N(\widetilde{\boldsymbol{u}}_N) \\
&= \left\{ \boldsymbol{G} * \boldsymbol{\nabla} \cdot \boldsymbol{u}_N \boldsymbol{u}_N + \boldsymbol{\nabla}\, \overline{p}_N \right\} - \left\{ \widetilde{\boldsymbol{G}} * \widetilde{\boldsymbol{\nabla}} \cdot \widetilde{\boldsymbol{F}}_N(\widetilde{\boldsymbol{u}}_N) + \boldsymbol{\nabla}\, \widetilde{p}_N \right\} .
\end{aligned}
\tag{3.6}
$$

For uniform viscosity and density the diffusive term is linear in terms of $\boldsymbol{u}_N$ and does not contribute to the SGS tensor. Provided the REYNOLDS number is large, numerical approximation errors of the diffusive flux are small and can be neglected in the further analysis.

The pressure gradient is included in Eq. (3.6) since it is directly coupled to the convective term by the pressure-POISSON equation (2.3). The pressure grid function $\overline{p}_N$ corresponds to the filtered velocity field $\overline{\boldsymbol{u}}_N$ whereas the MDE requires $\widetilde{p}_N$. The residual $\widetilde{\widetilde{p}}_N = \widetilde{p}_N - \overline{p}_N$ is the contribution of the pressure projection to the truncation error

$$
\boldsymbol{\mathcal{G}}_N = \left[\boldsymbol{G} * \boldsymbol{\nabla} \cdot \boldsymbol{u}_N \boldsymbol{u}_N - \widetilde{\boldsymbol{G}} * \widetilde{\boldsymbol{\nabla}} \cdot \widetilde{\boldsymbol{F}}_N(\widetilde{\boldsymbol{u}}_N) \right] - \boldsymbol{\nabla}\, \widetilde{\widetilde{p}}_N
\tag{3.7}
$$

which has to satisfy the continuity condition

$$
\boldsymbol{\nabla} \cdot \boldsymbol{\mathcal{G}}_N = 0 .
\tag{3.8}
$$

For an analytical expression of the first term on the right-hand side of (3.7) the filtered and the unfiltered solution are approximated in terms of TAYLOR expansions of $\overline{\boldsymbol{u}}_N$ truncated at order L

$$
\begin{aligned}
\boldsymbol{\mathcal{A}}_L(\overline{\boldsymbol{u}}) &= \boldsymbol{G} * \boldsymbol{\nabla} \cdot \breve{\boldsymbol{u}}_N \breve{\boldsymbol{u}}_N - \widetilde{\boldsymbol{G}} * \widetilde{\boldsymbol{\nabla}} \cdot \widetilde{\boldsymbol{F}}_N(\widetilde{\boldsymbol{u}}_N) \\
&= \boldsymbol{G} * \boldsymbol{\nabla} \cdot \boldsymbol{u}_N \boldsymbol{u}_N - \widetilde{\boldsymbol{G}} * \widetilde{\boldsymbol{\nabla}} \cdot \widetilde{\boldsymbol{F}}_N(\widetilde{\boldsymbol{u}}_N) + \mathcal{O}\left(h^L \right) .
\end{aligned}
\tag{3.9}
$$

Moreover, the implicit SGS model (3.7) is divergence free if the pressure residual satisfies

$$
\boldsymbol{\nabla} \cdot \boldsymbol{\nabla} \widetilde{\widetilde{p}}_N = \boldsymbol{\nabla} \cdot \boldsymbol{\mathcal{A}}_L(\overline{\boldsymbol{u}}) .
\tag{3.10}
$$

The difficulty in solving this POISSON equation analytically, see e.g. BATCHELOR [6, chapter 5], is the reason why a detailed evaluation of $\boldsymbol{\mathcal{G}}_N$ similarly as for the 1-D BURGERS equation - see Appendix A - is practically impossible. Since already the analytical expression of $\boldsymbol{\mathcal{A}}_L$ becomes extremely lengthy the 3-D problem is not tractable any longer even with symbolic-mathematics software.

Our preliminary results suggest that only two parameters, $\gamma_{2,1}^{+1/2}$ and σ, can be used to tune the second-order contribution to $\boldsymbol{\mathcal{A}}_3$ which is expected to be most relevant for SGS

modeling. The truncation error involves dissipative terms which resemble the artificial dissipation of VON NEUMANN and RICHTMYER [178]. Similar expressions have been found for the 1-D BURGERS model, see Appendix A. The form of the these terms is common for the modified equation of many nonlinear finite-volume schemes [143]. In our case, these contributions originate from the use of a numerical flux function and allow to reproduce the dimensional-splitting equivalent of a SMAGORINSKY SGS model with

$$C_S = \sqrt{\frac{1}{3}\sigma} \tag{3.11}$$

on equidistant grids. Using LILLY's asymptotic value for the SMAGORINSKY constant [99], we obtain

$$\sigma \approx 0.0867 \ . \tag{3.12}$$

A second group of terms is the truncation error of the 2nd-order numerical integration scheme, Eq. (2.18). These contribution cancel out if the 4th order quadrature scheme is used. The remaining terms result from the 2nd order accurate deconvolution operator. Most 2nd-order terms cancel out with

$$\gamma_{2,1}^{+1/2} = \frac{2}{3} \ . \tag{3.13}$$

The weights associated with the third-order deconvolution polynomials do not contribute to the second-order truncation error.

Since it was not feasible to analyze the higher order model terms, the reproduction of an explicit model fails. Also note that an interpretation of truncated TAYLOR series is difficult for a non-smooth solution and coarse grid resolution. We conclude that TAYLOR expansion is not the method of choice for analyzing complex discretizations in three-dimensional space. Appropriate model parameters will be directly identified from turbulence-theoretical results by another analysis detailed below.

3.2 Modified-Differential-Equation Analysis in Spectral Space

Linear discretization schemes for linear differential equations can be analyzed in FOURIER space with the modified-wavenumber concept [176]. LELE [91] successfully applied this method to optimize the spectral resolution of compact finite difference schemes, for example. For nonlinear discretizations, however, the modified wavenumber is a functional of the solution, which makes the analysis difficult and case dependent. In the following we develop a theoretical framework for the evaluation and optimization of the

spectral numerical dissipation of complex nonlinear discretization schemes for nonlinear three-dimensional differential equations. As reference for the spectral MDEA serves isotropic turbulence for which theoretical eddy-viscosity models are usually formulated in spectral space [23, 93].

3.2.1 Mathematical Formulation

We consider the discretization of a $(2\pi)^3$-periodic domain by N^3 grid points. The transformed MDE (2.7) reads

$$\frac{\partial \widehat{\overline{\boldsymbol{u}}}_C}{\partial t} + \widehat{\boldsymbol{G}} \, \mathrm{i}\boldsymbol{\xi} \cdot \widehat{\boldsymbol{N}}_C(\widehat{\boldsymbol{u}}_C) + \nu\boldsymbol{\xi}^2\widehat{\overline{\boldsymbol{u}}}_C = \widehat{\boldsymbol{\mathcal{G}}}_C \ , \tag{3.14a}$$

$$\mathrm{i}\boldsymbol{\xi} \cdot \widehat{\overline{\boldsymbol{u}}}_C = 0 \ , \tag{3.14b}$$

where the hat denotes the FOURIER transform, i is the imaginary unit, and $\boldsymbol{\xi}$ is the wavenumber vector.

Reference to spectral theories of turbulence implies isotropy. A physical-space discretization restricts contributions to the numerical solution to wavenumbers up to $|\boldsymbol{\xi}| = \sqrt{3}\xi_C$ where $\xi_C = N/2 - 1$ is the cut-off wavenumber. For consistency with isotropy, contributions with wavenumbers $|\boldsymbol{\xi}| > \xi_C$ need to be removed. For this purpose we define

$$\widehat{\overline{\boldsymbol{u}}}_C(\boldsymbol{\xi}) = \begin{cases} \widehat{\overline{\boldsymbol{u}}}_N(\boldsymbol{\xi}) & , \ |\boldsymbol{\xi}| \leq \xi_C \\ \boldsymbol{0} & , \ \text{otherwise} \end{cases} . \tag{3.15}$$

On the represented wavenumber range the kinetic energy of the deconvolved velocity

$$\widehat{\boldsymbol{u}}_C(\boldsymbol{\xi}) = \widehat{\boldsymbol{G}}^{-1}(\boldsymbol{\xi})\widehat{\overline{\boldsymbol{u}}}_C(\boldsymbol{\xi}) \ , \qquad \text{with} \quad |\boldsymbol{\xi}| \leq \xi_C \tag{3.16}$$

is

$$\widehat{E}(\boldsymbol{\xi}) = \frac{1}{2}\widehat{\boldsymbol{u}}_C(\boldsymbol{\xi}) \cdot \widehat{\boldsymbol{u}}_C^*(\boldsymbol{\xi}) \ . \tag{3.17}$$

Multiplying equation (3.14a) by the complex-conjugate $\widehat{\boldsymbol{u}}_C^*$ of $\widehat{\boldsymbol{u}}_C$ we obtain

$$\widehat{\boldsymbol{G}}(\boldsymbol{\xi})\frac{\partial \widehat{E}(\boldsymbol{\xi})}{\partial t} - \widehat{\boldsymbol{G}}(\boldsymbol{\xi})\widehat{T}_C(\boldsymbol{\xi}) + 2\nu\boldsymbol{\xi}^2\widehat{\boldsymbol{G}}\widehat{E}(\boldsymbol{\xi}) = \widehat{\boldsymbol{u}}_C^*(\boldsymbol{\xi}) \cdot \widehat{\boldsymbol{\mathcal{G}}}_C(\boldsymbol{\xi}) \ . \tag{3.18}$$

The nonlinear energy transfer

$$\widehat{T}_C(\boldsymbol{\xi}) = \ \mathrm{i}\widehat{\boldsymbol{u}}_C^* \cdot \boldsymbol{\xi} \cdot \widehat{\boldsymbol{N}}_C(\widehat{\boldsymbol{u}}_C) = \ \mathrm{i}\widehat{\boldsymbol{u}}_C^*(\boldsymbol{\xi}) \cdot \overset{3}{\boldsymbol{P}}(\boldsymbol{\xi}) \cdot \cdot \int\limits_{|\boldsymbol{\eta}|\leqq\xi_C} \widehat{\boldsymbol{u}}_C(\boldsymbol{\eta})\widehat{\boldsymbol{u}}_C(\boldsymbol{\xi}-\boldsymbol{\eta})d\boldsymbol{\eta} \tag{3.19}$$

is the Fourier transform of the nonlinear term. The tensor $\overset{3}{\boldsymbol{P}}(\boldsymbol{\xi})$ is defined by

$$\overset{3}{P}_{lmn}(\boldsymbol{\xi}) = \xi_m \delta_{ln} - \xi_l \xi_m \xi_n |\boldsymbol{\xi}|^{-2}, \tag{3.20}$$

see also POPE [136]. Finally, we deconvolve Eq. (3.18) by multiplication with the inverse filter coefficient $\widehat{\boldsymbol{G}}^{-1}(\boldsymbol{\xi})$ which is defined on the range of represented scales $|\boldsymbol{\xi}| \leqq \xi_C$ and obtain

$$\frac{\partial \widehat{E}(\boldsymbol{\xi})}{\partial t} - \widehat{T}_C(\boldsymbol{\xi}) + 2\nu\boldsymbol{\xi}^2 \widehat{E}(\boldsymbol{\xi}) = \widehat{\boldsymbol{G}}^{-1}(\boldsymbol{\xi})\widehat{\boldsymbol{u}}_C^*(\boldsymbol{\xi}) \cdot \widehat{\boldsymbol{\mathcal{G}}}_C(\boldsymbol{\xi}) . \tag{3.21}$$

The right-hand side of this equation is the numerical dissipation

$$\varepsilon_{num}(\boldsymbol{\xi}) = -\widehat{\boldsymbol{G}}^{-1}(\boldsymbol{\xi})\widehat{\boldsymbol{u}}_C^*(\boldsymbol{\xi}) \cdot \widehat{\boldsymbol{\mathcal{G}}}_C(\boldsymbol{\xi}) \tag{3.22}$$

implied by the discretization of the convective term. Now we investigate how to model the physical subgrid dissipation $\varepsilon_{SGS}(\boldsymbol{\xi})$ by $\varepsilon_{num}(\boldsymbol{\xi})$.

An exact analytical match between $\varepsilon_{num}(\boldsymbol{\xi})$ and $\varepsilon_{SGS}(\boldsymbol{\xi})$ cannot be achieved since $\varepsilon_{SGS}(\boldsymbol{\xi})$ involves interactions with non-represented scales. Modeling can be accomplished by invoking theoretical energy-transfer expressions. Employing an eddy-viscosity hypothesis the subgrid-scale dissipation is

$$\varepsilon_{SGS}(\boldsymbol{\xi}) = 2\nu_{SGS}(\boldsymbol{\xi})\xi^2 \widehat{E}(\boldsymbol{\xi}). \tag{3.23}$$

Similarly, the numerical dissipation can be expressed as

$$\nu_{num}(\boldsymbol{\xi}) = \frac{\varepsilon_{num}(\boldsymbol{\xi})}{2\xi^2 \widehat{E}(\boldsymbol{\xi})} . \tag{3.24}$$

In general ν_{num} is a function of the wavenumber vector $\boldsymbol{\xi}$. For isotropic turbulence, however, statistical properties of Eq. (3.21) follow from the scalar evolution equation for the 3-D energy spectrum

$$\frac{\partial \widehat{E}(\xi)}{\partial t} - \widehat{T}_C(\xi) + 2\nu\xi^2 \widehat{E}(\xi) = -\varepsilon_{num}(\xi) . \tag{3.25}$$

This equation is obtained from Eq. (3.21) by integration over spherical shells with radius $\xi = |\boldsymbol{\xi}|$, that is

$$\widehat{E}(\xi) = \oint\limits_{|\boldsymbol{\xi}|=\xi} \widehat{E}(\boldsymbol{\xi})d\boldsymbol{\xi} . \tag{3.26}$$

For a given numerical scheme $\nu_{num}(\xi)$ can be computed from

$$\nu_{num}(\xi) = -\frac{\widehat{G}^{-1}(\xi)}{2\xi^2 \widehat{E}(\xi)} \int\limits_{|\boldsymbol{\xi}|=\xi} \widehat{\boldsymbol{u}}_N^*(\boldsymbol{\xi}) \cdot \widehat{\boldsymbol{\mathcal{G}}}_N(\boldsymbol{\xi})d\boldsymbol{\xi} . \tag{3.27}$$

The concept of modeling nonlinear interactions in turbulence by a wavenumber-dependent spectral eddy viscosity was first proposed by HEISENBERG [60]. Convenient for our purposes is a normalization by

$$\nu_{SGS}^+(\xi^+) = \nu_{SGS}\left(\xi^+\xi_C\right)\sqrt{\frac{\xi_C}{\widehat{E}(\xi_C)}} \ , \tag{3.28}$$

with $\xi^+ = \frac{\xi}{\xi_C}$ as proposed by CHOLLET and LESIEUR [24]. For high REYNOLDS numbers and under the assumption of a KOLMOGOROV range $E(\xi) = C_K\varepsilon^{3/2}\xi^{-5/3}$ extending to infinity the Eddy-Damped Quasi-Normal MARKOVIAN (EDQNM) theory [93] leads to

$$\nu_{SGS}^+(\xi^+) = 0.441C_K^{-3/2}X(\xi^+) \ , \tag{3.29}$$

where C_K is the KOLMOGOROV constant and $X(\xi^+)$ is a non-dimensional function exhibiting a plateau at unity for small wavenumbers $\xi^+ \lesssim 1/3$ and a sharply rising cusp in the vicinity of the cut-off wavenumber $\xi^+ = 1$. CHOLLET [23] proposes the expression

$$\nu_{Chollet}^+(\xi^+) = 0.441C_K^{-3/2}\left(1 + 34.467e^{-3.03/\xi^+}\right) \tag{3.30}$$

as best fit to the exact solution.

3.2.2 Numerical Evaluation

In the following, an algorithm proposed by DOMARADZKI [38, 68, 69] is adapted. We consider freely decaying homogeneous isotropic turbulence in the limit of vanishing molecular viscosity. A numerical simulation is performed in a $(2\pi)^3$-periodic box, discretized by $32\times32\times32$ uniform finite volumes. The time-step size is adjusted according to Eq. (4.1) with CFL = 1.0. This COURANT number is identical to that used in all other simulations. Filtered and truncated LES data obtained by filtering and truncating data from separate simulations with a dynamic SMAGORINSKY SGS model at higher spatial resolution of 128^3 cells are used as initial condition $\overline{\boldsymbol{u}}_N(t_0)$. Solutions $\overline{\boldsymbol{u}}_N(t_n)$ at time $t_n = t_0 + n\Delta t$, n being an integer, are obtained by advancing n time steps with the discretization method. An *a-posteriori* analysis of the data allows to identify the spectral eddy viscosity of the implicit SGS model.

The computed velocity fields $\overline{\boldsymbol{u}}_N(t_n)$ are FOURIER-transformed and truncated at $\xi_C = 15$

$$\widehat{\overline{\boldsymbol{u}}}_C(\boldsymbol{\xi}, t_n) = \begin{cases} \mathcal{F}\{\overline{\boldsymbol{u}}_N\}(\boldsymbol{\xi}, t_n) & , |\boldsymbol{\xi}| \leq \xi_C \\ \boldsymbol{0} & , \text{otherwise} \end{cases} . \tag{3.31}$$

Energy spectra $\widehat{E}(\boldsymbol{\xi}, t_n)$ and spectral transfer functions $\widehat{T}_C(\boldsymbol{\xi}, t_n)$ are computed from (3.17) and (3.19). The convolution integral in (3.19) is computed in real space. The computation of the numerical-dissipation spectrum, see Eqs. (3.21) and (3.22), involves the spectral-energy decay which is approximated by

$$\left. \frac{\partial \widehat{E}(\boldsymbol{\xi})}{\partial t} \right|_{t_{n-1/2}} \approx \frac{\widehat{E}(\boldsymbol{\xi}, t_n) - \widehat{E}(\boldsymbol{\xi}, t_{n-1})}{\Delta t} \tag{3.32}$$

at times $t_{n-1/2} = \frac{1}{2}(t_{n-1} + t_n)$. Energy spectrum and spectral transfer function are interpolated as

$$\widehat{E}(\boldsymbol{\xi}, t_{n-1/2}) = \frac{\widehat{E}(\boldsymbol{\xi}, t_n) + \widehat{E}(\boldsymbol{\xi}, t_{n-1})}{2} \ , \tag{3.33a}$$

$$\widehat{T}_C(\boldsymbol{\xi}, t_{n-1/2}) = \frac{\widehat{T}_C(\boldsymbol{\xi}, t_n) + \widehat{T}_C(\boldsymbol{\xi}, t_{n-1})}{2} \ . \tag{3.33b}$$

Following Eq. (3.24) the spectral numerical viscosity is

$$\nu_{num}(\boldsymbol{\xi}, t_{n-1/2}) = \frac{1}{2\boldsymbol{\xi}^2 \widehat{E}(\boldsymbol{\xi}, t_{n-1/2})} \left(\widehat{T}_C(\boldsymbol{\xi}, t_{n-1/2}) - \left. \frac{\partial \widehat{E}(\boldsymbol{\xi})}{\partial t} \right|_{t_{n-1/2}} \right) - \nu \ . \tag{3.34}$$

The 3-D numerical-viscosity spectrum is obtained by summation over integer-wavenumber shells $\xi - \frac{1}{2} \le |\boldsymbol{\xi}| \le \xi + \frac{1}{2}$

$$\nu_{num}(\xi, t_{n-1/2}) = \frac{4\pi\xi^2}{M(\xi)} \sum_{\boldsymbol{\xi}} \nu_{num}(\boldsymbol{\xi}, t_{n-1/2}) \ , \tag{3.35}$$

where $M(\xi)$ is the number of integer wavenumbers on each shell with radius ξ. A subsequent normalization gives

$$\nu_{num}^+(\xi^+, t_{n-1/2}) = \nu_{num}(\xi_C \xi^+, t_{n-1/2}) \sqrt{\frac{\xi_C}{\widehat{E}(\xi_C, t_{n-1/2})}} \ . \tag{3.36}$$

Since the analysis is performed in spectral space, the normalization term $\sqrt{\xi_C/\widehat{E}(\xi_C)}$ is readily evaluated. However, the magnitude of the resulting ν_{num}^+ then depends strongly on the energy spectrum's highest wavenumbers. An integral and therefore more robust normalization follows from the identity

$$\sqrt{\frac{\xi_C}{\widehat{E}(\xi_C)}} = C_K^{-1/2} \varepsilon^{-1/3} \xi_C^{4/3} \ , \tag{3.37}$$

which is valid for an idealized KOLMOGOROV inertial range.

This methodology can be applied to any discretization scheme, only a de-aliased spectral discretization will yield $\nu_{num}^+ \equiv 0$. DOMARADZKI *et al.* [38] first conducted an analysis of the implicit model provided by MPDATA. More recently, HICKEL *et al.* [75] reported results for a vortex-in-cell method, where particles carry the solution. Figure 3.1 shows the spectral numerical viscosities of standard finite difference (FD) methods. Central differencing methods are usually energy conserving, however, their dispersive errors redistribute the kinetic energy between the scales. In average, energy is transferred from medium to large wavenumbers. For most wavenumbers the spectral numerical viscosity of the considered central FD schemes is positive. However, a large negative peak is found at the cutoff wavenumber. Negative dissipation at high wavenumbers results in an energy accumulation. This can lead to numerical instability unless the method is stabilized by adding artificial dissipation, e.g., by an approximate interpolation scheme as proposed by RHIE and CHOW, see [40]. These results are consistent with the analysis of GHOSAL [48].
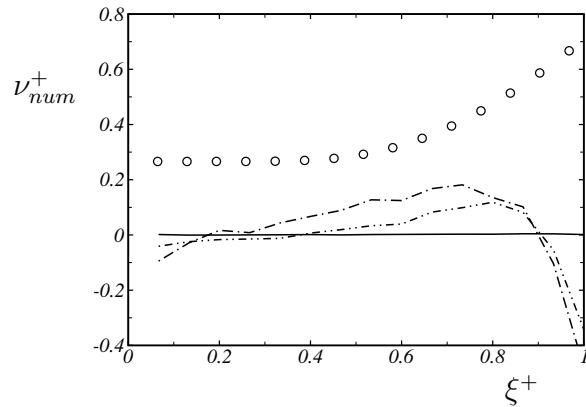
Figure 3.1: Spectral numerical viscosity of ———— de-aliased spectral scheme, ·—·—·— 2nd order central FD with a collocated grid, —··—··— 4th order central FD with a collocated grid. ∘ eddy viscosity of EDQNM theory [23].

3.3 Calibration of Model Coefficients

3.3.1 Cost Function

Isotropic decaying turbulence does not lose memory of the initial data. An evaluation of ν_{num}^+ for one data set only does not necessarily represent the statistical average. To cope with this problem the spectral numerical viscosity from 10 uncorrelated realizations is

evaluated and averaged. Each realization is advanced by one time step so that compu-
tational cost amounts to 10 time steps per evaluated numerical viscosity. Therefore the
evaluation procedure is sufficiently efficient for an automatic optimization of the free
parameter values of the discretization scheme.

The cost function used for evaluating a set of ALDM discretization parameters is the
root-mean-square difference

$$
\mathcal{C}\left(\gamma_{2,0}^{+1/2}, \gamma_{3,0}^{+1/2}, \gamma_{3,1}^{+1/2}, \gamma_{3,1}^{0}, \sigma\right) = \sqrt{\frac{1}{\xi_C - 1} \sum_{\xi^+ = 2/\xi_C}^{1} \left(\langle \nu_{num}^+(\xi^+) \rangle - \nu_{Chollet}^+(\xi^+)\right)^2} \quad (3.38)
$$

between the spectral numerical viscosity $\nu_{num}^+(\xi^+)$ and the spectral eddy viscosity
$\nu_{Chollet}^+(\xi^+)$ of EDQNM.

3.3.2 Evolutionary Optimization

The employed automatic optimization algorithm follows an evolutionary strategy in
which natural biological processes are modeled by simple stochastic search methods.
Evolutionary optimization strategies are particularly suitable for treating non-smooth
cost functions, where gradient-based methods fail. A set of free parameters is considered
as genome of a living individual. The algorithm operates on a population of individuals
and applies the survival-of-the-fittest principle of the DARWINian theory of evolution.
At each generation, a new set of individuals is created by modeled natural processes,
such as selection according to the level of fitness, recombination, and random mutation.
This process leads to the evolution of a population of individuals that is better adapted
to a cost function than the population that it was created from.

We use the following four-step algorithm:

1) **Selection of parents**: Pairs of two parameter sets are selected by a random process
either with probability proportional to their fitness or by tournament selection.

2) **Recombination**: Offspring is generated by recombination of their parents' genes.
Recombination can take place either by 2-point cross-over or by arithmetic cross-over.

3) **Mutation**: Random change of offspring genes. The random data are normally
distributed with zero mean. Their variance is adapted depending on how close the
generation is to an optimum.

4) **New generation selection**: The new generation of individuals is selected from the
current generation plus offspring either by fitness selection or by tournament selection.

These four steps are looped over until an optimality criterion is satisfied or, as in our investigations, until a maximum number of generations is reached.

Normally distributed random numbers are used as an initial guess for the first population. The subsequent generations are created by a four-step algorithm consisting of parent selection, recombination, mutation, and new-population selection. Performance and convergence of the employed optimization algorithm strongly depend on the mutation model of step 3. We employ normally distributed random numbers. The variance is initially set to $\sigma_{mut}^2 = 0.1$ and updated by a factor of $0.95^{\pm 1}$ after every generation, where successful mutations enlarge the target area and unsuccessful mutations make it smaller. For further details on the algorithm see Tab. 3.2.

parameter	optimal value
$\mathcal{C}$	0.0054850
$\gamma_{3,1}^{0}$	0.0500300
$\gamma_{2,0}^{+1/2}$	1.0000000
$\gamma_{3,0}^{+1/2}$	0.0190200
$\gamma_{3,1}^{+1/2}$	0.0855000
σ	0.0689100

Table 3.1: Result obtained by evolutionary optimization for the discretization parameters of ALDM.

Since this algorithm works on populations instead of single individuals, the search is performed in an efficient parallel manner. The numbers of time-steps and realizations for evaluation of the cost function $\mathcal{C}$ are chosen as a compromise between accuracy and computational feasibility. Surely, they are less than what would be necessary to completely remove the effect of stochastic fluctuations. Thus the resulting cost function is not smooth but exhibits residual fluctuations. Unlike standard gradient-approximation based optimization methods, evolutionary algorithms can handle such non-smooth cost functions [4]. For further details the reader is referred to BACK *et al.* [4], BEASLEY *et al.* [9, 10], and the references therein.

Parameter	Value
Number of genes per individual	5
Initialization	Random numbers, equally distributed on $[0, 0.3333)$
Number of generations	200
Population	50
Offspring per generation	40
Selection of parents	Tournament
Offspring generation	Arithmetic cross-over and mutation
Mutation model	GAUSSIAN normal distribution, zero mean
Initial mutation variance	0.1
Mutation-variance update factor	0.95
Admissible parameter range	$[0.0, 1.0]$
Admissible mutation-variance range	$[10^{-6}, 10^{+3}]$

Table 3.2: Parameters of the evolutionary optimization algorithm.

	best 50 individuals	best 200 individuals	all individuals
$\mathcal{C}$	0.0054860 ± 0.0000004	0.0054878 ± 0.0000071	0.2377798 ± 3.6380424
$\gamma_{3,1}^{0}$	0.0501310 ± 0.0001948	0.0501456 ± 0.0003782	0.0652569 ± 0.1125736
$\gamma_{2,0}^{+1/2}$	1.0000000 ± 0.0000000	1.0000000 ± 0.0000000	0.9741133 ± 0.1789786
$\gamma_{3,0}^{+1/2}$	0.0845990 ± 0.0001628	0.0847430 ± 0.0010236	0.1221711 ± 0.2100462
$\gamma_{3,1}^{+1/2}$	0.0189470 ± 0.0001435	0.0186506 ± 0.0013708	0.0289264 ± 0.1117276
σ	0.0689194 ± 0.0000965	0.0689116 ± 0.0001884	0.0664319 ± 0.0947205

Table 3.3: Mean values and standard deviation of cost function and parameter values demonstrate the convergence of the evolutionary optimization algorithm.

3.3.3 Optimized Eddy-Viscosity Model

The finally selected set of parameters is given in Table 3.1. It was determined after evaluating 200 generations, each with 40 individuals. The convergence of the optimization algorithm is demonstrated by comparing the best 50 sets, the best 200 sets, and all tested sets of parameters in Tab. 3.3. The spectral eddy viscosity of the implicit model with the optimized parameter set, Tab. 3.1, yields an excellent match with theoretical predictions as shown in Fig. 3.2. It exhibits a low-wavenumber plateau at the correct level and reproduces the typical cusp shape up to the cut-off wavenumber at the correct magnitude.
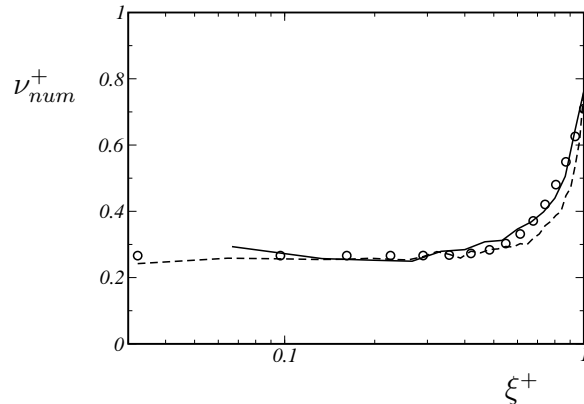
Figure 3.2: Numerical viscosity of ALDM with optimized parameters compared to the prediction of turbulence theory. ——— LES with $N = 32$, $----$ LES with $N = 64$, ∘ EDQNM theory [23].

ALDM nonlinearly combines interpolants from several central, upwind, and downwind stencils. The truncation error therefore is not purely dissipative. The Probability Density Function (PDF) of the numerical viscosity $\nu_{num}^+(\boldsymbol{\xi})$, shown in Fig. 3.3, exhibits significant anti-dissipative contributions which represent backscatter. Analysis of DNS data gives a wide distribution of $\nu_{SGS}^+(\boldsymbol{\xi})$ including negative values since the magnitude of local backscatter is comparable with and often even larger than the average subgrid energy transfer [135, e.g.].

The shell-averaged spectral eddy viscosity of CHOLLET $\nu_{Chollet}^+(\xi^+)$ considers the net SGS dissipation only and is always positive, see Fig. 3.3. Modeling backscatter renders a SGS model more realistic [37, 96, e.g.], whereas the particular way in which it is accounted for appears to be less important. Most explicit backscatter models follow a suggestion of LESLIE and QUARINI [96] and consider outscatter and backscatter separately from the mean energy transfer which is well reproduced by explicit eddy-viscosity
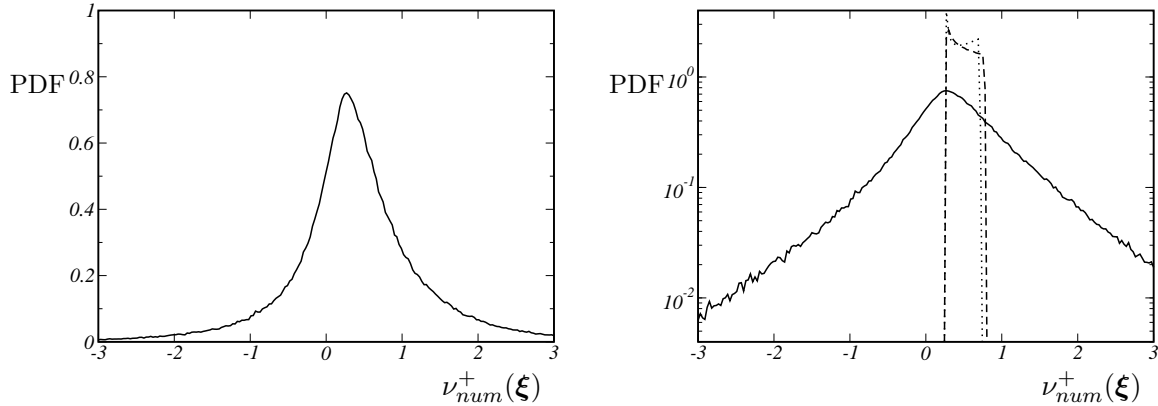
Figure 3.3: PDF of normalized spectral numerical viscosity $\nu_{num}^{+}(\boldsymbol{\xi})$ in integer-wavenumber FOURIER space for LES with 64^3 cells. ———— ALDM with optimized parameters; ·········· Eq. (3.30), CHOLLET (1984) ; ———— CHOLLET (1983)

models. An analysis of CARATI *et al.* [18] revealed no major differences between the performance of stochastic and deterministic backscatter models.

3.4 Summary

Implicit SGS modeling requires systematic procedures for design and analysis of appropriate discretization schemes. For this purpose the modified differential equation is analyzed. MDEA of complicated nonlinear discretization schemes of nonlinear three-dimensional differential equations becomes tedious if TAYLOR series expansion is employed. For calibrating model parameters an alternative approach is pursued where the modified differential equation is analyzed in spectral space and the spectral numerical viscosity is determined *a posteriori*. A spectral analysis is well suited for isotropic turbulence for which theoretical models are usually formulated in spectral space [23, 93]. Optimal model parameters are determined by minimizing a cost function which measures the difference between spectral numerical viscosity and the eddy viscosity from EDQNM theory. With the finally selected parameters the implicit SGS model yields an excellent match with theoretical requirements of EDQNM. The effective spectral eddy viscosity exhibits a low-wavenumber plateau at the correct level and reproduces the typical cusp shape up to the cut-off wave number at the correct magnitude. It is important to note that the CHOLLET-LESIEUR eddy viscosity is not enforced. Only for inertial-range isotropic turbulence the EDQNM eddy viscosity is necessarily recovered due to the parameter calibration.

VALIDATION FOR ISOTROPIC TURBULENCE

For *a posteriori* validation of the implicit SGS model provided by ALDM we perform LES of large-scale forced turbulence and of decaying isotropic turbulence. As an example for transitional flows we also consider the instability and breakdown of the 3-D TAYLOR-GREEN vortex.

4.1 Computational Setup

All simulations presented in this chapter are carried out on $(2\pi)^3$-periodic computational domains using a collocated grid arrangement for velocity and pressure. The computational domain is discretized by 64^3 cells unless specified otherwise. For time advancement, we use an explicit third-order RUNGE-KUTTA scheme of SHU [153], see also GOTTLIEB and SHU [50]. The time step Δt is adjusted dynamically according to a COURANT-FRIEDRICHS-LEWY limit evaluated as

$$\Delta t = \text{CFL} \ \min \left(\frac{\overline{u}_i}{h_i} + \frac{\nu}{h_i^2} \right)^{-1} , \tag{4.1}$$

where CFL is the so-called COURANT number [29]. The time-discretization scheme is total-variation diminishing (TVD) for CFL ≤ 1, provided the underlying spatial discretization is TVD, whereas the linear stability bound is larger. We found for ALDM stable time advancement up to the linear bound CFL = 1.7. For all our simulations we use CFL = 1.0.

ALDM applies only to the convective term of the NSE. The discretization schemes for dissipative terms and the pressure-POISSON equation are based on 4th-order approximation polynomials. First derivatives are approximated on 5-point central stencils

$$(\partial_x \overline{\varphi})_j = \frac{1}{h} \left[\frac{8}{12} \left(\overline{\varphi}_{j+1} - \overline{\varphi}_{j-1} \right) - \frac{1}{12} \left(\overline{\varphi}_{j+2} - \overline{\varphi}_{j-2} \right) \right] . \tag{4.2}$$

In this chapter we consider periodic domains only. Therefore, the HELMHOLTZ projection of the velocity onto a divergence-free field is done in spectral space, where modified wavenumbers corresponding to the underlying discretization (4.2) are applied. See VICHNEVETSKY and BOWLES [176] for an introduction to the modified-wavenumber concept.

4.2 Decaying Homogeneous Isotropic Turbulence

We integrate the NAVIER-STOKES equation by initially prescribing $\widehat{E}(\xi)$ as inertial-range spectrum for homogeneous isotropic turbulence in the limit $Re \longrightarrow \infty$. After an initial transient during which the randomly oriented initial phases re-align by NAVIER-STOKES dynamics the energy spectrum decays self-similarly while preserving the $\xi^{-5/3}$ law up to the largest wavenumbers, see Fig. 4.1. This finding is consistent with LES results obtained with CHOLLET's eddy viscosity model available in the literature [24, 118, 184].
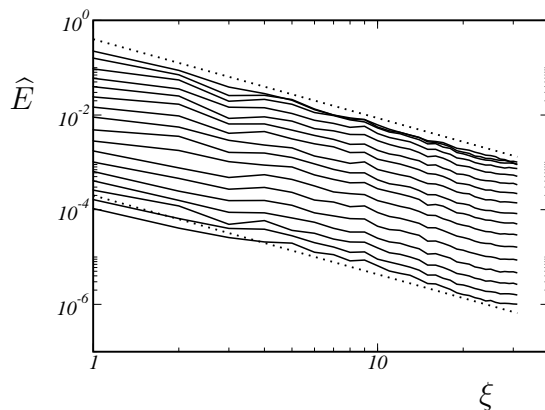
Figure 4.1: Instantaneous 3-D energy spectra for LES of decaying homogeneous isotropic turbulence at the inviscid limit. ———— instantaneous spectra ; ·········· $\widehat{E} \sim \xi^{-5/3}$.

The observed decay rate

$$\varepsilon = -\partial k / \partial t \tag{4.3}$$

of the resolved turbulent kinetic energy

$$k(t) = \sum_{1}^{\xi_C} \widehat{E}(\xi, t) \tag{4.4}$$

is proportional to the turbulent kinetic energy to the power of 3/2, see Fig. (4.2), as predicted by the scaling

$$\varepsilon \sim k^{3/2} L^{-1}$$

for self-similar decay of an inertial-range spectrum, i.e. $L = \text{const.}$
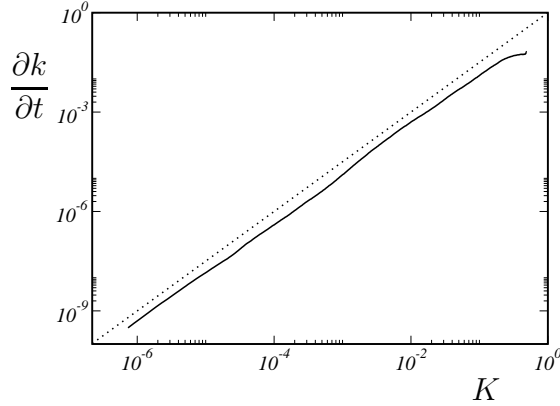
Figure 4.2: Phase diagram of turbulent kinetic energy for decaying homogeneous isotropic turbulence at Re $\longrightarrow \infty$. $\cdots\cdots\cdots \varepsilon \sim k^{3/2}$.

Decay rate and energy-spectrum shape can be assessed simultaneously by the KOL-MOGOROV function

$$C_K(\xi, t) = \varepsilon(t)^{-2/3} \, \xi^{5/3} \, \widehat{E}(\xi, t) \tag{4.5}$$

which is plotted in Fig. 4.3. For an ideal setting the KOLMOGOROV function should be constant. For our simulations, we find a $C_K(\xi, t)$ which is almost constant in time and has a wide plateau in ξ at $C_K \approx 1.8$. This value slightly differs from theoretical predictions, but is in reasonable agreement with other published results. A comprehensive account of the value of the KOLMOGOROV constant in numerical simulations of isotropic turbulence is given by YEUNG and ZHOU [186].
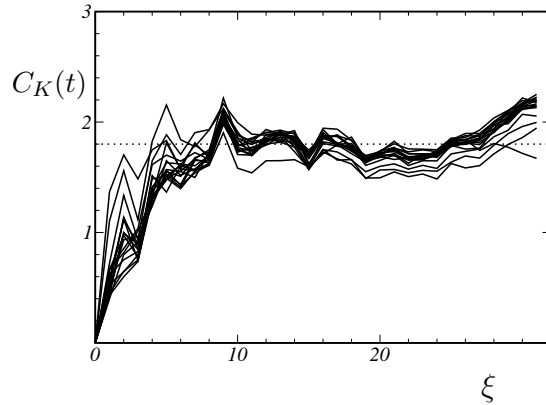
Figure 4.3: KOLMOGOROV function for decaying homogeneous isotropic turbulence at Re $\longrightarrow \infty$. $\cdots\cdots\cdots C_K = 1.8$.

4.3 Forced Homogeneous Isotropic Turbulence

As second test case, ALDM is applied to forced isotropic turbulence governed by

$$\frac{\partial \overline{\boldsymbol{u}}_N}{\partial t} + \widetilde{G} * \widetilde{\boldsymbol{\nabla}} \cdot \widetilde{\boldsymbol{N}}_N(\widetilde{\boldsymbol{u}}_N) - \nu \boldsymbol{\nabla} \cdot \boldsymbol{\nabla} \overline{\boldsymbol{u}}_N = \boldsymbol{S}(\overline{\boldsymbol{u}}_N) \ , \tag{4.6a}$$

$$\boldsymbol{\nabla} \cdot \overline{\boldsymbol{u}}_N = 0 \ . \tag{4.6b}$$

The forcing $\boldsymbol{S}(\overline{\boldsymbol{u}}_N)$ is added to the right-hand side as an extra source term. It is defined in spectral space through its Fourier transform

$$\widehat{\boldsymbol{S}}(\boldsymbol{\xi}) = - C_S(\xi) \widehat{\overline{\boldsymbol{u}}}(\boldsymbol{\xi}) \ , \tag{4.7}$$

where $\xi = |\boldsymbol{\xi}|$. The forcing results in a production of kinetic energy that compensates dissipation while preserving the shape of the kinetic-energy spectrum. By construction of the linear compensation factor $C_S(\xi)$ only large scales are affected by the forcing

$$C_S(\xi) = \begin{cases} \left(2\widehat{E}'(\xi,t)\right)^{-1} \dfrac{\partial \widehat{E}'(\xi,t)}{\partial t} & ,\xi \leq \xi_S \\ 0 & ,\text{otherwise} \end{cases} \ , \tag{4.8}$$

where $\widehat{E}'$ is an intermediate energy spectrum obtained by first solving Eq. (4.6) with $\boldsymbol{S} = \boldsymbol{0}$ at the known time level. In this section the threshold wavenumber is $\xi_S = 4$.

We perform simulations for four different cases corresponding to the combination of two different grids with two different REYNOLDS numbers. The coarser grid is composed of $N^3 = 32^3$, the finer one of $N^3 = 64^3$ evenly-spaced cells. The computational REYNOLDS numbers Re $= 1/\nu$ are Re $= 10^2$ and Re $= 10^5$. For the lower REYNOLDS number the KOLMOGOROV length scale

$$\eta_K = \frac{\nu^{3/4}}{\varepsilon^{1/4}} \tag{4.9}$$

is on the order of the mesh size $h = 2\pi/N$ for $N = 64$. The initial condition is a divergence-free velocity field with random phases and with a 3-D energy spectrum $\widehat{E}(\xi) = \frac{1}{2}\xi^{-5/3}$. After an initial transient of 250 time steps, samples of the 3-D energy spectra were collected until a converged mean spectrum was observed.

The resulting 3-D energy spectra are shown in Figure 4.4. For Re $= 10^2$ the largest resolved wave numbers are within the dissipative range. A comparison with DNS data show that the energy spectra computed with ALDM are also correct at low REYNOLDS numbers. A characteristic and grid independent observation is that the energy spectra

level out in the immediate neighborhood of the cut-off wavenumber ξ_C. For $Re = 10^5$ the 3-D mean energy spectra coincide for both mesh resolutions and follow the KOL-MOGOROV law. This result verifies a posteriori the optimum parameter set which was based on the corresponding theoretical prediction.
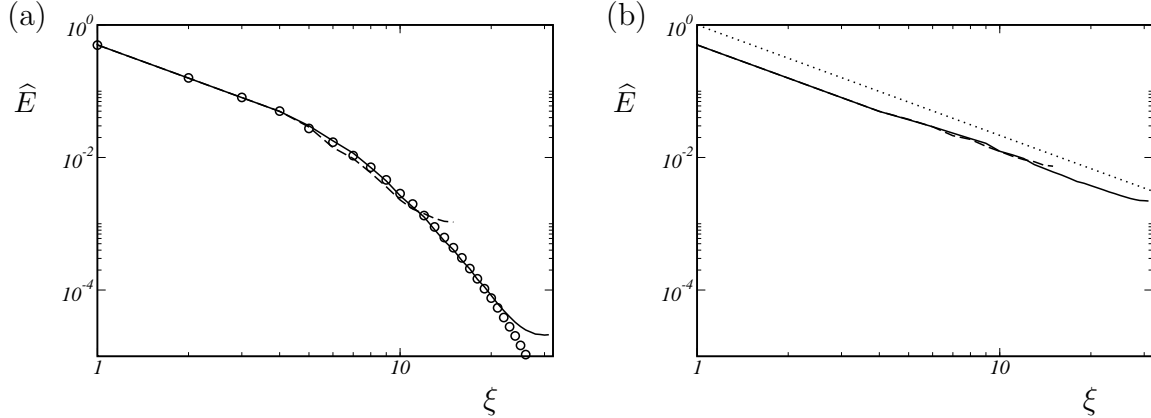
Figure 4.4: Mean 3-D energy spectra for the large-scale forced NAVIER-STOKES equation at (a) Re = 100, (b) Re = 100000 ; ——— LES with 64^3 cells ; − − − − LES with 32^3 cells ; ○ DNS ; ········· line $\sim \xi^{-5/3}$.

Figure (4.5) shows results obtained with a pseudo-spectral code, where CHOLLET's spectral eddy viscosity is added explicitly. We note an excellent agreement between the CHOLLET-LESIEUR SGS model, ALDM, and the theoretical prediction $\widehat{E}(\xi) \sim \xi^{-5/3}$, and DNS data respectively. For a dissipative-range spectrum EDQNM predicts, e.g, a considerably lower plateau value for ν_{SGS}^+ [118, e.g.] which has also been noticed in DNS analyses [35, e.g.]. On this account the performance of the unmodified CHOLLET-LESIEUR SGS model at Re $= 10^2$ is remarkable. A possible explanation is that the low-wavenumber forcing immediately compensates an overestimated SGS dissipation.

For Re $= 10^2$ the isotropic TAYLOR micro scale λ_T can be approximated in terms of the resolved 3-D energy spectrum [115]. The micro-scale REYNOLDS number is

$$Re_\lambda = \frac{\lambda_T u'}{\nu} , \tag{4.10}$$

with

$$\lambda_T \doteq \sqrt{\frac{5 \sum\limits_{\xi=1}^{\xi_C} \widehat{E}(\xi)}{\sum\limits_{\xi=1}^{\xi_C} \xi^2 \widehat{E}(\xi)}} \qquad u' \doteq \sqrt{\frac{2}{3} \sum\limits_{\xi=1}^{\xi_C} \widehat{E}(\xi)} . \tag{4.11}$$
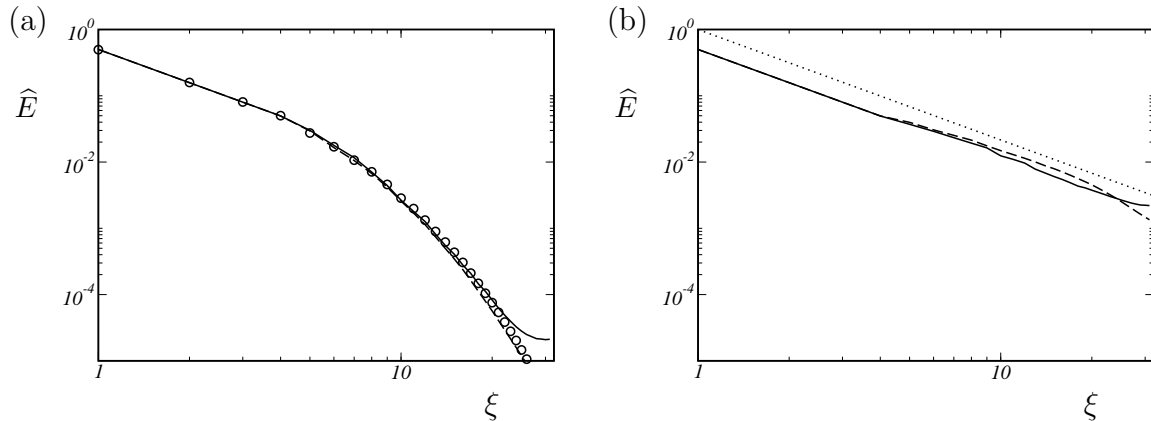
Figure 4.5: Mean 3-D energy spectra for LES of the large-scale forced Navier-Stokes equation at (a) Re = 100, (b) Re = 100000 with 64^3 cells ; ———— ALDM ; −−−− Chollet-Lesieur model ; ○ DNS ; ·········· line $\sim \xi^{-5/3}$.

The DNS predicts $Re_\lambda = 74$. Using ALDM we obtain $Re_\lambda = 78$ with $N = 32$ and $Re_\lambda = 73$ with $N = 64$. For the high-Re case λ_T cannot be computed by (4.11) since dissipative scales are not resolved. To quantify the SGS dissipation rate of ALDM at $Re \longrightarrow \infty$ we consider freely decaying turbulence in the following section.

We conclude that with the model parameters found by an optimum match of a theoretical prediction for isotropic turbulence at $Re \longrightarrow \infty$, see Section 3.3, the SGS dissipation predicted by ALDM correctly models the local energy transfer. This holds for cut-off wavenumbers ξ_C within the inertial range. The results also show that even for lower Reynolds numbers, for which ξ_C is in the dissipative range, the predicted spectral energy distribution and dissipation rate for the same parameter set are correct. This indicates that the used model parameters may be valid universally for isotropic turbulence.

4.4 Comte-Bellot - Corrsin Experiment

A more complex situation is encountered for decaying grid-generated turbulence for which also the correct representation of the energy-containing range of the spectrum is important [136]. Computations are initialized with energy spectrum and Reynolds numbers adapted to the wind-tunnel experiments of Comte-Bellot and Corrsin [27], denoted hereafter as CBC.

Among other space-time correlations CBC provides streamwise energy spectra for grid-generated turbulence at three positions downstream of a mesh with a width $M = 5.08$cm. Table 3 of Comte-Bellot and Corrsin [27] gives corresponding 3-D energy spectra

which were obtained under the assumption of isotropy. The grid REYNOLDS number of the experiment is $\mathrm{Re}_M = 34000$, the TAYLOR-microscale REYNOLDS number is given as $\mathrm{Re}_\lambda = 71.6$ at the first and $\mathrm{Re}_\lambda = 60.6$ at the last position.
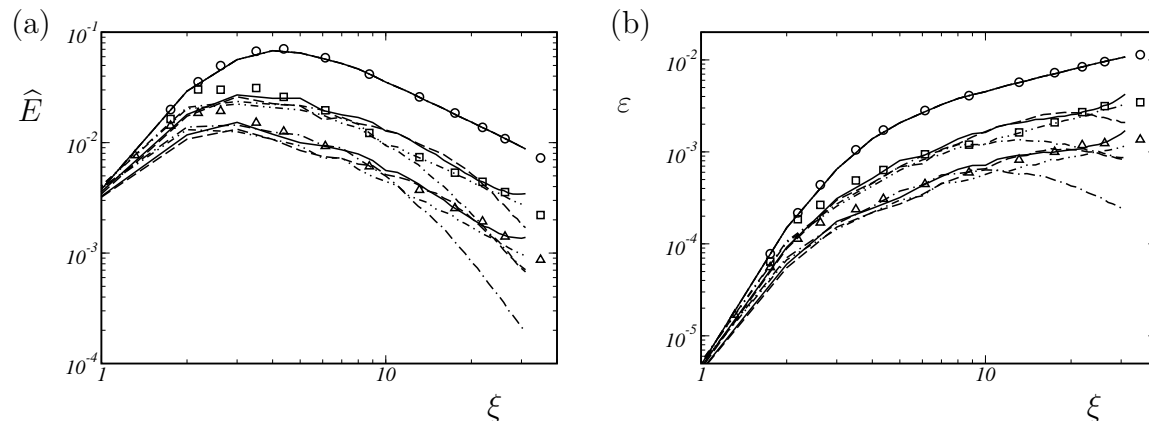
Figure 4.6: LES with 64^3 cells for the COMTE-BELLOT - CORRSIN test case. (a) Instantaneous 3-D energy spectra (b) Instantaneous 3-D dissipation spectra — — — — CHOLLET's spectral eddy viscosity model, ·—·—·— SMAGORINSKY model, —··—··— dynamic SMAGORINSKY model, ——— ALDM ; ○ $t' = 42$, □ $t' = 98$ and △ $t' = 171$ experimental data of COMTE-BELLOT and CORRSIN [27].

In the simulation this flow is modeled as decaying turbulence in a $(2\pi)^3$-periodic computational domain. Based on the TAYLOR hypothesis the temporal evolution in the simulation corresponds to a downstream evolution in the wind-tunnel experiment with the experimental mean-flow speed which is approximately constant. The energy distribution of the initial velocity field is matched to the first measured 3-D energy spectrum of CBC. The SGS model is verified by comparing computational and experimental 3-D energy spectra at later time instants which correspond to the other two measuring stations.

The experimental data are non-dimensionalized as proposed by MISRA and LUND [119] and GHOSAL *et al.* [49]. The reference velocity is $U_{ref} = \sqrt{3/2}\ 22.2$ cm/s , the reference length is $L_{ref} = 10.8M/2\pi$, and the reference time is $t_{ref} = L_{ref}/U_{ref}$. In order to create the initial velocity field a random field was allowed to develop for about one large-eddy turnover time while maintaining the 3-D energy spectrum (Eqs. (4.6-4.8) with $\xi_S = \sqrt{3}\xi_C$) as given for the first measuring station.

Results of ALDM are compared with those obtained with a 4th-order central discretization and an explicit SMAGORINSKY SGS model and with a pseudo-spectral code and an explicit CHOLLET-LESIEUR model. The SMAGORINSKY model is used in its conventional and in its dynamic version. For the conventional model [99, 161] the parameter is

set to $C_S = 0.18$. LILLY [100] derived this value for sufficiently large REYNOLDS numbers and a sharp spectral cut off in the inertial range assuming $C_K \approx 1.4$. The dynamic algorithm was proposed by GERMANO *et al.* [46]. Here, C_S is computed according to LILLY [101] and an average over the entire flow field is taken.

Examining the computed energy spectra, Fig. 4.6, and dissipation spectra, Fig. 4.6, we note that ALDM performs just as well as the dynamic SMAGORINSKY SGS model. It should be noted that we use the the dynamic SMAGORINSKY model as an example for state-of-the-art SGS models and as a benchmark for isotropic turbulence. The conventional SMAGORINSKY model requires an ad-hoc adjustment of C_S. The theoretical value is based on the assumption of a wide inertial range about ξ_C , i.e. a high-REYNOLDS-number spectrum, which is not the case for the CBC experiments. We found that a somewhat smaller C_S gives better results which are close to those of the dynamic SMAGORINSKY model. For the CHOLLET-LESIEUR model with the eddy viscosity of Eq. (3.30) the overall results are similar to ALDM and the dynamic SMAGORINSKY model. At large wave numbers the energy drops and approaches that of the standard SMAGORINSKY model.

For the decay of total kinetic energy K, Fig. 4.7, we find $\partial K/\partial t \sim t^{-n}$ with $n = 1.25$. This corresponds to $\varepsilon = \partial K/\partial t \sim t^{-2.25}$ or $\varepsilon \sim K^{1.8}$. The exponent $n = 1.25$ is in a reasonable agreement with published experimental data [2, 27, 83] which range from $n = 1.2$ to $n = 1.3$.
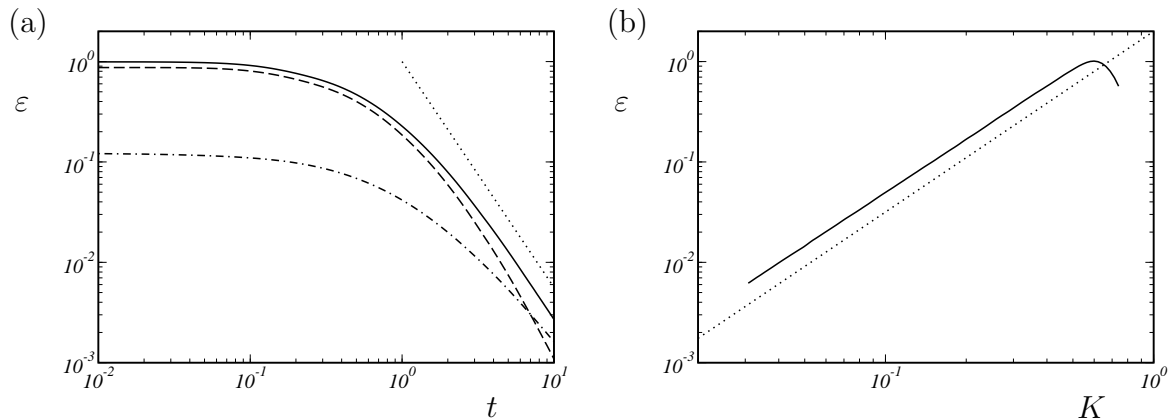
Figure 4.7: Energy decay rate of ALDM results for decaying homogeneous isotropic turbulence for the COMTE-BELLOT - CORRSIN experiment. (a) Sources of dissipation: ·—·—·— molecular dissipation, − − − − implicit SGS dissipation, ——— total dissipation, ·········· $\varepsilon \sim t^{-2.25}$; (b) Power law of total dissipation: ——— total dissipation, ·········· $\varepsilon \sim K^{1.8}$ (equivalent to $K \sim t^{-1.25}$)

Fig. 4.8 shows iso-surfaces of a constant vorticity magnitude at the last position. The
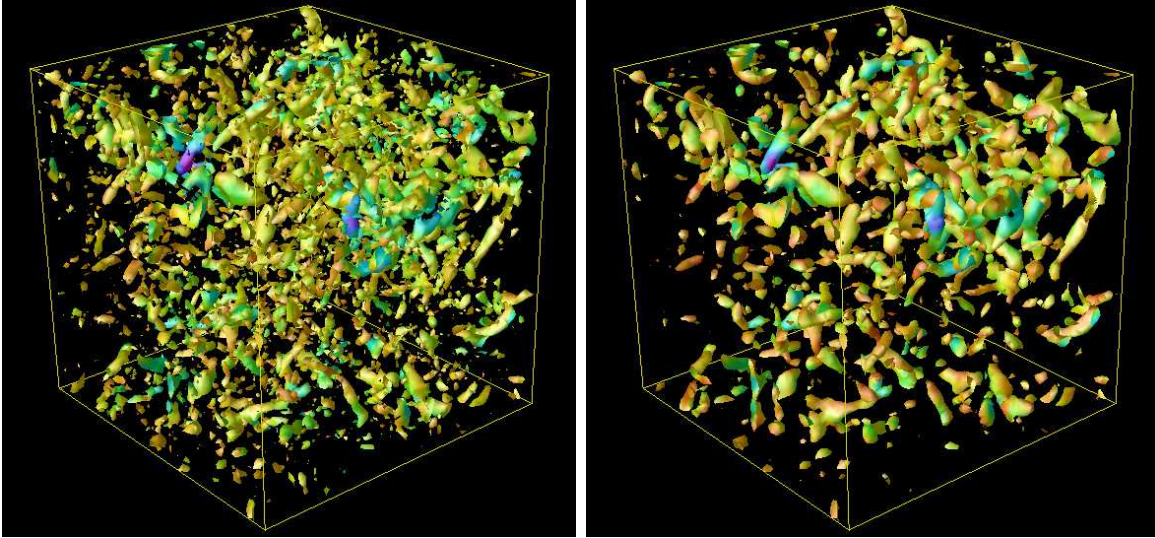
Figure 4.8: Iso-surfaces of constant vorticity magnitude at the final station of the CBC experiment for implicit LES with ALDM. *Left:* original data from ALDM, *right:* filtered with top-hat filter width 2Δ. Colors indicate kinetic energy.

threshold value is chosen to 3.5 times the mean vorticity. The visualization shows worm-like vorticity structures and indicates that ALDM reproduces basic mechanisms of turbulence. Even though GARNIER *et al.* [44] investigated the inviscid EULER equation they obtained similar images using a threshold of 2.5 times the mean vorticity and a higher spatial resolution of 128^3 grid cells. The visual impression of the 64^3-point simulation of GARNIER *et al.* [44] can be reproduced when we filter our ALDM results to the effective resolution of 32^3, see Fig. (4.8).

4.5 Transition of the Three-Dimensional TAYLOR–GREEN Vortex

One of the most demanding test cases for SGS models is laminar-turbulent transition. For the onset of transition the SGS model must not affect the instability modes of the laminar flow. Most eddy-viscosity models, for instance the SMAGORINSKY model and the structure-function model of MÉTAIS and LESIEUR [93, 95, 118], do not satisfy this requirement without modifications.

A suitable test scenario for a periodic computational domain is the 3-D TAYLOR–GREEN

Vortex (TGV). This flow is characterized by the initial data

$$\overline{\boldsymbol{u}}(t=0) \approx \boldsymbol{u}(t=0) = \begin{bmatrix} 0 \\ \cos(x)\sin(y)\cos(z) \\ -\sin(x)\cos(y)\sin(z) \end{bmatrix}. \qquad (4.12)$$

At $t = 0$ the entire kinetic energy is contained within eight Fourier modes on the wave-number shell $\xi = \sqrt{3}$. At early times the TGV evolution is laminar and strongly anisotropic, see Fig. (4.11). Then energy is transferred to larger wave numbers by vortex stretching. Visualizations of vortices show that they roll up, divide and re-connect, see Fig. (4.11). Preserving spatial symmetries the flow eventually becomes turbulent. In the final steps the small scales are nearly isotropic and exhibit an $\xi^{-5/3}$ inertial range of the kinetic-energy spectrum.

We compare our LES with DNS of BRACHET *et al.* [15] which were originally performed on a grid of 256^3 modes and repeated with 864^3 modes about 10 years later [16]. These spectral simulations exploit spatial symmetries of the TGV to reduce the effective computational cost by a factor of 8. BRACHET *et al.* [15] were therefore able to resolve REYNOLDS numbers up to Re = 3000.

For LES spatial symmetries are not imposed. The computational domain is a $(2\pi)^3$ box that contains 8 counter-rotating vortices. It is discretized with 64^3 cells and has periodic boundary conditions. To assess the quality of the LES the characteristic growth and decay of the dissipation rate is compared between the present LES and Fig. 7 of BRACHET *et al.* [15], see Fig. 4.9. The considered Reynolds numbers range from Re = 100 to Re = 3000. For an assessment of ALDM with respect to standard LES, we also show results for the conventional ($C_S = 0.18$) SMAGORINSKY model, the dynamic SMAGORINSKY model, and the CHOLLET-LESIEUR model at the same resolution. To demonstrate the effect of the SGS models simulations without SGS model were performed. These simulations became unstable as soon as the energy transfer reached the highest resolved wave numbers, see Fig. 4.9.

The SMAGORINSKY model with constant parameter C_S is obviously not well suited for transitional flows. Even in the fully resolved Re = 100 case excessive dissipation affects the flow evolution. At larger Re the conventional SMAGORINSKY model gives wrong dissipation rates and a completely wrong flow structure. If the SMAGORINSKY parameter is adjusted dynamically the behavior improves significantly. The SGS viscosity vanishes for laminar flow. The prediction is good for the two lowest REYNOLDS numbers throughout the entire time interval and up to $t = 8$ for Re = 400. An advantage
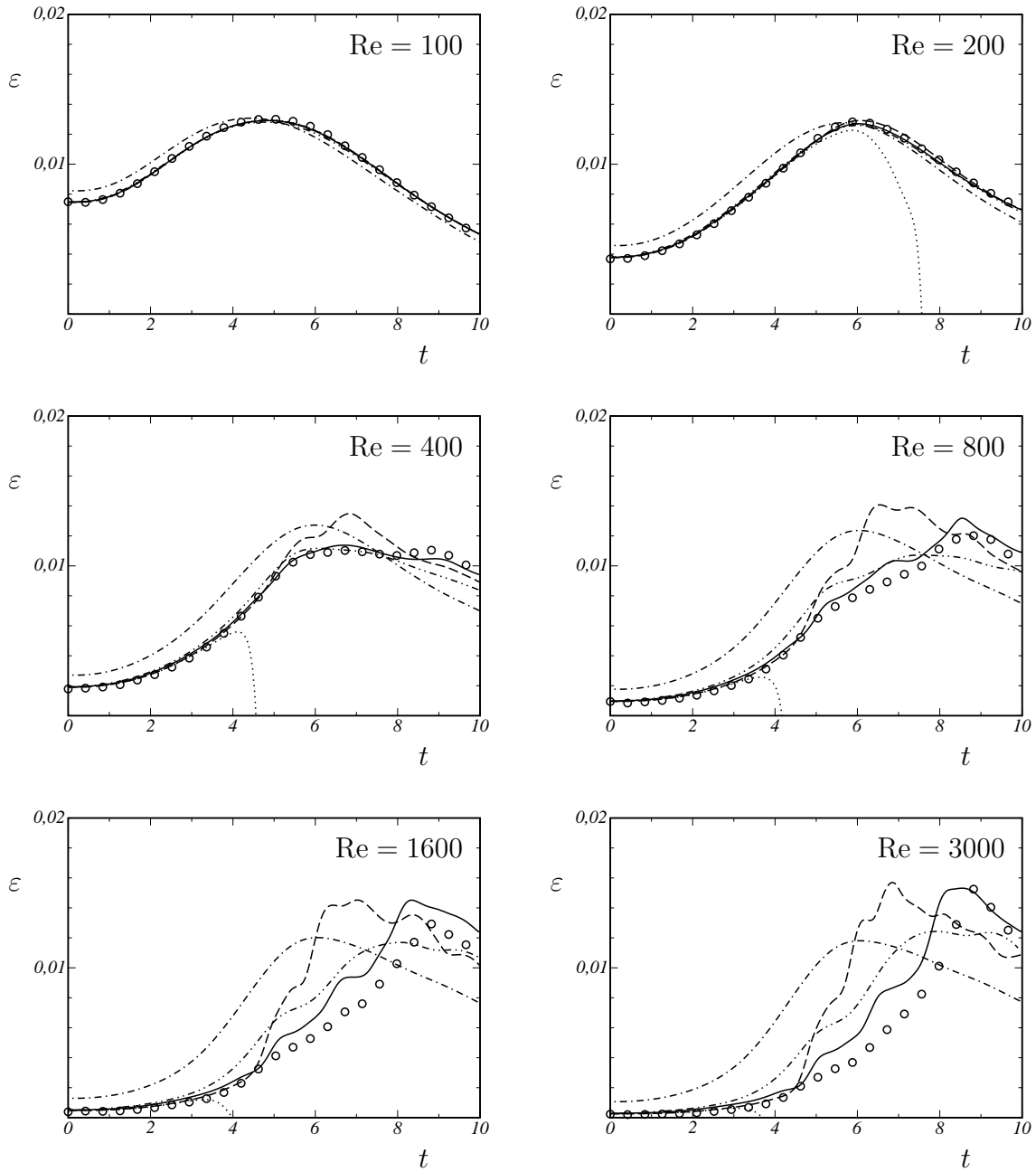
Figure 4.9: Rate of energy dissipation for LES of the TAYLOR-GREEN vortex ; ·········· without SGS model, — — — — CHOLLET's spectral eddy viscosity model, ·—·—·— SMAGORIN-SKY model, —··—··— dynamic SMAGORINSKY model, ——— ALDM, ∘ DNS data from BRACHET *et al.* [15].
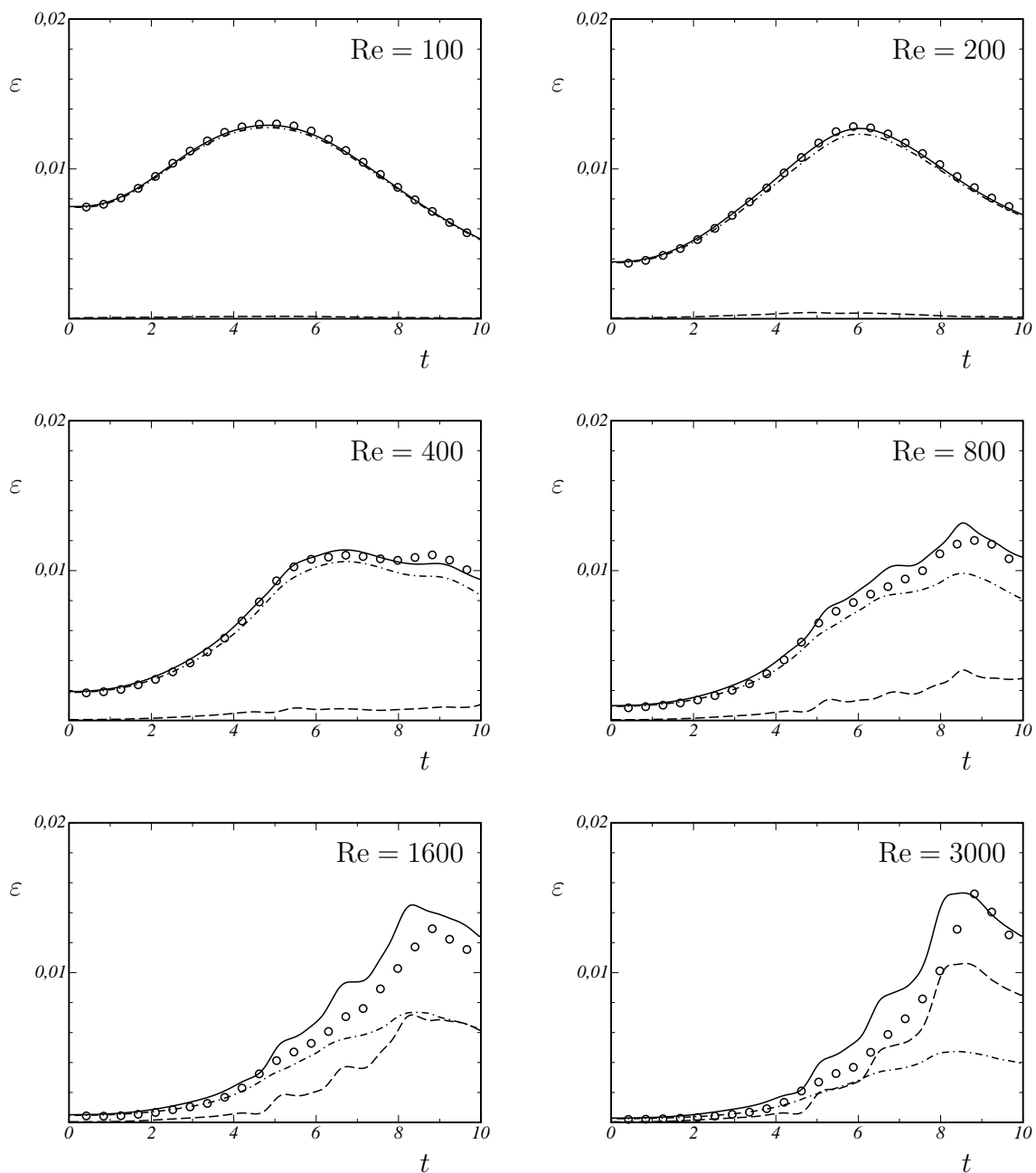
Figure 4.10: Contributions to energy dissipation in ALDM for LES of the TAYLOR-GREEN vortex ; ·—·—·— molecular dissipation, ———— implicit SGS dissipation, ———— total dissipation, ∘ DNS data from BRACHET *et al.* [15].
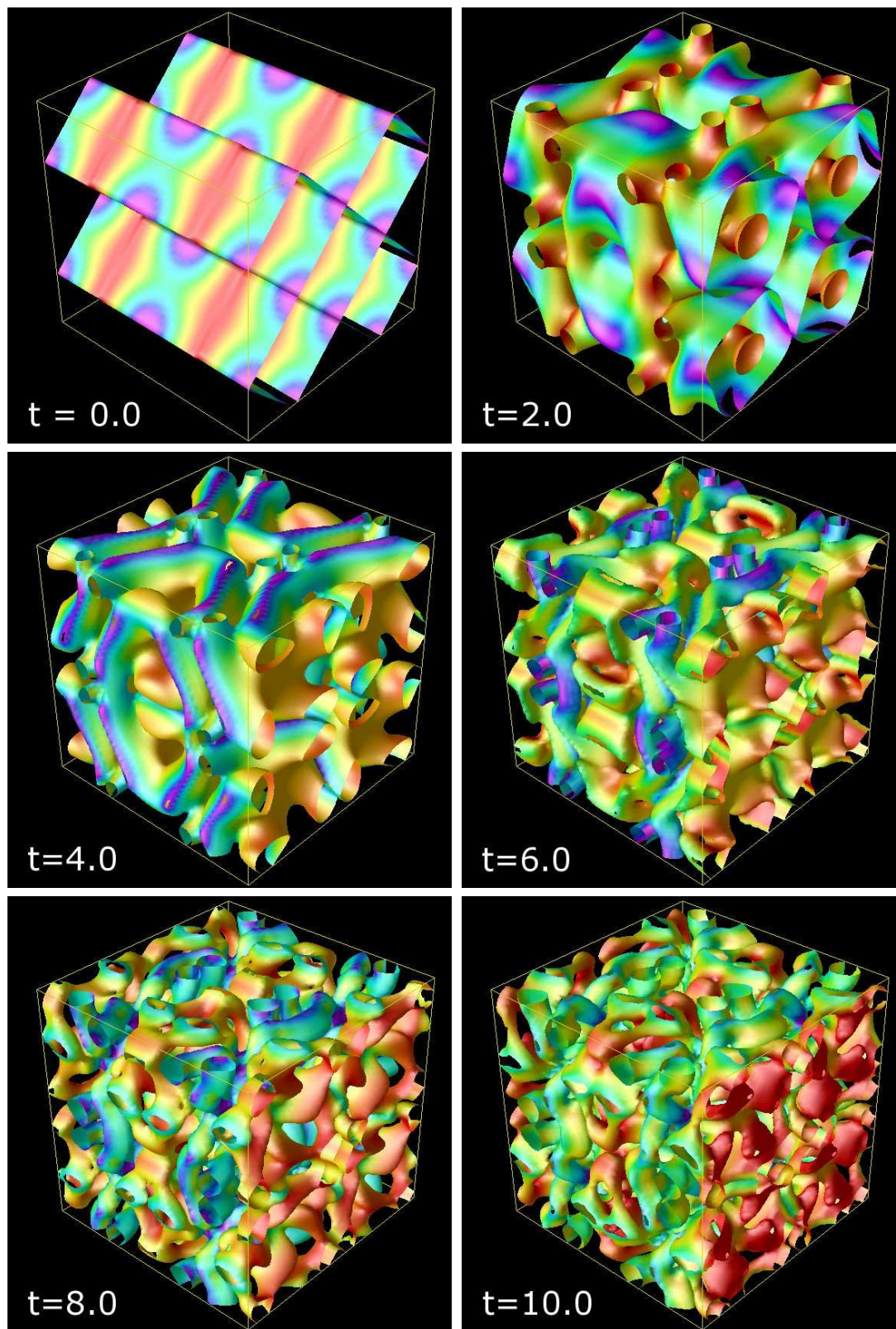
Figure 4.11: Iso-surfaces for the zero Q-criterion (see Jeong and Hussain [79]) for implicit LES of Taylor-Green vortex with ALDM at Re = 400. Colors indicate kinetic energy.

of the CHOLLET-LESIEUR model is that no energy is dissipated by the model in the early stages of the cascade, when no energy has yet reached the cut-off wavenumber. At later stages, however, it is too dissipative.

Much better results are obtained with ALDM. The error increases with increasing REYNOLDS number but stays at all times significantly smaller than for the dynamic SMAGORINSKY model. Up to Re = 800 the difference between ALDM and DNS is negligibly small. Note that the resolution requirement of a DNS of Re = 800 is two orders of magnitude higher than that of the LES.

The dissipation as shown in Figure 4.9 generally can originate from three sources. One source is molecular dissipation which is inversely proportional to the REYNOLDS number. The second source is transfer which is explicitly modeled by SGS dissipation. The third source is numerical dissipation which should be negligible for proper explicit SGS modeling. For implicit SGS modeling, however, the third source replaces the second one. This is the case with ALDM as shown in Figure 4.10. At low Re the discretization does not significantly contribute to the energy dissipation. However, the implicit model activates itself with increasing REYNOLDS number and finally dominates the molecular dissipation at Re = 3000. These results for the TGV confirm that the implicit model, owing to its solution adaptivity, over a large range of REYNOLDS numbers functions as intended.

4.6 Summary

The performance of the implicit model was evaluated by simulations of different flow configurations. Large-scale forced and decaying three-dimensional homogeneous isotropic turbulence were considered. For transitional flows the model performance was tested by an application to instability and breakdown of the 3-D Taylor-Green vortex. For all test cases the implicit model shows an excellent agreement with theory and experimental data. It is demonstrated that physically optimized implicit SGS models can perform at least as well as established explicit models.

— CHAPTER FIVE —

ADAPTATION FOR WALL-BOUNDED TURBULENCE

In this chapter the implicit SGS model of ALDM is analyzed for wall-bounded turbulence. First, ALDM is applied to incompressible, turbulent channel flow. Computational results are presented for REYNOLDS numbers, based on friction velocity and channel half-width, of $Re_\tau = 180$, $Re_\tau = 395$, $Re_\tau = 590$, and $Re_\tau = 950$. All simulations compare well with Direct Numerical Simulation data and yield better results than the dynamic SMAGORINSKY model at same resolution. The near-wall accuracy of ALDM can be further improved by a simple modification which is described below. Finally, ALDM is tested for laminar turbulent transition of zero-pressure-gradient boundary layer flow, which is one of the most demanding tests for SGS models[1].

5.1 Application to Turbulent Channel Flow

5.1.1 Computational Method

In the following we report on the application of ALDM to turbulent channel flow. The incompressible NAVIER-STOKES equations are discretized on a staggered CARTESian mesh. For time advancement an explicit third-order RUNGE-KUTTA scheme with coefficients as proposed by SHU [50, 153] is used. We use a COURANT-FRIEDRICHS-LEWY limit of CFL = 1.0 for all simulations. The pressure-Poisson equation and diffusive terms are discretized by second-order centered differences. The POISSON solver employs fast Fourier transforms in the streamwise and spanwise directions and performs direct tridiagonal-matrix inversions in the wall-normal direction. The oddball modes remain part of the solution. Modified wavenumbers for a second-order discretization of the LAPLACE operator are used. It should be noted that the POISSON equation is solved at every RUNGE-KUTTA substep.

---

[1] This chapter is based on Refs. [62, 65, 73]

Since ALDM is based on a WENO-like discretization, computational cost are comparable to such schemes. The adaptive deconvolution scheme causes an overhead which is comparable to that of the test-filtering procedure of the dynamic SMAGORINSKY SGS model. A computationally more efficient implementation of the original ALDM results in the simplified adaptive local deconvolution method (SALD) [63]. All results presented in this chapter and in the following chapters are obtained by this version, which is outlined in Appendix B.

Results of implicit LES are compared with those obtained by a dynamic SMAGORINSKY SGS model combined with a second-order central discretization scheme. The SMAGORINSKY constant is computed using LILLY's version [101] of the dynamic procedure of GERMANO *et al.* [46], and an average over the two homogeneous flow directions is taken. Following PIOMELLI [132], no test filtering is performed in the wall-normal direction.

5.1.2 Grid and Boundary Conditions

In order to validate the new model for wall-bounded flows, implicit LES have been conducted, where computational setup and REYNOLDS number are adapted to the reference DNS of MOSER *et al.* [121]. First we consider the case with nominal $\mathrm{Re}_\tau = 395$. The flow is driven by a mean pressure gradient that is controlled to maintain a constant mass flow corresponding to $\mathrm{Re}_{bulk} = 6875$.

The computational domain has the extent $2\pi H \times 2H \times \pi H$ in the streamwise, wall-normal, and spanwise direction, respectively. Periodic boundary conditions are imposed in streamwise and spanwise direction. No wall model is used in the simulations, rather the no-slip condition is imposed directly, i.e., we set

$$\overline{\boldsymbol{u}}_{wall} = \boldsymbol{0} \quad , \quad \left.\frac{\partial \overline{p}}{\partial y}\right|_{wall} = 0 \ . \tag{5.1}$$

The computational domain is discretized by $64 \times 68 \times 48$ cells. The grid is stretched in wall-normal direction by a hyperbolic tangent function

$$y'_j = -\frac{H}{\tanh\left(C_G\right)}\tanh\left(C_G - 2C_G\frac{j}{N_y}\right) \tag{5.2}$$

in order to increase resolution in the vicinity of the walls, c.f. GULLBRAND and CHOW [56]. N_y is the number of cells in the wall-normal direction and $C_G = 2.5$ is the grid-stretching parameter. Computational-grid parameters are given in Tab. 5.1. This

streamwise direction	$L_x = 2\pi H$	$N_x = 64$	$h_x^+ = 38.8$
wall-normal direction	$L_y = 2H$	$N_y = 68$	$h_y^+ = 1.2 - 25.0$
spanwise direction	$L_z = \pi H$	$N_z = 48$	$h_z^+ = 25.9$

Table 5.1: Grid for LES of turbulent channel flow at $\mathrm{Re}_\tau = 395$.

parameter choice is based on an earlier study [86] employing the dynamic SMAGORIN-SKY SGS model and second-order centered schemes on staggered grids.

5.1.3 Results

The implicit LES is initialized with a laminar POISEUILLE profile superimposed with white-noise fluctuations. The flow goes through transition and reaches a stationary turbulent state. Figure 5.1 shows the evolution of the velocity fluctuations (averaged over the entire domain) during the initial transient for five different amplitudes of the random initial disturbance ranging from $u_{rms}(t_0) = 10^{-7}U_{bulk}$ to $u_{rms}(t_0) = 10U_{bulk}$.
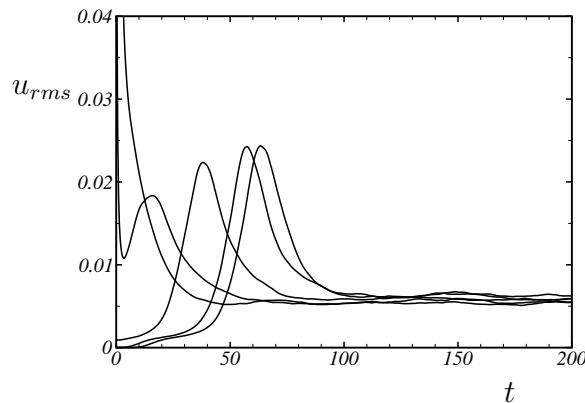
Figure 5.1: Evolution of instantaneous r.m.s. velocity fluctuations during the initial transient in implicit LES of channel flow. The lines correspond to different amplitudes of the initial disturbance superposed on the laminar state ranging from $u_{rms}(t_0) = 10^{-7}u_{bulk}$ to $u_{rms}(t_0) = 10u_{bulk}$.

The implicit LES scheme is sufficiently robust to handle very strong disturbances but also allows for the growth of amplified modes even for very small amplitudes. The results suggest that ALDM is able to reproduce of laminar-turbulent transition for a wide range of disturbance amplitudes, thus confirming an earlier observation for transitional 3-D TAYLOR-GREEN flow (see Section 4.5). Additional results for LES of laminar-turbulent transition of a BLASIUS boundary layer will be given in Section 5.3.3. A detailed study

of transition, however, is beyond the scope of this work. Initial data for the LES with the dynamic SMAGORINSKY model are provided by the developed turbulent solution from an earlier simulation.
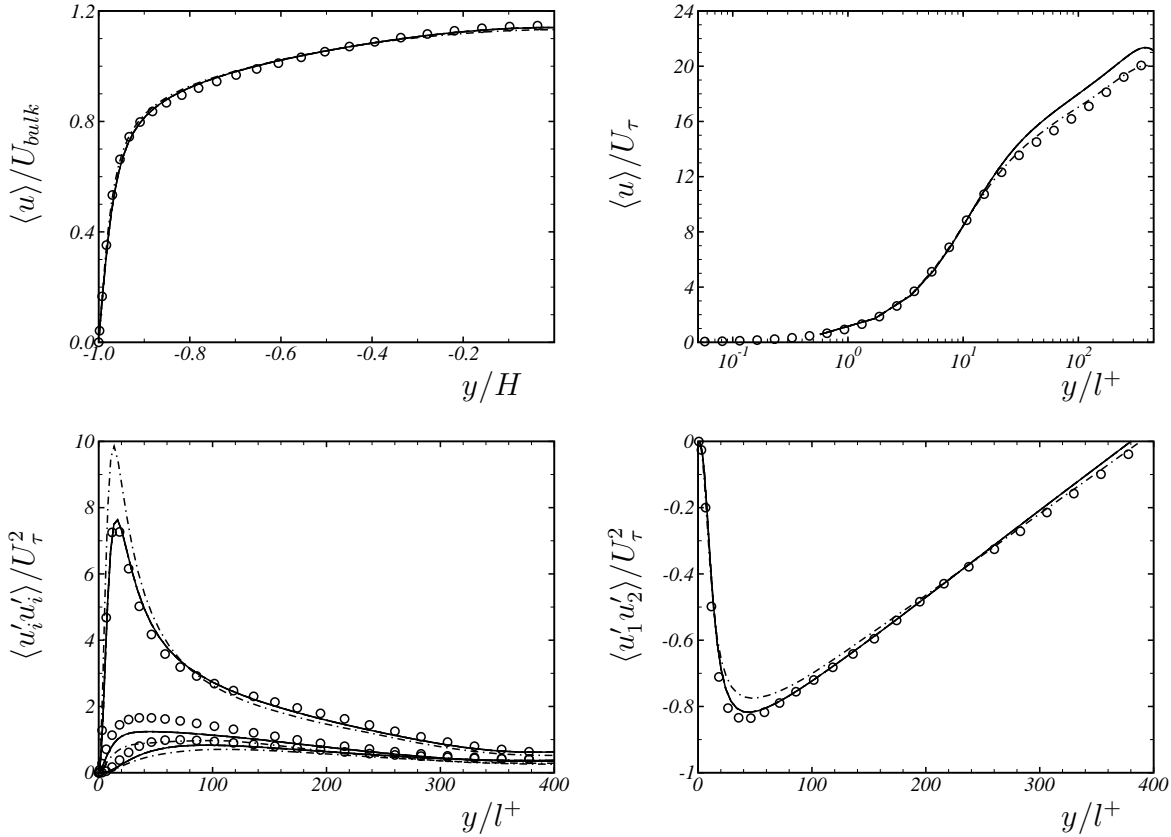
Figure 5.2: Mean velocity profile and REYNOLDS stresses for LES of turbulent channel flow at $Re_\tau = 395$. ———— baseline ALDM formulation, ·—·—·— dynamic SMAGORINSKY model. ○ reference DNS of MOSER *et al.* [121].

Figure 5.2 shows mean velocity profile and REYNOLDS stresses. Here and in the following, computational results are normalized with the bulk velocity

$$U_{bulk} = \frac{1}{2H} \int\limits_{-H}^{+H} \langle u \rangle dy \qquad (5.3)$$

and the channel half width H, or with the wall-friction velocity

$$U_\tau = \sqrt{\nu \langle \partial_y u \rangle_{wall}} \qquad (5.4)$$

and the viscous length scale

$$l^+ = \nu/U_\tau . \qquad (5.5)$$

The velocity vector $\boldsymbol{u} = \{u_1, u_2, u_3\}$ is synonymous with $\{u, v, w\}$.

Results of both explicit and implicit LES are in good agreement with the reference DNS data. The dynamic SMAGORINSKY model shows the well-known overestimation of the streamwise normal REYNOLDS stress and underestimation of the other normal stresses. Albeit yielding better results in general, ALDM predicts a slightly too low wall-friction velocity. For the present configuration, U_τ is underestimated by 3.5%. This issue is addressed in the following section.

5.2 Near-Wall Modeling

5.2.1 Subgrid Dissipation

Underprediction of the friction velocity can be attributed to an overestimation of SGS-turbulence energy resulting in a too large dissipation due to the SGS model. The spectral numerical dissipation of ALDM has been analyzed for the case of homogeneous isotropic turbulence [69]: The solution-adaptive stencil selection scheme generates the cusp of the spectral numerical viscosity of ALDM at large wavenumbers whereas it has no or even a slightly negative contribution at small wavenumbers, see Fig. 5.3a. The numerical flux function of ALDM generates a numerical viscosity $\overline{\nu}_{\widetilde{F}}^+$ that is almost constant at a level which can be adjusted by the model parameter σ, see Fig. 5.3b. A linear curve fit for this contribution gives

$$\overline{\nu}_{\widetilde{F}}^+ \approx 3.5\ \sigma \ . \tag{5.6}$$
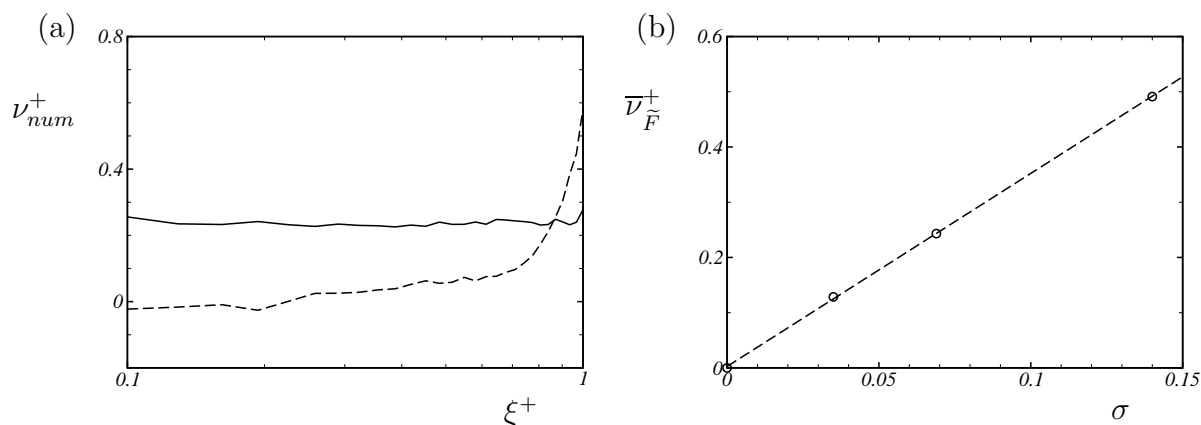
Figure 5.3: (a) Contributions of ———— numerical flux function and — — — — adaptive deconvolution operator to the spectral numerical viscosity of ALDM for homogeneous isotropic turbulence at infinite REYNOLDS number. (b) Correlation between the parameter σ and the mean viscosity of the numerical flux function $\overline{\nu}_{\widetilde{F}}^+$ for homogeneous isotropic turbulence at high REYNOLDS number. — — — — linear fit.

Fig. 5.3 suggests that the contribution of the numerical flux function to the SGS model is very similar to a spectral discretization of a SMAGORINSKY-type eddy-viscosity model. In fact, weights of the deconvolution operator could be determined such that σ functions as the SMAGORINSKY constant of an implicit reproduction. Results of such a model, however, are inferior to ALDM results obtained with evolutionary optimized parameters (see Appendix A). Working on truncation errors of different order, ALDM exploits spectral information at multiple scales resulting in a more complex SGS model. Not only the spectral shape but also the magnitude of the numerical-viscosity adjusts dynamically to the flow [69]. Fig. 5.3a and Eq. (5.6) apply to the calibration case of inertial-range turbulence only.
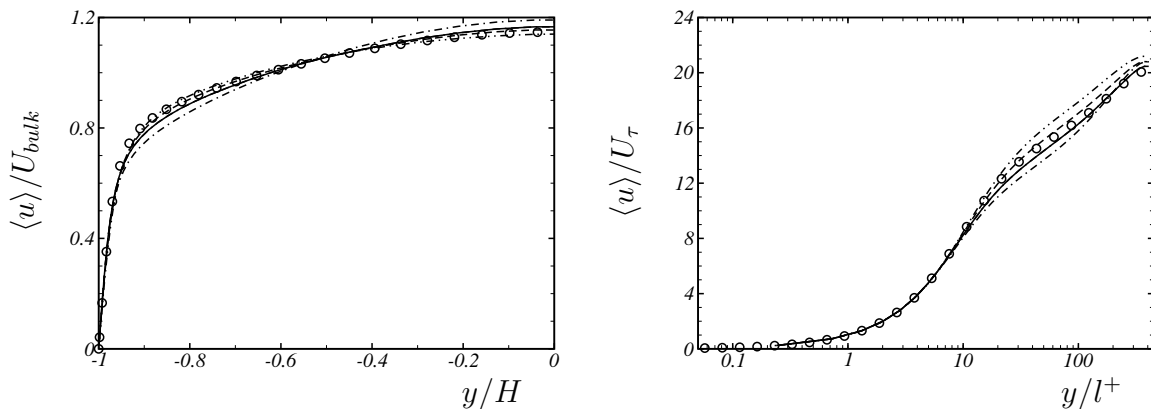
Figure 5.4: Effect of the ALDM parameter σ on the mean velocity profile in turbulent channel flow at $\mathrm{Re}_\tau = 395$. $\cdot—\cdot—\cdot—$ $\sigma = 0.010$; $————$ $\sigma = 0.020$; $————$ $\sigma = 0.035$; $—\cdot\cdot—\cdot\cdot—$ $\sigma = 0.068$; $\circ$ DNS.

The model parameters of ALDM have been calibrated for isotropic turbulence. Due to similar experiences with explicit eddy-viscosity models [97], it is possible that the model parameters of ALDM may depend on the REYNOLDS number. This is investigated on the example of the parameter σ. One could argue that σ should vary for shear flows. Appropriate values may range from $\sigma = 0$ to the optimal value for isotropic turbulence $\sigma = 0.069$. Computational results for different values of σ are shown in Figures 5.4 and 5.5. Since simulations with $\sigma = 0$ turned out to be unstable, the smallest value shown is $\sigma = 0.01$. The optimal parameter value with respect to the prediction of the wall shear stress in turbulent channel flow is in the range $0.02 \leq \sigma \leq 0.035$. However, the overall prediction of the mean velocity profile, especially in the logarithmic layer and in the wake region, deteriorates for σ being different from that calibrated for isotropic turbulence. Disregarding the wall shear stress, the best results are obtained with σ being identical to that for high REYNOLDS number isotropic turbulence. A remaining issue is the near-wall behavior of ALDM which is investigated further in the following section.
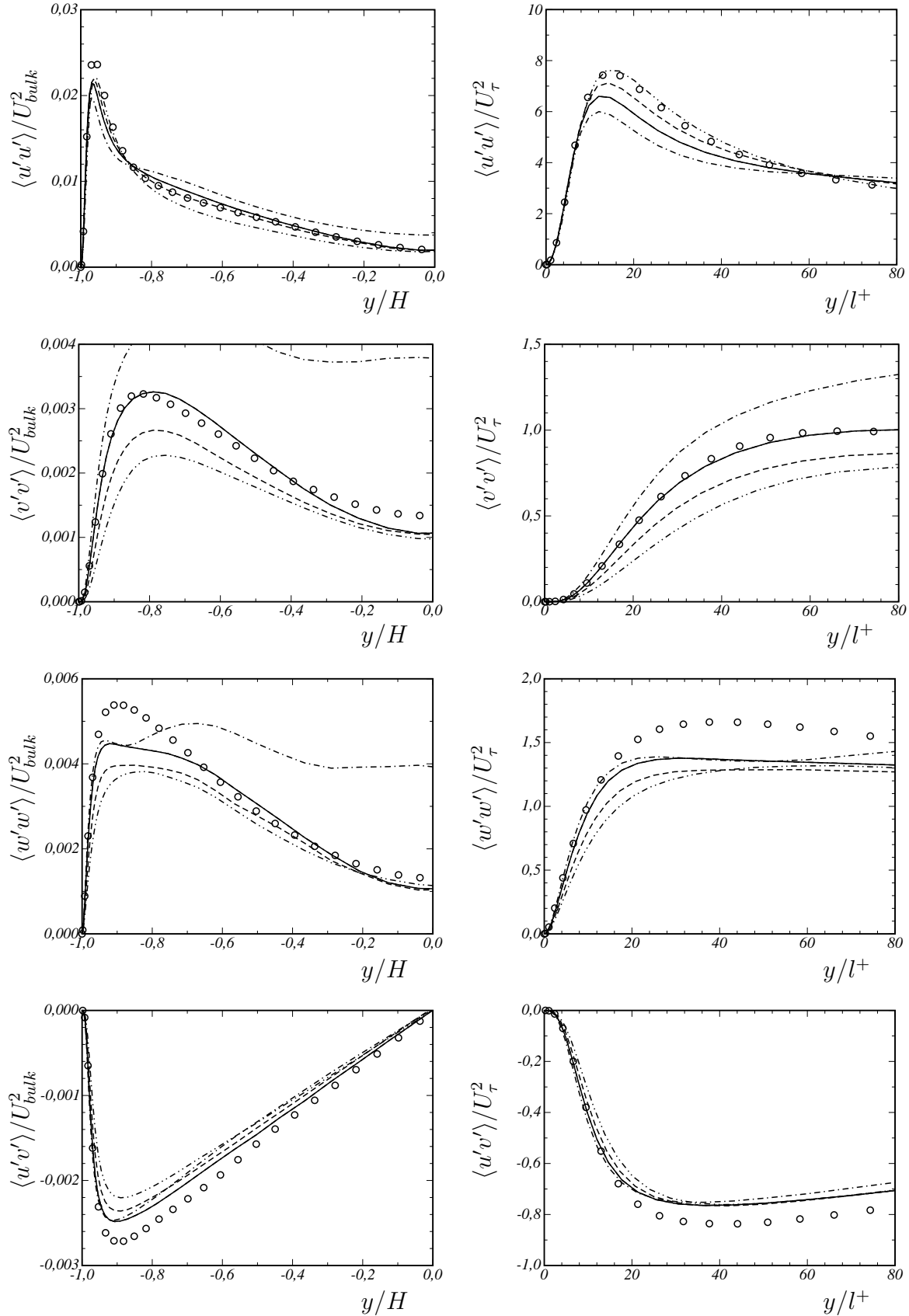
Figure 5.5: Effect of the ALDM parameter σ on the REYNOLDS stresses. $\cdot$—$\cdot$—$\cdot$— $\sigma = 0.010$; ——— $\sigma = 0.020$; — — — — $\sigma = 0.035$; —$\cdot\cdot$—$\cdot\cdot$— $\sigma = 0.068$; $\circ$ DNS.

5.2.2 Near-Wall Effects

With ALDM a local approximation $\widetilde{u}$ of the unfiltered solution u is computed from a solution-adaptive superposition

$$\widetilde{u}_N^\lambda(x_{i+\lambda}) = \sum_{k=1}^{K}\sum_{r=0}^{k-1} \omega_{k,r}^\lambda(\overline{u}_N, x_i) \sum_{l=0}^{k-1} \alpha_{k,r,l}^\lambda(x_i)\, \overline{u}_N(x_{i-r+l}),$$

of HARTEN-type deconvolution polynomials with $K = 3$. The coefficients $\alpha_{k,r,l}^\lambda$ are grid-dependent, see Chapter 2. The solution-adaptive behavior is controlled by dynamic weight functionals $\omega_{k,r}^\lambda(\overline{u})$. By construction, the statistical average of these weights resembles a central reconstruction scheme for isotropic turbulence. Near solid walls, however, velocity fluctuations are strongly anisotropic. Time-averaged values of selected weight functions of the reconstruction operator are shown in Fig. 5.6 for turbulent channel flow, the complete set of profiles for mean values and fluctuations is given in Appendix C.
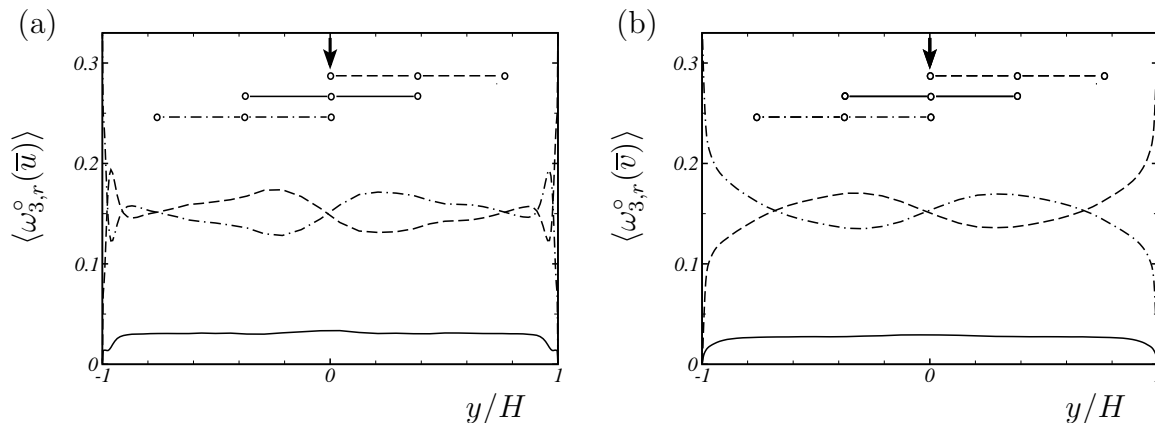
Figure 5.6: Time-averaged ALDM weight functions for central deconvolution of the streamwise and wall-normal velocity component. Implicit LES of turbulent channel flow at $\mathrm{Re}_\tau = 395$.

We note that ALDM responds to flow anisotropy by becoming anisotropic in the near-wall region. The resulting weights always prefer the stencil that is closer to the wall as shown, e.g., for the wall-normal velocity component in Fig. 5.6b. This weight distribution leads to an upwind bias for fluid moving away from the wall and to a downwind bias for fluid moving towards the wall. A central scheme is reproduced only at the channel centerline and at 1 or 2 other planes within the logarithmic layer.

The effect of the non-symmetric stencil selection on the implicit SGS model can be analyzed indirectly. For turbulent channel flow the total shear stress follows a linear
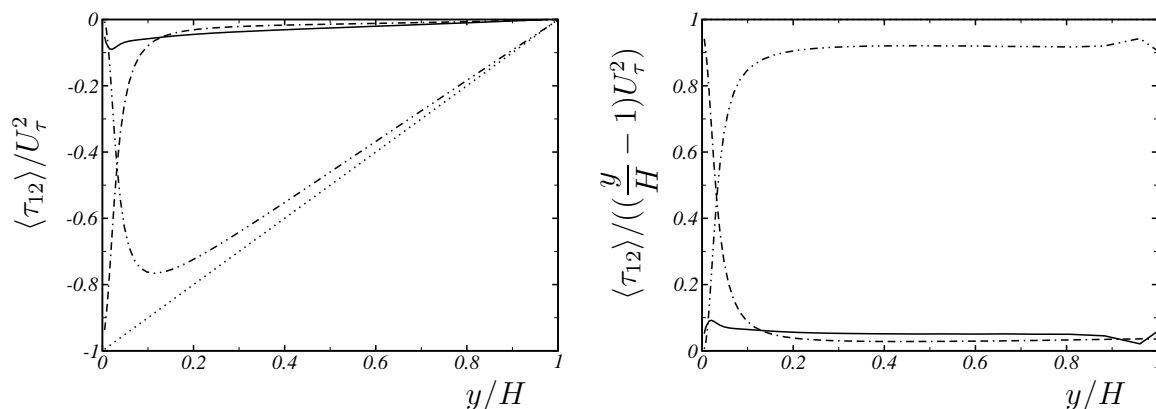
Figure 5.7: Shear stress balance for LES of turbulent channel flow at $Re_\tau = 395$. ——— SGS stress, ·——·—— viscous stress, —··—··— REYNOLDS shear stress, ·········· total shear stress.

law, where the individual contributions of mean REYNOLDS shear stress and viscous stress can be computed directly from the solution. The statistical average of the residual stress of the implicit SGS model follows from the global shear-stress balance, i.e.,

$$\langle \tau_{12}^{SGS} \rangle = (\frac{y}{H} - 1)U_\tau^2 - \langle u'v' \rangle + \nu \frac{\partial \langle u \rangle}{\partial y} \ . \tag{5.7}$$

Fig. 5.7 shows the SGS stress for implicit LES of turbulent channel flow. The overall behavior agrees well with results from DNS analyses. However, the position of maximum SGS stress is closer to the wall than expected. The location of the SGS stress maximum does not coincide with the location of the resolved-Reynolds-shear-stress maximum. Rather, it is shifted towards the region of large turbulent-kinetic-energy gradient. This shift can be attributed to the anisotropic stencil selection, causing increased SGS stresses near walls.

5.2.3 Wall Correction

Approaches to reduce discretization anisotropy at walls can be based on constraining or damping the dynamic range of the stencil weights. An alternative is to compensate for increased SGS dissipation by reducing the dissipative weight of the numerical flux function. The latter approach turned out to be more practical, in particular because the first one bears the risk of losing essential properties such as numerical stability.

The compensation coefficients $(\boldsymbol{h}_{i,j,k}/h_0)^{-s}$ in

$$\boldsymbol{\sigma}_{i,j,k} = \sigma \left(\frac{\boldsymbol{h}_{i,j,k}}{h_0} \right)^{-s} \tag{5.8}$$

have been introduced in Ref. [69] to compensate for grid-width effects in the numerical flux function of ALDM, see Sections 2.4 and 3.3.3. For simulations of isotropic turbulence, it was found that $s = 1/3$ ensures correct scaling of the numerical viscosity. Since model parameters were calibrated for this resolution, the reference grid width is $h_0 = L_0/32$, where L_0 is an integral flow scale. The integral length scale L_0 in turbulent channel flow is of the order of H. We use the estimate $L_0 = 2H/3$, which is based on energy spectra obtained from DNS data. Note that computational results are insensitive to a small variation of L_0 due to the exponent $s = 1/3$ in Eq. (5.8).

For the purpose of wall modeling Eq. (5.8) can be reformulated as

$$
\begin{aligned}
\boldsymbol{\sigma}_{i,j,k} &= \sigma \left(\frac{L_0}{L_{i,j,k}} \frac{\boldsymbol{h}_{i,j,k}}{h_0} \right)^{-s} \\
&= \sigma \left(32 \frac{\boldsymbol{h}_{i,j,k}}{L_{i,j,k}} \right)^{-s}
\end{aligned}
\tag{5.9}
$$

introducing the VAN DRIEST damping

$$
L_{i,j,k} = L_0 - L_0 \exp\left(- \left(\frac{l_W \, \widetilde{u}_\tau}{a \, \nu} \right)^d \right) \;,
\tag{5.10}
$$

where l_W is the wall distance and $\widetilde{u}_\tau$ is the friction velocity at the closest wall. d and a are free parameters. The original scheme is recovered at large wall distances where $L_{i,j,k} \to L_0$. The wall-asymptotic behavior of the effective change of the model parameter σ can be determined by Taylor series expansion of $f_{vD} = (L_0/L_{i,j,k})^{-s}$. The leading-order term gives

$$
f_{vD}|_{wall} \approx \frac{1}{a^{d s}} y^{+d s} \;.
\tag{5.11}
$$

The exponent d determines the shape of the damping functional. It is worth mentioning that PIOMELLI [132] proposed

$$
f_{vD}|_{wall} \sim y^3
$$

based on *a priori* tests [131] for the SMAGORINSKY model, corresponding to $d = 3/s$ with Eq. (5.10). By computational experimentation it was found that the improvement by the damping of Eq. (5.10) is rather insensitive to the particular choice of d and a. Given d, an optimal value for the length scale a can be selected such that the correct wall-shear stress is obtained. Based on several LES at varying REYNOLDS number and grid resolution, optimal values for ALDM were estimated as

$$
\begin{aligned}
d &= \frac{1}{s} = 3 \;, \\
a &= 50.0 \;.
\end{aligned}
\tag{5.12}
$$
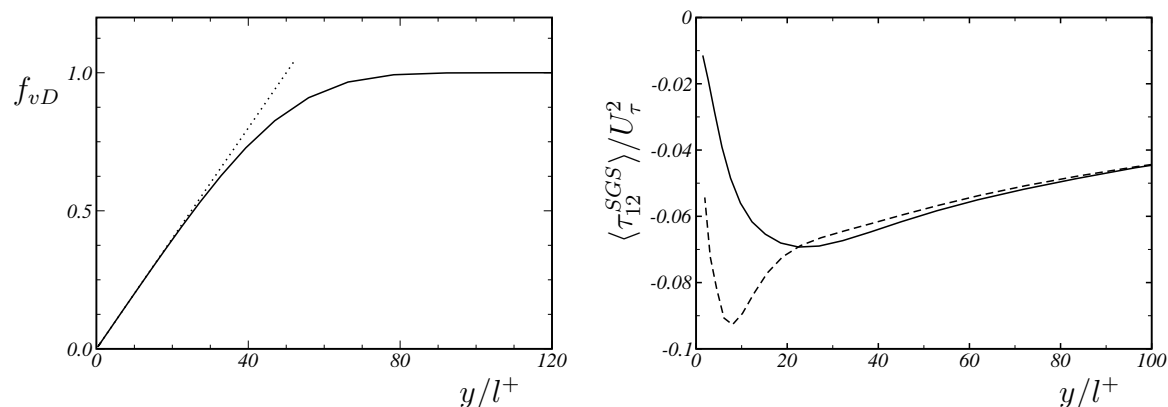
Figure 5.8: *Left:* Effective VAN DRIEST damping, ——— damping functional used with ALDM (parameters $s = 1/3$, $d = 3$, $a = 50$) and ········· linear approximation $f_{vD} = 0.02\ y/l^+$. *Right:* Modeled REYNOLDS shear stress in LES of turbulent channel flow for ——— ALDM with VAN DRIEST damping, ———— original homogeneous-turbulence ALDM formulation.

With these parameters, the proposed VAN DRIEST damping does not affect the implicit model at wall distances larger than $80l^+$. The effective damping function is plotted in Fig. 5.8. The modeled SGS shear stress is analyzed in Fig. 5.8 for ALDM with van Driest damping. The shear-stress maximum observed for the original ALDM formulation is reduced and moves away from the wall.
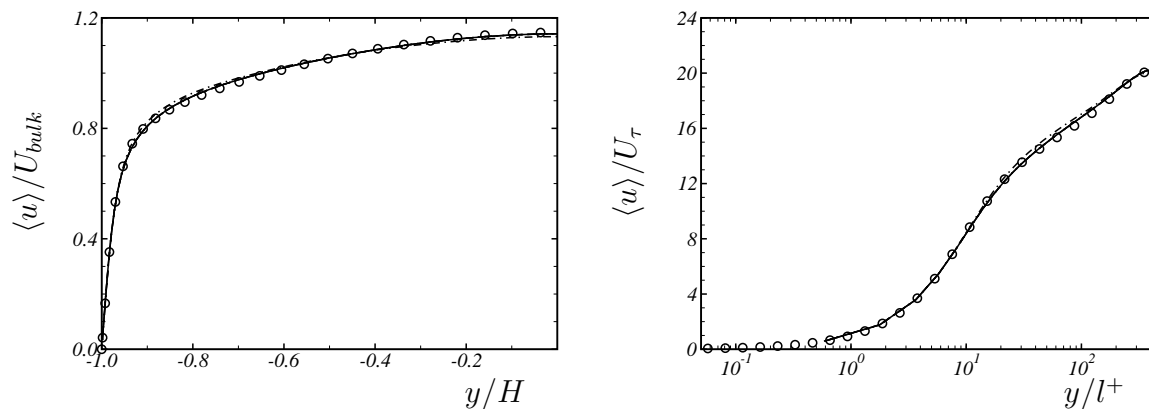
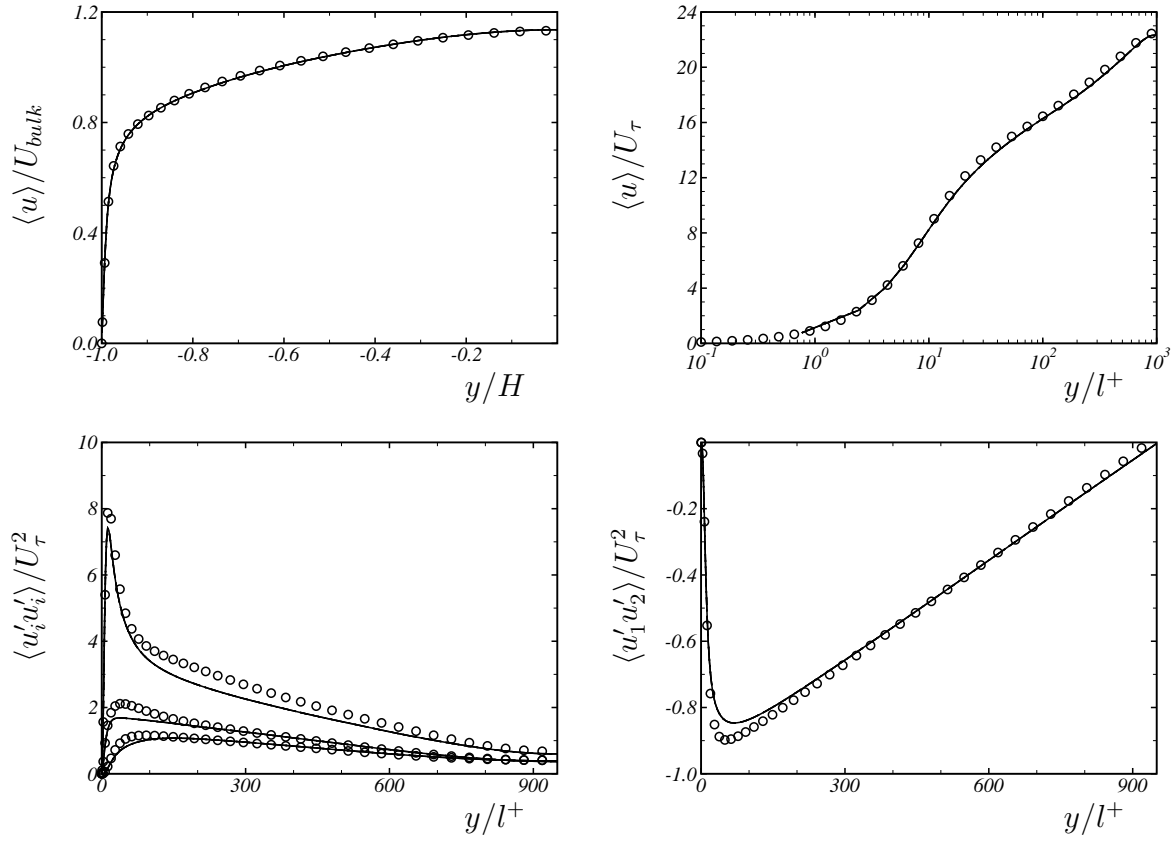**Figure 5.9:** Mean velocity profile for LES of turbulent channel flow at $Re_\tau = 395$. ——— ALDM with VAN DRIEST damping, ·—·—·— dynamic SMAGORINSKY model. ○ DNS of MOSER *et al.* [121].

Computational results of implicit LES with VAN DRIEST damping are shown in Fig. 5.9 and 5.10. The damping leads to the expected reduction of SGS dissipation near walls without deteriorating the REYNOLDS-stress anisotropy. The observed underestimation
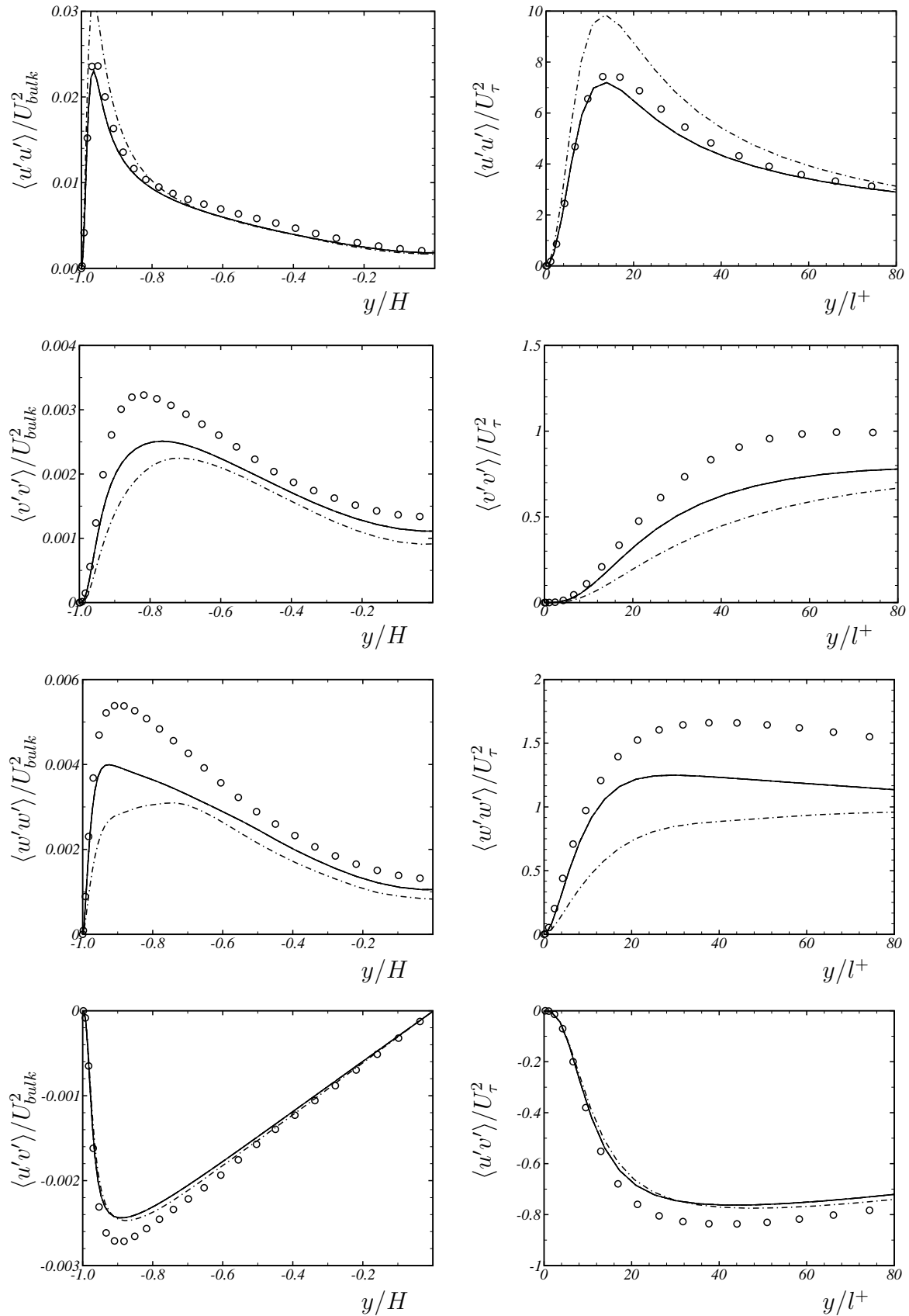
Figure 5.10: REYNOLDS stresses for LES of turbulent channel flow at $\mathrm{Re}_\tau = 395$. ——— ALDM with VAN DRIEST damping, $\cdot$—$\cdot$—$\cdot$— dynamic SMAGORINSKY model. $\circ$ DNS.

of the SMALL CAPS REYNOLDS-normal and REYNOLDS-shear stresses is consistent with the fact that the DNS reference data are not filtered. The prediction of REYNOLDS stresses by ALDM is better than by the dynamic SMAGORINSKY model. It is evident that VAN DRIEST damping improves the prediction of the wall-shear stress significantly. The effect on the logarithmic layer is clearly visible in the compensated mean velocity profiles of Fig. 5.11.
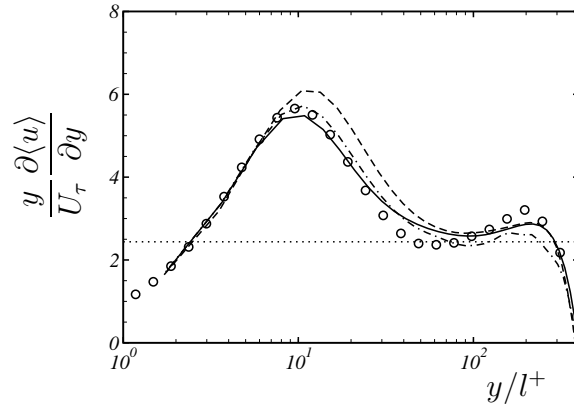
Figure 5.11: Compensated log-law for the mean velocity profile in turbulent channel flow at $\mathrm{Re}_\tau = 395$. ———— ALDM with VAN DRIEST damping, — — — — original ALDM formulation, ·—·—·— dynamic SMAGORINSKY model. ∘ DNS [121]. ·········· log law with $\kappa = 0.41$.

5.3 Validation

5.3.1 Effect of REYNOLDS Number

In addition to the case considered in the previous section we address turbulent channel flow at a higher REYNOLDS number $\mathrm{Re}_\tau = 950$ according to the DNS of DEL ÁLAMO *et al.* [32] and results for LES at a lower REYNOLDS number $\mathrm{Re}_\tau = 180$ according to the DNS of KIM *et al.* [87]. The grid parameters of the LES are summarized in Table 5.2.

Computational results for mean velocity profiles and REYNOLDS stresses from implicit LES and DNS of turbulent channel flow at $\mathrm{Re}_\tau = 180$ and $\mathrm{Re}_\tau = 950$ are shown in Figures 5.12 and 5.13, respectively. Good agreement with the reference data is observed. These results suggest that the optimal values for the model parameters are sufficiently independent of the REYNOLDS number. Turbulence statistics are accurately predicted for a wide range of REYNOLDS numbers.
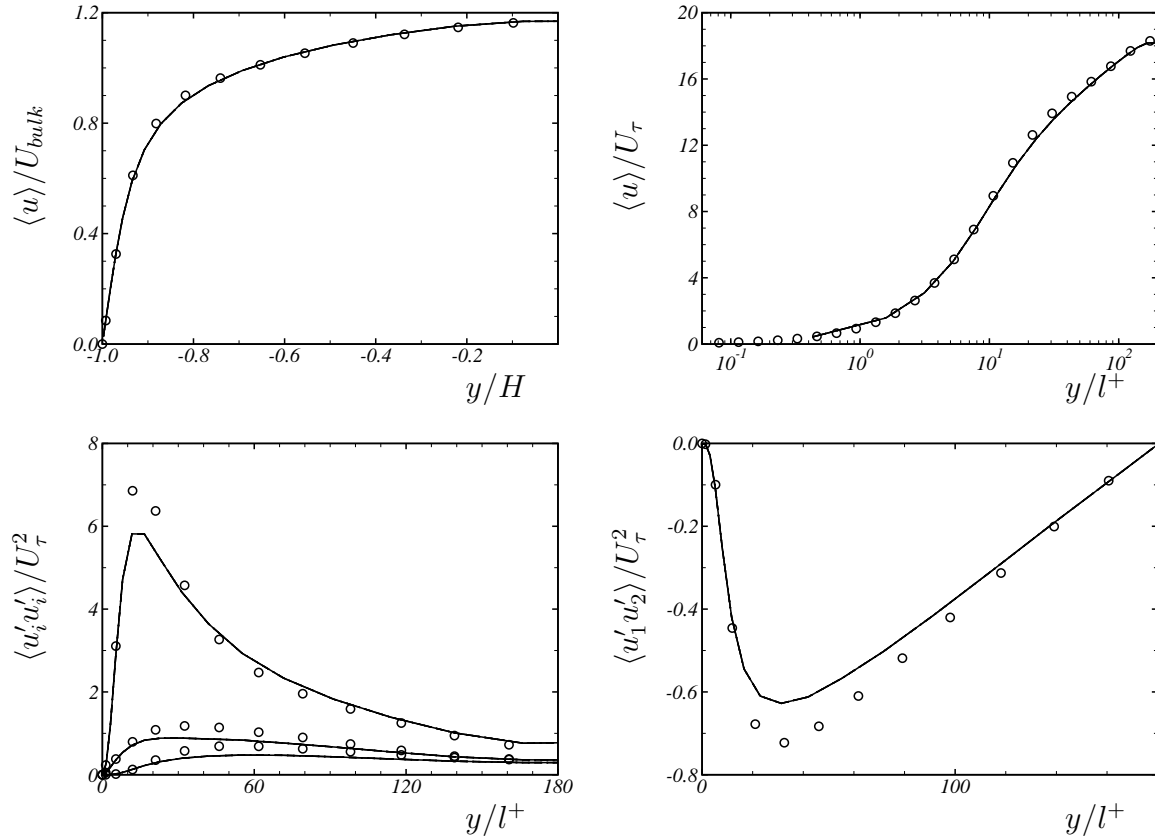
Figure 5.12: Mean velocity profile and resolved Reynolds stresses for LES of turbulent channel flow at $Re_\tau = 180$. ——— ALDM with van Driest damping, ○ DNS of Kim *et al.* [87].

$Re_\tau = 180$	streamwise direction	$L_x = 2\pi H$	$N_x = 32$	$h_x^+ = 35.3$
	wall-normal direction	$L_y = 2H$	$N_y = 32$	$h_y^+ = 0.9 - 27.3$
	spanwise direction	$L_z = \pi H$	$N_z = 32$	$h_z^+ = 17.7$
$Re_\tau = 950$	streamwise direction	$L_x = 2\pi H$	$N_x = 128$	$h_x^+ = 46.6$
	wall-normal direction	$L_y = 2H$	$N_y = 128$	$h_y^+ = 1.5 - 33.7$
	spanwise direction	$L_z = \pi H$	$N_z = 128$	$h_z^+ = 23.3$

Table 5.2: Grid for LES of turbulent channel flow at $Re_\tau = 180$ and at $Re_\tau = 950$, respectively

Figure 5.13: Mean velocity profile and resolved REYNOLDS stresses for LES of turbulent channel flow at $Re_\tau = 950$.———— ALDM with VAN DRIEST damping, ○ DNS of DEL ÁLAMO *et al.* [32].
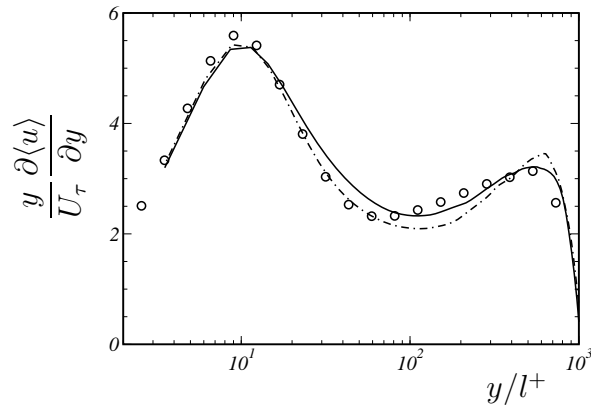
Figure 5.14: Compensated mean velocity profile for turbulent channel flow at $Re_\tau = 950$. ———— ALDM with VAN DRIEST damping, ·—·—·— dynamic SMAGORINSKY model, ○ DNS.

5.3.2 Grid-Resolution Study for Channel Flow

The choice of an appropriate computational grid is crucial for obtaining reliable predictions. This is the case for explicit and implicit LES. Whereas explicit LES may use grid-independent filtering, the grid resolution directly defines the range of resolved scales with implicit LES. In the following the effect of spatial resolution on the implicit SGS model of ALDM is studied qualitatively.

In smooth or well-resolved flow regions, discretization schemes of the ALDM family become equivalent to a second-order accurate centered scheme. A formal grid-convergence study of a numerical method would amount to increasing the grid resolution towards that required for DNS where the implicit LES reaches its formal order of accuracy. Note in particular that a consistent and stable implicit LES does always converge to DNS for increasing resolution. However, implicit-LES discretization schemes are not intended for use on DNS grids, where competitive results can be obtained by simpler methods.

ALDM is designed for finite grid size in under-resolved turbulence simulations, where the truncation error of the discretization scheme functions as SGS model. Analyses of turbulence models are often performed on the basis of pre-computed DNS data. However, these so called *a priori* analyses suppress the inherent dynamics of an LES and can lead to questionable conclusions concerning the behavior in actual LES. SGS models represent the statistical effect on the resolved scales of their non-linear interaction with unknown SGS. Hence, LES cannot deliver an exact instantaneous reproduction of the turbulent SGS stresses computed from DNS data. Accuracy of LES can be measured only in a statistical sense with respect to an accurate prediction of statistical properties of the resolved scales. It can be argued that results from LES should be compared with statistics computed from filtered DNS solutions. For implicit LES, however, grid resolution and filter width are linked so that for the purpose of a grid-resolution study, implicit-LES data for different spatial resolutions are compared with unfiltered DNS data.

We perform an LES of turbulent channel flow at $\mathrm{Re}_\tau = 590$ according to the reference DNS data provided by MOSER *et al.* [121] using four different grids with 12^3 to 72^3 cells. The grid parameters are given in Tab. 5.3. Using a spectral flow solver, the reference DNS was conducted on a grid with $384 \times 257 \times 384$ modes.

The two coarser LES grids do not allow for an accurate computation of the friction velocity from the viscous sublayer. For this reason, the mean velocity profile and resolved REYNOLDS stresses are plotted in outer scaling, i.e., they are normalized with bulk velocity (5.3) and channel half-width. The results in Fig. 5.15 show convergence towards

G12	streamwise direction	$L_x = 2\pi H$	$N_x = 12$	$h_x^+ = 308.9$
	wall-normal direction	$L_y = 2H$	$N_y = 12$	$h_y^+ = 19.2 - 227.2$
	spanwise direction	$L_z = \pi H$	$N_z = 12$	$h_z^+ = 154.5$
G24	streamwise direction	$L_x = 2\pi H$	$N_x = 24$	$h_x^+ = 154.5$
	wall-normal direction	$L_y = 2H$	$N_y = 24$	$h_y^+ = 6.1 - 122.8$
	spanwise direction	$L_z = \pi H$	$N_z = 24$	$h_z^+ = 77.2$
G48	streamwise direction	$L_x = 2\pi H$	$N_x = 48$	$h_x^+ = 77.2$
	wall-normal direction	$L_y = 2H$	$N_y = 48$	$h_y^+ = 2.3 - 60.7$
	spanwise direction	$L_z = \pi H$	$N_z = 48$	$h_z^+ = 38.6$
G72	streamwise direction	$L_x = 2\pi H$	$N_x = 72$	$h_x^+ = 51.5$
	wall-normal direction	$L_y = 2H$	$N_y = 72$	$h_y^+ = 1.4 - 41.5$
	spanwise direction	$L_z = \pi H$	$N_z = 72$	$h_z^+ = 25.7$

Table 5.3: Grids for LES of turbulent channel flow at $Re_\tau = 590$. The cell dimensions are computed from the nominal Re_τ.

the DNS with decreasing grid width. This tendency is most visible for the wall-normal REYNOLDS stress and the REYNOLDS shear stress, whereas the streamwise REYNOLDS stress is rather insensitive to the grid resolution. Generally, we observe a monotone convergence towards the DNS.

Whereas for most explicit SGS models insufficient resolution can lead to numerical instability, apparently the grid resolution for ALDM can be chosen only with respect to the desired accuracy. ILES at insufficient resolution degenerates to laminar flow. At least 8^3 cells are required to maintain turbulence for the present channel flow.
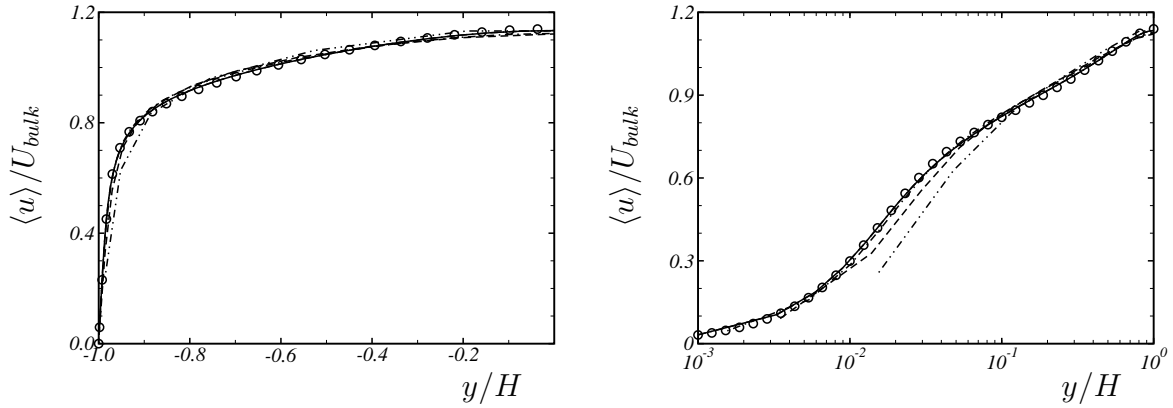
Figure 5.15: Grid resolution study for LES of turbulent channel flow at $Re_\tau = 590$. Mean velocity profile for implicit LES using ALDM with VAN DRIEST damping on grid ——— G72 , ·—·—·— G48 , ———— G24 , —··—··— G12. ○ DNS.
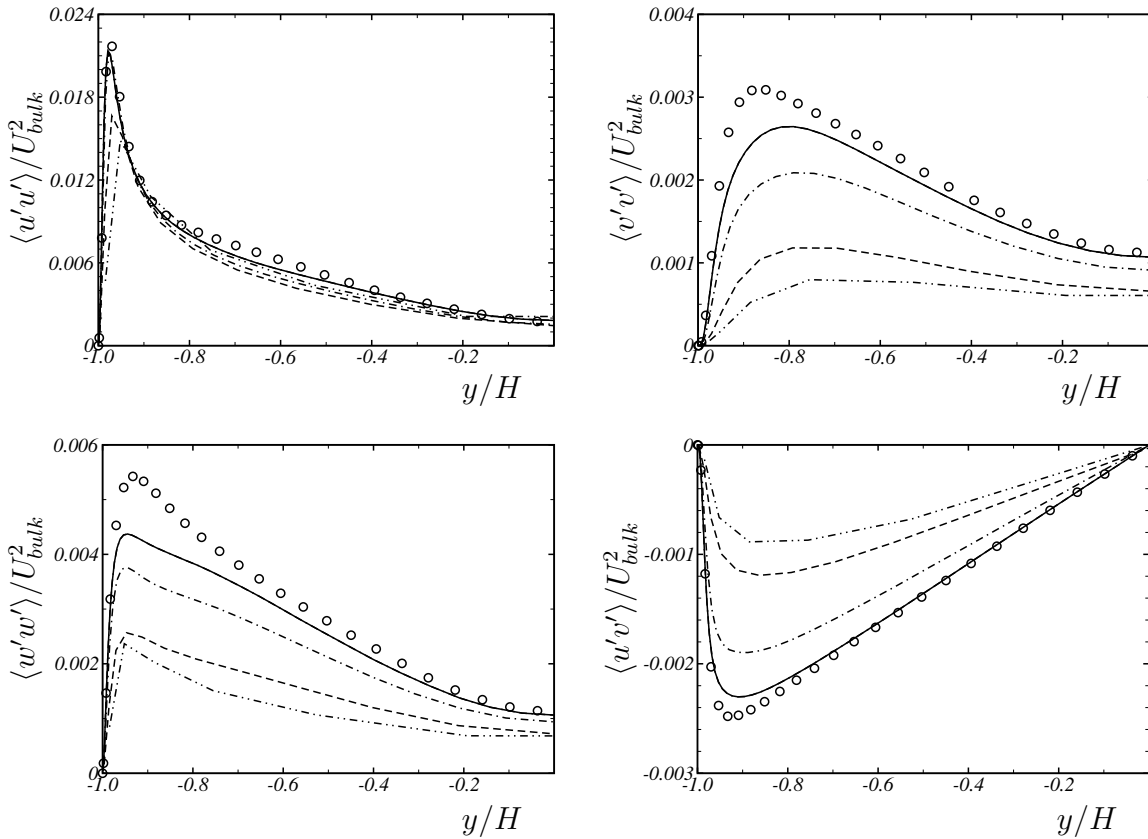
Figure 5.16: Grid resolution study for LES of turbulent channel flow at $Re_\tau = 590$. Profile of resolved REYNOLDS stresses for implicit LES using ALDM with VAN DRIEST damping on grid ——— G72 , ·—·—·— G48 , ———— G24 , —··—··— G12. ○ DNS.

5.3.3 Zero-Pressure-Gradient Turbulent Boundary-Layer Flow

A suitable test scenario for validation of the numerical method for boundary layer flows is a zero-pressure-gradient (ZPG) boundary layer, where many analytical and computational data are available for reference. The intuitive approach would be to simulate the spatial development of a boundary layer using an extensive computational domain. A popular alternative is temporal boundary layer simulation, where the spatial evolution is modeled by the temporal evolution in a narrow computational box moving with the flow. The temporal approach requires only a fraction of the computational time of a spatial simulation. The transferability of numerical results between temporal and spatial description is limited by effects of finite domain size and boundary conditions. These differences are important if processes leading to laminar turbulent transition are to be studied, but the impact on many integral quantities, such as mean velocity profile and skin friction coefficient, is small.

We perform a temporal simulation of ZPG boundary-layer flow in a double-periodic computational domain. The computational box has the extents $48\delta \times 124\delta \times 128\delta$ and is discretized with $48 \times 96 \times 256$ cells in streamwise $\times$ wall-normal $\times$ spanwise directions, respectively. A no-slip condition is imposed at the wall and the free-stream interface is modeled by the decay condition, see Sec. 7.2.4. Periodic boundary conditions are imposed in streamwise and spanwise direction. The flow is initialized at time $t = t_0$ as a laminar BLASIUS boundary-layer profile with thickness δ and free-stream velocity U_∞, superimposed with low-amplitude white-noise fluctuations. This initial disturbance is expected to grow during the simulation and eventually leads to transition of the flow to a turbulent state.

Laminar-turbulent transition is one of the most demanding test cases for LES. When white noise is used, most energy is injected into decaying modes and only a low percentage of the disturbance excites the instability modes of the laminar flow. For the onset of transition the SGS model must not affect the growth and amplification of these unstable modes. Most eddy-viscosity SGS models do not satisfy this requirement without ad hoc modifications.

The large spanwise extent of the computational domain was chosen in order to improve the accuracy of turbulence statistics that are computed from instantaneous snapshots by spatial averaging. Fig. 5.17a shows the friction coefficient

$$C_f = \frac{2U_\tau^2}{U_\infty^2} \tag{5.13}$$
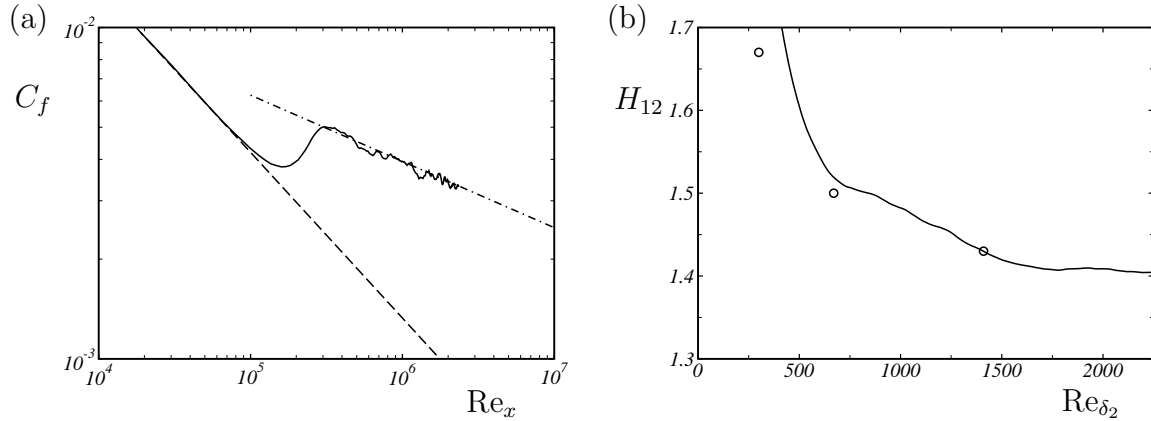
Figure 5.17: (a) Evolution of friction coefficient C_f in temporal LES of ZPG flow. —— present LES, −−−− laminar theory $C_f \sim (\mathrm{Re}_x)^{-1/2}$, ·—·—·— turbulent theory $C_f \sim (\mathrm{Re}_x)^{-1/5}$. (b) Evolution of the shape factor H_{12}. —— present LES, ∘ DNS [166].

for a temporal LES using ALDM. During the growth of the laminar boundary layer the friction coefficient follows the theoretical solution

$$C_f \sim (\mathrm{Re}_x)^{-1/2} \; , \tag{5.14}$$

where the REYNOLDS number is defined as

$$\mathrm{Re}_x = \frac{tU_\infty^2}{\nu} \; . \tag{5.15}$$

One can clearly see that the boundary layer undergoes laminar-turbulent transition. Eventually the friction coefficient follows the turbulent law

$$C_f \sim (\mathrm{Re}_x)^{-1/5} \; . \tag{5.16}$$

The evolution of the shape factor H_{12} (7.9) is shown in Fig. 5.17b. The prediction of our temporal LES with ALDM is in good agreement with DNS by SPALART [166] in the later turbulent stages. Results from LES and DNS do not match for the lowest REYNOLDS number $\mathrm{Re}_{\delta_1} = 500$ ($\mathrm{Re}_{\delta_2} \approx 300$). SPALART's DNS give turbulent velocity profiles that can hardly be obtained by natural transition at this small REYNOLDS number. Note that the critical REYNOLDS number for linear stability theory [146, 173] of a BLASIUS profile is $\mathrm{Re}_{\delta_1} = 520$. In order to remedy this disagreement, SPALART [166] proposed to distinguish between *developed* turbulence and *sustained* turbulence and argued that boundary-layer turbulence cannot be fully developed at REYNOLDS number lower than $\mathrm{Re}_{\delta_2} = 600$, but the turbulence, once imposed, can be sustained in the simulations at much lower REYNOLDS numbers.
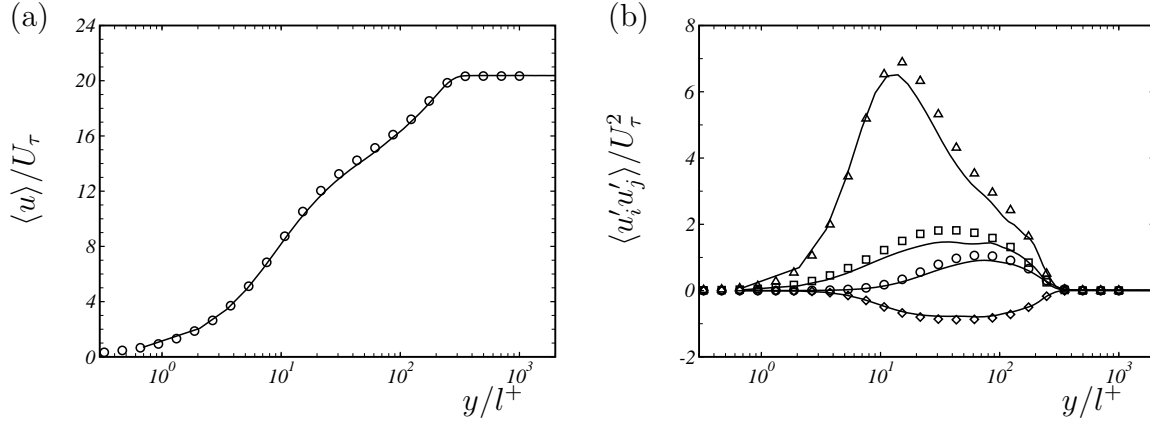
Figure 5.18: Profiles of mean velocity and Reynolds stresses for turbulent ZPG boundary layer flow at $\mathrm{Re}_{\delta_2} = 670$. —— present LES, symbols denote reference DNS [166].
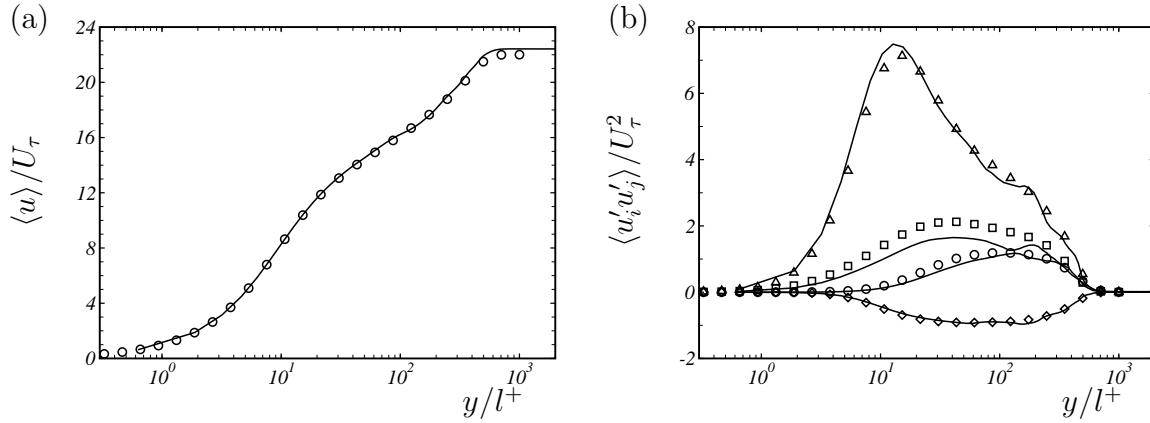
Figure 5.19: Profiles of mean velocity and Reynolds stresses for turbulent ZPG boundary layer flow at $\mathrm{Re}_{\delta_2} = 1410$. —— present LES, symbols denote reference DNS [166].

In the turbulent regime the performance of the implicit SGS model is evaluated by comparing profiles of mean velocity and Reynolds stresses with DNS data. Fig. 5.18 and Fig. 5.19 show results for the mean velocity profile and Reynolds stresses from LES and DNS at $\mathrm{Re}_{\delta_2} = 670$ and at $\mathrm{Re}_{\delta_2} = 1410$, respectively. ALDM apparently predicts the anisotropic turbulence statistics correctly. Characteristic boundary-layer parameters are given in Tab. 5.4.

		Re_{δ_2}	Re_{δ_1}	$C_f \cdot 10^3$	H_{12}	H_{32}
1st station	reference	670	1000	4.8	1.49	n/a
	present	662.8	1008.0	4.79	1.52	1.74
2nd station	reference	1410	2000	4.2	1.42	n/a
	present	1419.9	2028.3	4.07	1.43	1.76

Table 5.4: Characteristic parameters of the temporal boundary-layer simulations.

5.4 Summary

In this chapter, the implicit SGS model based on ALDM has been applied for LES of wall-bounded flows. Model parameters have been determined previously for isotropic turbulence at infinite REYNOLDS number. It is possible that the optimal values of these parameters might be weakly REYNOLDS-number dependent. However, contrary to common experience with most eddy-viscosity models, the current results do not support such a conclusion for the implicit model of ALDM. It is found that these parameters give good predictions also for the logarithmic region of boundary layers in terms of mean flow and turbulence statistics.

The response of the nonlinear deconvolution scheme to flow anisotropy is analyzed. With standard weight functionals based on total variation, the effective discretization becomes a strongly anisotropic near walls resulting in a modest underestimation of the wall-friction velocity. The prediction of the wall-shear stress can be improved if this effect is properly compensated by a VAN DRIEST-type damping functional. The particular choice of the damping functional plays a minor role.

For validation, several LES have been performed for incompressible channel flow and for transition to turbulence in a BLASIUS boundary layer. Results from implicit LES compare well with DNS data. Predictions for the anisotropic REYNOLDS stresses show improvement over results obtained at same resolution with the dynamic Smagorinsky model, which is one of the classical explicit SGS models. This improvement can be attributed to the tensor character of the effective viscosity of the implicit model. The computational results provide convincing evidence that ALDM can be employed for the prediction of wall-bounded flows without adjustment of parameters.

EXTENSION TO
PASSIVE-SCALAR MIXING

In this chapter, ALDM is extended to LES of passive-scalar mixing. We demonstrate that an optimized discretization scheme can be derived within the same framework as for the momentum equation. Specific problems of the turbulent transport of passive scalars are addressed with respect to their consequences on SGS modeling. A new implicit model is derived and analyzed for freely decaying three-dimensional homogeneous isotropic turbulence. The resulting new adaptive advection algorithm is then applied to scalar transport in turbulent channel flow, demonstrating that the implicit model correctly predicts mean flow and turbulence statistics for a flow configuration exhibiting anisotropic and inhomogeneous turbulence[1].

6.1 The Passive-Scalar Transport Equation

We consider the turbulent transport of *passive* scalars, which do not measurably affect the velocity field. This case represents a one-way coupling of the scalar to the fluid. Hence, the closure problem is restricted to the scalar transport equation. Turbulence modeling and discretization for the momentum equations remain unchanged.

The transport of a passive scalar c in an incompressible fluid is governed by

$$\partial_t c + \boldsymbol{\nabla} \cdot \boldsymbol{F}(\boldsymbol{u}, c) = 0 \ , \tag{6.1}$$

supplemented with appropriate initial and boundary conditions. The scalar flux function is

$$\boldsymbol{F}(\boldsymbol{u}, c) = \boldsymbol{u}c - \frac{1}{\text{ScRe}} \boldsymbol{\nabla} c \ , \tag{6.2}$$

where $\boldsymbol{u}$ and Re are velocity vector and REYNOLDS number of the transporting flowfield. Sc is the SCHMIDT number. $\text{Sc} = \nu/\kappa$ is defined as the ratio of kinematic viscosity ν and the diffusivity κ associated with the scalar quantity c. Depending on the application, c can be concentration, temperature, or any kind of passive marker.

---

[1] This chapter is based on Refs. [70, 71]
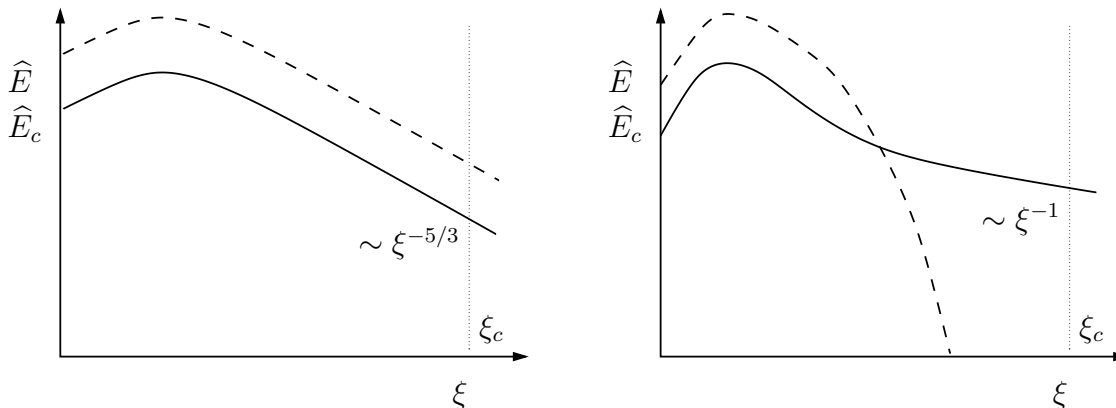
Figure 6.1: Critical test cases for predicting the proper subgrid diffusion in large-eddy simulations of scalar mixing. *Left:* Low SCHMIDT number regime. *Right:* High SCHMIDT number regime at moderate REYNOLDS number. ——— scalar variance ; ———— kinetic energy ; ·········· numerical cutoff wavenumber.

Following LEONARD [92], the discretized equation is obtained by convolution with a homogeneous filter kernel G

$$\partial_t \bar{c} + G * \boldsymbol{\nabla} \cdot \boldsymbol{F}(\boldsymbol{u}, c) = 0 \; , \tag{6.3}$$

and subsequent grid truncation

$$\partial_t \bar{c}_N + G * \boldsymbol{\nabla} \cdot \boldsymbol{F}_N(\boldsymbol{u}_N, c_N) = -G * \boldsymbol{\nabla} \cdot \boldsymbol{\tau}_{SGS} \; . \tag{6.4}$$

The overbar denotes the filtering $\bar{c} = G * c$ and the subscript N indicates grid functions obtained by projecting continuous functions onto a numerical grid with finite resolution.

The flux (6.2) is formally linear in c. However, the evolution of a non-uniform scalar field is subject to the velocity dynamics. Small-scale fluctuations of velocity and scalar are correlated in the presence of a scalar-concentration gradient. The subgrid tensor

$$\boldsymbol{\tau}_{SGS} = \boldsymbol{F}(\boldsymbol{u}, c) - \boldsymbol{F}_N(\boldsymbol{u}_N, c_N) \tag{6.5}$$

originates from the grid projection of advective terms. It represents the effect of the action of subgrid scales and has to be approximated by a SGS model to close Eq. (6.4). This modeling task is far from trivial. One reason is that the various regimes that exist for the passive-scalar variance spectrum have to be recovered by the SGS model. These regimes originate from the difference between typical length scales characterizing the viscous cutoff of the velocity field and the diffusive range of the scaler field [8]. In the following, two cases that are of particular interest in LES are discussed for homogeneous, isotropic turbulence.

The scalar fluctuations are driven by the stirring induced by the velocity field. Different scalar-transport regimes are associated with certain ranges of Reynolds and SCHMIDT numbers. The first regime is associated with small Schmidt numbers $Sc \leq 1$. With respect to LES, this regime is most relevant for large REYNOLDS numbers, where the kinetic-energy spectrum develops a broad inertial range

$$\widehat{E}(\xi) = C_K \varepsilon^{2/3} \xi^{-5/3} \tag{6.6}$$

at wavenumbers $\xi \ll \xi_K$,

$$\xi_K = \frac{\varepsilon^{1/4}}{\nu^{3/4}} \tag{6.7}$$

being the KOLMOGOROV wavenumber. In this regime, the scalar-variance behaves similar to the kinetic-energy. OBUKHOV and CORRSIN applied KOLMOGOROV's equilibrium theory to the scalar variance and derived a diffusive cutoff at

$$\xi_D = \frac{\varepsilon^{1/4}}{\kappa^{3/4}} \ . \tag{6.8}$$

The scalar-variance spectrum depends on the kinetic-energy transfer ε and the scalar diffusion χ. From dimensional arguments [28] follows that it exhibits an inertial-convective range

$$\widehat{E}_c(\xi) = C_{OC} \varepsilon^{-1/3} \chi \xi^{-5/3} \tag{6.9}$$

with scaling $\widehat{E}_c(\xi) \sim \xi^{-5/3}$ at wavenumbers $\xi \ll \xi_D$. C_K and C_{OC} are KOLMOGOROV constant and OBUKHOV–CORRSIN constant, respectively. An analysis of the shape of $\widehat{E}_c(\xi)$ in the diffusive-range $\xi_D \ll \xi$ is presented by BATCHELOR *et al.* [7].

In LES, the filter width is typically chosen in such a way that the numerical cutoff wavenumber ξ_C is within the inertial range (6.6). For a coarse representation of the scalar dynamics, we also assume that $\xi_C \ll \xi_D$ such that the SGS energy transfer does not directly depend on Re and Sc. A representative example for this regime is LES of isotropic turbulence at $Sc \approx 1$ and $Re \gg 1$.

A more complex situation is encountered if the SCHMIDT number is much larger than unity, $Sc \gg 1$. In this regime two distinct inertial ranges exist for the scalar-variance spectrum. An inertial-convective range (6.9) is observed for scales within the KOLMOGOROV inertial range $\xi \ll \xi_K$ of the kinetic-energy spectrum. At smaller scales, the energy spectrum already decays exponentially whereas the scalar fluctuations are not yet affected by diffusion. A second inertial range, the viscous-convective range, is observed for the scalar-variance spectrum at $\xi_K \ll \xi \ll \xi_B$, ξ_B being the BATCHELOR wavenumber

$$\xi_B = \frac{\varepsilon^{1/4}}{\nu^{1/4} \kappa^{1/2}} \ . \tag{6.10}$$

Based on an analytical model for the distortion of small scalar blobs, BATCHELOR [8] derived

$$\widehat{E}_c(\xi) = C_B \nu^{1/2} \varepsilon^{-1/2} \chi \xi^{-1} \tag{6.11}$$

for the viscous-convective range $\xi \ll \xi_B$ and an exponential decay

$$\widehat{E}_c(\xi) = C_B \nu^{1/2} \varepsilon^{-1/2} \chi \xi^{-1} \exp(-C_B(\xi/\xi_B)^2) \tag{6.12}$$

in the viscous-diffusive range $\xi \gg \xi_B$. Employing a more sophisticated statistical method, the LAGRANGEan-history direct-interaction (LHDI) approximation, KRAICH-NAN [88] found further evidence for the ξ^{-1} scaling in the viscous-convective range, but a less rapid decay in the viscous-diffusive range

$$\widehat{E}_c(\xi) = C_B \nu^{1/2} \varepsilon^{-1/2} \chi \xi^{-1} \left(1 + (6C_B)^{1/2}\xi/\xi_B\right) \exp(-(6C_B)^{1/2}\xi/\xi_B) \ . \tag{6.13}$$

Recent numerical studies (see BOGUCKI *et al.* [12] and YEUNG *et al.* [185], e.g.) tend to favor the results of KRAICHNAN. The numerical parameter C_B is the Batchelor constant. Various experimental, analytical, and numerical determinations of the numerical constants C_B, C_K, and C_{OC} have been proposed. Unfortunately, the reported values scatter a lot. This inherent uncertainty has consequences on the calibration of SGS models, as will be discussed in Section 6.3.

If the grid cutoff ξ_C lies within the inertial-convective range the same SGS modeling can be used as for the Sc ≤ 1 case. A different approach is required if the numerical cutoff is chosen within the viscous-convective range. This velocity-resolving case is typically associated with low REYNOLDS numbers in LES. Generic sketches of corresponding kinetic energy spectra, scalar variance spectra, and numerical cutoff for the two regimes Sc ≤ 1 and Sc $\gg 1$ are shown in Fig. 6.1.

Another difficulty in solving scalar transport equations is associated with a numerical problem. At high SCHMIDT numbers, even an incompressible and smooth flowfield will generate a filtered scalar field with steep concentration gradients that can only be captured and not resolved by the numerical discretization. Standard centered differencing schemes tend to non-physical oscillations unless they are supplemented with a numerical regularization.

6.2 Discretization-Scheme Design

For brevity of notation and without loss of generality, the following summary is given only for one coordinate direction. A staggered arrangement of velocity, pressure, and
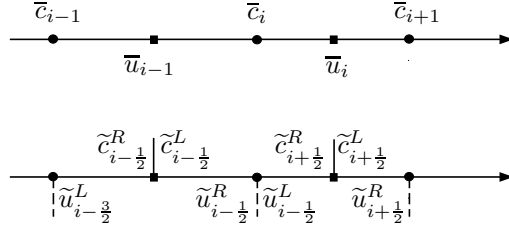
Figure 6.2: Staggered grid arrangement. *Top:* Filtered solution. *Bottom:* Reconstructions of unfiltered solution in a finite volume discretization.

scalar (see Fig. 6.2) is used to allow for an accurate and stable solution of the pressure-POISSON equation in 3-D incompressible flows.

As mentioned above, the framework for our implicit LES is provided by the finite-volume method of SCHUMANN [148] that implies reconstruction of the unfiltered solution at cell faces and the approximation of the physical flux function by a numerical flux function. The unfiltered velocity solution at cell faces is reconstructed, i.e., deconvolved and interpolated, by ALDM as proposed in Chapter 2. This operator can also be employed for reconstruction of the unfiltered scalar concentration without modifications. The approximately deconvolved solution $(\widetilde{u}_N, \widetilde{c}_N)$ is inserted into a consistent numerical flux function $\widetilde{F}_N$. The numerical flux applies to advection only; diffusion is discretized by standard finite differences. Based on dimensional arguments and numerical experimentation led to the following modification of the LAX-FRIEDRICHS flux

$$
\left.\widetilde{F}_N\right|_{i\pm1/2} = F\left(\frac{\widetilde{u}^R_{i\pm1/2} + \widetilde{u}^L_{i-1\pm1/2}}{2}, \frac{\widetilde{c}^R_{i\pm1/2} + \widetilde{c}^L_{i\pm1/2}}{2}\right)
$$
$$
- \sigma_{i\pm1/2}\left(\widetilde{c}^L_{i\pm1/2} - \widetilde{c}^R_{i\pm1/2}\right) \;, \tag{6.14}
$$

where $\sigma_{j\pm1/2}$ can be any shift-invariant functional. Note that velocity and scalar are defined at different positions, as shown in Fig. 6.2. The indices are given in specific coordinate systems relative to the original position on a staggered grid. From a dimensional argument follows that $\sigma_{j\pm1/2}$ is a velocity. In order to obtain a GALILEIan invariant discretization, we define

$$
\sigma_{i\pm1/2} = \sigma_c \left|\widetilde{u}^R_{i\pm1/2} - \widetilde{u}^L_{i-1\pm1/2}\right| \;, \tag{6.15}
$$

where σ_c is another free parameter of the discretization.

The extension to three dimensions is straight forward and follows the approach for the momentum equation. All LES presented throughout this chapter are based on

an implementation of the simplified adaptive local deconvolution (SALD) method, see Appendix B.

6.3 Implicit SGS Modeling

We employ the approach detailed in Chapter 3 and analyze the spectral numerical diffusivity of discretization methods for the passive-scalar transport equation. The *a posteriori* analysis revealed that the solution-adaptive deconvolution operator with parameters $\gamma_{k,r}$ is responsible for a sharply rising cusp of the spectral numerical diffusivity at high wavenumbers. The spectral numerical diffusivity due to the flux function (6.14) is almost constant at a level which can be adjusted by the free parameter σ_c. A similar observation was made for ALDM, where it was found that adaptive stencil selection provides an approximation for the cusp of the spectral eddy viscosity and the numerical flux function is responsible for the plateau value, see Figure 5.3a. We opted for adjusting σ_c only, while using the same values for $\gamma_{k,r}$ as for the momentum equation, since no reliable closed-form expression for the subgrid diffusivity spectrum $\kappa_{SGS}(\xi)$ is available.

An EDQNM analysis leads to the conclusion that $\kappa_{SGS}(\xi)$ is proportional to the spectral eddy viscosity $\nu_{SGS}(\xi)$. However, this finding is questionable because several contradictory results from measurements and direct simulations are pointed out in the literature (see LESIEUR [93], e.g.). On the other hand, the integral amount of necessary subgrid diffusion can be estimated by a simple analysis. In our test configurations, isotropic turbulence at high PÉCLET numbers $\mathrm{Pe} = \mathrm{Sc} \cdot \mathrm{Re}$, diffusion is exclusively provided by the SGS model, i.e.,

$$\chi_{SGS} \approx \chi \ . \tag{6.16}$$

We define the equivalent subgrid diffusivity

$$\overline{\kappa}_{SGS} = \frac{\int \kappa_{SGS}(\xi)\xi^2 \widehat{E}_c(\xi)d\xi}{\int \xi^2 \widehat{E}_c(\xi)d\xi} \ . \tag{6.17}$$

From Eqs. (6.6), (6.9), and (6.16) follows

$$
\begin{aligned}
\overline{\kappa}_{SGS} &= \frac{2}{3}C_{OC}^{-1}\varepsilon^{1/3}\xi_c^{4/3} \\
&= \frac{2}{3}C_{OC}^{-1}C_K^{-1/2}\widehat{E}(\xi_c)^{1/2}\xi_c^{-1/2} \tag{6.18} \\
&= \frac{C_K}{C_{OC}}\overline{\nu}_{SGS} \tag{6.19}
\end{aligned}
$$

for the low SCHMIDT number test case. Assuming identical spectral distributions, the equivalent subgrid diffusivity is obtained from the subgrid viscosity by multiplication with the ratio of KOLMOGOROV constant and OBUKHOV–CORRSIN constant. Available data for both constants scatter a lot. The OBUKHOV–CORRSIN constant is commonly in the range $0.68 \leq C_{OC} \leq 0.83$ (MCCOMB [115]). The range of reported values for the KOLMOGOROV constant is even larger, mostly within $1.4 \leq C_{OC} \leq 1.8$ (YEUNG and ZHOU [186]).

Our initial estimate for the proportionality constant in Eq. (6.19) was $C_K/C_{OC} = 2.0$. However, with parameters optimized accordingly, the scalar-variance spectrum was found to vary strongly in time even if the case considered was statistically stationary. At time instants it can be as flat as ξ^{-1} for LES of low SCHMIDT number isotropic turbulence. The slope of the mean spectrum is close to $\xi^{-5/3}$ but clearly not steep enough. Numerical experimentation led us to

$$C_K/C_{OC} \approx 2.3 \tag{6.20}$$

which gives much better results.

The theoretical scalar-variance spectrum in high SCHMIDT number isotropic turbulence is given by Eq. (6.11). The presence of the viscosity in this equation does not imply that the scalar SGS model has to incorporate the REYNOLDS number, but rather that $\boldsymbol{\tau}_{SGS}$ depends on the shape of the viscous range of the kinetic-energy spectrum. The characteristic time scale $(\nu/\varepsilon)^{1/2}$ can be computed analytically in velocity-resolving simulations. This leads to an exact constraint for the equivalent eddy-diffusivity

$$\overline{\kappa}_{SGS} = C_B^{-1} \left(\frac{\nu}{\varepsilon}\right)^{-1/2} \xi_c^{-2} \, , \tag{6.21}$$

which has to be met by the implicit SGS model.

Considerable uncertainty remains regarding the value of the BATCHELOR constant. BATCHELOR [8] originally proposed $C_B = 2.0$. Using analytical theories, KRAICHNAN [88] derived $C_B = 2.04$ for a GAUSSIAN velocity field but, by taking into account experimental data, stated C_B likely to be considerably larger for actual NAVIER-STOKES turbulence. Later QIAN [141] found $C_B = 4.47$. When fitting experimental or direct numerical simulation (DNS) data, the chosen functional law for the viscous-diffusive range can be a reason for large differences in C_B: BOGUCKI et al. [12] found $C_B = 3.9$ for DNS data at $3 \leq \mathrm{Sc} \leq 7$ fitted to the BATCHELOR spectrum, whereas a fit of the same data to the KRAICHNAN spectrum gives $C_B = 5.26$. YEUNG et al. [185] came to the conclusion that the value of C_B is not universal. Rather, C_B required for an optimal fit of the KRAICHNAN spectrum with their DNS data increases with SCHMIDT number,

	$\gamma_{2,0}^{+1/2}$	$\gamma_{2,1}^{+1/2}$	$\gamma_{3,0}^{+1/2}$	$\gamma_{3,1}^{+1/2}$	$\gamma_{3,2}^{+1/2}$	σ_c
if Sc $\leq$ 1	1.00000	0.00000	0.01902	0.08550	0.89548	0.61500
if Sc $\gg$ 1	1.00000	0.00000	0.01902	0.08550	0.89548	0.30000

Table 6.1: Optimized discretization parameters for LES of passive-scalar mixing.

being $C_B = 3.5$ for Sc = 1 and $C_B = 5.5$ for Sc = 64. Since the spectra at Sc $\simeq$ 1 do not exhibit a visible viscous-convective range, only the latter value can be considered as a relevant measure for C_B, which we note is in reasonable agreement with $C_B = 5.26 \pm 0.25$ found by BOGUCKI *et al.* [12] for relatively low SCHMIDT numbers $3 \leq$ Sc ≤ 7. We opted for

$$C_B = 5.0 \tag{6.22}$$

for calibration of the implicit SGS dissipation in the regime of high SCHMIDT numbers.

Table 6.1 summarizes the values for the free discretization coefficients that were selected. These parameters are optimized based on an analysis of the numerical diffusivity of the model in LES of passive-scalar mixing in freely decaying isotropic turbulence at high PÉCLET number. This analysis also revealed that different parameters are required for the two SCHMIDT-number regimes. Hence, two sets of parameters were determined representing two SGS models: one for the low-SCHMIDT-number regime and one for the high-SCHMIDT-number regime.

6.4 Validation for Forced Isotropic Turbulence

As first test case the new model is applied to passive-scalar mixing in forced isotropic turbulence. An extra source term was added to the right-hand side of the NAVIER-STOKES equations and the scalar-transport equation. This forcing results in a production of scalar variance and kinetic energy that compensates diffusion and dissipation while preserving the shape of the spectra. By construction, only large scales $|\boldsymbol{\xi}| \leq 2$ are directly affected by the forcing.

We have performed two simulations, one for each scalar-mixing regime. For the low-SCHMIDT-number regime, the computational REYNOLDS number Re = $1/\nu$ is Re = 10^4 and the SCHMIDT number is Sc = 1. The high SCHMIDT number model is tested for REYNOLDS number Re = 20 and SCHMIDT number Sc = 400. The grid is composed out of 32^3 evenly-spaced cells. For the lower REYNOLDS number, the KOLMOGOROV length scale is on the order of the mesh size.
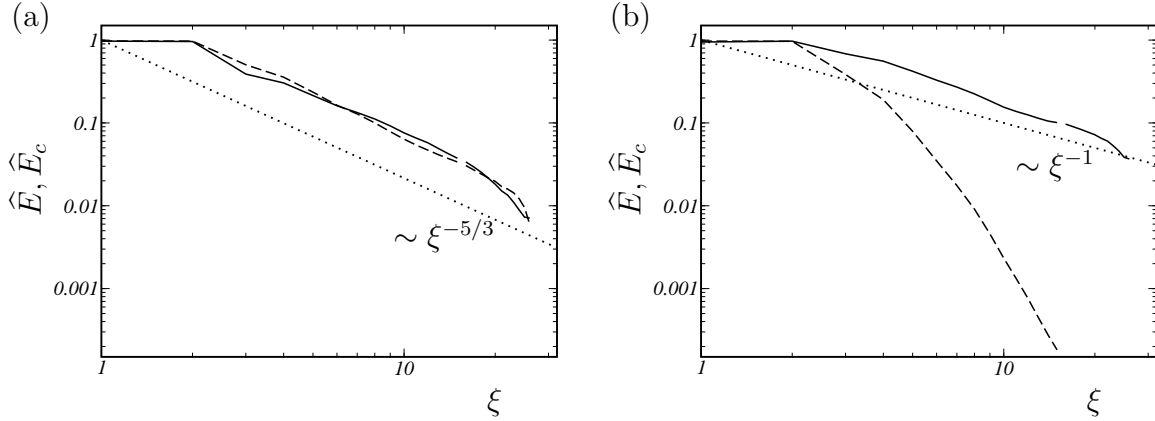
Figure 6.3: Mean 3-D spectra of kinetic energy and scalar variance for implicit LES of large-scale forced isotropic turbulence. (a) $Re = 10^4$ and $Sc = 1$. (b) $Re = 20$ and $Sc = 400$. ——— scalar variance; – – – – kinetic energy; ·········· analytical expressions for scalar variance.

After an initial transient, samples of the 3-D scalar-variance and kinetic-energy spectra were collected until the mean spectra were converged. The resulting 3-D mean spectra are shown in Fig. 6.3. A small gap in the lines marks the wavenumber $\xi_C = 15$. Wavenumbers $\xi_C < |\boldsymbol{\xi}| < \sqrt{3}\xi_C$ are only partially represented in CARTESian-grid physical-space simulations. Results of both simulations agree reasonably well with the theoretical expectation, which verifies *a posteriori* the parameter selection which was based on the corresponding theoretical prediction.

6.5 Application to Turbulent Channel Flow

6.5.1 Test case and computational setup

Reliable reference data are very rare for flows at higher SCHMIDT numbers. Most SGS models for scalar transport have been validated only for $Sc < 1$ since DNS of developed turbulent flows at SCHMIDT numbers $Sc \gg 1$ have only recently become feasible. Today, such DNS are still limited to very moderate REYNOLDS numbers. SCHWERTFIRM and MANHART [150] performed DNS of the transport of passive scalars in turbulent channel flow at REYNOLDS number $Re_\tau = 180$ and at SCHMIDT numbers $Sc = 1, 3, 10$, and 25. In order to validate the new model for wall-bounded flows, implicit LES have been conducted, where computational setup, REYNOLDS number, and SCHMIDT numbers are adapted to the DNS reference.

The computational domain is a plane channel that has the extents $2\pi H \times 2H \times \pi H$ in streamwise, wall-normal, and spanwise direction, respectively. Periodic boundary
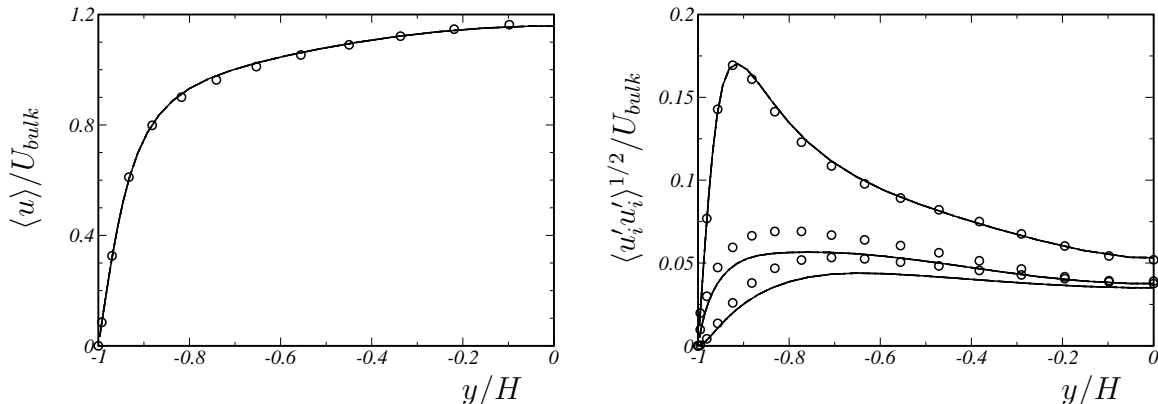
Figure 6.4: Mean velocity profile and Reynolds stresses in turbulent channel flow at $\mathrm{Re}_\tau = 180$. ——— implicit LES with SALD, ○ DNS data of Moser *et al.* [121].

conditions are imposed in streamwise and spanwise direction. No wall model is used in the simulations, rather the no-slip condition is imposed directly on the velocity field. The scalar is added to the fluid at one wall and removed at the opposite wall, i.e., the wall concentration

$$C_W = \pm 1 \tag{6.23}$$

of the scalar is kept constant.

The computational domain is discretized by $48 \times 48 \times 48$ cells. The grid is stretched in wall-normal direction using the hyperbolic tangent function (5.2) to increase resolution in the vicinity of the walls.

6.5.2 Velocity Field

Figure 6.4 shows mean velocity profile and Reynolds stresses from implicit LES. We observe a good agreement with the reference DNS data. The profiles of higher-order moments show small discrepancies, which are inevitable when an unfiltered DNS is compared with LES on coarser grids (see also section 6.5.4). Note that similar results for the velocity field alone can be obtained with fewer grid points than used here. However, the relative resolution requirement for the scalar field increases with the square root of the Schmidt number. This scaling holds for the Batchelor scale

$$\eta_B = \frac{\nu^{1/4}\kappa^{2/4}}{\varepsilon^{1/4}} = \frac{\eta_K}{\sqrt{\mathrm{Sc}}} \ , \tag{6.24}$$

the equivalent of the Kolmogorov scale $\eta_K = (\nu^3/\varepsilon)^{1/4}$, and for the thickness of the diffusive sublayer. To be able to use the same computational grid for Schmidt numbers
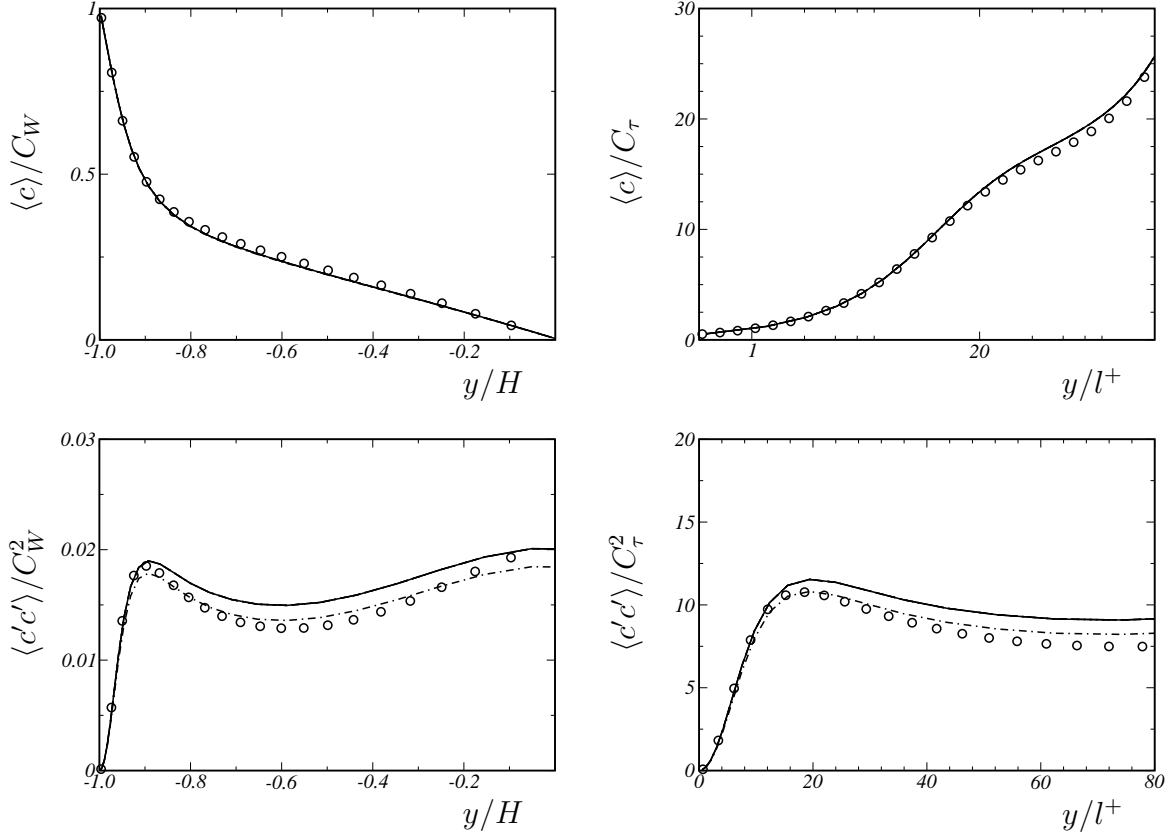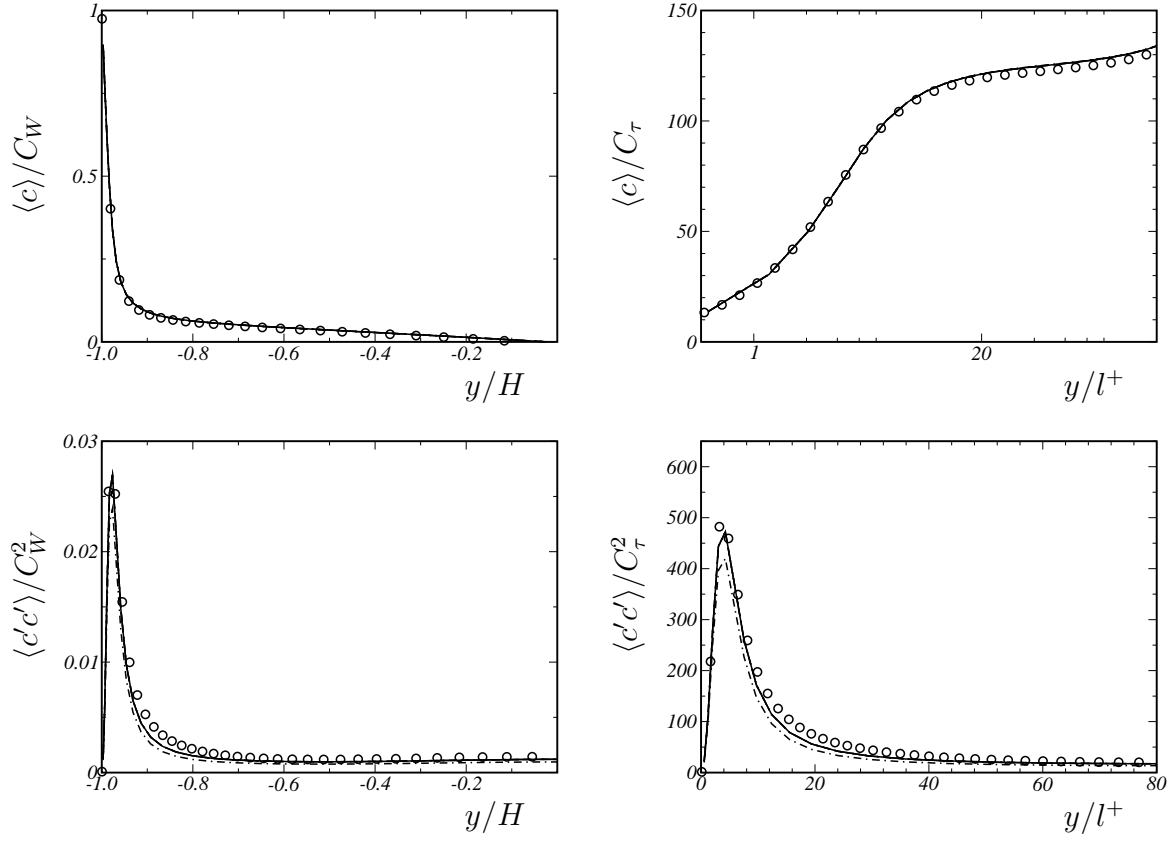
Figure 6.5: Profiles of mean scalar concentration and scalar variance in plane channel flow at $\mathrm{Re}_\tau = 180$ and $\mathrm{Sc} = 1$. Implicit LES with parameters optimized for ———— high SCHMIDT numbers, ·—·—·— low SCHMIDT numbers, ○ DNS of SCHWERTFIRM and MANHART [150].

between $1 \leq \mathrm{Sc} \leq 25$, we chose a grid with 48^3 cells.

6.5.3 Scalar Statistics

In the following, the computational results are normalized with bulk velocity U_{bulk}, channel half width H, and wall concentration C_W, or with friction velocity $U_\tau = \sqrt{\nu \langle \partial_y u \rangle_{wall}}$, viscous length scale $l^+ = \nu/U_\tau$, and friction concentration

$$C_\tau = \kappa \langle \partial_y c \rangle_{wall}/U_\tau \ . \tag{6.25}$$

We have performed implicit LES at SCHMIDT numbers $\mathrm{Sc} = 1, 3, 10$, and 25 with model parameters optimized for high and for low SCHMIDT numbers. Figures 6.5 and 6.7 show profiles of mean scalar concentration $\langle c \rangle$ at $\mathrm{Sc} = 1$ and $\mathrm{Sc} = 25$. The mean concentration scales as $\langle c \rangle = \mathrm{Sc}\,y^+$ at the wall and obeys a logarithmic law as y^+ increases. Since the scalar is transferred from one wall to the other, the wake region shows $\partial_y \langle c \rangle \neq 0$ at
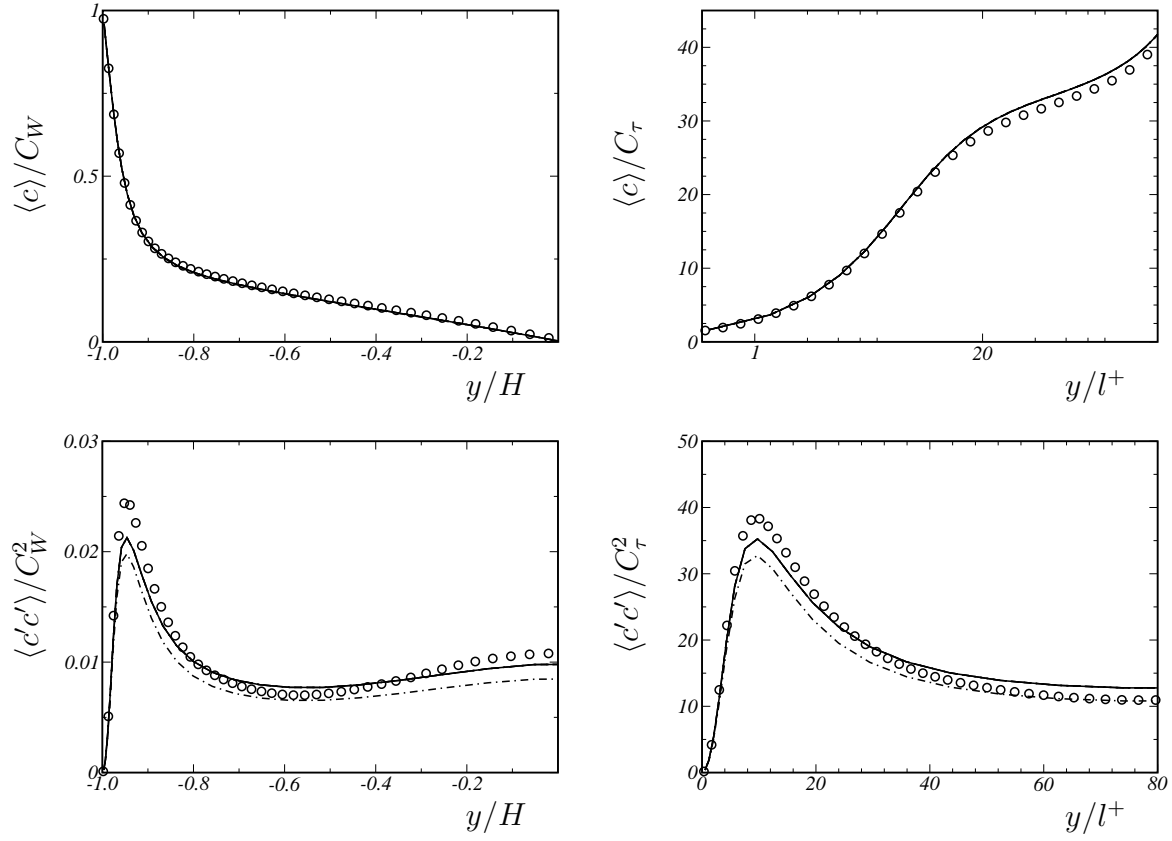
Figure 6.6: Profiles of mean scalar concentration and scalar variance in plane channel flow at $\mathrm{Re}_\tau =$ 180 and Sc = 3. Implicit LES with parameters optimized for ——— high SCHMIDT numbers, ·—·—·— low SCHMIDT numbers, ∘ DNS of SCHWERTFIRM and MANHART [150].

the centerline of the channel. The LES results agree well with the reference DNS. Differences between the predictions of the two proposed models are marginal for the mean concentration profiles. This changes when the scalar variance $\langle c'c' \rangle$ is considered. Comparing both models, the parameter set optimized for high SCHMIDT numbers gives always slightly higher fluctuations. The low-SCHMIDT-number model gives better results at Sc = 1, see Fig. 6.5, whereas it underestimates the scalar variance at Sc = 25, see Fig. 6.7. The model optimized for high SCHMIDT numbers gives excellent results for Sc = 25. Implicit LES at Sc = 3 (see Fig. 6.6 and 6.9) and Sc = 10 (see Fig. 6.12 and 6.13) show the same tendency as the Sc = 25 case. Profiles of the turbulent scalar transport $\langle c'u' \rangle$ and $\langle c'v' \rangle$ are displayed in Fig. 6.8 and Fig. 6.10 for Sc = 1 and Sc = 25, respectively. The two proposed variants of model parameters perform equally well. An excellent agreement with the DNS is observed for the streamwise component normalized with U_{bulk} and C_W. The same quantity shows a small bias towards lower values when normalized with U_τ and C_τ. The wall-normal component $\langle c'v' \rangle$ shows the

Figure 6.7: Profiles of mean scalar concentration and scalar variance in plane channel flow at $\mathrm{Re}_\tau = 180$ and $\mathrm{Sc} = 25$. Implicit LES with parameters optimized for ——— high SCHMIDT numbers, ·—·—·— low SCHMIDT numbers, ○ DNS of SCHWERTFIRM and MANHART [150].

opposite behavior; the values are slightly lower when normalized with U_{bulk} and C_W, but match the DNS perfectly with normalization by U_τ and C_τ.

We note that the implicit modeling approach gives good results for scalar mixing in turbulent channel flow although the model parameters were derived for isotropic turbulence. For the SCHMIDT-number range considered, the role of an optimal parameter choice is less important for turbulent channel flow than for isotropic turbulence. Results from both versions of the implicit model are in good agreement with DNS. Although differences are small, nevertheless for the low-SCHMIDT-number scheme slightly better predictions can be observed at $\mathrm{Sc} = 1$, whereas the high-SCHMIDT-number scheme performs slightly better at $\mathrm{Sc} > 1$.

A rigorous test for validating simulations of the heat or mass transfer from a wall to a
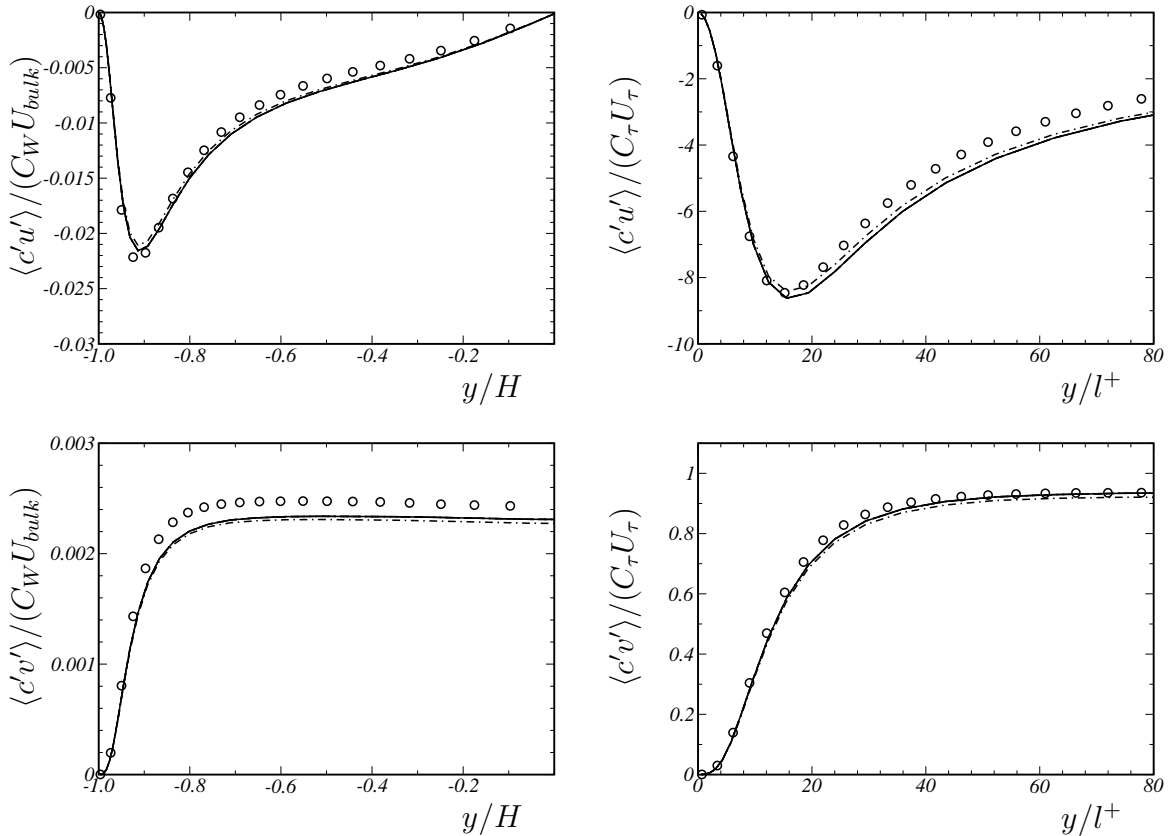
Figure 6.8: Turbulent transport of a passive scalar in plane channel flow at $Re_\tau = 180$ and $Sc = 1$. Implicit LES with parameters optimized for ——— high SCHMIDT numbers, ·—·—·— low SCHMIDT numbers, ∘ DNS of SCHWERTFIRM and MANHART [150].

fluid is based on the non-dimensional transfer coefficient

$$
\begin{aligned}
K^+ &= \frac{\kappa}{U_\tau \Delta c}\langle \partial_y c\rangle_{wall} \\
&= C_\tau/|C_W| \ ,
\end{aligned}
\tag{6.26}
$$

made dimensionless with the friction velocity U_τ and the potential Δc. The transfer coefficients is presented as a function of the SCHMIDT number in Fig. 6.11. Results for implicit LES agree very well with the reference DNS. The error of K^+ for the LES is less than 2.2% at $Sc = 1$ and 1.6% at $Sc = 25$. Results for the two proposed SGS models deviate by less than 0.25%. It is observed that the models perform slightly better for their respective calibration range.

As mentioned before, data for profiles of scalar variance and turbulent transport are very rare, especially at high SCHMIDT numbers. The transfer coefficient K^+ offers the opportunity for a comparison of different modeling approaches in the asymptotic regime
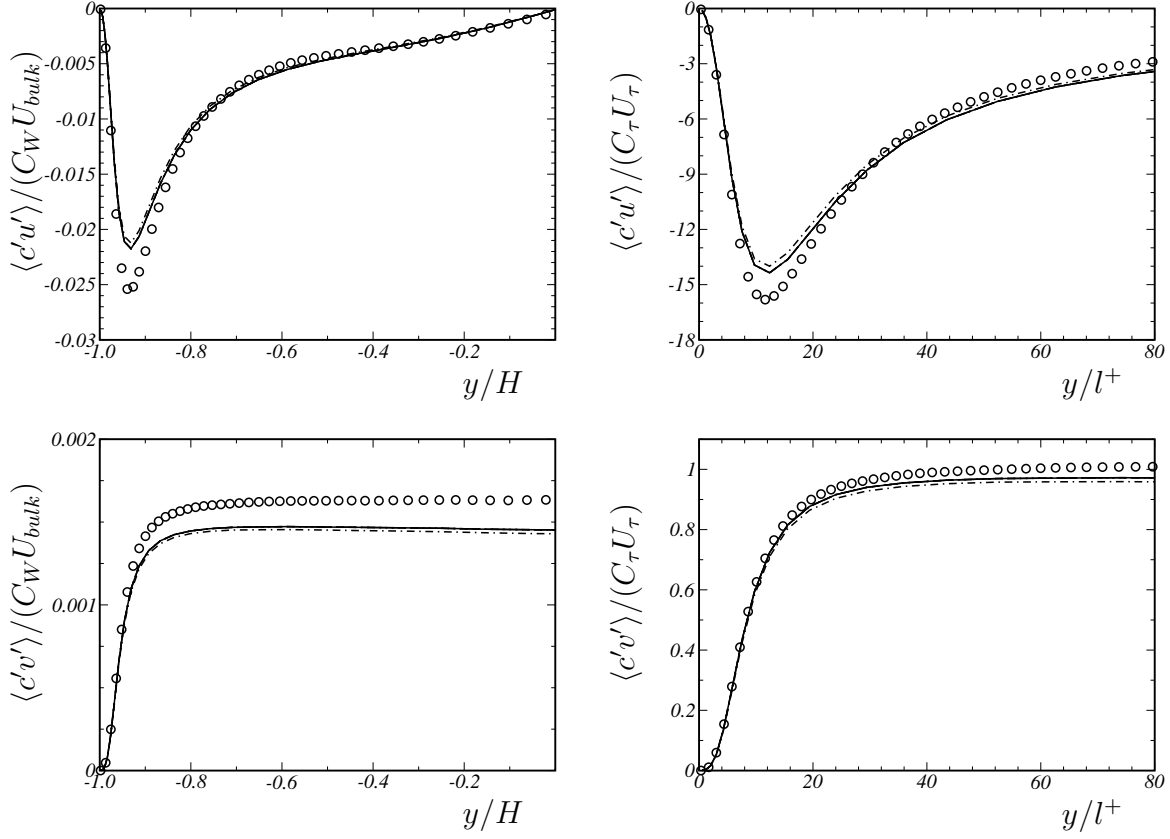
Figure 6.9: Turbulent transport of a passive scalar in plane channel flow at $Re_\tau = 180$ and $Sc = 3$. Implicit LES with parameters optimized for ——— high SCHMIDT numbers, ·—·—·— low SCHMIDT numbers, ○ DNS of SCHWERTFIRM and MANHART [150].

at higher SCHMIDT numbers. For this purpose, implicit LES have been performed at SCHMIDT numbers up to $Sc = 1000$. We use the same computational grid as before, noting that for the highest SCHMIDT numbers even the mean scalar gradients are barely resolved. In spite of that, the SGS model gives physically meaningful predictions for the mass transfer coefficient K^+, see Fig. 6.11. Since DNS data are not available, the LES results are compared with experimental data for turbulent pipe flow. Fig. 6.11 shows two experimental correlations by SHAW and HANRATTY [152]: The fit

$$K^+ = 0.0889 Sc^{-0.704} \qquad (6.27)$$

is preferred by the authors because it gives a better overall correlation with their measurements, whereas the alternative form

$$K^+ = 0.0649 Sc^{-2/3} \qquad (6.28)$$

is more appropriate from a theoretical point of view [81]. The LES results support either correlation, depending on whether the magnitude of K^+ or on the trend with increasing
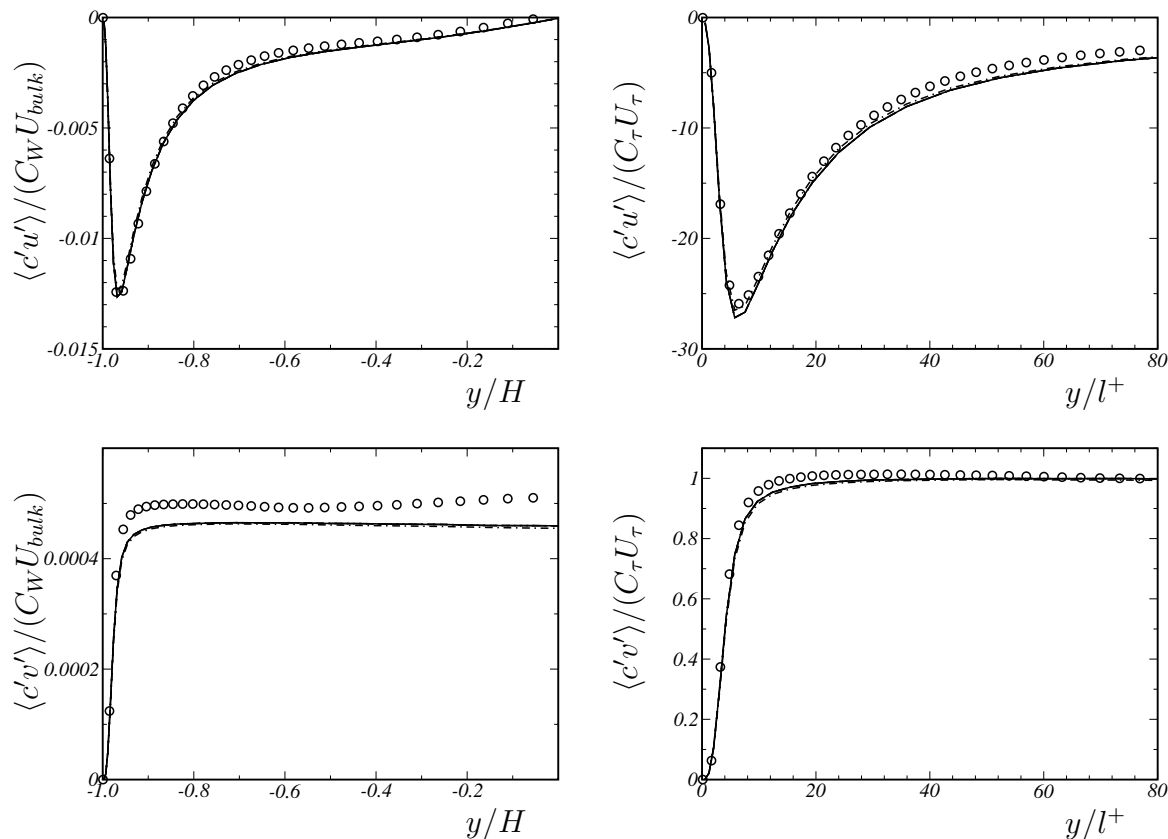
Figure 6.10: Turbulent transport of a passive scalar in plane channel flow at $Re_\tau = 180$ and $Sc = 25$. Implicit LES with parameters optimized for ——— high SCHMIDT numbers, ·—·—·— low SCHMIDT numbers, ○ DNS of SCHWERTFIRM and MANHART [150].

SCHMIDT number is considered. Nevertheless, the observed agreement is very good considering the coarse resolution, and the fact that different REYNOLDS numbers and different flow geometries, plane channel and pipe, are compared.

Because EULERian DNS are prohibitively expensive at high SCHMIDT numbers, PAPAVASSILIOU and HANRATTY [127] developed a LAGRANGEan technique which they applied to turbulent channel flow. These simulations at a slightly lower REYNOLDS number of $Re_\tau = 150$ predict significantly larger values of the transfer coefficient [127, 128], see Fig. 6.11. NA *et al.* [124] supported such results by EULERian DNS for the smaller SCHMIDT numbers. The results demonstrate the high sensitivity with respect to the REYNOLDS number and the importance of an accurate representation of the turbulent velocity field. We note that the effect of REYNOLDS number diminishes quickly as the SCHMIDT number increases and is negligible for $Sc \geq 100$. For low SCHMIDT numbers $Sc \leq 10$ the fit

$$K^+ = 0.0509Sc^{-0.546} \tag{6.29}$$
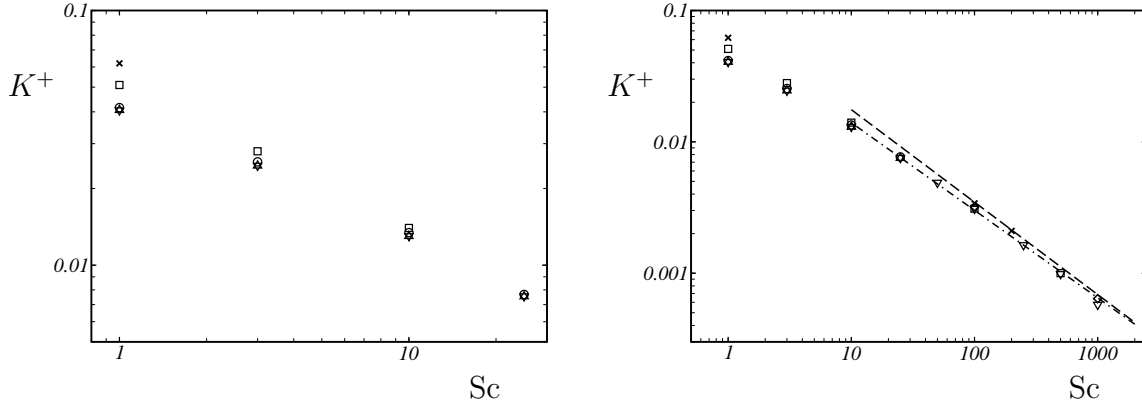
Figure 6.11: Dimensionless mass transfer coefficient K^+ for channel flow at $Re_\tau = 180$: $\triangle$ implicit LES with parameters for low SCHMIDT numbers, ∇ implicit LES with parameters for high SCHMIDT numbers, $\circ$ DNS [150], $\diamond$ semi DNS [149]. $\square$ K^+ for DNS [124, 127, 128] of channel flow at $Re_\tau = 150$. $\times$ K^+ for LES of channel flow at $Re_\tau = 640$ using the dynamic mixed SGS model [17]. Lines denote curve fits of SHAW and HANRATTY [152] to experimental data for turbulent pipe flow: $\cdot—\cdot—\cdot—$ $K^+ = 0.0649$ $Sc^{-2/3}$ $————$ $K^+ = 0.0889$ $Sc^{-0.704}$.

is proposed by NA *et al.* [124], whereas our LES results and the reference DNS at $Re_\tau = 180$ rather give

$$K^+ = 0.041 Sc^{-0.5} \ . \tag{6.30}$$

To deal with the resolution requirements at high SCHMIDT numbers, SCHWERTFIRM and MANHART [149] propose a semi-DNS methodology. Semi-DNS is an accurate but still rather expensive method, where the flow field is fully resolved and an SGS model is added to the scalar transport equation. Fig. 6.11 shows results for semi DNS at $Sc = 100$ and 1000. The semi-DNS data for $Sc = 100$ are in perfect agreement with our LES data and the LAGRANGEan DNS, whereas the LES result for $Sc = 1000$ lie 10% below that for the semi-DNS, suggesting that the grid-resolution limit of the implicit LES is reached. Satisfying the resolution requirements imposed by the momentum equation, our computational grid is relatively coarse for LES of scalar mixing at high SCHMIDT numbers. Nevertheless, the computational results suggest that LES on this grid can deliver reliable results up to $Sc = 500$. For the present study no wall modeling is applied. Whether the resolution limit can be pushed to higher SCHMIDT numbers by using wall models remains an open question to be studied in future work.

Classical LES of turbulent channel flow at high SCHMIDT number have been performed by CALMET and MAGNAUDET [17] using the dynamic mixed model (DMM) of ZANG *et al.* [190]. The chosen REYNOLDS number of $Re_\tau = 640$ made it necessary to use much finer grids than in the present study. The DMM results for K^+ lie above all other
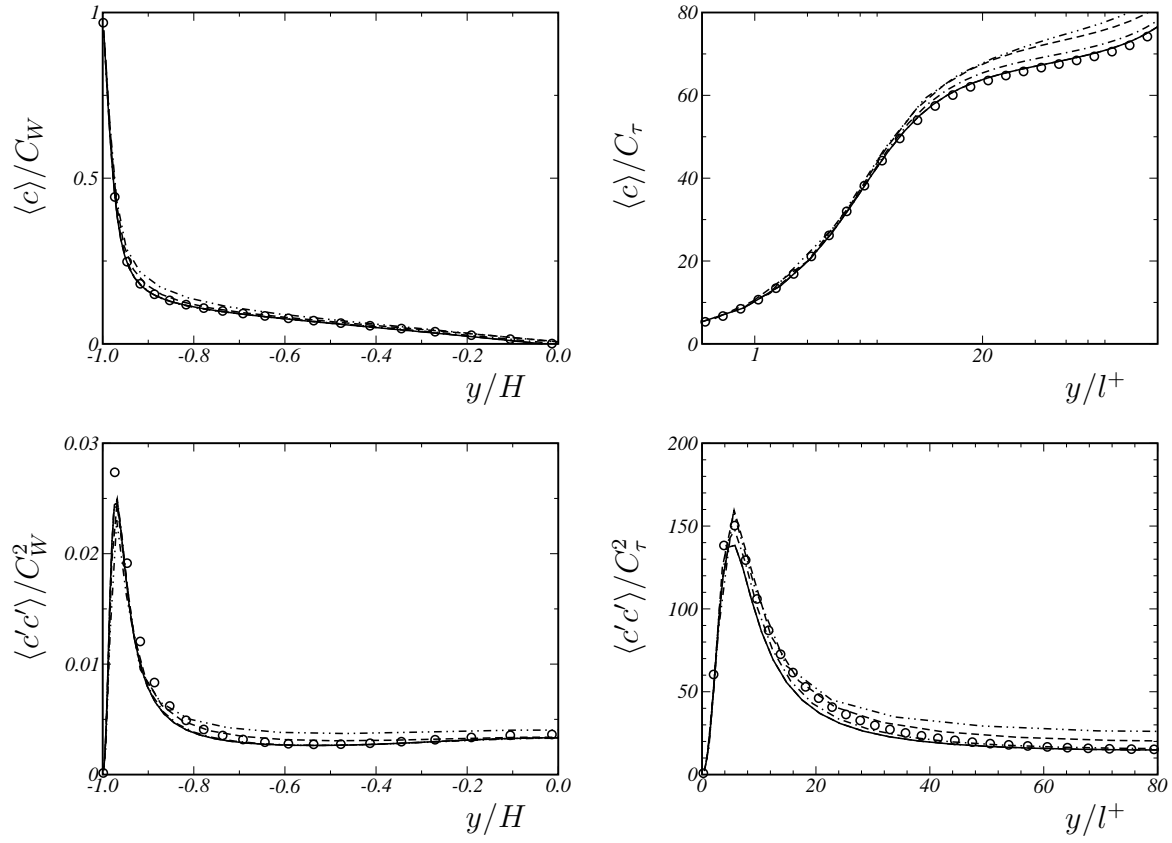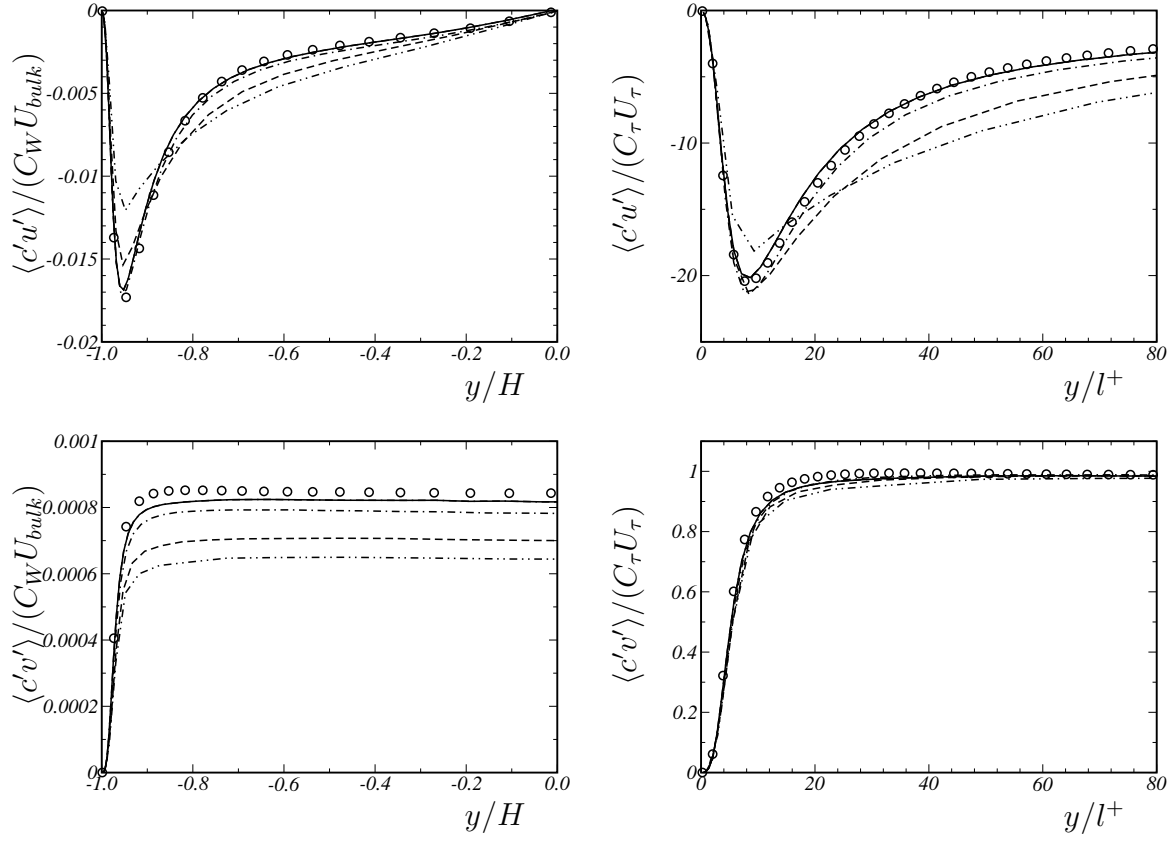
Figure 6.12: Grid-convergence study for implicit LES of passive-scalar transport in turbulent channel flow at $Re_\tau = 180$ and $Sc = 10$. Implicit LES using the high SCHMIDT number SALD method on a grid with ———— 64^3 cells , ·—·—·— 48^3 cells , ———— 32^3 cells —··—··— 24^3 cells. ○ DNS of SCHWERTFIRM and MANHART [150]

numerical predictions for channel flow but match well with Eq. 6.27. The discrepancy with other channel-flow data is opposite to the REYNOLDS-number trend predicted by the DNS cited above, which give larger K^+ for smaller Re_τ. Therefore, it is unclear whether this result can be attributed to the REYNOLDS number or reflects modeling uncertainties.

6.5.4 Grid-Resolution Study

The LES presented in the preceding section were performed on identical grids with 48^3 cells. Although this resolution was chosen somewhat arbitrarily, implicit LES using this grid accurately predicts the passive-scalar statistics for SCHMIDT numbers $1 \leq Sc \leq 25$. In the following we study the effect of grid resolution qualitatively. Statistics of LES data at different spatial resolutions are compared with statistics of unfiltered DNS data. For

Figure 6.13: Grid-convergence study for implicit LES of passive-scalar transport in turbulent channel flow at $\mathrm{Re}_\tau = 180$ and $\mathrm{Sc} = 10$. Implicit LES using the high SCHMIDT number SALD method on a grid with ——— 64^3 cells , $\cdot$—$\cdot$—$\cdot$— 48^3 cells , $-\,-\,-\,-$ 32^3 cells $-\cdot\cdot-\cdot\cdot-$ 24^3 cells. $\circ$ DNS of SCHWERTFIRM and MANHART [150]

increasing resolution, LES results should converge to those of DNS. Figures 6.12 and 6.13 show profiles of mean scalar concentration, scalar variance, and turbulent transport for DNS and LES of turbulent channel flow at $\mathrm{Re}_\tau = 180$ and $\mathrm{Sc} = 10$. The reference DNS was conducted by SCHWERTFIRM and MANHART [150] on a grid with $720 \times 300 \times 384$ cells. DNS data are compared to four LES on grids with 24^3, 32^3, 48^3, and 64^3 cells, respectively. The results from implicit LES with 64^3 cells are in very good agreement with the reference DNS. The results for lower resolutions show convergence towards the DNS with decreasing grid width. This tendency is most visible for the turbulent scalar transport, Fig. 6.13, whereas the scalar variance itself is rather insensitive to the grid resolution, Fig. 6.12. Generally, we observe monotonic convergence toward the DNS.

6.6 Summary

The implicit SGS modeling environment provided by the adaptive local deconvolution method has been extended to LES of passive-scalar mixing. A difficulty of this modeling task is that the various regimes that exist for the passive-scalar variance spectrum have to be recovered by the SGS model. Our analysis revealed that two different parameter sets are required: one set for low SCHMIDT numbers and one set for high SCHMIDT numbers. The choice of model parameters has been validated for forced isotropic turbulence and for turbulent channel flow. Both applications demonstrate that implicit LES provides reliable predictions of the turbulent transport of passive scalars for a wide range of SCHMIDT numbers.

A key issue in LES is how an SGS model that is calibrated for isotropic turbulence handles the near wall turbulence. We conclude that the implicit modeling approach gives good results for the turbulent transfer of heat or mass from walls without additional modeling. ALDM results compare well with experimental data and with numerical predictions obtained from considerably more expensive numerical methods.

LES OF TURBULENT BOUNDARY-LAYER SEPARATION

Highly resolved large-eddy simulations of turbulent boundary-layer separation are presented in this chapter. The behavior of incompressible fully-turbulent flat-plate boundary-layer flow subjected to a constant adverse pressure gradient (APG) is investigated. REYNOLDS number and pressure-gradient parameters are adapted to the experimental setup of INDINGER *et al.* [77] who conducted measurements in a closed-circuit water tunnel. A special focus of the analysis is placed on scaling laws for the mean-velocity profiles under non-equilibrium conditions approaching pressure-induced separation[1].

7.1 Introduction

There is considerable controversy regarding the behavior of the mean-velocity profile of turbulent boundary layers approaching separation [45, 77, 108]. Asymptotic expansions predict a pressure-gradient independent inner region, provided that the REYNOLDS number is sufficiently large [126]. While some experiments [103, 159, e.g.] suggest that the classical logarithmic law of the wall is valid even under a strong adverse pressure gradient and non-equilibrium conditions, other experiments indicate that, based on inner scaling, the mean velocity profile is not self-similar when approaching separation [33, 125, e.g.].

Recently, INDINGER *et al.* [77, 78] have presented measurements for a fully-turbulent flat-plate boundary layer with a constant APG. Fig. 7.1 shows the experimental setup in the test section of a closed-circuit water tunnel with flow from left to right. The measurements were conducted in the boundary layer developing on an inclined flat plate. A flexible curved wall on the opposite side is used to generate a pressure gradient, where

---

[1] This presentation is based on Refs. [64, 67]

the pressure-gradient parameters can be controlled by adjusting the curvature. The test section has an overall length of 0.8 meters and a cross section area of 0.4×0.4 square meters. The flat plate, inclined by 4 degrees, has an overall length of 0.725 meters and a flap at the end to prevent trailing-edge separation. The plate surface is made from mirrored glass, which facilitates optical measurements close to the wall. Several auxiliary devices are necessary to control the flow quality. A bypass system below the flat plate and a suction system have been installed to control the stagnation-point flow at the elliptic leading edge of the plate. To prevent boundary-layer separation at the opposite wall due to curvature effects, a second suction system consisting of three slots is installed at the upper rear end of the test section. For a detailed description of the experimental facilities refer to INDINGER [76].

In the spanwise center plane, the static wall pressure and profiles of the streamwise velocity component were measured using pressure taps and a one-component LASER DOPPLER anemometry (LDA) system, respectively. For measurements of the wall shear stress, a PRESTON tube was employed.
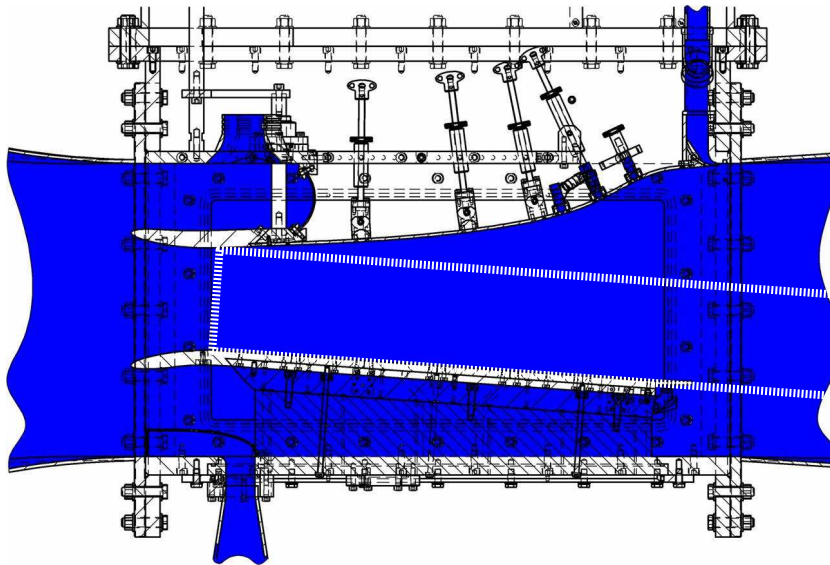
Figure 7.1: Experimental setup in the test section of a water tunnel [78]. The computational domain of the present LES is marked by the dashed white line.

The available measurement data do not provide the fully-3-D statistics that are essential for an analysis of the turbulent non-equilibrium flow. To gain a deeper understanding of wall-bounded turbulence in the vicinity of massive pressure-induced separation a numerical investigation by LES was carried out that is reported in the following.

Numerical investigations of boundary-layer separation are rare in the literature. The

applicability constraints of available turbulence models are well known for pressure-induced boundary-layer separation. Direct numerical simulations provide high accuracy but are limited to low REYNOLDS number and moderate flow complexity. A frequently cited study is that by NA and MOIN [122, 123] where turbulence is barely developed. SPALART and COLEMAN [167] performed DNS of weakly separated boundary-layer flows. MANHART and FRIEDRICH [109] presented DNS of weak separation adapted to the experiment by KALTER and FERNHOLZ [82], where REYNOLDS number of the DNS is half of the experimental one.

To our knowledge, this work represents the first successful reproduction of an experiment of massively separated flow by LES. The REYNOLDS number based on the local free-stream velocity and momentum thickness is $\mathrm{Re}_{\delta_2} = 670$ at the inflow and $\mathrm{Re}_{\delta_2} = 5100$ at the separation point. CLAUSER's pressure-gradient parameter increases monotonically from $\beta = 0$ up to around $\beta = 100$ since a constant pressure gradient is prescribed corresponding to the reference experiment. It should be noted that under the conditions considered here the adverse pressure gradient leads to a highly unsteady and massive separation. Neither separation nor reattachment are fixed in space. Showing a strongly irregular shape, the instantaneous separation line has spanwise and temporal excursions that are significantly larger than the mean boundary-layer thickness.

7.2 Computational Setup

7.2.1 Numerical Method

The incompressible NAVIER-STOKES equations are discretized on a staggered CARTESian mesh. For time advancement the explicit third-order RUNGE-KUTTA scheme of SHU [153] is used. The time-step is dynamically adapted to satisfy a COURANT-FRIEDRICHS-LEWY condition with CFL = 1.0. All results presented in this chapter are obtained by the SALD method, see Appendix B, which represents a computationally efficient implementation of ALDM. The pressure-POISSON equation and diffusive terms are discretized by second-order centered differences. The POISSON solver employs fast FOURIER transforms in the spanwise direction and the stabilized bi-conjugate gradient (BiCGstab) method [160, 174] in the streamwise and wall-normal directions. The POISSON equation is solved at every RUNGE-KUTTA substep.

Computational results presented in Section 5.3.3 have approved that our numerical methodology allows for accurate predictions of turbulent boundary-layer flows. The applicability of ALDM for separated flows has been established by Ref. [74].

7.2.2 Computational Grid

The computational domain considered in the LES is indicated by a dashed white line in Fig. 7.1. It has an overall physical length of 1.01 meters. The spanwise and wall-normal extents are 0.036 meters and 0.15 meters, respectively. For comparison, the displacement thickness of the inflow boundary layer is $\delta^*(x = 0) = 0.0008$ meters. In the following all data are made dimensionless with reference length 1 meter and reference velocity 1 meter per second, i.e., all measures are given in SI units except if mentioned otherwise. The CARTESian grid consists of $2038 \times 144 \times 144$ finite volumes. The spacing is homogeneous in streamwise and in spanwise directions, where the cell dimensions are $h_x = 5 \cdot 10^{-4}$ and $h_y = 2.5 \cdot 10^{-4}$, respectively. In the wall-normal direction a hyperbolic stretching is used to increase resolution near the wall. The computational grid classifies the present LES as highly resolved. Cell sizes are chosen as to allow for a reliable simulation of the incoming ZPG boundary layer flow, see Tab. D.5.

7.2.3 Statistical Analysis

For statistical analysis, the simulation was run for $t_{ave} = 23.7$ seconds of physical time[2] after reaching a stationary state. A clearer picture of the sample size is obtained from the averaging time expressed in typical boundary-layer time scales, i.e., $t_{ave}/(\delta^*/U_\infty)$ for the outer region and $t_{ave}/(l^+/U_\tau)$ near the wall. A typical timescale of the wall-turbulence, the ratio of turbulent kinetic energy to its production rate, is about 15 wall time units l^+/U_τ [166]. As shown in Tab. D.5, the statistical analysis is conclusive for the attached flow up to $x \leq 0.475$ meters. The separation bubble itself exhibits a much larger time scale than the boundary-layer turbulence. Fully converged statistics from the available samples cannot be expected for higher-order statistics at locations within the separated zone.

7.2.4 Boundary Conditions

The computational domain considered in the LES as indicated in Fig. 7.1 represents only a part of the experimental facility. The flow within the computational domain is determined by the surrounding flow which has to be represented by imposing appropriate boundary conditions. At the domain boundaries three layers of ghost cells are added so that stencils reaching beyond the domain boundary can be used. The methods employed for assigning data to these ghost cells are described in the following.

---

[2] $t_{ave} = 23.7$ seconds correspond to roughly $11\,500$ CPU hours on a NEC SX8 vector machine.

Spanwise periodicity was imposed since the flow is supposed to be homogeneous in this direction. At the surface of the flat plate a no-slip condition $\overline{\boldsymbol{u}} = \boldsymbol{0}$ and a homogeneous NEUMANN condition for the pressure $\partial_y \overline{p} = 0$ is imposed. The viscous sublayer layer is resolved and no wall model is used. The ghost cells are filled with the analytical solution for STOKES flow as recommended by MORINISHI *et al.* [120].

The free-stream interface is modeled by prescribing a DIRICHLET condition for the pressure $\overline{p} = \overline{p}_{fs}(x,t)$. The velocity is locally split in the instantaneous spanwise mean

$$\overline{\boldsymbol{u}}_{mean} = \frac{\int \overline{\boldsymbol{u}} dz}{\int 1 dz}$$

and local instantaneous fluctuations

$$\overline{\boldsymbol{u}}_{fluc} = \overline{\boldsymbol{u}} - \overline{\boldsymbol{u}}_{mean} \ .$$

Mean velocity and fluctuations are extrapolated from the computed domain to the ghost cells in such a manner that $\partial_y \overline{\boldsymbol{u}}_{mean} = \boldsymbol{0}$ and $\partial_y \overline{\boldsymbol{u}}_{fluc} = -\alpha \overline{\boldsymbol{u}}_{fluc}$ are fulfilled, respectively. The latter results in the decay condition $\overline{\boldsymbol{u}}_{fluc}(y) \propto \exp\left(-\alpha y\right)$. The value of the parameter $\alpha = 1/(4hy)$ was determined from the wavelength of numerically induced oscillations that were observed when the decay condition was not used. This free-stream boundary condition allows for both outflow and inflow. Ghost cells are filled by using a discrete second-order approximation of the above equations.

In the experiments, the pressure has been measured at the plate surface only. For optimum agreement of the wall-pressure distribution with the experimental data, the free-stream pressure boundary condition for the present LES was reconstructed by a large number of low-resolution trial computations. The resulting free-stream pressure boundary condition is a function of the streamwise coordinate defined by

$$\overline{p}_{fs}(x,t) = \rho \int\limits_0^x (0.79 - 0.60 \ x')\ b(x',t)\ dx' \ , \tag{7.1}$$

where ρ is the fluid's density. In the experimental facility, flow separation causes a breakdown of the constant pressure gradient by its displacement effect. Therefore a positive pressure gradient should be imposed only within the zone of attached boundary

layer flow. In order to ensure smooth transients, we define

$$
b(x,t) = \begin{cases}
0 & , \quad x < (x_B - x_{RB}) \\
1 + \frac{x-x_B}{x_{RB}} - \frac{1}{2\pi}\sin(2\pi\frac{x-x_B}{x_{RB}}) & , \quad (x_B - x_{RB}) \leq x < x_B \\
1 & , \quad x_B \leq x < x_E \\
1 - \frac{x-x_E}{x_{RE}} + \frac{1}{2\pi}\sin(2\pi\frac{x-x_E}{x_{RE}}) & , \quad x_E \leq x < (x_E + x_{RE}) \\
0 & , \quad (x_E + x_{RE}) \leq x
\end{cases} \tag{7.2}
$$

Time dependency enters trough $x_E = x_D(t) + 0.1$ where $x_D(t)$ is the instantaneous position of the spanwise averaged detachment line. A summary of all parameters is given in Table 7.1.

Parameter		Value
x_B	starting point of nominal pressure gradient	-0.025
x_{RB}	length of starting ramp	0.02
x_E	end nominal pressure gradient	$x_D + 0.1$
x_{RE}	length of end ramp	0.15
x_D	location of spanwise averaged detachment line	variable

Table 7.1: Parameters for the free-stream pressure boundary condition.

At the inlet, fully turbulent inflow data are generated using a recycling technique, similar to that of LUND *et al.* [106]: Instantaneous turbulent structures are extracted at a downstream distance $l_{rec} \approx 40\delta^*$. Inside the boundary layer, target profiles for the fluctuating velocities are taken from SPALART's zero-pressure-gradient boundary-layer DNS [166] at $\mathrm{Re}_{\delta_2} = 670$. In the outer flow region, isotropic turbulence is assumed with a turbulence level of $Tu = 0.03$ matched to the experiment. For the pressure a homogeneous NEUMANN condition $\partial_x \overline{p} = 0$ is used. Figure 7.2 shows mean velocity profile and REYNOLDS stresses at $x = 0$, the inflow plane is located at $x = -0.045$.

Recycling techniques can sustain spurious oscillations with a wavelength proportional to the recycling length. In order to damp these oscillations the re-scaling factors are computed for each ghost-cell plane separately: For the innermost ghost-cell plane, target profiles are taken from the DNS of SPALART [166]. For the remaining two upstream planes, the target fluctuation profiles are damped in such a way that $\partial_x \langle \boldsymbol{u}'\boldsymbol{u}' \rangle = \langle \boldsymbol{u}'\boldsymbol{u}' \rangle / l_{rec}$ is satisfied.

(a)

(b)
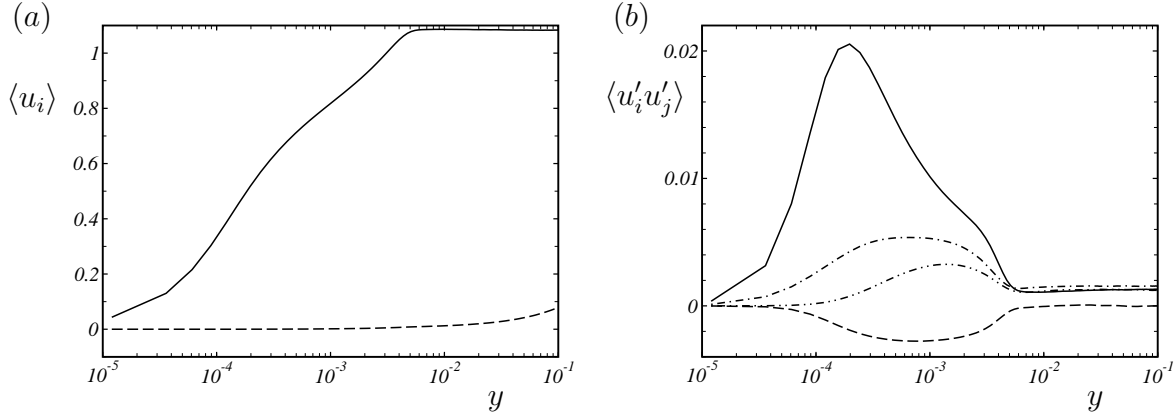
Figure 7.2: Mean velocity profile and Reynolds stresses at $x = 0$.
(a) ——— $\langle u \rangle$, − − − − $\langle v \rangle$. (b) ——— $\langle u'u' \rangle$, ·—·—·— $\langle v'v' \rangle$, —··—··— $\langle w'w' \rangle$, − − − − $\langle u'v' \rangle$.

At the outlet the ghost cells are filled by extrapolation. For a second-order centered discretization $\partial_x \overline{p} = 0$ and $\partial_x^2 \overline{\boldsymbol{u}} = \boldsymbol{0}$ are fulfilled . No artificial damping or sponge zone is used.

7.3 Results and Discussion

7.3.1 General Overview

A first impression of the investigated flow can be obtained from the mean streamlines in Fig. 7.3. Contour plots of the mean velocity solution as well as for mean pressure are shown for the entire computational domain in Fig. 7.4. The influence of a strong
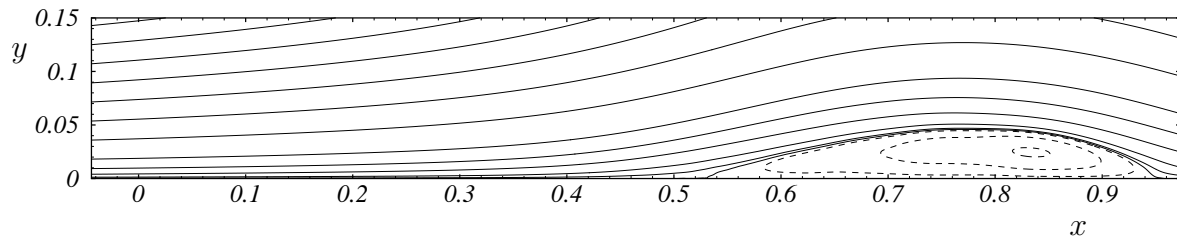
Figure 7.3: Mean streamlines.

adverse pressure gradient is evident. The mean-flow deceleration results in an increasing fraction of back-flow events and eventually causes strong boundary-layer separation. The boundary-layer separation is accompanied by a large wall-normal velocity component and intense interactions with the outer flow.

(a)

(b)

(c)
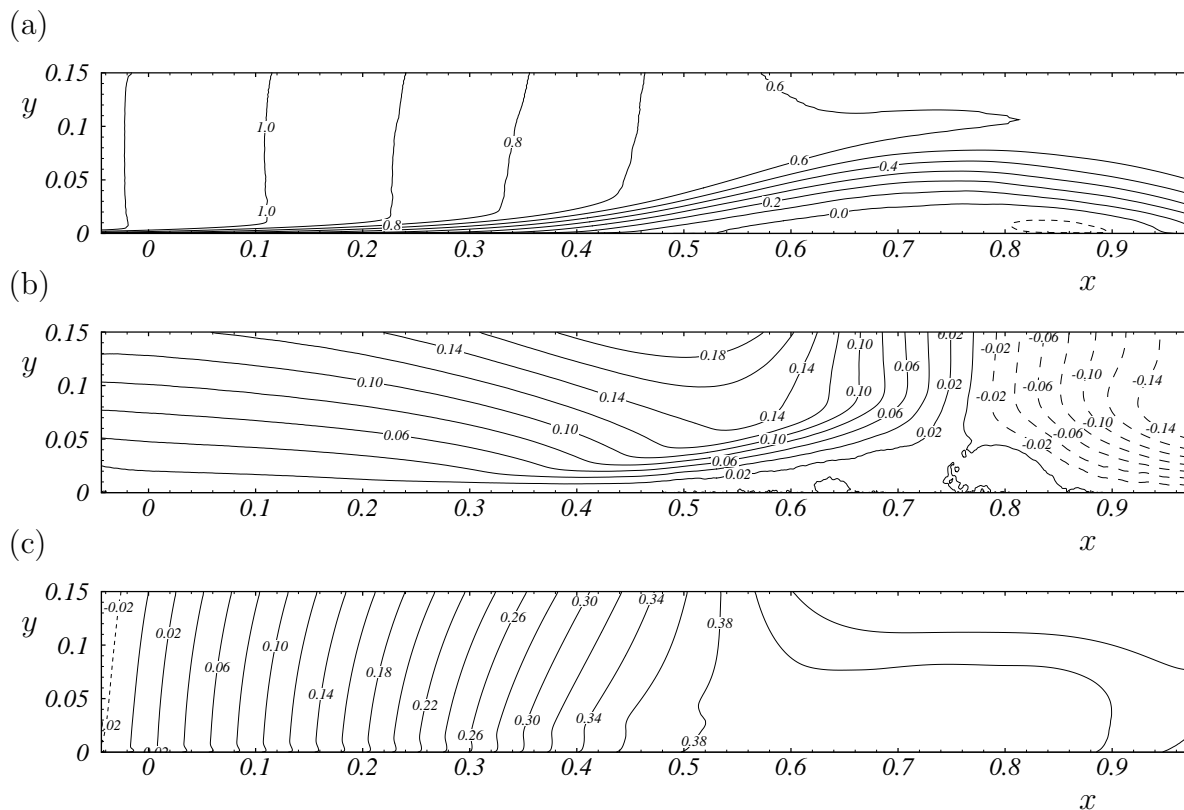
Figure 7.4: Contours of (a) mean streamwise velocity, (b) mean wall-normal velocity, and (c) mean pressure.

Fig. 7.5 shows mean profiles of the streamwise and wall-normal velocity components for several downstream stations. In this figure, the shape of the separation bubble is indicated by two lines that represent different criteria: The locations where the mean streamwise velocity component does vanish, i.e. $\langle u \rangle = 0$, and the locations where forward flow and upstream flow have equal probability ($\chi = 0.5$). Both criteria give a similar result, however, some differences can be observed close to the separation point. The wall-normal extent of the separated region is slightly thicker for $\chi = 0.5$ than for $\langle u \rangle = 0$.

The probability of back flow is quantified by the reverse-flow parameter

$$\chi = \frac{1}{2} - \frac{1}{2} \left\langle \frac{u}{|u|} \right\rangle \tag{7.3}$$

which measures the fraction of time that the flow moves upstream. Wall-normal profiles of χ are shown in Fig. 7.6 and streamwise profiles are shown in Fig. 7.7a. We observe that flow separation is accompanied by the shift of the location of maximum χ away from the wall towards the detached shear layer.
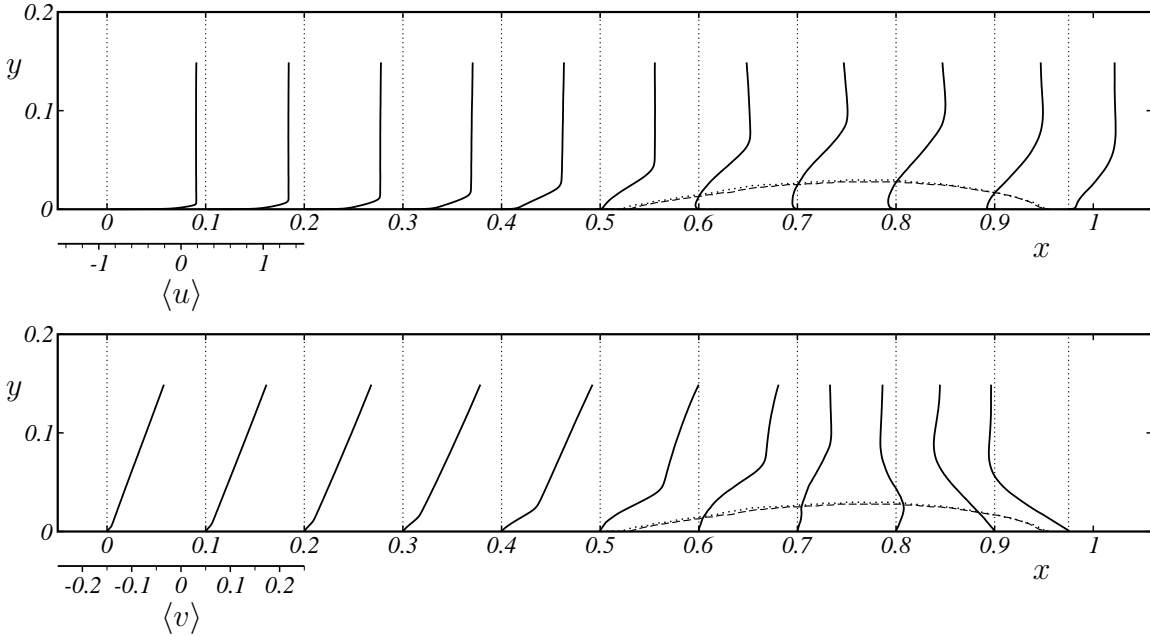
Figure 7.5: Mean velocity profiles at several downstream stations. ——— mean velocity, ————
$\langle u \rangle = 0$, ·········· $\chi = 0.5$.
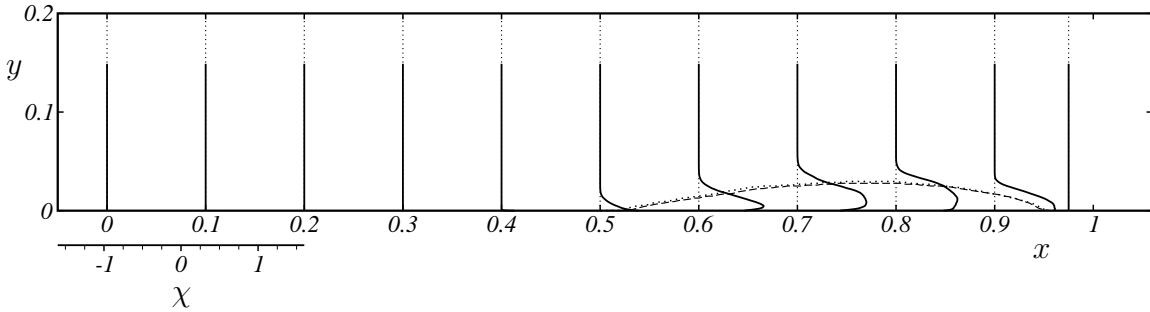
Figure 7.6: Reverse-flow-parameter profiles at several downstream stations.

The following terminology has been proposed by SIMPSON [156, 158] to define the separation state quantitatively: *Incipient detachment* (ID) occurs with $\chi = 0.01$, *intermittent transitory detachment* (ITD) occurs with $\chi = 0.2$, *transitory detachment* (TD) occurs with $\chi = 0.5$, and *detachment* (D) occurs where the time-averaged wall shearing stress is zero. The corresponding locations for the LES of the present configuration are given in Tab. 7.2. In agreement with most available data, our computational results confirm that TD and D occur at the same location.

Term		Definition	Location
ID	incipient detachment	$\chi = 0.01$	$x = 0.287$
ITD	intermittent transitory detachment	$\chi = 0.2$	$x = 0.457$
TD	transitory detachment	$\chi = 0.5$	$x = 0.502$
D	detachment	$\langle \tau_w \rangle = 0$	$x = 0.502$

Table 7.2: Separation state near the wall for present LES in SIMPSON's terminology.
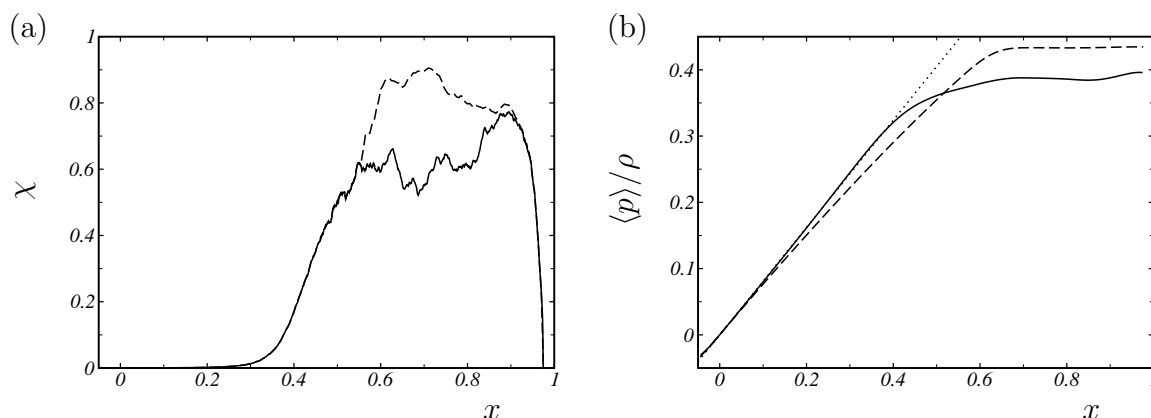
Figure 7.7: (a) Reverse-flow parameter: ——— at the wall and − − − − maximum value. (b) Mean static pressure at the − − − − free-stream interface and at the ——— wall. The ·········· dotted line denotes the target pressure gradient of 810 Pa/m according to experimental reference data.

7.3.2 Separation Dynamics

The separated-flow region reflects the turbulent nature of the incoming boundary layer and shows a rather complex behavior. In front of the large separated zone, small zones of reverse flow are continuously formed which then either slowly move downstream and join the separated region or disappear shortly after their appearance. This highly active zone ranges from $x = 0.4$ to $x = 0.55$. We have observed that the separated zone can be divided into two subregions that move independently. Also typical for this configuration is secondary flow separation which occurs inside large separated regions. Figure 7.8 shows the footprint of the turbulent boundary layer separation, i.e., the locations with zero instantaneous wall-shear stress as a function of time. Figure 7.9 shows contours of the instantaneous streamwise wall-shear stress. Different regimes of wall turbulence can be distinguished. Typical streaky structures dominate the boundary layer at the inflow. As the flow experiences the adverse pressure gradient, the average width of the streaks
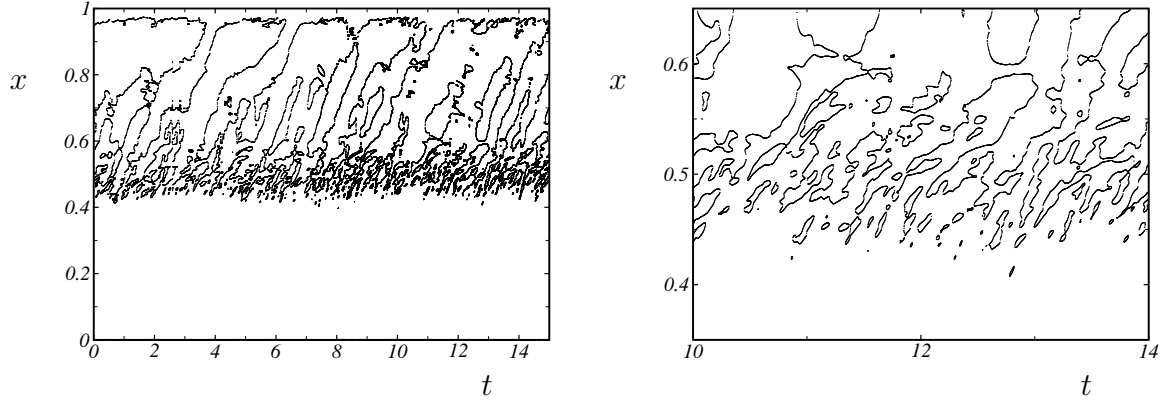
Figure 7.8: Footprint of the spanwise averaged separation bubble. Shown are locations of zero instantaneous wall-shear stress. The right figure is a closeup of the most active region.

grows and their relative length decreases. Intermittent backflow is observed from $x = 0.1$ onwards. There is no well-defined separation line, instead the fraction of separated flow zones increases gradually. Energetic streak-like structures can penetrate deeply into the detached region. Within the separated region eddies with large spanwise extents are dominating. Secondary flow reversion occurs in several regions. Streaky structures are found again shortly before the reattachment.
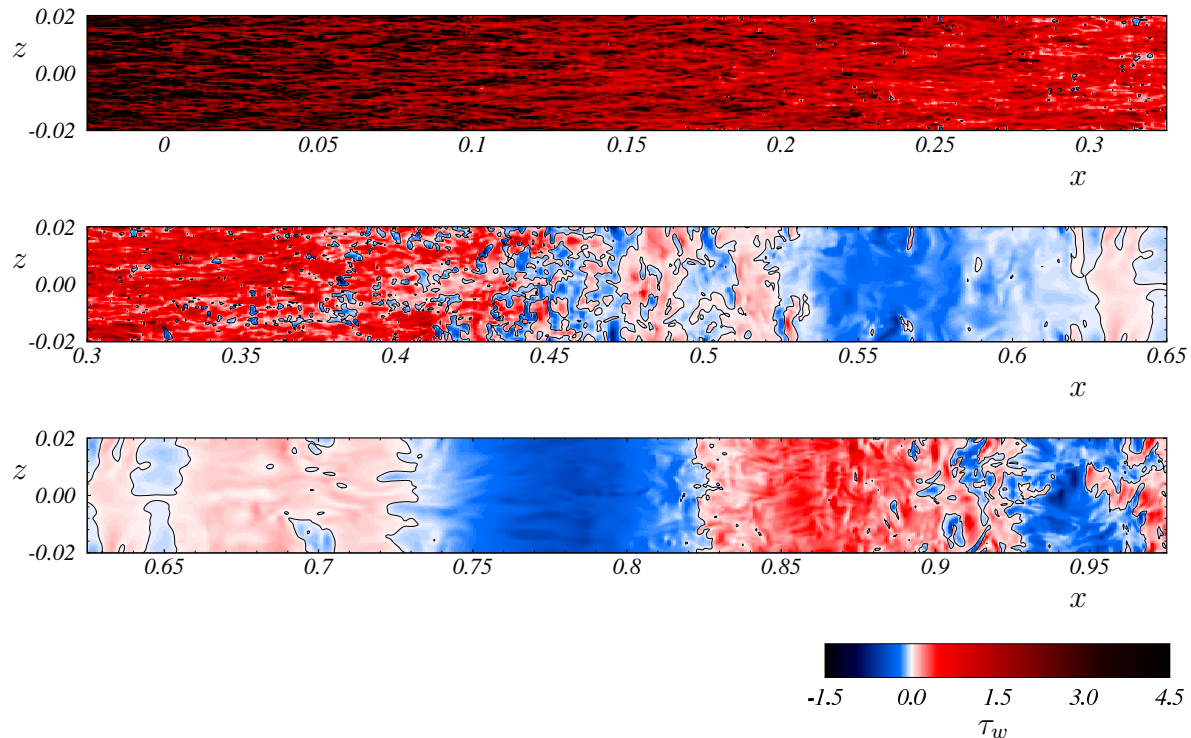
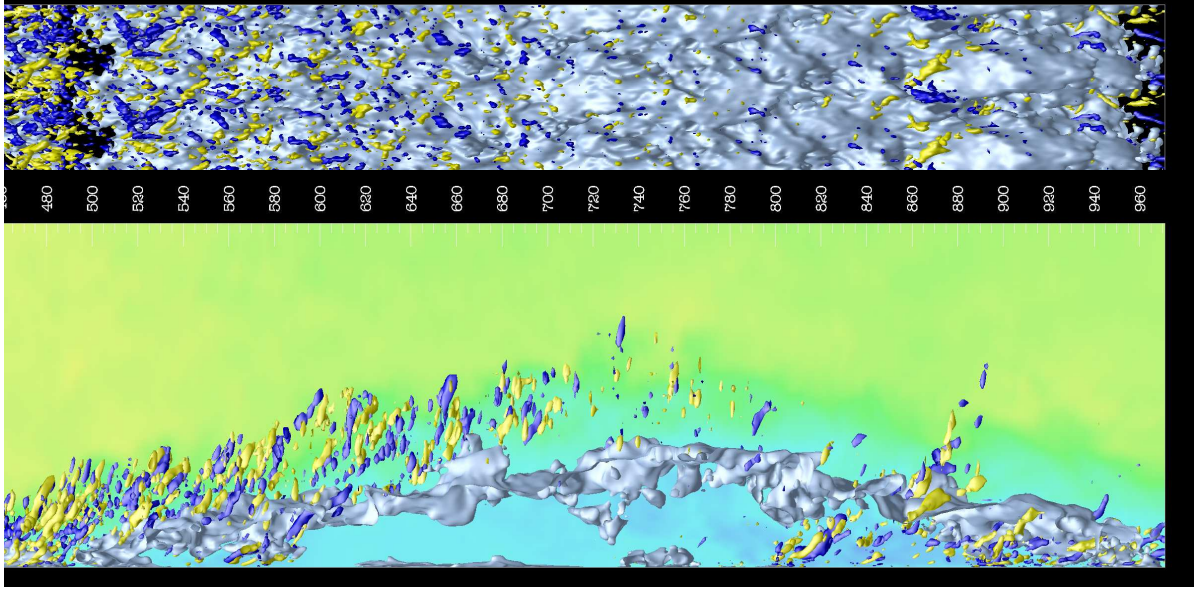**Figure 7.9:** Instantaneous contours of the wall-shear stress.
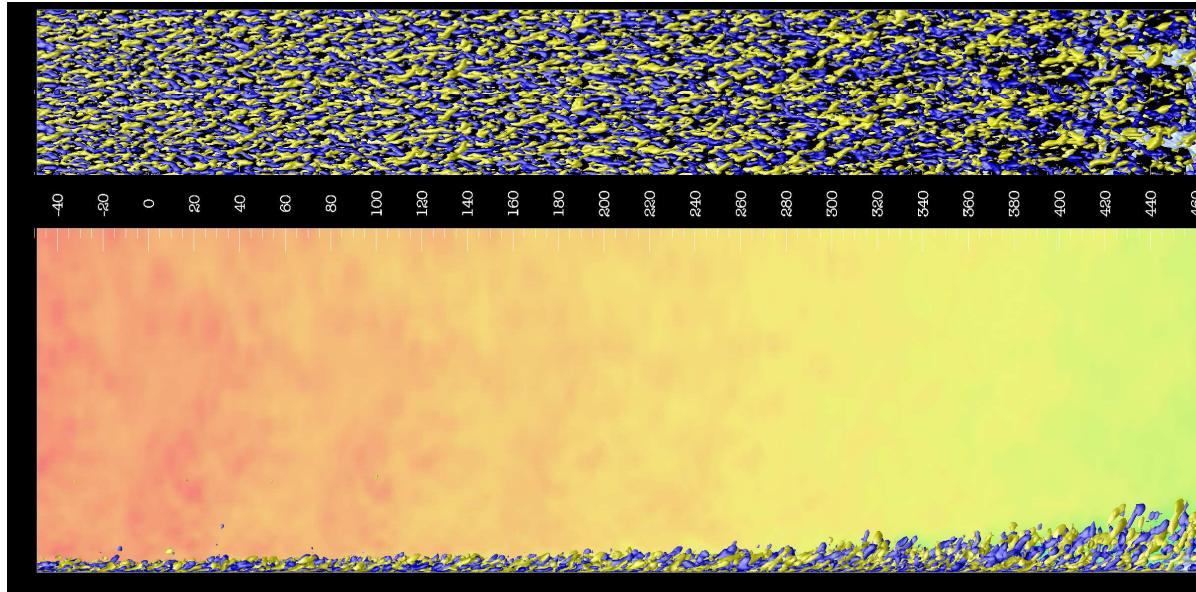
Figure 7.10: Instantaneous snapshot of vortical structures visualized by iso-surfaces of the Q criterion
and flow separation visualized by the iso-surface of zero streamwise velocity, part one.

The reattachment line is much smoother than the detachment line. Generally, the flow
structures observed at and after reattachment are one order of magnitude larger than
those within the attached boundary layer before separation. A flow visualization is
presented in Fig. 7.10.

7.3.3 Comparison of Numerical and Experimental Results

The mean static pressure imposed as a boundary condition at the free-stream interface is
shown in Fig. 7.7b. The mean pressure distribution at the wall is the nonlinear response
of the flow and strongly influenced by the boundary-layer separation. The oscillatory
motion of detached flow regions has a significant effect on the upstream flow resulting in
a deviation of the wall pressure from the imposed free-stream condition, see Fig. 7.7b.

The resulting wall-pressure gradients $\langle \partial_x p \rangle_{wall} / \rho$ for LES and the experiment are shown
in Fig. 7.12a. Taking into account the noise in derivatives computed from experimen-
tal data, LES results and experiment agree well. This first impression is confirmed
by the observed deceleration of the free-steam velocity U_∞, see Fig. 7.12b, that can
be measured more accurately. Mean-flow deceleration is directly caused by the APG
through BERNOULLI's equation and the excellent agreement of U_∞ confirms that both
the pressure gradient and the mean streamline curvature are reproduced correctly.

Figure 7.11: Instantaneous snapshot of vortical structures visualized by iso-surfaces of the Q criterion and flow separation visualized by the iso-surface of zero streamwise velocity, part two.

A turbulent boundary layer can by characterized by several length scales. The boundary-layer thickness δ serves as a measure for the largest structures in the boundary-layer flow. It is defined as the distance away from the wall where 99 percent (δ_{99}) of the free-stream velocity U_∞ is reached. In APG boundary layer flow, however, the velocity is not constant in the free stream. For the experimental data, INDINGER [76] has manually selected the LDA measurement points representing the transition region between boundary layer and free stream. For the LES, the boundary layer edge is determined as the point where the streamwise velocity starts to diverge from the linear dependency on wall distance of the external flow. The velocity at this point is defined as U_∞ and δ follows from

$$\delta = y\left(\langle u \rangle = U_\delta\right) \tag{7.4}$$

with

$$U_\delta = 0.99\, U_\infty \;. \tag{7.5}$$

Length scales based on integral definitions are less sensitive to errors. Fig. 7.13 shows the boundary-layer displacement thickness

$$\delta_1 = \int_0^\infty \left(1 - \frac{\langle u \rangle}{U_\delta}\right) dy \;, \tag{7.6}$$
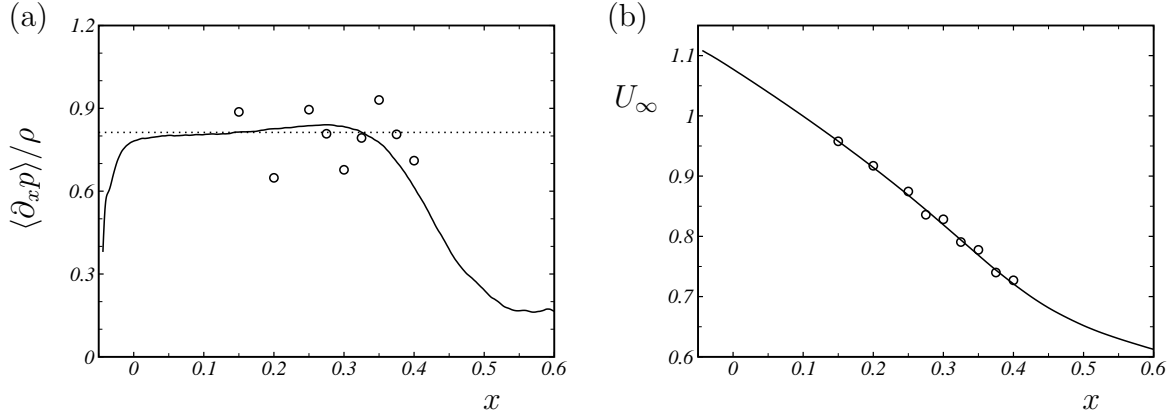
Figure 7.12: (a) Mean pressure gradient at the wall, and (b) free-stream velocity at the boundary-layer edge for ∘ experiment and ———— LES.

the boundary-layer momentum thickness

$$\delta_2 = \int_0^\infty \frac{\langle u \rangle}{U_\delta} \left(1 - \frac{\langle u \rangle}{U_\delta} \right) dy \ , \tag{7.7}$$

and the boundary-layer energy thickness

$$\delta_3 = \int_0^\infty \frac{\langle u \rangle}{U_\delta} \left(1 - \left(\frac{\langle u \rangle}{U_\delta} \right)^2 \right) dy. \tag{7.8}$$

Pressure gradient and incipient separation result in a fast growth of the boundary-layer thicknesses, see Tab. D.5. We observe a very good agreement between experiment and simulation for δ_1, δ_2, and δ_3, see Fig. 7.13.

The different thickness measures are used to define non-dimensional parameters which characterize the shape variation of the mean velocity profile. The parameters H_{12} and H_{32}, see Fig. 7.14, are defined as the ratio of displacement thickness to momentum thickness

$$H_{12} = \frac{\delta_1}{\delta_2} \ , \tag{7.9}$$

and as the ratio of energy thickness to momentum thickness

$$H_{32} = \frac{\delta_3}{\delta_2} \ , \tag{7.10}$$

respectively. Near the inflow, H_{12} is around 1.5. The parameter H_{12} increases with incipient backflow and doubles its value before boundary-layer separation. H_{32} shows
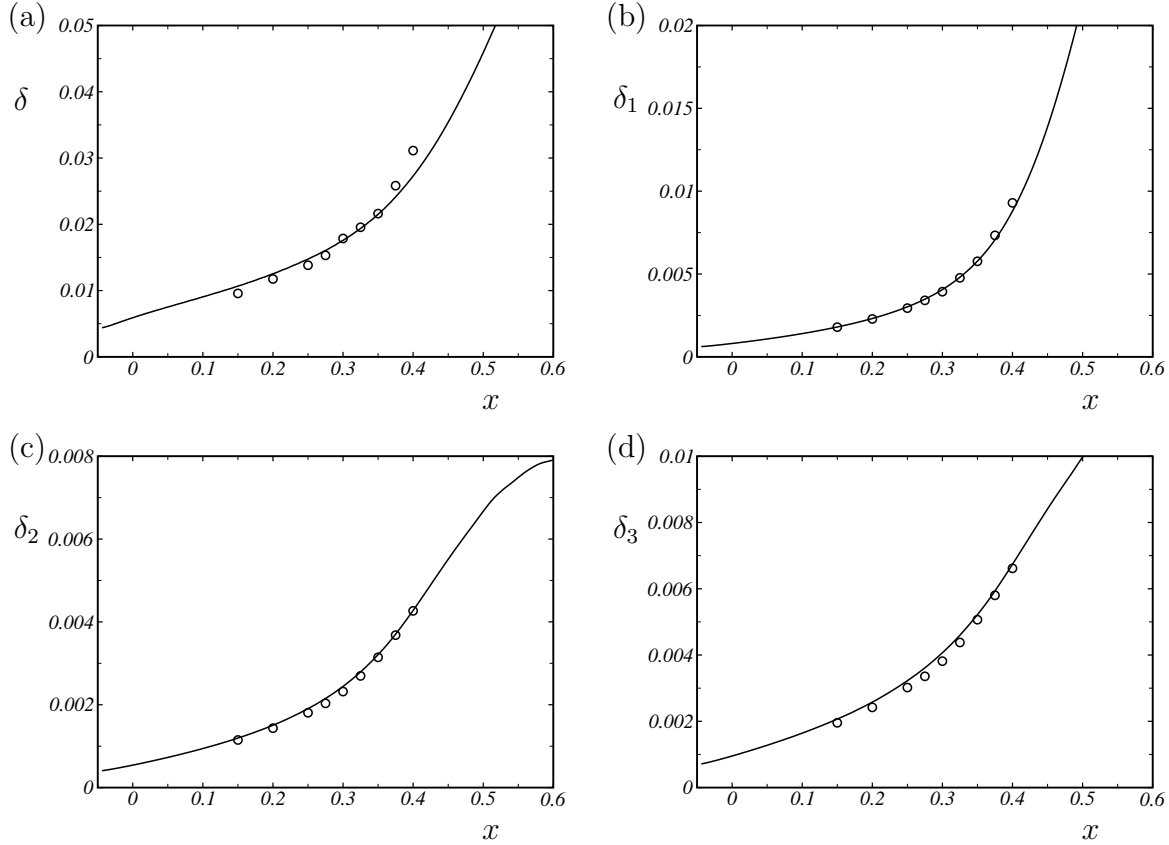
Figure 7.13: Integral measures for the boundary-layer thickness: (a) boundary-layer thickness, (b) displacement thickness, (c) momentum thickness, (d) energy thickness. ———— LES , ○ measurement.

a notable inflow transient, that might result from the fact that the pressure gradient adjusts rapidly behind the inflow boundary. After this transient, H_{32} decreases from about 1.75 to a minimum of about 1.5 at detachment. Simulation and experiment show essentially the same behavior, where the LES predicts slightly higher values for H_{32} and slightly lower values for H_{12} than those determined experimentally.

Dimensionless pressure-gradient parameters are frequently used to classify and to compare APG boundary-layer flows. Fig. 7.15 shows four widely used parameters, namely the CLAUSER pressure parameter [25]

$$\beta = \frac{\delta_1}{\rho U_\tau^2} \langle \partial_x p \rangle \, , \tag{7.11}$$

the PATEL pressure gradient [129]

$$\Delta_P = \frac{\nu}{\rho U_\tau^3} \langle \partial_x p \rangle \, , \tag{7.12}$$
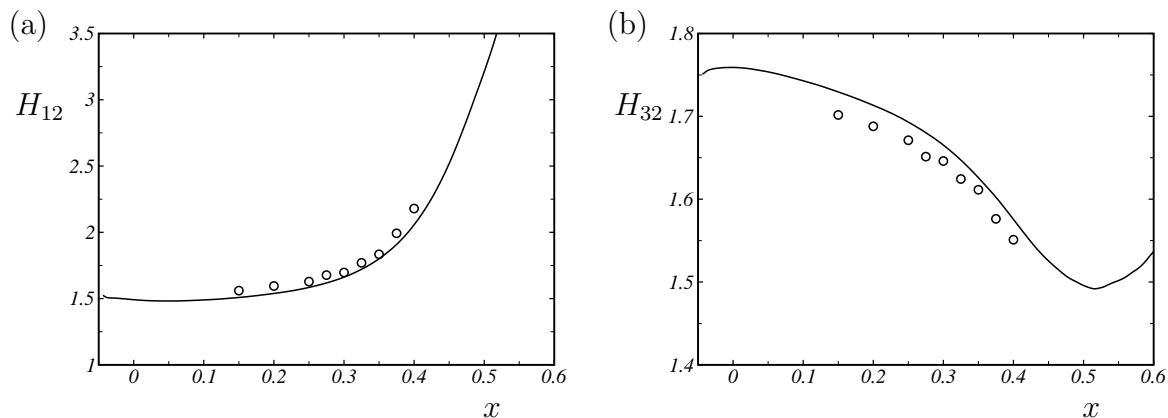
Figure 7.14: Shape parameters: (a) H_{12} displacement thickness to momentum-loss thickness, (b) H_{32} energy-loss thickness to momentum-loss thickness. —— present LES , ○ LDA measurement.

the pressure-gradient parameter of CASTILLO *et al.* [19, 20]

$$\Lambda_{\delta_2} = \frac{\delta_2}{\rho U_\delta^2 \partial_x \delta_2} \langle \partial_x p \rangle \, ,$$ (7.13)

and the acceleration parameter

$$K = \frac{\nu}{U_\delta^2} \langle \partial_x U_\delta \rangle \, .$$ (7.14)

The latter parameter has the advantage that it does not incorporate the pressure gradient and the wall-shear stress. By BERNOULLI's equation its link to the pressure gradient is

$$K = -\frac{\nu}{\rho \, U_\delta^3} \langle \partial_x p_\delta \rangle \, .$$ (7.15)

CLAUSER [25] proposed $\beta = const$ as criterion for determining the equilibrium similarity state of boundary layers with pressure gradient. The pressure-gradient parameter Δ_P was used by PATEL [129] for grading the severity of the pressure gradient as it affects PRESTON-tube measurements. In more recent analysis, CASTILLO and GEORGE [19] argued that rather a constant value of the pressure parameter

$$\Lambda = \frac{\delta}{\rho U_\delta^2 \partial_x \delta} \langle \partial_x p \rangle \, ,$$ (7.16)

is the necessary condition for equilibrium. CASTILLO *et al.* [20] found that $\Lambda_{\delta_2} \approx \Lambda$ has nearly the same value, $\Lambda_{\delta_2} = 0.21 \pm 0.01$, for most APG equilibrium boundary layers
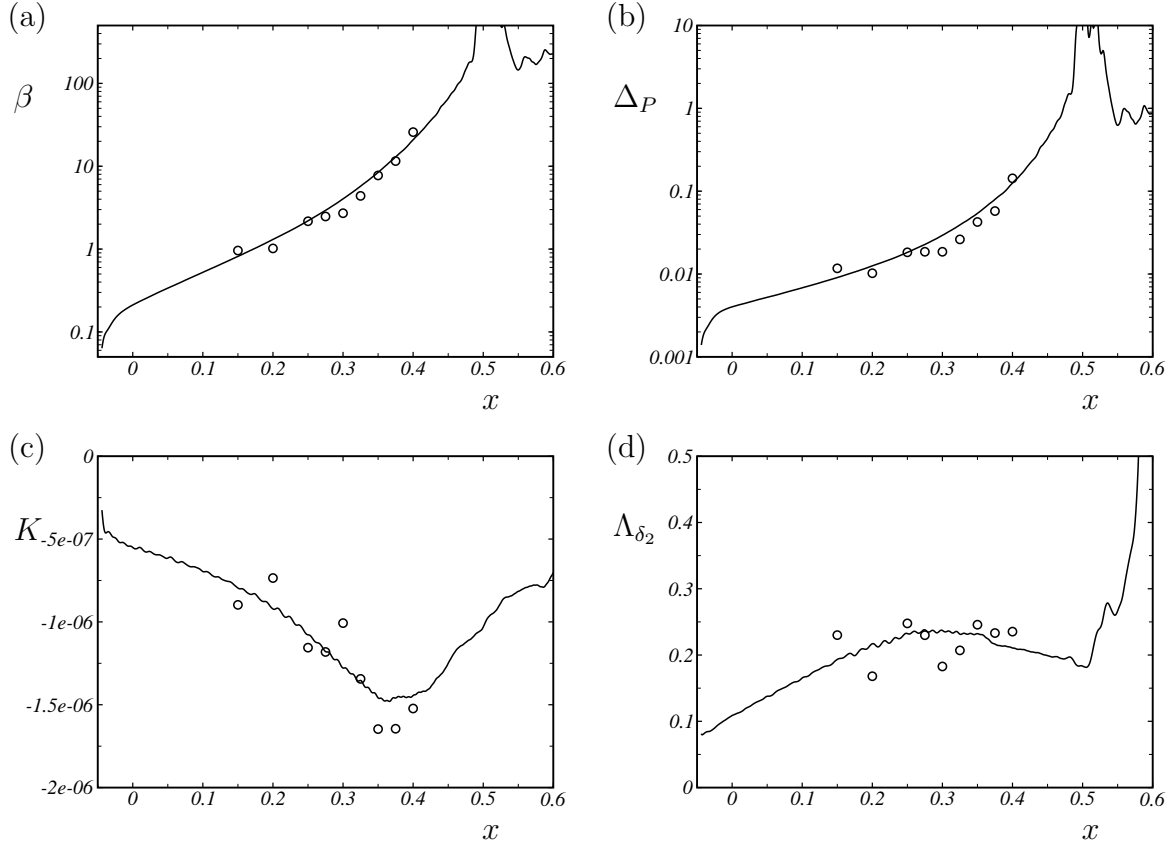
Figure 7.15: Pressure-gradient parameters (a) CLAUSER pressure-gradient parameter, (b) PATEL
pressure gradient, (c) dimensionless pressure-gradient parameter K, (d) dimensionless
pressure-gradient parameter Λ_{δ_2}. ———— present LES , ∘ experiment.

and that even separating boundary layers have a tendency to remain in an equilibrium
state. Following this result, most experimentally studied boundary layers are equilibrium
boundary layers. The boundary layer flow investigated in this work is in strong non-
equilibrium state under both the β criterion and the Λ_{δ_2} criterion, see Tab. D.5. The
parameter values computed from the LES and the experimental data agree well, see Fig.
7.15.

The characteristic velocity of the near-wall region is the wall-friction velocity $U_\tau = \sqrt{\nu|\langle\partial_y u\rangle|_{wall}}$. Fig. 7.16a shows the experimental wall-friction velocity and that of the
present LES. Some differences between LES and experiment are evident. They become
more visible for the local non-dimensional wall-friction coefficient $C_f = 2U_\tau^2/U_\delta^2$ shown
in Fig. 7.16b. We believe that these differences result mostly from uncertainties in the
experimental determination of the wall friction[3]. INDINGER used a PRESTON tube to
measure the dynamic pressure at the wall from which the wall-friction velocity U_τ was

---

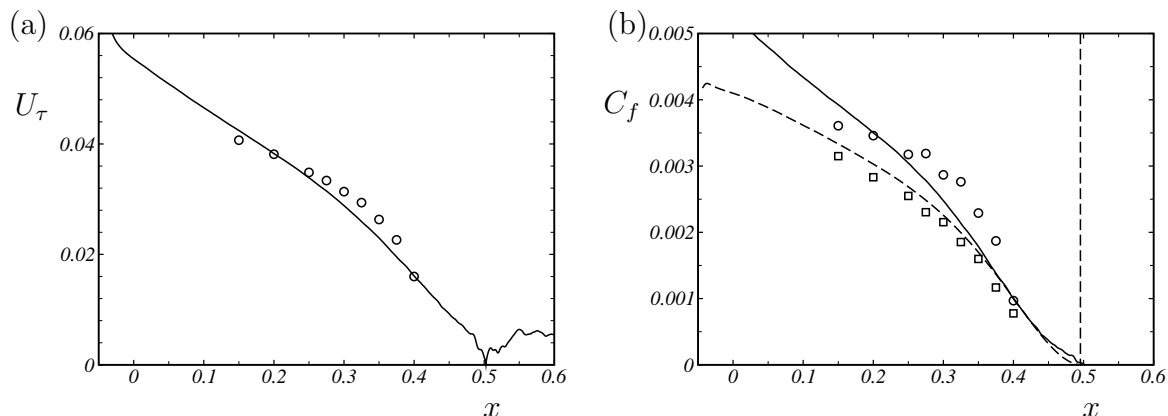[3] INDINGER, personal communication

Figure 7.16: (a) Wall-friction velocity U_τ ——— present LES, ∘ Preston-tube measurement. (b) Local wall-friction parameter C_f ——— from present LES, ∘ Preston-tube measurement, – – – – correlation of Fernholz [39] using LES data, □ correlation of Fernholz [39] using LDA measurements.

computed by means of tabulated calibration data of HEAD and RAM [59]. By construction, PRESTON-tube measurements are inaccurate for flow regions with instantaneous backflow, i.e. from ID onwards. Even for attached flow the accuracy is limited under the presence of strong pressure gradients [129].

This issue is now investigated more closely by using another means of computing C_f from experimental data. Following FERNHOLZ [39], the functional

$$C_f = 0.058 \lg \left(\left(\frac{8.05}{H_{12}} \right)^{1.818} \right)^{1.705} \text{Re}_{\delta_2}^{-0.268} \tag{7.17}$$

allows to approximate the local wall-friction coefficient from the non-dimensional integral parameters H_{12} (7.9) and Re_{δ_2} (7.20) which are less sensitive to measurement errors. In Fig. 7.16b this correlation is applied to both the experimental and the numerical data. A good agreement of simulation and experiment is observed. In the region with significant backflow, between ID and D, the correlation functional of FERNHOLZ [39] gives C_f almost identical to that computed from the wall-friction of the LES.

The viscous length scale $l^+ = \nu/U_\tau$ characterizes the size of the smallest coherent structures that occur close to the wall. An integral scale based on an defect formulation and the wall-friction velocity is the ROTTA-CLAUSER length

$$\Delta_{RC} = \int_0^\infty \frac{U_\delta - \langle u \rangle}{U_\tau} dy. \tag{7.18}$$
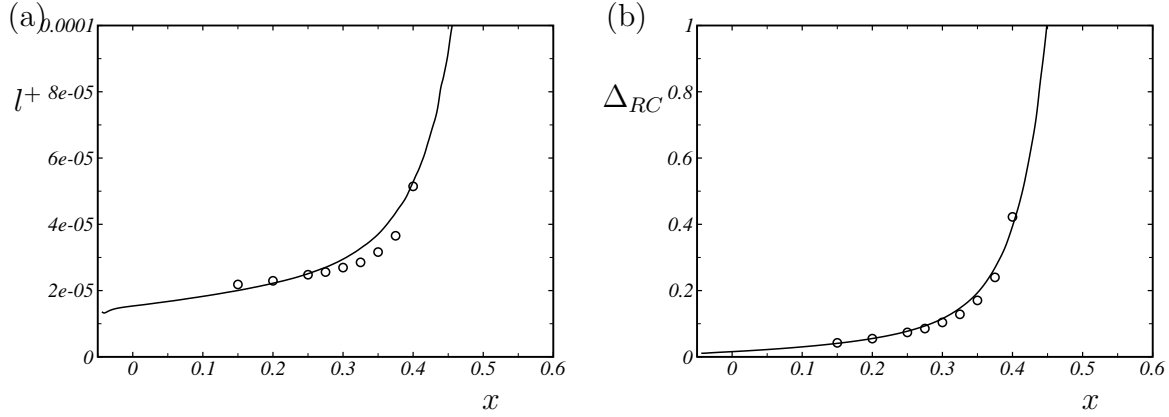
Figure 7.17: Length scales based on wall-friction for ———— present LES and for ∘ INDINGER's PRE-STON-tube measurement. (a) viscous length-scale. (b) ROTTA-CLAUSER length.

Graphs for both length scales are presented in Fig. 7.17 showing a good agreement between LES and experiment. Differences between LES and experiment can be attributed to the PRESTON-tube measurement of U_τ as mentioned before.

From the characteristic scales of the boundary layer various non-dimensional REYNOLDS numbers can be computed. Fig. 7.18 shows the displacement-thickness REYNOLDS number

$$\mathrm{Re}_{\delta_1} = \frac{U_\delta \delta_1}{\nu} \tag{7.19}$$

and the momentum-thickness REYNOLDS number

$$\mathrm{Re}_{\delta_2} = \frac{U_\delta \delta_2}{\nu} \ , \tag{7.20}$$

for experiment and computation, which are in good agreement.
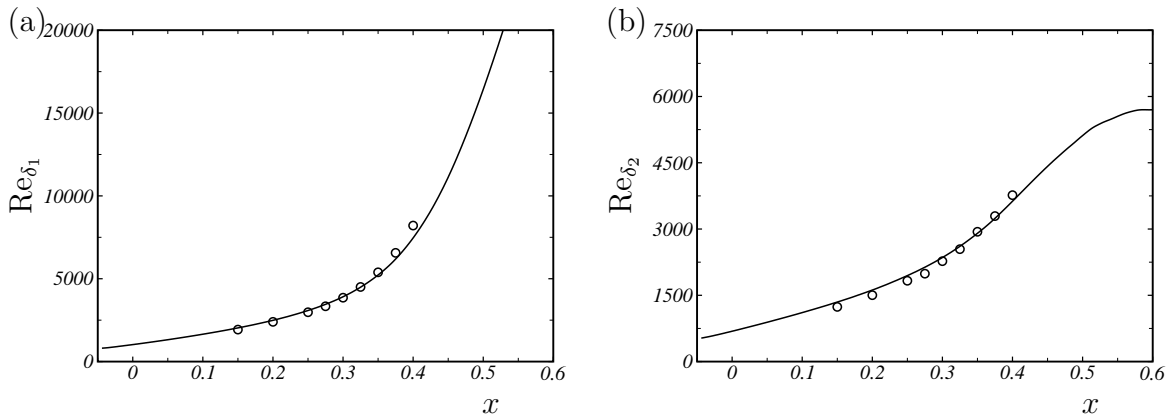
Figure 7.18: (a) REYNOLDS number based on momentum-loss thickness, (b) REYNOLDS number based on displacement thickness, and ———— present LES and ∘ LDA measurement.

Figure 7.19 shows mean velocity profiles at six downstream stations that are representative for APG turbulent boundary-layer flow approaching separation. Also shown are available measurements. The data are not normalized in order to allow for a direct and unbiased comparison of experimental and numerical results. The mean velocity profiles of the present LES are in excellent agreement with the experiment.

7.3.4 REYNOLDS Stress and Anisotropy Tensor

In addition to mean-velocity profiles, INDINGER provides second-order correlations of the streamwise velocity. LES and experiment compare well for the streamwise-normal component of the REYNOLDS-stress tensor, see Fig. 7.21. We observe a characteristic change of the shape of the REYNOLDS-stress profiles. With decreasing distance from separation the stress maximum associated with the buffer layer weakens and a new maximum is formed in the outer part. Contours of the turbulent kinetic energy and the REYNOLDS shear stress for the LES prediction are shown in Fig. 7.20.
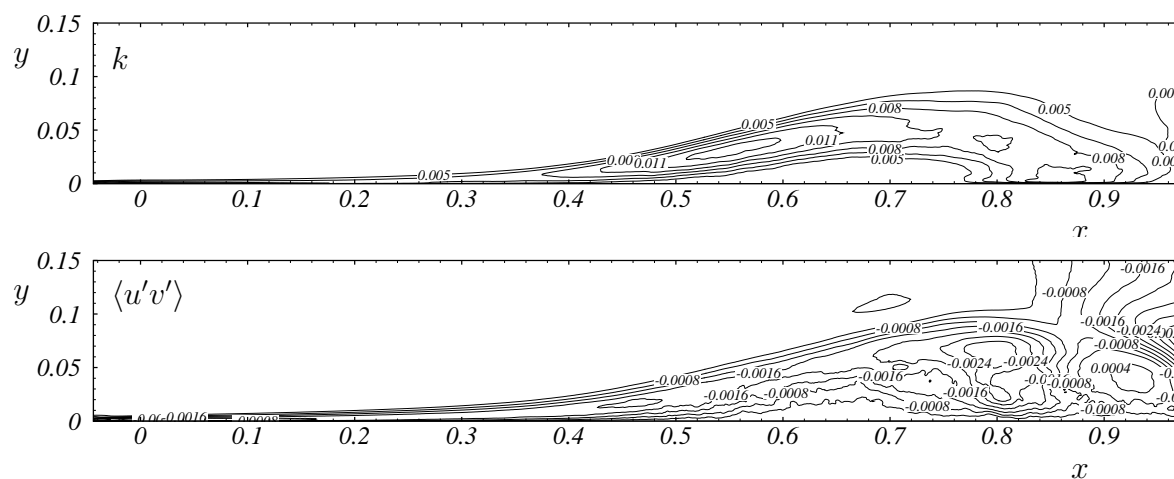

Figure 7.20: Contours of turbulence energy and mean REYNOLDS shear stress.

Both the simulation and the experiment show the same quantitative profiles and tendencies. After a perfect match at the first stations the experimental fluctuations are slightly lower than the prediction at the later stations. Noted that this finding is consistent with the fact that not only the LES but also the measured data are filtered. INDINGER [76], page 182 states $5.6 \cdot 10^{-4}$ for the spanwise extent of the LDA system's measurement volume, which corresponds to twice the LES filter width. Additional smoothing operations are involved in the analysis of the LDA data.
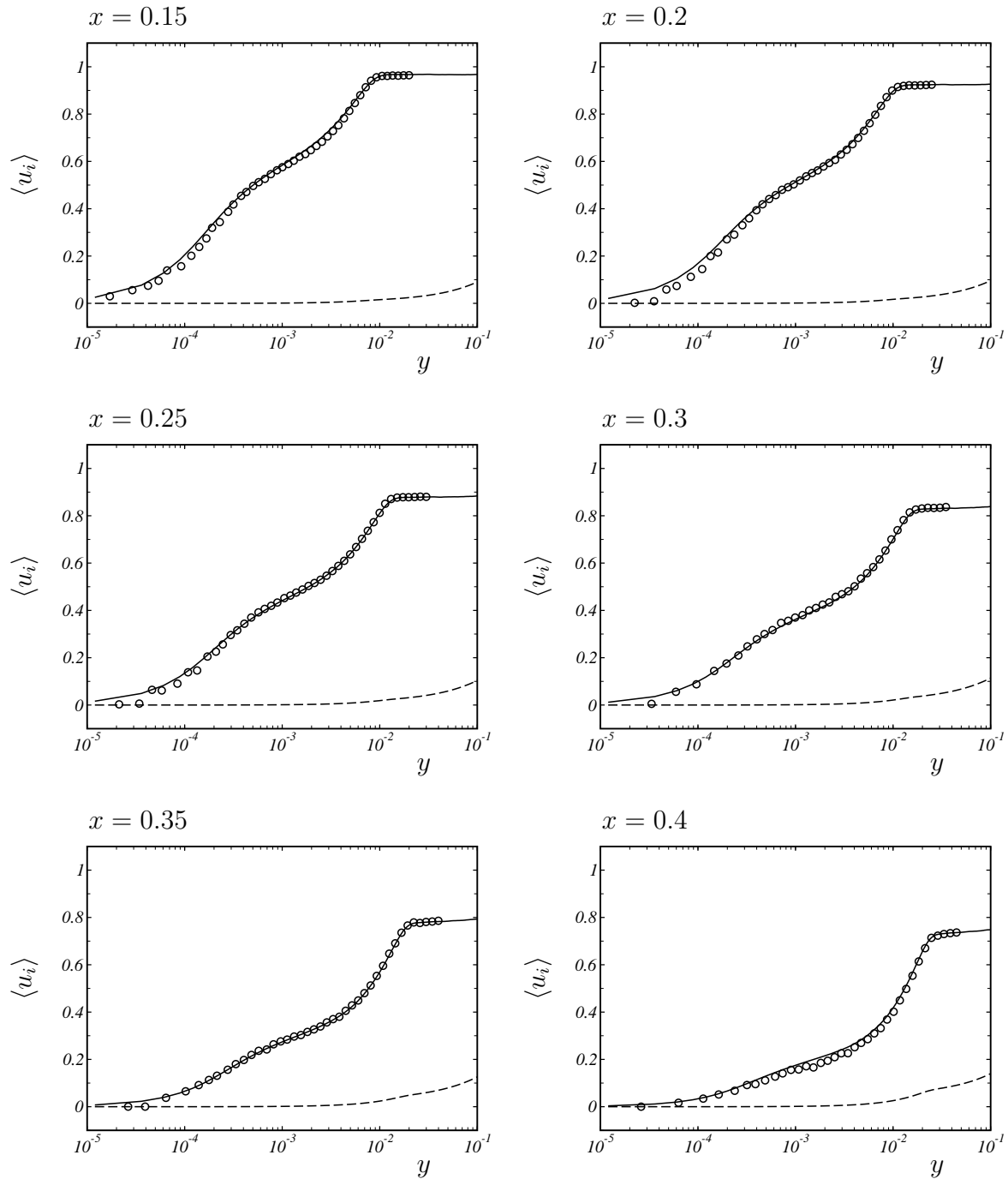
Figure 7.19: Mean velocity profiles (raw data) ———— $\langle u \rangle$ and – – – – $\langle v \rangle$ for LES, $\circ$ $\langle u \rangle$ for LDA.
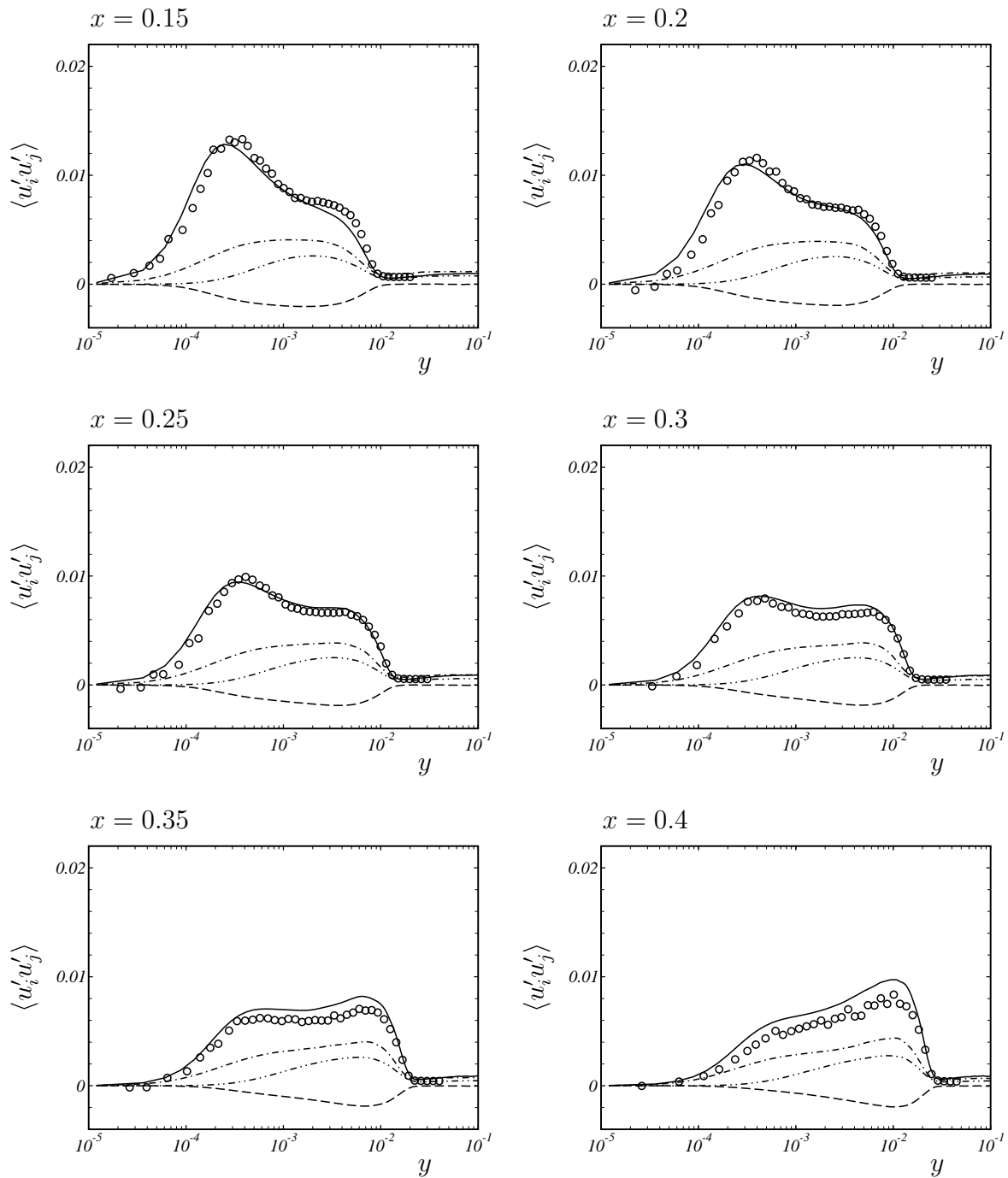
Figure 7.21: REYNOLDS stress tensor (raw data) ——— $\langle u'u' \rangle$, —·—·—·— $\langle v'v' \rangle$, ·—·—·— $\langle w'w' \rangle$, and ———— $\langle u'v' \rangle$ for LES, ∘ $\langle u'u' \rangle$ for LDA.

The traceless REYNOLDS stress anisotropy tensor is

$$a_{ij} = \frac{\langle u_i' u_j' \rangle}{\langle u_k' u_k' \rangle} - \frac{1}{3}\delta_{ij} \; , \tag{7.21}$$

where δ_{ij} is KRONECKER's delta. Following LUMLEY and NEWMAN [105] and LUMLEY [104], the local REYNOLDS-stress anisotropy can be characterized by the invariants

$$I_2 = -\frac{a_{ij}a_{ji}}{2} \tag{7.22a}$$

$$I_3 = \frac{a_{ij}a_{jk}a_{jk}}{3} \tag{7.22b}$$

of the anisotropy tensor. Note that for the first invariant immediately follows $I_1 = a_{ii} \equiv 0$ from definition (7.21). Typical anisotropy states correspond to certain regions in the $(I_3,\ I_2)$ plane, the so-called anisotropy-invariant map. Isotropic turbulence corresponds to $(0,\ 0)$. Axisymmetric two-component turbulence is found at $(-1/108,\ -1/12)$ and perfect one-component turbulence corresponds to $(2/27,\ -1/3)$. All realizable states of turbulence are found within a triangular region, the LUMLEY triangle, spanned by these three limits. The thin dashed lines in Fig. 7.23 denote the edges of the physically realistic region which are given by the states of axisymmetric turbulence $|I_3/2|^{1/3} = (-I_2/3)^{1/2}$ (where $I_3 < 0$ corresponds to axisymmetric contraction and $I_3 > 0$ to axisymmetric expansion) and by the two-component state $1/9 + I_2 + 3I_3 = 0$.

Non-zero components of a_{ij} are shown in Fig. 7.22. We study the anisotropy state at four stations of attached flow, at separation, and at one station for detached flow. The curves are very similar. In the logarithmic layer of attached flow we find a plateau with $a_{11} = 0.2\ldots0.3$, $a_{22} = -0.15\ldots-0.2$, $a_{33} = -0.03\ldots-0.06$, and $a_{12} = 0.12\ldots-0.15$. a_{11} shows a peak with amplitudes up to ≈ 0.5 near the wall. This peak disappears at separation but develops again within the separated flow region. Although isotropic fluctuations were induced at the inflow plane, the free-stream turbulence is not isotropic due to the deceleration trough the pressure gradient and due to the unsteady forcing by the separation bubble. Nevertheless, the REYNOLDS stresses develop towards an isotropic state at the boundary layer edge. The invariant maps, Fig. 7.23, show clear differences between the anisotropy state of attached flow and of flow being about to separate. However, the paths of the anisotropy state with increasing wall distance show a common pattern for the considered stations. All paths start with two-component turbulence at the wall and then move along the upper bound towards the one-component state. Within the buffer layer the paths turn and follow the line of axisymmetric expansion towards isotropic turbulence. A kink is observed in the log layer, where all components of a_{ij} exhibit a plateau. All paths end close to the isotropic state.
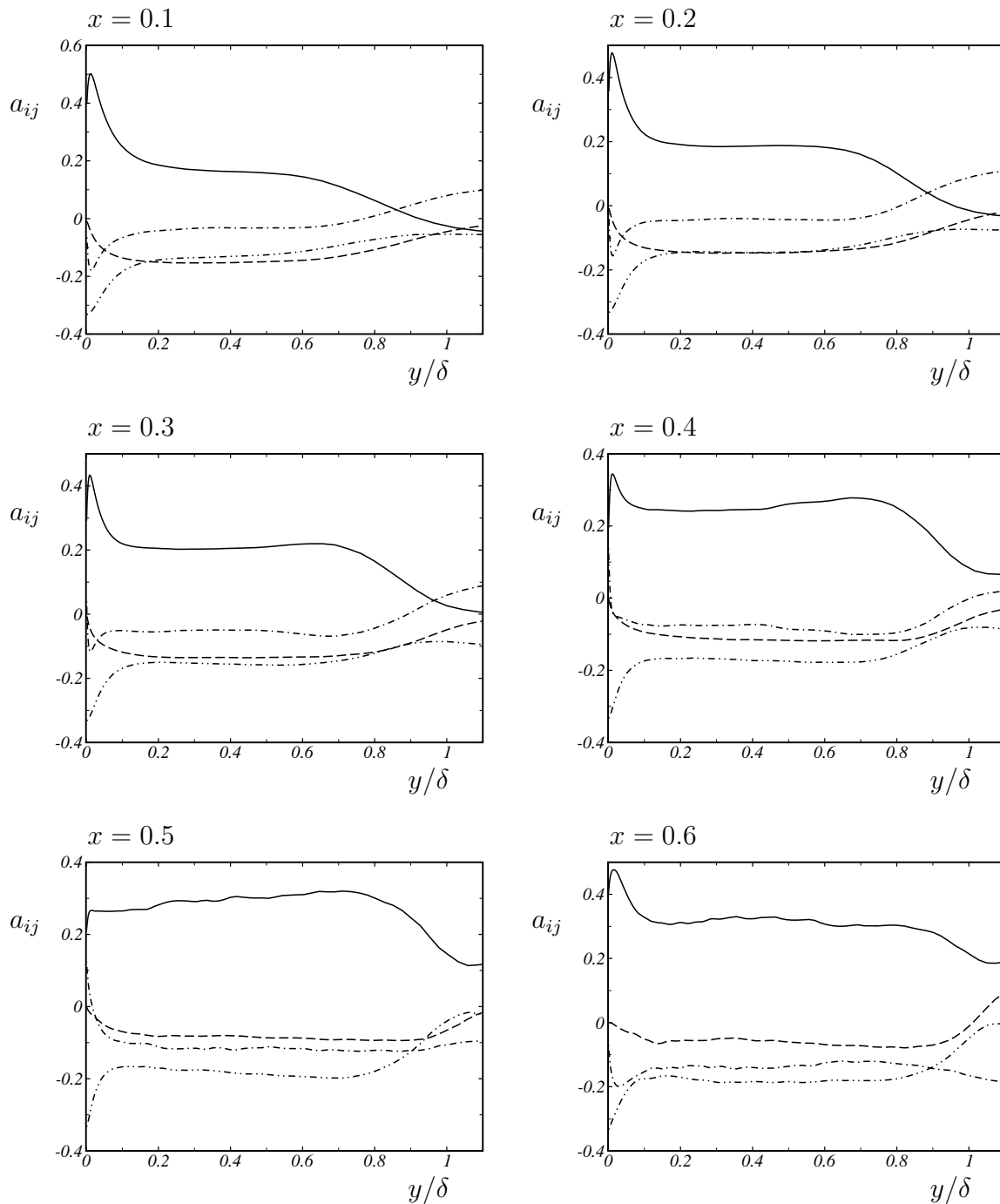
Figure 7.22: Components of the REYNOLDS stress anisotropy tensor ——— a_{11}, —·—··—·— a_{22}, ·—·—·— a_{33}, ———— a_{12}.
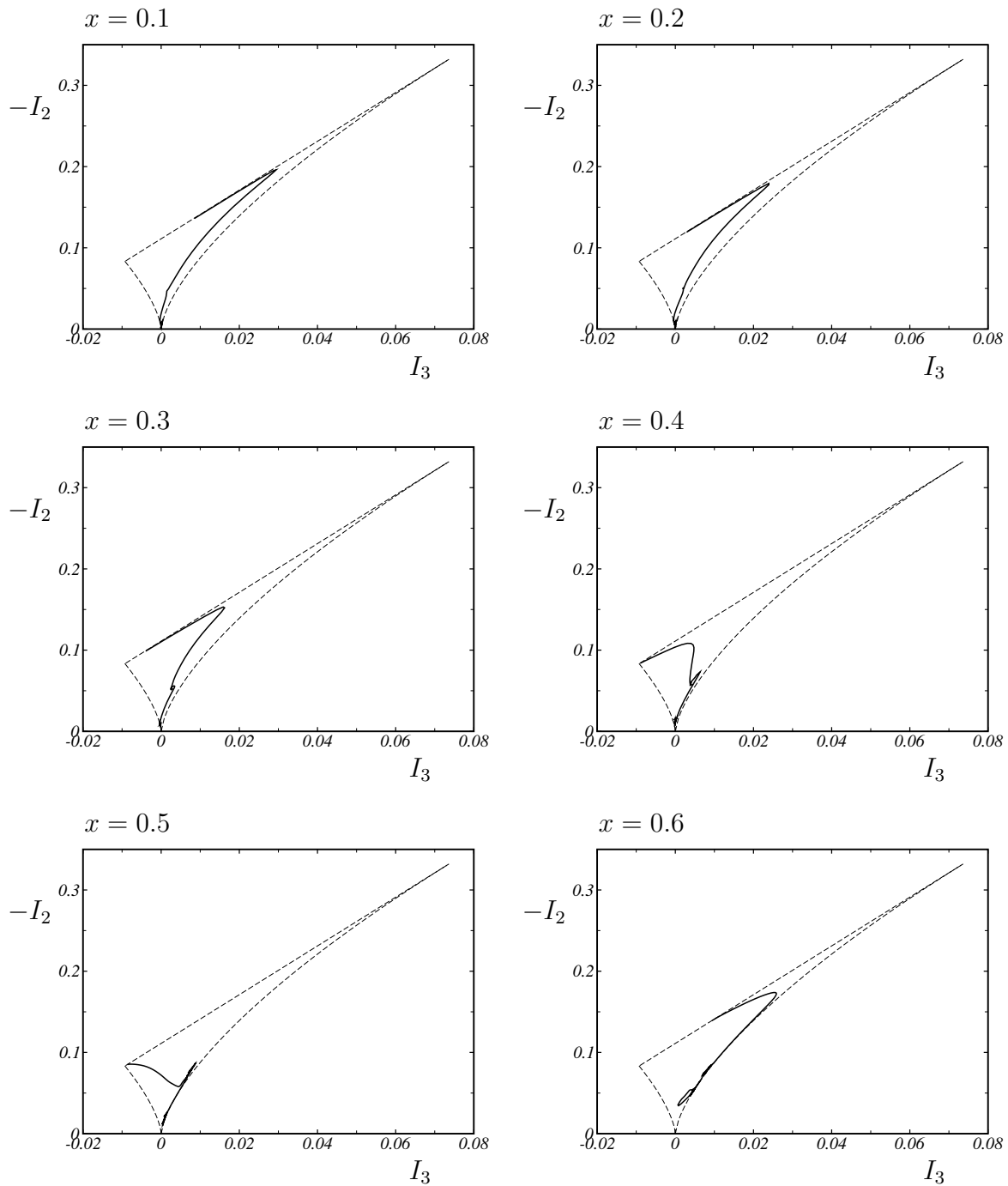
Figure 7.23: LUMLEY's invariant maps for the REYNOLDS stress anisotropy tensor. Turbulence can occur only within the − − − − triangular region.

7.3.5 Skewness and Kurtosis

INDINGER has sampled sufficiently large data sets so as to allow for the computation of higher-order statistics of the streamwise velocity. We present experimental and numerical results for skewness

$$\gamma_1 = \frac{\langle u'^3 \rangle}{\langle u'u' \rangle^{3/2}} \tag{7.23}$$

and excess kurtosis

$$\gamma_2 = \frac{\langle u'^4 \rangle}{\langle u'u' \rangle^2} - 3 \tag{7.24}$$

in Fig. 7.24 and in Fig. 7.25, respectively. Despite some scatter near the wall and some spurious data points at the later stations, an excellent match is observed between experiment and LES.

The turbulence is not exactly but close to GAUSSian in the log layer, whereas pronounced non-GAUSSian statistics are found in the laminar sublayer and in the wake region. From this we may conclude that the flow is in an equilibrium-turbulence state in the log layer and in the free stream, whereas non-equilibrium dominates the near wall region and the outermost part of the boundary layer.

For the streamwise component a constant wall-asymptotic value of $\gamma_1(u) \approx 1.25$ is found for all stations $0.15 \leq x \leq 0.4$. Characteristic excursions to the opposite sign (with respect to the wall asymptote) are observed at the boundary layer edge. As expected, the skewness of the spanwise velocity w is zero. The skewness of the wall-normal velocity is approximately proportional to that of the streamwise component with opposite sign. At the wall, $\gamma_1(v)$ is in the range of $0.35 \ldots 0.7$. For all components the wall asymptotes agree well with the expectation for ZPG wall-bounded turbulence based on DNS and experiments, see KIM *et al.* [87], e.g.. We conclude that the pressure gradient's influence on the skewness is relatively small.

The excess kurtosis is essentially positive for all velocity components within the boundary layer. Only the streamwise component shows slightly negative values for the logarithmic layer where the other components tend to the GAUSSian value $\gamma_2 = 0$. Sharply rising cusps are found at the boundary layer edge, the peak is strongest for $\gamma_2(u)$. We note that the magnitude of this peak is very sensitive and may change if more samples were taken. The wall-asymptotic value of the streamwise component is $\gamma_2(u) \approx 3.8$ at $x = 0.15$ and rises to about $\gamma_2(u) \approx 4.3$ at $x = 0.4$. The kurtosis of w is always positive and follows about the same trends as that of u.
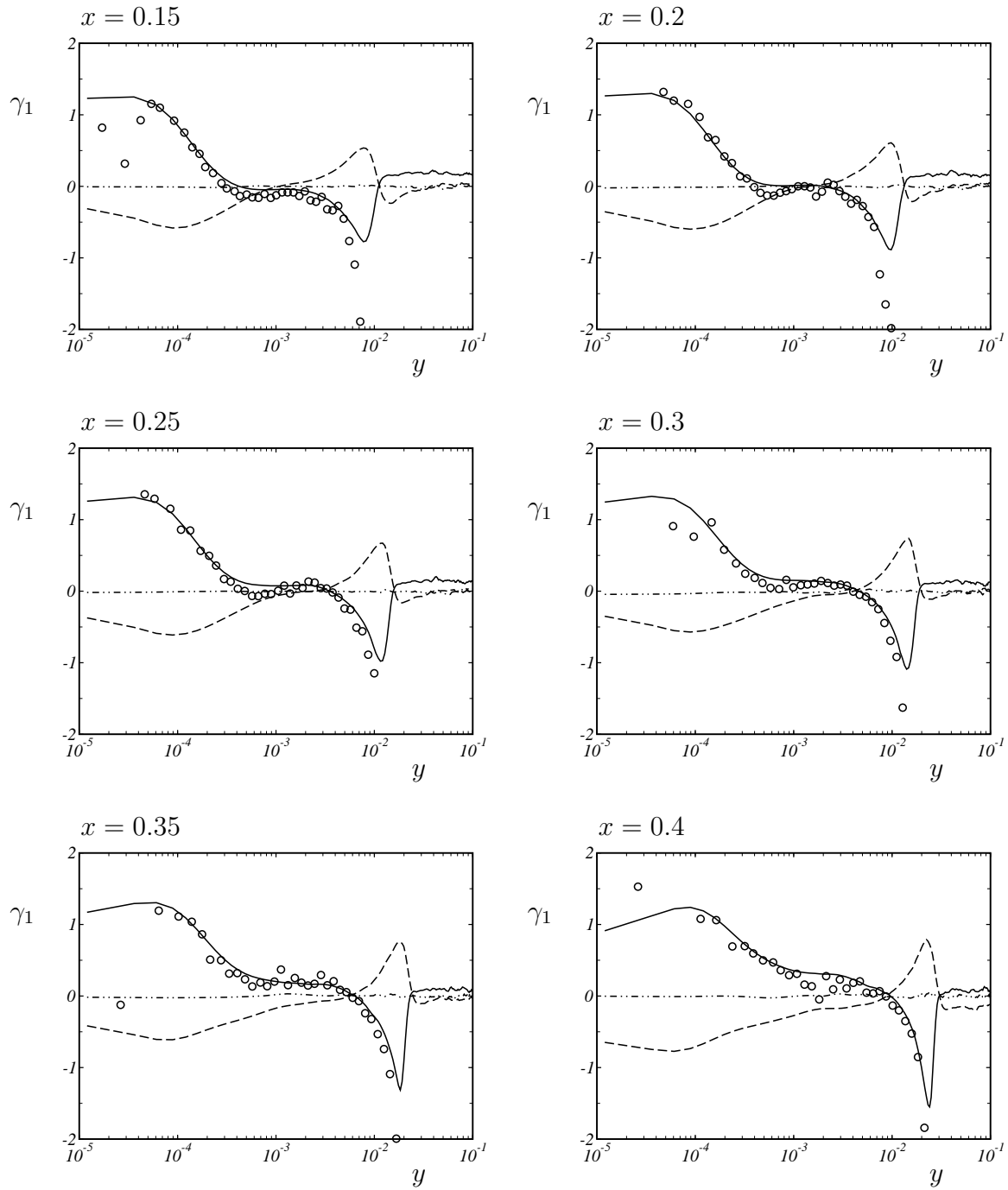
Figure 7.24: Skewness: ——— streamwise, – – – – wall-normal, and —··—··— spanwise component
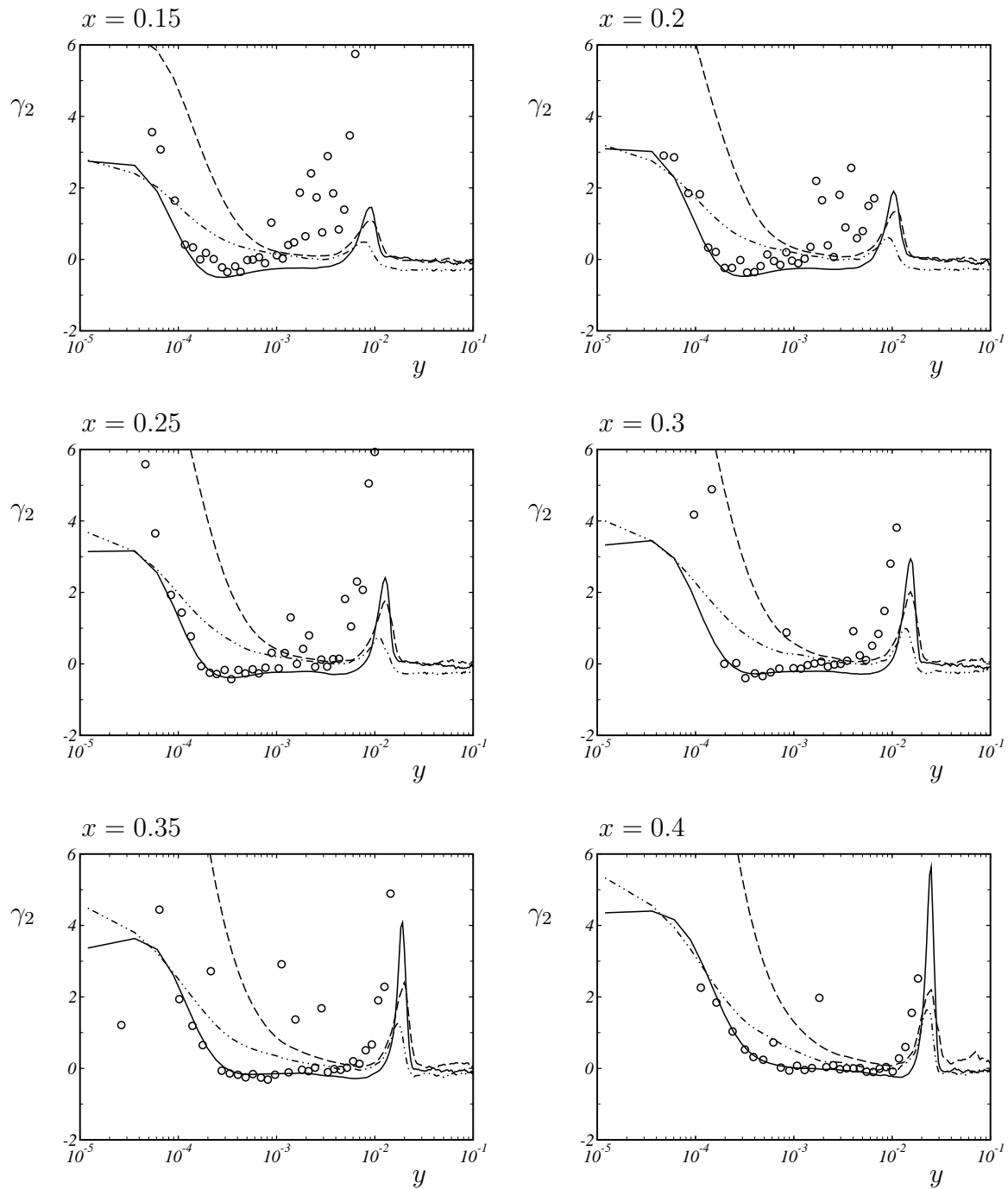for LES. ∘ streamwise component for LDA.

Figure 7.25: Excess kurtosis: ———— streamwise, ———— wall-normal, and —··—··— spanwise component for LES. ○ streamwise component for LDA.

The wall-normal component, however, shows a steep rise towards the wall. The wall asymptotic value reaches $\gamma_2(v) \approx 6.5$ at $x = 0.15$ and $\gamma_2(v) \approx 27$ at $x = 0.4$. A similar behavior of the wall-normal kurtosis was reported for DNS of ZPG turbulence. KIM *et al.* [87], for example, found values of $\gamma_2(v) = 19$ in the viscous sublayer of turbulent channel flow at low REYNOLDS number. In contrast, most experiments indicate a maximum of $\gamma_2(v)$ in the buffer layer and a decrease towards the GAUSSian value as the wall is approached. LYONS *et al.* [107] argue that this frequently observed discrepancy is caused by filter operations involved in the analysis of measurement data. A detailed analysis by XU *et al.* [183] corroborated this hypothesis. They found that high values of the wall-normal kurtosis result from characteristic spikes with large negative values in the time series of v. These events are associated with exceptionally strong sweeps that are very rare in space and time.

7.3.6 Scaling Laws for the Mean Velocity Profile

Scaling in inner coordinates

Present LES and experimental results show consistently that the mean velocity profile can no longer be described by the classical log law alone. Figure 7.3.6 shows mean velocity profiles from LES in inner scaling with the friction velocity U_τ and viscous length scale l^+. The scaled velocity profiles do not collapse in the wake region and the classical log region is shortened.
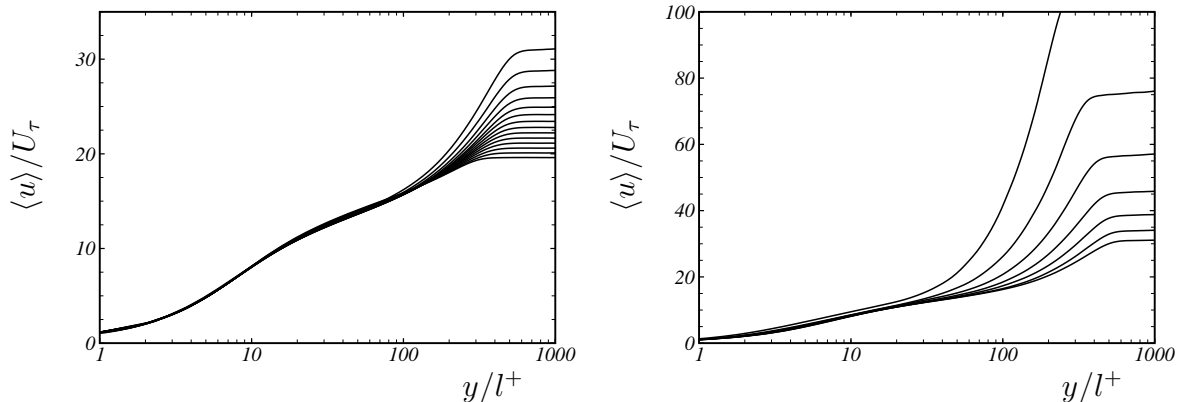

Figure 7.26: Classical inner scaling tested for mean velocity profiles for LES of attached, decelerated boundary layer flow. *Left:* with negligible backflow; *Right:* approaching separation $0.1 \leq \chi \leq 0.5$.

INDINGER *et al.* [77] claimed also that the log region is affected by the pressure gradient and reasoned that the failure of the classical inner scaling coincides with the first

occurrence of instantaneous reverse flow. Indeed, the experimental data, see Fig. 7.3.6, shows a systematic downshift of the log layer with increasing reverse-flow frequency.
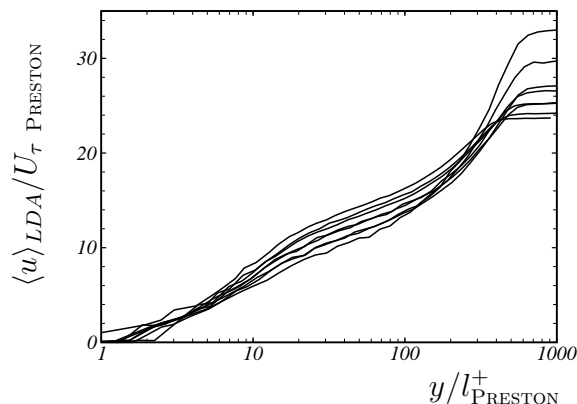

Figure 7.27: Experimental data in inner coordinates with wall-friction measured by PRESTON tube.

The present LES, however, reveals that inner scaling remains valid even for substantial backflow and *intermittent transitory detachment*, see Fig. 7.3.6. The inner scaling is valid up to the point where the wall-friction velocity becomes smaller than twice the value of SIMPSON's [157] velocity scale

$$U_p = \left(\frac{\nu}{\rho}|\partial_x p|\right)^{1/3} \tag{7.25}$$

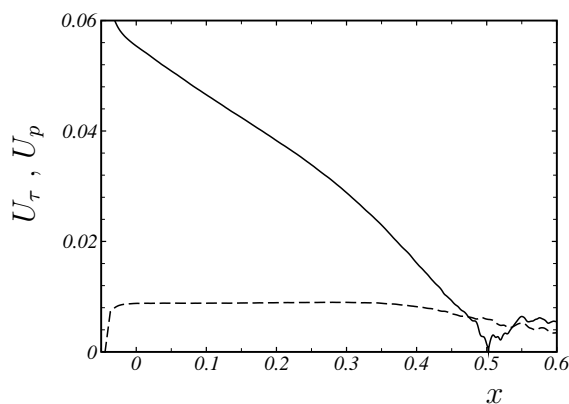based on the pressure gradient, see Fig. 7.28. This mismatch between experiment and

Figure 7.28: Friction velocity ——— U_τ compared to pressure-gradient velocity scale ———— U_p.

LES is attributed to the PRESTON-tube measurement technique used for determining the wall-shear stress. A small systematic difference in the determined wall friction can lead to the observed trend of the logarithmic law. Evidence is provided in Fig. 7.29 where

the experimental velocity profiles are normalized with the numerical prediction for the wall-shear stress at the respective positions. We find that now also the experimental data support the inner scaling for the entire range.
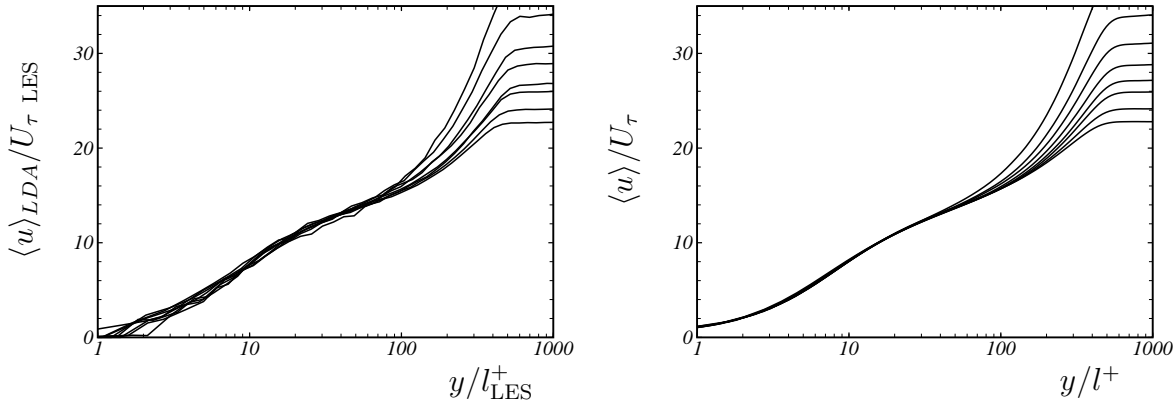

Figure 7.29: *Left:* Experimental velocity profiles scaled with wall-friction from LES. *Right:* Numerical velocity profiles for identical positions.

Other approaches to scalings in inner coordinates [11, 110, e.g.] showed no improvement over the classical scaling with U_τ and l^+ for the wall near region of attached APG boundary-layer flow with moderate reverse flow frequency.

Scaling in mixed and outer coordinates

The classical approach to scaling in outer coordinates based on U_δ and δ does not give satisfactory results for our boundary layer data, see Fig. 7.30. In order to improve on this, VON KÁRMÁN [177] proposed a defect form for the mean velocity and a mixed scaling based on the friction velocity and the boundary layer thickness. As a variant of VON KÁRMÁN's scaling, the ROTTA-CLAUSER length (7.18) can be used for scaling the wall distance. Both scalings have been developed for ZPG boundary layers. The application to the present case shows that neither the original nor the modified VON KÁRMÁN scaling reproduce pressure-gradient effects correctly, see Figures 7.31 and 7.32.

ZAGAROLA and SMITS [187] found that velocity profiles of ZPG turbulent pipe flow approximately coincide if they are scaled in a defect form with the velocity scale $U_\delta \delta_1/\delta$. This scaling leads to a reasonable collapse of the velocity profiles of the present APG boundary layer. The region for which good agreement is observed covers almost 90 percent of the boundary layer thickness, see Fig. 7.33. To our surprise the collapse is even better for the later stations with frequent flow reversal.
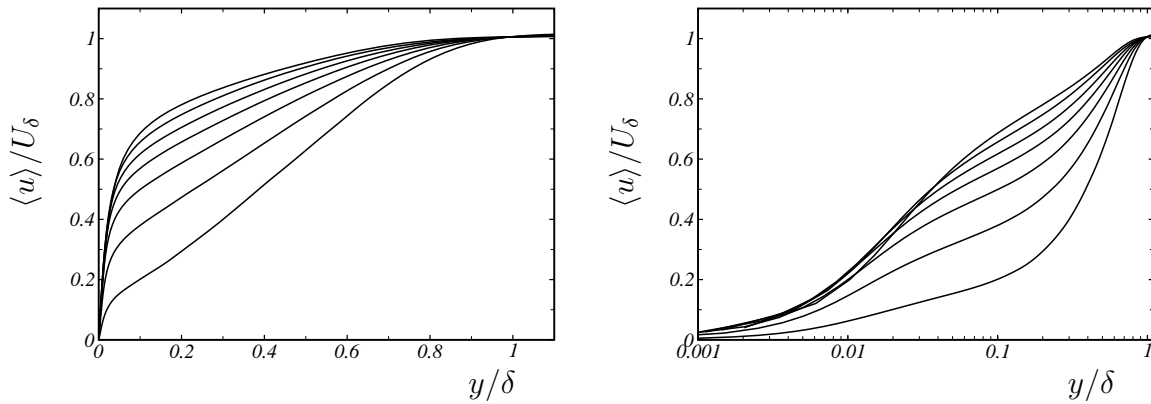
Figure 7.30: Classical outer scaling tested for mean velocity profiles of attached, decelerated boundary layer flow. *Left:* linear plot; *Right:* semi-logarithmic plot.

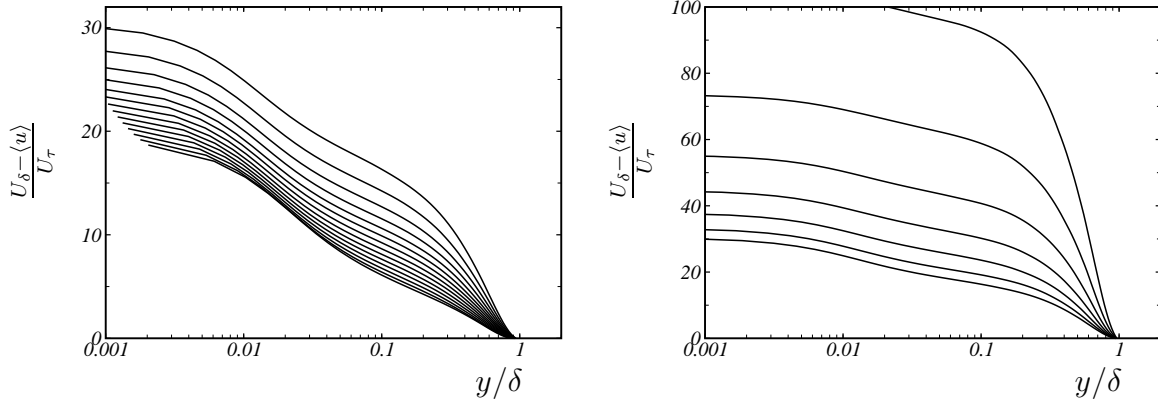**Figure 7.31:** VON KÁRMÁN scaling [177] tested for mean velocity profiles of attached, decelerated boundary layer flow. *Left:* profiles for negligible backflow; *Right:* approaching separation $0.1 \leq \chi \leq 0.5$.

Figure 7.32: Modified VON KÁRMÁN scaling based on the ROTTA-CLAUSER length. *Left:* profiles for negligible backflow; *Right:* approaching separation $0.1 \leq \chi \leq 0.5$.

Figure 7.33: ZARAGOLA-SMITS scaling tested for mean velocity profiles of attached, decelerated boundary layer flow. *Left:* profiles for negligible backflow; *Right:* approaching separation $0.1 \leq \chi \leq 0.5$.
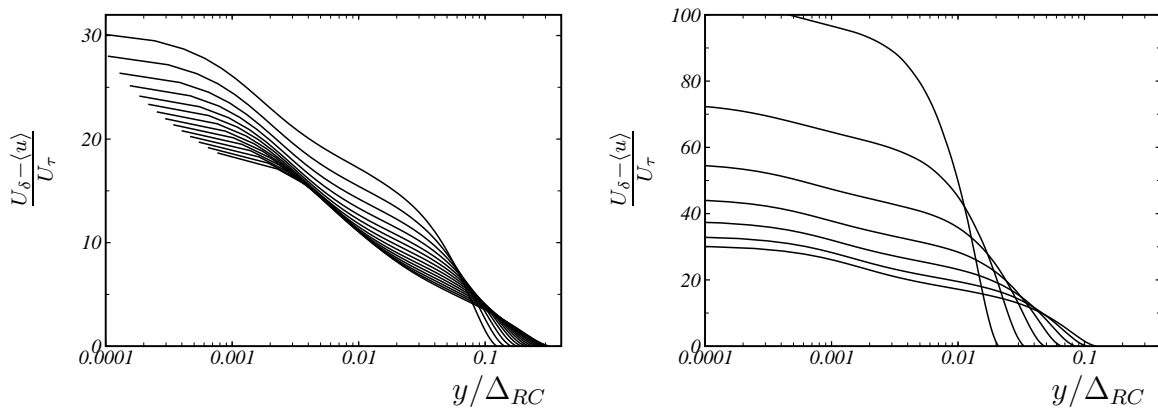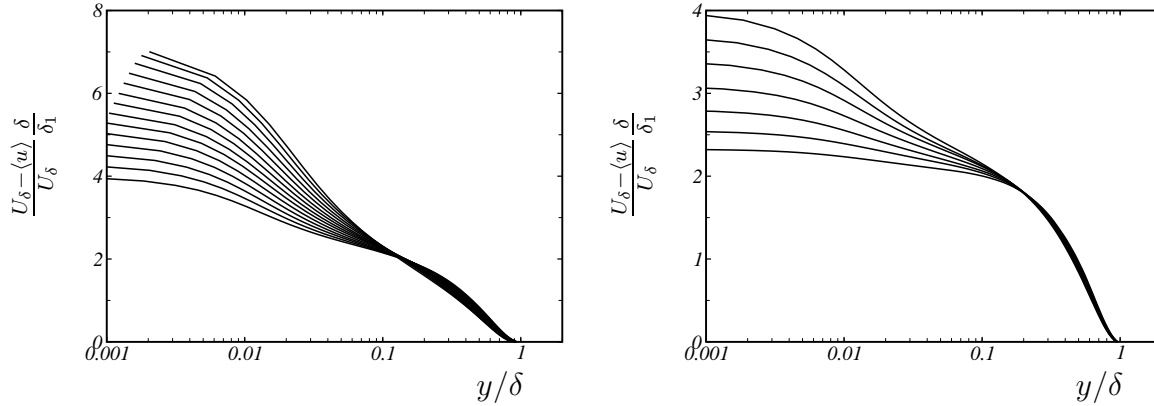
7.4 Summary

We have presented well resolved LES of an incompressible fully-turbulent flat-plate boundary layer subjected to a constant adverse pressure gradient. The APG leads to a streamwise increasing fraction of back-flow events that eventually results in strong boundary-layer separation. REYNOLDS number and pressure-gradient parameters are adapted to measurements conducted by INDINGER *et al.* [76–78] in a closed-circuit water tunnel. The computational results are discussed in detail and validated against experimental data. Experimental and numerical flow data agree very well thus confirming both the quality of the experimental setup (spanwise homogeneity, e.g.) and the applicability of our LES methodology.

Conclusions are drawn concerning the scaling of the mean velocity profile of turbulent boundary-layer flow under non-equilibrium conditions in the vicinity of pressure-induced separation. The present LES and the experimental results show consistently that the mean velocity profile can no longer be described by the classical log law. However, while INDINGER found that the failure of inner scaling coincides with the very first occurrence of instantaneous reverse flow, the present numerical study reveals that inner scaling and the logarithmic law of the wall remain valid. This mismatch between experiment and LES is traced back to the PRESTON-tube measurement technique that was used to determine the wall-shear stress experimentally. The agreement with the LES improves significantly when the numerically predicted wall-shear stress is used for determining the scaling parameters of the experimental velocity profiles. Our results suggest that inner scaling is valid even under strong adverse pressure gradients if the wall-friction

velocity is larger than SIMPSON's velocity scale based on the pressure gradient and that the outer scaling of ZAGAROLA and SMITS [187] is valid for $0.1\delta < y \leq \delta$. The latter finding is consistent with experimental results of INDINGER *et al.* [77].

The main objective of this work is SGS-model development and validation. For this reason, results of a physical flow analysis are not discussed in depth. The reader is encouraged to refer to Appendix D of this work, where supplementary data are presented.

CONCLUSION

Further development of large-eddy simulation faces a major obstacle in the strong coupling between subgrid-scale modeling and the truncation error of the numerical discretization. SGS models generally operate on scales that are marginally resolved by the underlying numerical method. This mutual interference can have large and generally unpredictable effects on the accuracy of the solution. On the other hand, one can exploit this link by developing discretization methods from subgrid-scale models, or vice versa. Approaches where SGS models and numerical discretizations are fully merged are called implicit LES.

Previous approaches to implicit SGS modeling relied on the application of preexisting discretization schemes to fluid-flow turbulence. Consequently methods with suitable implicit SGS model were usually found by trial and error, which had frequently led to the belief that an implicit subgrid-scale model is merely inferred by the choice of discretization. Comparative studies have shown that stabilizing under-resolved simulations by upwind or non-oscillatory schemes is insufficient for accurately representing SGS turbulence. Employing implicit LES for prediction requires numerical methods that are specially designed, optimized, and validated for the particular differential equation to be solved. A full coupling of SGS model and discretization scheme cannot be achieved without incorporating physical reasoning into the design of the implicit SGS model.

The starting point of this work was to improve on these modeling uncertainties by exploring how implicit subgrid-scale models can be derived systematically. A procedure for design, analysis, and optimization of nonlinear discretization schemes for implicit LES was proposed: First, a general non-linear discretization scheme with yet undetermined but adjustable truncation error is to be designed. The resulting method should be as simple as possible to facilitate computation at reasonable cost, but as complex as necessary to allow for implicit modeling. In a second step, this general method is analyzed with respect to its implicit SGS modeling capabilities. This is accomplished by the identification and modification of discretization parameters inherent to the discretization scheme. Finally, appropriate values of the discretization parameters have to be determined in such a way that the truncation error of the method acts as a physical SGS model.

This procedure has then been applied in the development of a novel nonlinear discretization for implicit LES. Implicit SGS modeling has been carried out for several canonical situations including isotropic turbulence, wall-bounded flows, and passive-scalar mixing.

A suitable environment for the discretization design was provided by SCHUMANN's concept of a finite-volume method. Finite-volume discretizations involve averaging and reconstruction steps that are related to filtering and deconvolution well known in explicit SGS modeling. The numerical truncation error of finite-volume methods readily appears as a divergence of a tensor which is advantageous with respect to physically motivated implicit modeling. Explicit deconvolution-type SGS models so far had been limited to linear deconvolution. By employing methods that are well established for essentially non-oscillatory finite-volume discretizations, the concept of approximate deconvolution was extended to the solution-adaptive nonlinear case: With the new method a local reconstruction of the unfiltered solution is obtained from a solution-adaptive combination of HARTEN-type deconvolution polynomials. Deconvolution is regularized by limiting the degree k of local approximation polynomials to $k \leq K$ and by permitting all polynomials of degree $1 \leq k \leq K$ to contribute to the approximately deconvolved solution. Adaptivity of the deconvolution operator is achieved by dynamically weighing the respective contributions. A suitable consistent numerical flux function operating on the approximately deconvolved solution provides secondary regularization. The solution-adaptive stencil-selection scheme and the numerical flux function contain free parameters which can be used to adjust the spatial truncation error of the discretization. The resulting method which we refer to as the adaptive local deconvolution method, ALDM for short, represents a full merging of numerical discretization and SGS model. Incorporating the essential elements of LES, filtering and deconvolution, the implicit model of ALDM combines an implicit tensor-dissipation regularization with a generalized scale-similarity approach.

In classical numerical analysis, the truncation error is analyzed in the limit of small grid size compared to the smallest flow scale, and discretization coefficients are chosen in such a way that the formal order of accuracy of the discretization is maximum. In LES the chosen grid size essentially defines the smallest represented physical scale. At a finite grid size, the numerical truncation errors interfere with the subgrid-scale model. In particular for implicit LES, numerical discretization and turbulence model are indistinguishable. Unlike with high-order shock-capturing schemes, such as the WENO method where one tries to maximize the formal order of accuracy for smooth solutions, free parameters of ALDM were selected in such a way that the truncation error of the discretization functions as physically motivated SGS model. For the purpose of finding suitable discretization parameters the modified differential equation of the discretization

method was analyzed by measuring the spectral numerical dissipation in numerical simulations of freely decaying homogeneous isotropic turbulence. This *a posteriori* analysis followed from the hypothesis that the primary purpose of an SGS model is to provide the correct spectral distribution of the dissipation of resolved scales by interactions with modeled SGS stresses. A semi-analytical expression for the eddy-viscosity spectrum of isotropic turbulence at high Reynolds numbers has been provided by CHOLLET and LESIEUR based on the eddy-damped quasi-normal MARKOVian (EDQNM) theory. A robust automatic optimization procedure based on an evolutionary approach was then used for minimizing a functional that measures the difference between the spectral numerical viscosity of ALDM and the eddy viscosity from EDQNM. With the optimized discretization parameters the numerical viscosity matches the theoretical requirements of EDQNM when isotropic turbulence at high Reynolds numbers is considered. The normalized eddy-viscosity spectrum of ALDM exhibits a low-wavenumber plateau at the correct level and reproduces the typical cusp shape up to the cutoff wavenumber at the correct magnitude. Note that the CHOLLET–LESIEUR eddy viscosity is not enforced. Only for inertial-range isotropic turbulence it is necessarily recovered due to the parameter calibration.

The final implicit SGS model was validated for decaying homogeneous isotropic turbulence with a KOLMOGOROV spectrum throughout all represented wavenumbers in the limit case of large REYNOLDS number. The energy spectrum decayed self-similarly while preserving the $\xi^{-5/3}$ law up to the largest wavenumbers. The observed decay rate of the resolved turbulent kinetic energy agrees well with theory. This agreement is not surprising but confirms the parameter calibration for this particular case at large REYNOLDS numbers. Assuming an ideal KOLMOGOROV spectrum constitutes a theoretical test that cannot be studied experimentally because this spectrum does not possess a developed infra-red range and because the integral length scale is not allowed to grow. As physically more relevant test, LES initialized with spectrum and REYNOLDS numbers adapted to the wind-tunnel experiments of COMTE-BELLOT and CORRSIN were performed. These and other validation cases for unbounded flows suggest that the model may be more generally valid. It is possible that the optimal values of the model parameters might be weakly REYNOLDS-number dependent, however, contrary to common experience with most eddy-viscosity models, our up-to-date results do not support such a conclusion for ALDM.

The response of the nonlinear deconvolution scheme of ALDM to flow anisotropy was analyzed for turbulent channel flow. With standard weight functionals based on total variation, ALDM possesses a strongly anisotropic discretization near walls resulting in a modest underestimation of the wall-friction velocity. The prediction of the wall-shear

stress can be improved if this effect is properly compensated by a VAN DRIEST-type damping functional. The particular choice of the damping functional plays a minor role. Results for implicit LES of turbulent channel flow compare well with DNS data in terms of mean flow and turbulence statistics. Predictions for the anisotropic REYNOLDS stresses show improvement over results obtained at same resolution with the dynamic SMAGORINSKY model, which is one of the most advanced classical explicit SGS models. This improvement is attributed to the tensor character of the effective viscosity of the implicit model. The computational results provide convincing evidence that ALDM can be employed for the prediction of wall-bounded flows without additional adjustment of model parameters.

The implicit SGS modeling environment provided by ALDM was also extended to LES of passive-scalar mixing. An adaptive advection algorithm for passive scalars was developed where free parameters in the discretization of the passive-scalar transport equation were calibrated in such a way that the implicit SGS model matches the requirements of turbulence theory in freely decaying isotropic turbulence at high PÉCLET number. A difficulty of this modeling task was that the various regimes that exist for the passive-scalar variance spectrum have to be recovered by the SGS model. The presented analysis revealed that two different parameter sets are required; one set for low SCHMIDT numbers and one set for high SCHMIDT numbers. The choice of model parameters was validated for passive-scalar mixing in forced isotropic turbulence and in turbulent channel flow. Both applications demonstrate that implicit LES can provide reliable predictions of the turbulent transport of passive scalars for a wide range of SCHMIDT numbers.

As a final test case an incompressible fully-turbulent flat-plate boundary-layer flow subjected to a constant adverse pressure gradient was considered. REYNOLDS number and pressure-gradient parameters were adapted to the experimental setup of INDINGER. The computational predictions were validated against the experimental data. Experimental and numerical results agree very well thus providing a final validation of the ILES methodology proposed here. Conclusions were drawn concerning the scaling of the mean velocity profile of turbulent boundary-layer flow under non-equilibrium conditions in the vicinity of pressure-induced separation. Present LES and experimental results showed consistently that the mean velocity profile can no longer be described by the classical log law. However, while INDINGER found that the failure of inner scaling coincides with the very first occurrence of instantaneous reverse flow, the present numerical study reveals that inner scaling and the logarithmic law of the wall remain valid for intermittent detachment. This mismatch between experiment and LES was traced back to the PRESTON-tube measurement technique that was used to determine the wall-shear stress experimentally. The agreement with the LES improved significantly when the nu-

merically predicted wall-shear stress was used for determining the scaling parameters of the experimental velocity profiles. The results suggest that inner scaling is valid in the near-wall region even under strong adverse pressure gradients if the wall-friction velocity is larger than SIMPSON's velocity scale based on the pressure gradient. Consistently with experimental results of INDINGER, it was found that the scaling of ZAGAROLA and SMITS is valid for the outer region.

In conclusion, ALDM has shown the potential to be a reliable, accurate, and efficient discretization method for implicit large-eddy simulation. The novel method and the resulting implicit subgrid-scale model were formulated for turbulent flows governed by the incompressible NAVIER-STOKES equations and for passive-scalar mixing. Various applications demonstrated the good performance of the implicit model. Computational results agree well with theory and experimental data and show that the implicit SGS model performs at least as well as established explicit models. This is possible because physical reasoning was incorporated into the design of the discretization scheme, and because discretization effects were fully taken into account within the SGS model formulation.

BURGERS TURBULENCE

This chapter gives a brief report on the development of an implicit SGS model for the one-dimensional viscous BURGERS equation that paved the way to implicit LES of three-dimensional NAVIER-STOKES turbulence. The presentation is based on Refs. [1, 61, 72].

A.1 BURGERS Equation

The underlying conservation law is the viscous BURGERS equation, where the flux

$$F(u) = \frac{1}{2}u^2 - \nu\frac{\partial u}{\partial x} \tag{A.1}$$

is to be substituted in

$$\frac{\partial u}{\partial t} + \frac{\partial F(u)}{\partial x} = 0 \ . \tag{A.2}$$

The initial-value problem is solved on a mesh $x_i = ih$ with equidistant spacing h and $i \in \mathbb{Z}$. We call x_i the cell centers and $x_{i\pm1/2}$ the cell faces of cell i. The grid function $u_N = \{u_i\}$ represents a discrete approximation of $u(x)$ by $u_i \doteq u(x_i)$.

A.1.1 Discretization design

Consistently with the finite-volume approach of Chapter 2, top-hat filtering (2.10) applied to the flux derivative $\partial F(u)/\partial x$ in Eq. (A.2) returns

$$G * \frac{\partial F(u)}{\partial x} = \frac{F(u_{i+1/2}) - F(u_{i-1/2})}{h} \ , \tag{A.3}$$

which requires an approximation of the solution $u(x)$ at each cell face. The use of a top-hat filter G allows for a primitive-function reconstruction $\tilde{u}_N$ of $u(x)$ from $\overline{u}_N$ at $x_{i\pm1/2}$ by the ALDM reconstruction scheme, see Section 2.3. The resulting reconstructions at the left and right faces of cell i are denoted by $\tilde{u}_{i-1/2}^L$ and $\tilde{u}_{i+1/2}^R$, respectively.

Specifically for the underlaying conservation law, an appropriate numerical flux function $\tilde{F}_N$ needs to be devised which approximates the respective physical flux F. One choice for the 1-D BURGERS equation is a modified LAX-FRIEDRICHS flux function

$$\tilde{F}_N(x_{i+1/2}) = \frac{1}{2}\left(F(\tilde{u}_{i+1/2}^R) + F(\tilde{u}_{i+1/2}^L)\right) - \sigma_{i+1/2}\left(\tilde{u}_{i+1/2}^L - \tilde{u}_{i+1/2}^R\right) \ ,$$

where $\sigma_{i+1/2}$ is a shift-invariant functional of $\overline{u}_N$. During computational experimentation we found that the following numerical flux function for our purposes leads to favorable error cancelations

$$\tilde{F}_N(x_{i+1/2}) = F\left(\frac{\tilde{u}_{i+1/2}^R + \tilde{u}_{i+1/2}^L}{2}\right) - \sigma_{i+1/2}\left(\tilde{u}_{i+1/2}^L - \tilde{u}_{i+1/2}^R\right) \ . \tag{A.4}$$

The dissipative weight in Eq. (A.4) can be chosen as $\sigma_{i+1/2} = |\overline{u}_{i+1} - \overline{u}_i|$, e.g..

A.1.2 Modified-Differential Equation Analysis

The modified differential equation for $\overline{u}_N$ is

$$\frac{\partial \overline{u}_N}{\partial t} + \frac{\partial F_N(u_N)}{\partial x} = \mathcal{G}_N \ . \tag{A.5}$$

A finite-volume approximation of Eq. (A.2) is given by

$$\frac{\partial \overline{u}_N}{\partial t} + G * \frac{\partial \tilde{F}_N(\tilde{u}_N)}{\partial x} = 0 \ , \ , \tag{A.6}$$

where the truncation error of the discretization is

$$\mathcal{G}_N = G * \frac{\partial F_N(u_N)}{\partial x} - G * \frac{\partial \tilde{F}_N(\tilde{u}_N)}{\partial x} \ . \tag{A.7}$$

If $\mathcal{G}_N$ approximates the physical subgrid stress in some sense for finite h we obtain an implicit subgrid-scale model contained within the discretization.

The exact expression for the convective part of the BURGERS equation is

$$G * \frac{\partial F_N(u_N)}{\partial x} = \overline{u}_N \frac{\partial \overline{u}_N}{\partial x} + \frac{1}{12}\frac{\partial \overline{u}_N}{\partial x}\frac{\partial^2 \overline{u}_N}{\partial x^2} - \frac{1}{720}\frac{\partial \overline{u}_N}{\partial x}\frac{\partial^4 \overline{u}_N}{\partial x^4}h^4 +$$
$$+ \frac{1}{30240}\frac{\partial \overline{u}_N}{\partial x}\frac{\partial^6 \overline{u}_N}{\partial x^6}h^6 + \mathcal{O}\left(h^8\right) \ , \tag{A.8}$$

where derivatives are to be taken at the cell centers x_N.

MDEA is performed here for the semi-discretization only. This is consistent with the spatially-filtered interpretation of the LES equations, the time step being sufficiently small for the spatial truncation error to be dominant. Based on the results of Section A.2.3 we argue that this is indeed the case for a time-step size Δt chosen according to the COURANT-FRIEDRICHS-LEWY limit [29]

$$\Delta t = \text{CFL}\frac{h}{\max\limits_{x}\left|\dfrac{\partial F}{\partial u}\right|} \tag{A.9}$$

with CFL ≤ 1. For time-integration we have tested two different explicit RUNGE-KUTTA schemes, as detailed below. For implicit time integrations or larger time-step sizes an extension of MDEA to full discretizations should be considered. In this case, however, the LES is in effect space and time filtered [3]. For all computations the diffusive terms are discretized by a 4th-order central finite difference.

A.2 Adaptation for Given Explicit SGS Model

On the example of the SMAGORINSKY model we demonstrate in this section how a given explicit SGS model can be matched by adjusting parameters of the generic implicit SGS model. The SMAGORINSKY model formulated for the BURGERS equation is

$$\tau_{Smag} = -C_S h^2 \left|\frac{\partial \overline{u}}{\partial x}\right| \frac{\partial \overline{u}}{\partial x} \ .$$

The effective explicit SGS model that is to be inserted on the right-hand side of the filtered equations is

$$\overline{\mathcal{G}}_{SGS} = -\frac{\partial \tau_{Smag}}{\partial x} = 2C_S h^2 \left|\frac{\partial \overline{u}}{\partial x}\right| \frac{\partial^2 \overline{u}}{\partial x^2} \ .$$

Since our concern is not to assess the quality of the SMAGORINSKY model itself, the particular value of the SMAGORINSKY constant C_S is unimportant. In the following computational experiments we will use $C_S = 0.2$. With the implicit SGS approach, we can identify model parameters in such a way that the resulting implicit formulation matches with the explicit model for K=3 up to order $\mathcal{O}(h^3)$ as given in Tab. A.1. Choosing $\sigma_{i+1/2} = 9\,C_S\left|\tilde{u}_{i+1/2}^{-} - \tilde{u}_{i+1/2}^{+}\right|$ in Eq. (A.4), the truncation error $\mathcal{G}_N$ follows as

$$\mathcal{G}_N = 2\,C_S\left|\frac{\partial \overline{u}}{\partial x}\right|\frac{\partial^2 \overline{u}}{\partial x^2}\,h^2 - \frac{1}{6}\,C_S\left|\frac{\partial \overline{u}}{\partial x}\right|\frac{\partial^4 \overline{u}}{\partial x^4}\,h^4 + \mathcal{O}\left(h^6\right) \ . \tag{A.10}$$

Parameter	$\gamma_{1,0}^{+1/2}$	$\gamma_{2,0}^{+1/2}$	$\gamma_{2,1}^{+1/2}$	$\gamma_{3,0}^{+1/2}$	$\gamma_{3,1}^{+1/2}$	$\gamma_{3,2}^{+1/2}$
Value	1	$\dfrac{1}{3}$	$\dfrac{2}{3}$	$\dfrac{4}{10}$	$\dfrac{3}{10}$	$\dfrac{3}{10}$

Table A.1: Result for the discretization parameters $\gamma_{k,r}$ to match the explicit SMAGORINSKY model.

A.2.1 Results for Forced BURGERS Turbulence

A relevant one-dimensional model for NAVIER-STOKES turbulence is a properly forced BURGERS equation. Here we employ a stochastic force as suggested by CHEKHLOV and YAKHOT [22],

$$\frac{\partial u}{\partial t} + \frac{1}{2}\frac{\partial u\,u}{\partial x} = \nu\frac{\partial^2 u}{\partial x^2} + f(x,t) \ , \tag{A.11}$$

on a 2π-periodic computational domain. As REYNOLDS number we choose $1/\nu = 10^5$. The random force $f(x,t)$ is defined in wavenumber space as

$$\hat{f}(\xi) = A\frac{e^{\mathrm{i}\phi}}{\sqrt{|\xi|}\sqrt{\Delta t}} \ , \tag{A.12}$$

where $A = 0.04$ and $-\pi \le \phi \le \pi$ is randomly chosen for every wavenumber and at every time step. With this forcing a resemblance of NAVIER-STOKES small-scale dynamics is obtained which is different from the large-scale forced or decaying BURGERS solution, where the small scales are shocks. After an initial transient a stationary state is reached which exhibits an $\langle \hat{E}(\xi)\rangle \sim \xi^{-5/3}$ inertial range where

$$\hat{E}(\xi) = \frac{1}{2}|\hat{\overline{u}}(\xi)|^2 \tag{A.13}$$

and $\hat{\overline{u}}(\xi)$ is the FOURIER transform of $\overline{u}(x)$ at wavenumber ξ. The dissipation scale is of order $\eta_K \approx 10^{-3}$. The time-step size Δt is determined from Eq. (A.9) with CFL = 0.5. Time integration is performed with the TVD RUNGE-KUTTA scheme of SHU [153].

Discretizations of Eq. (A.11) were integrated up to $t = 500$. Averages were gathered after a short initial transient. Figure A.1 compares the prediction of the implicit SMAGORIN-SKY model with results obtained with a spectral and dealiased discretization where the SMAGORINSKY model is added explicitly.

We note that the prediction by the implicit SMAGORINSKY model agrees for the inertial-range well with that of the explicit SMAGORINSKY model. Discrepancies at large wavenumbers are caused by terms of $\mathcal{O}(h^4)$ by which the implicit model differs from the explicit one.
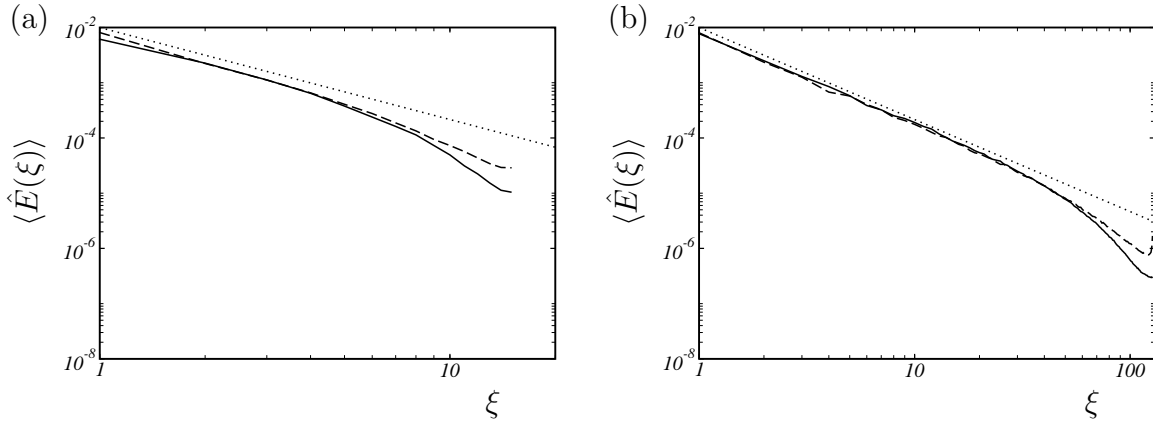
Figure A.1: Averaged energy spectra $\langle \hat{E}(\xi) \rangle$ for the stochastically forced BURGERS equation; ——— implicit SMAGORINSKY model, ———— explicit SMAGORINSKY model, ·········· line with $\xi^{-5/3}$ rule; (a) with $N = 32$, (b) with $N = 256$.

A.2.2 Results for Decaying BURGERS Turbulence

The solution u is L-periodic. For consistency with the results of ALDAMA [3] we set $\nu = 0.02$, $L = 500$. The initial data are computed from a distribution with initial spectrum

$$\hat{E}(\xi) = A\xi'^4 e^{-\sigma^2 \xi'^2/2} \ ,$$

where $\xi' = 2\pi\xi/L$, $A = 10722.08$, $\sigma = 19.89$. The time-step size Δt is determined by Eq. (A.9) with CFL $= 0.5$. For reference we perform a direct simulation with a de-aliased spectral discretization at a resolution of 8192 points, for which it was shown that the mesh-REYNOLDS number is on the order of unity [3], and a LES with a de-aliased spectral discretization and an explicit SMAGORINSKY model.

In Figure A.2 the decay of total energy

$$k(t) = \frac{1}{2} \int_{-\infty}^{+\infty} |\hat{\bar{u}}(\xi)|^2 \, d\xi \tag{A.14}$$

of the different LES computations is compared with the direct simulation, showing a reasonable agreement between implicit and explicit SMAGORINSKY model.

For illustration we show in Fig. A.3a snapshots of the solutions at time $t = 180$. Instantaneous energy spectra follow the theoretical ξ^{-2} drop-off and show again a good agreement between explicit and implicit SMAGORINSKY model, an example at $t = 180$ for $N = 256$ is shown in Figure A.3b.
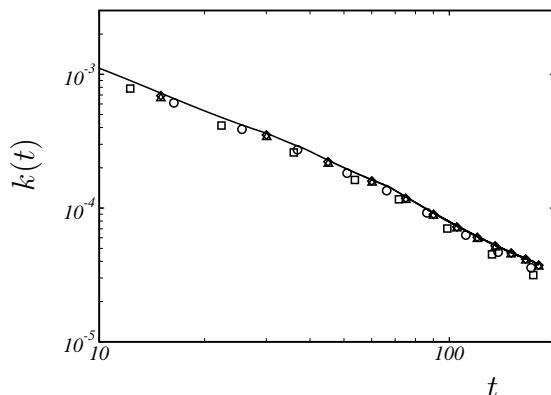
Figure A.2: Temporal evolution of total energy $k(t)$ as predicted by the implicit SMAGORINSKY model compared with the direct simulation ———— ; $\triangle$ implicit SMAGORINSKY model with $N = 256$, $\diamond$ implicit SMAGORINSKY model $N = 512$, $\square$ explicit SMAGORINSKY model with $N = 256$, $\bigcirc$ explicit SMAGORINSKY model $N = 512$.

A.2.3 Effect of Time Integration

To check for the effect of time integration we have repeated some of the above computations with the third-order low-storage RUNGE-KUTTA scheme of WILLIAMSON [182] and with different CFL numbers.

Figure A.4 shows for the forced BURGERS case that changing the integration scheme has only very little effect on the results. Reducing the time-step size to CFL = 0.1 and to CFL = 0.01 has no visible effect on the results, Figure A.5. A similar behavior was found for the case of decaying BURGERS turbulence.

A.3 SGS Modeling by Evolutionary Optimization

For determining optimal parameters we consider the case of the stochastically forced BURGERS equation as described in section A.2.1. Here, however, a large-scale forcing is employed which maintains a $\langle \hat{E}(\xi) \rangle \sim \xi^{-2}$ spectrum. We consider this reference case for optimization since we found that the cost-function sensitivity on the parameter set is more pronounced than for the $\langle \hat{E}(\xi) \rangle \sim \xi^{-5/3}$ case. Also, the dependency on the choice of the initial random seed is less strong which facilitates ensemble averaging. Finally, having derived optimal parameters for one case we can test their prediction quality for other cases.
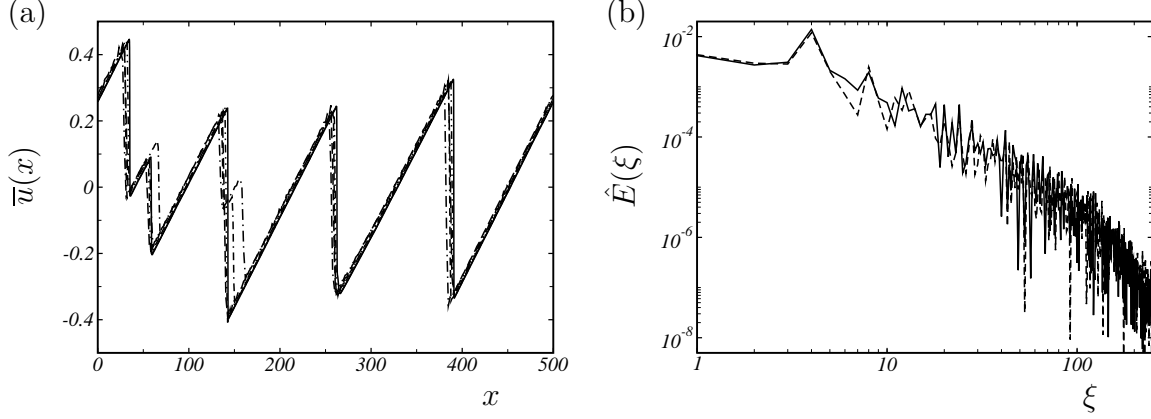
Figure A.3: (a) Instantaneous solution compared with the direct simulation ——— at time $t = 180$; ———— implicit SMAGORINSKY model with $N = 256$, ·—·—·— explicit SMAGORINSKY model with $N = 512$, —··—··— implicit SMAGORINSKY model with $N = 256$, ·——·—— explicit SMAGORINSKY model with $N = 512$.   (b) Instantaneous spectra at $t = 180$ and $N = 512$, ——— implicit SMAGORINSKY model, ———— explicit SMAGORINSKY model.

We add the inverse FOURIER-transform of

$$\hat{f}(\xi) = \begin{cases} A\dfrac{e^{i\phi}}{|\xi|\sqrt{\Delta t}} & , \quad |\xi| \leq \xi_N/4 \\ 0 & , \qquad \text{otherwise} \end{cases} \tag{A.15}$$

to the right-hand side of Eq. (A.11). In (A.15) $-\pi \leq \phi \leq \pi$ is randomly chosen for every wavenumber and at time t and $A = 0.04$. The cost function used for optimization is

$$C = |p - p_{th}| + \sqrt{\frac{1}{|\xi_1 - \xi_2|} \sum_{\xi=\xi_1}^{\xi_2} \left(\ln\langle \hat{E}(\xi)\rangle - a - p\ln\xi \right)^2}. \tag{A.16}$$

p and a are the parameters of the estimate

$$\langle \ln \hat{E}(\xi)\rangle \approx p\ln\xi + a \tag{A.17}$$

which is fitted to $\langle \hat{E}(\xi)\rangle$ by a least-squares estimate over the wavenumber range $\xi_1 = 0.1\xi_N \leq \xi \leq \xi_2 = 0.9\xi_N$. The second term on the right-hand side of Eq. (A.16) measures the deviation from a logarithmic law, whereas the first term measures the deviation from the theoretically predicted exponent p_{th}. For the solution of the BURGERS equation the periodic interval $-\pi \leq x \leq \pi$ is partitioned into $N = 128$ intervals. Time integration is performed for $0 \leq t \leq 140$ and statistical samples for computing the cost function are collected for $t > 7$, after an initial time transient. For all computations the time-step size is adjusted according to Eq. (A.9) with CFL $= 0.5$.
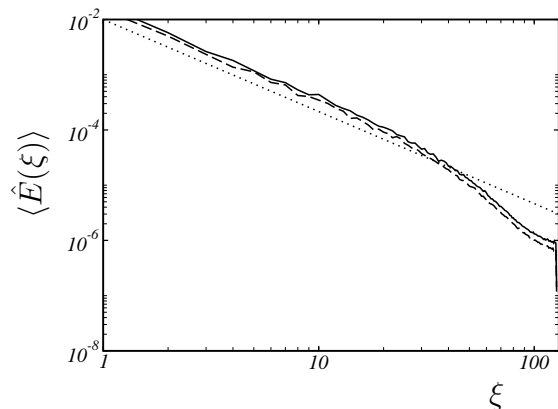
Figure A.4: Averaged energy spectra $\langle \hat{E}(\xi) \rangle$ ——— implicit SMAGORINSKY model with TVD RUNGE-KUTTA, −−−− implicit SMAGORINSKY model with low-storage RUNGE-KUTTA, ········· line with $\xi^{-5/3}$ rule; $N = 256$.

A representative example for the convergence history of the evolutionary algorithm is shown in Figure A.6. The mutation variance decreases exponentially over the number of generations with a fitted convergence rate of -0.03, whereas the cost function decreases algebraically. For the cost function the variation over the statistical ensemble at each generation is indicated by the dashed line for the best cost function and the dash-dotted line for the worst cost function.

Optimal parameters are determined for two different choices of the smoothness measure $\beta_{k,r}$, the total-variation (TV) form Eq. (2.33) and the WENO form defined by JIANG and SHU [80] as

$$\beta_{k,r} = \sum_{l=1}^{k-1} \int_{x_{i-1/2}}^{x_{i+1/2}} h_x^{2l-1} \left(\frac{\partial^l \check{\varphi}_{k,r}(x)}{\partial^l x} \right)^2 \, dx \; , \tag{A.18}$$

where $\check{\varphi}_{k,r}(x)$ is the interpolation polynomial for a generic filtered grid function φ_N on the respective stencil (k, r). Evaluating Eq. (A.18) for the employed HARTEN
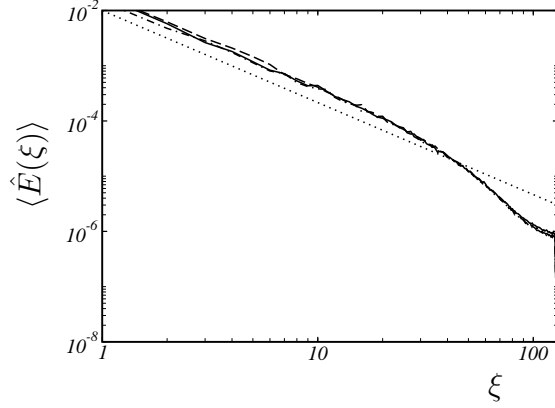
Figure A.5: Averaged energy spectra $\langle \hat{E}(\xi) \rangle$ ——— implicit SMAGORINSKY model with CFL $= 0.5$, $----$ implicit SMAGORINSKY model with CFL $= 0.1$, $\cdot - \cdot - \cdot -$ implicit SMAGORINSKY model with CFL $= 0.01$, $\cdots\cdots$ line with $\xi^{-5/3}$ rule; $N = 256$ grid points.

reconstruction polynomials, we obtain

$$\beta_{1,0} = 1 \;,$$

$$\beta_{2,0} = (\overline{\varphi}_{i+1} - \overline{\varphi}_i)^2 \;,$$

$$\beta_{2,1} = (\overline{\varphi}_i - \overline{\varphi}_{i-1})^2 \;,$$

$$\beta_{3,0} = \frac{13}{12}(\overline{\varphi}_i - 2\overline{\varphi}_{i+1} + \overline{\varphi}_{i+2})^2 + \frac{1}{4}(3\overline{\varphi}_i - 4\overline{\varphi}_{i+1} + \overline{\varphi}_{i+2})^2 \;,$$

$$\beta_{3,1} = \frac{13}{12}(\overline{\varphi}_{i-1} - 2\overline{\varphi}_i + \overline{\varphi}_{i+1})^2 + \frac{1}{4}(\overline{\varphi}_{i-1} - \overline{\varphi}_{i+1})^2 \;,$$

$$\beta_{3,2} = \frac{13}{12}(\overline{\varphi}_{i-2} - 2\overline{\varphi}_{i-1} + \overline{\varphi}_i)^2 + \frac{1}{4}(\overline{\varphi}_{i-2} - 4\overline{\varphi}_{i-1} + 3\overline{\varphi}_i)^2 \;.$$

The resulting optimal parameters are given in Tab. A.2. Note that for the WENO choice of the smoothness measure the stencil is effectively fixed and nonlinear effects of subgrid-scale smoothness on the candidate-stencil weights are suppressed.

Given the numerical flux function Eq. (A.4) with $\sigma_{i+1/2} = |\overline{u}_{i+1} - \overline{u}_i|$ the implicit SGS
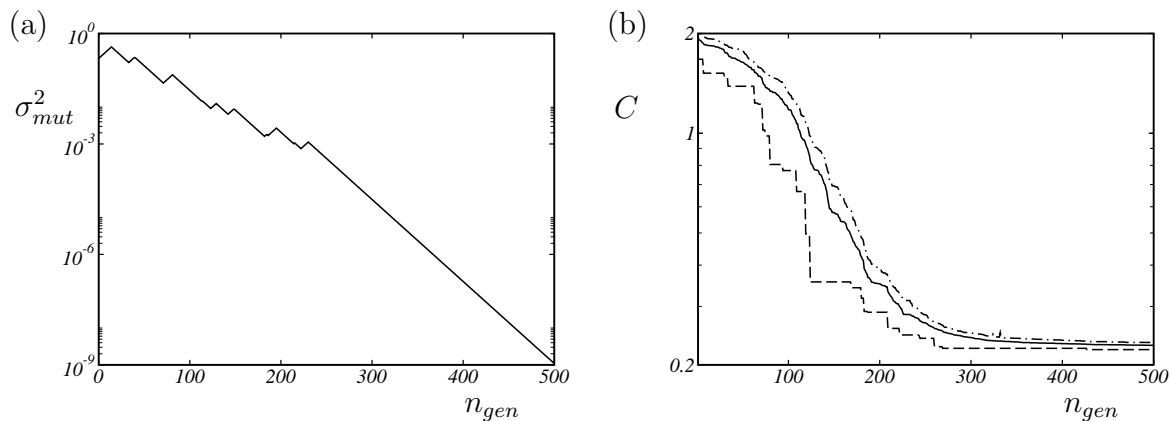
(a)

(b)

Figure A.6: Convergence histories for the stochastically forced BURGERS equation monitored over 500 generations: (a) mutation variance, (b) cost function; ———— average cost function, − − − − best cost function in ensemble, ·—·—·— worst cost function in ensemble.

Parameter	$\gamma_{1,0}^{+1/2}$	$\gamma_{2,0}^{+1/2}$	$\gamma_{2,1}^{+1/2}$	$\gamma_{3,0}^{+1/2}$	$\gamma_{3,1}^{+1/2}$	$\gamma_{3,2}^{+1/2}$
TV measure (2.33)	1	0.999847	0.000153	0.998532	0.001326	0.000142
WENO measure (A.18)	1	1	0	1	0	0

Table A.2: Result obtained by evolutionary optimization for the parameters $\gamma_{k,r}^{+1/2}$, for the TV form and the WENO form of the smoothness measure $\beta_{k,r}$.

model can be determined with MDEA according to section A.1.2 as

$$
\begin{aligned}
\mathcal{G}_N = &\left(-0.11108\left(\frac{\partial \overline{u}}{\partial x}\frac{\partial^2 \overline{u}}{\partial x^2} + \overline{u}\frac{\partial^3 \overline{u}}{\partial x^3}\right) + 0.66667\left|\frac{\partial \overline{u}}{\partial x}\right|\frac{\partial^2 \overline{u}}{\partial x^2}\right)h^2 + \\
&+\left(-0.00371\frac{\partial \overline{u}}{\partial x}\frac{\partial^4 \overline{u}}{\partial x^4} + 0.16661\frac{\left|\frac{\partial \overline{u}}{\partial x}\right|}{\frac{\partial \overline{u}}{\partial x}}\frac{\partial^2 \overline{u}}{\partial x^2}\frac{\partial^3 \overline{u}}{\partial x^3} - 0.02174\frac{\partial^2 \overline{u}}{\partial x^2}\frac{\partial^3 \overline{u}}{\partial x^3}\right. + \\
&+0.00005\,\overline{u}\left(\frac{\frac{\partial^2 \overline{u}}{\partial x^2}}{\frac{\partial \overline{u}}{\partial x}}\right)^2\frac{\partial^3 \overline{u}}{\partial x^3} + 0.11095\left|\frac{\partial \overline{u}}{\partial x}\right|\frac{\partial^4 \overline{u}}{\partial x^4} - 0.00014\,\overline{u}\frac{\frac{\partial^2 \overline{u}}{\partial x^2}}{\frac{\partial \overline{u}}{\partial x}}\frac{\partial^4 \overline{u}}{\partial x^4} + \\
&\left.+0.00005\frac{\left(\frac{\partial^2 \overline{u}}{\partial x^2}\right)^3}{\frac{\partial \overline{u}}{\partial x}} + 0.00010\frac{\left|\frac{\partial \overline{u}}{\partial x}\right|}{\frac{\partial \overline{u}}{\partial x}}\frac{\left(\frac{\partial^2 \overline{u}}{\partial x^2}\right)^3}{\frac{\partial \overline{u}}{\partial x}} + 0.00555\,\overline{u}\frac{\partial^5 \overline{u}}{\partial x^5}\right)h^4 + \mathcal{O}\left(h^6\right)
\end{aligned}
\tag{A.19}
$$

for the case of the TV smoothness measure and

$$
\begin{aligned}
\mathcal{G}_N = \quad & \left(-0.11111 \left(\frac{\partial \overline{u}}{\partial x} \frac{\partial^2 \overline{u}}{\partial x^2} + \frac{\partial^3 \overline{u}}{\partial x^3} \overline{u} \right) + 0.66667 \left| \frac{\partial \overline{u}}{\partial x} \right| \frac{\partial^2 \overline{u}}{\partial x^2} \right) h^2 + \\[2mm]
+ & \left(-0.00370 \frac{\partial \overline{u}}{\partial x} \frac{\partial^4 \overline{u}}{\partial x^4} + 0.16667 \frac{\left| \frac{\partial \overline{u}}{\partial x} \right|}{\frac{\partial \overline{u}}{\partial x}} \frac{\partial^2 \overline{u}}{\partial x^2} \frac{\partial^3 \overline{u}}{\partial x^3} - 0.02160 \frac{\partial^2 \overline{u}}{\partial x^2} \frac{\partial^3 \overline{u}}{\partial x^3} + \right. \\[2mm]
& \left. +0.11111 \left| \frac{\partial \overline{u}}{\partial x} \right| \frac{\partial^4 \overline{u}}{\partial x^4} + 0.00556 \, \overline{u} \frac{\partial^5 \overline{u}}{\partial x^5} \right) h^4 + \mathcal{O}\left(h^6\right)
\end{aligned}
\tag{A.20}
$$

for the case of the WENO smoothness measure.

A.3.1 Results for Forced BURGERS Turbulence

In this section we compare the optimal implicit SGS model results with results for the implicit SMAGORINSKY model, as discussed in Section A.2. Recall that the results obtained for the implicit SMAGORINSKY model were in reasonable agreement with those obtained with an explicit SMAGORINSKY model in combination with a spectral discretization.

In Figure A.7 averaged energy spectra are shown for the case of the stochastically forced BURGERS equation with $\langle \hat{E}(\xi) \rangle \approx \xi^{-5/3}$ spectrum, Eq. (A.12). Since the leading-order terms of the truncation error in Eqs. (A.19) and (A.20) are nearly the same the computed average spectra hardly differ for the two choices of the smoothness function. For both formulations the agreement with the theoretical spectrum is significantly better than for the implicit SMAGORINSKY model.

Similar observations hold for the stochastically forced BURGERS equation with $\langle \hat{E}(\xi) \rangle \approx \xi^{-2}$ spectrum, Eq. (A.15), see Figure A.8. Except for wavenumbers near the NYQUIST wavenumber ξ_N the prediction of both formulations result in very similar predictions. Near ξ_N the higher-order contributions of the truncation error in Eqs. (A.19) and (A.20) become more significant and cause some differences.

It should be emphasized that although the optimal model parameters have been derived for the ξ^{-2}-forcing a good prediction capability is also achieved for the $\xi^{-5/3}$-forcing case.
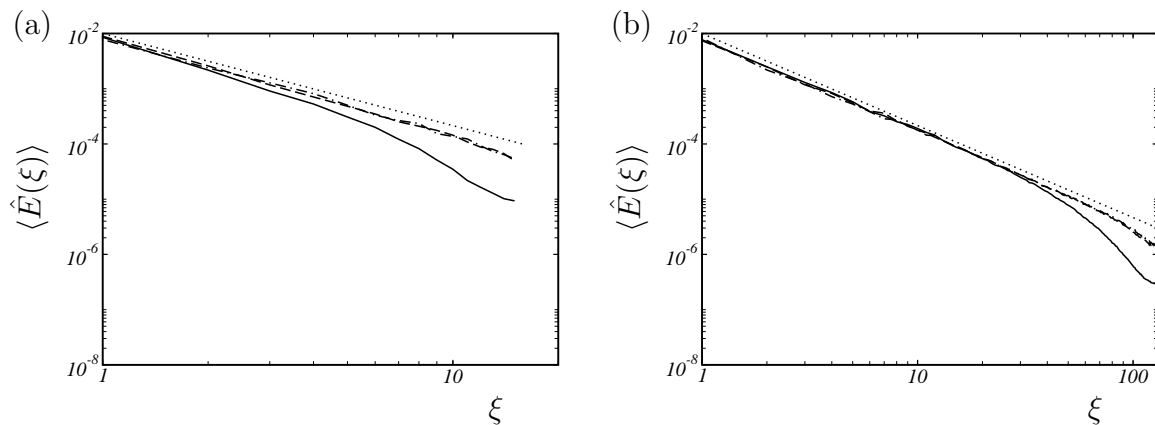
Figure A.7: Averaged energy spectra for forced BURGERS turbulence with $\langle \hat{E}(\xi) \rangle \approx \xi^{-5/3}$ spectrum: (a) $N = 32$, (b) $N = 256$; —— implicit SMAGORINSKY model, ·—·—· optimal parameters with TV smoothness measure, ———— optimal parameters with WENO smoothness measure, ········· line with $\xi^{-5/3}$ rule.
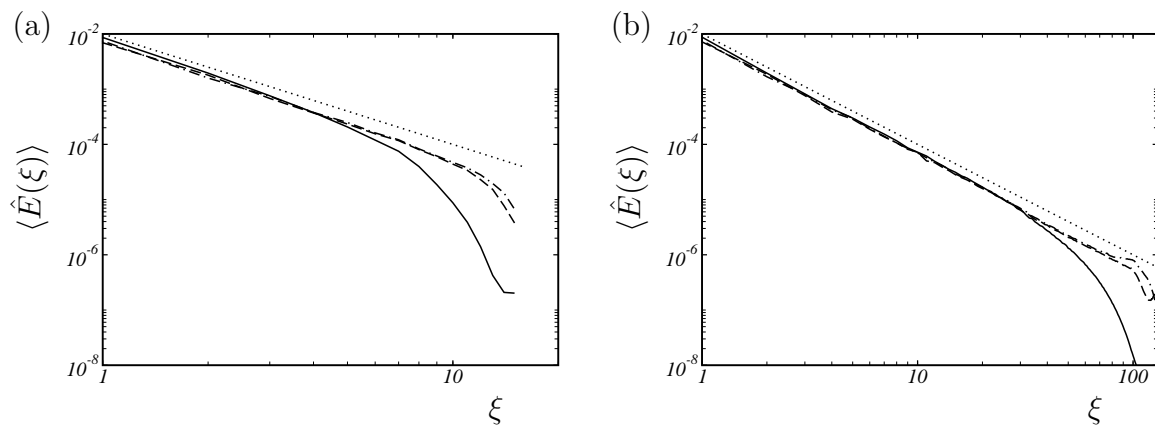

Figure A.8: Averaged energy spectra for forced BURGERS turbulence with $\langle \hat{E}(\xi) \rangle \approx \xi^{-2}$ spectrum: (a) $N = 32$, (b) $N = 256$; —— implicit SMAGORINSKY model, ———— optimal parameters with TV smoothness measure, ·—·—· optimal parameters with WENO smoothness measure, ········· line $\approx \xi^{-2}$.

A.3.2 Results for Decaying BURGERS Turbulence

In this section we apply the implicit SGS models derived above to the case of decaying BURGERS turbulence, according to Section A.2.2. In Figure A.9 the decay of total kinetic energy over time is compared between the optimal implicit SGS model with the TV smoothness measure, the optimal implicit SGS model with the WENO smoothness measure, and the implicit SMAGORINSKY model of Section A.2.
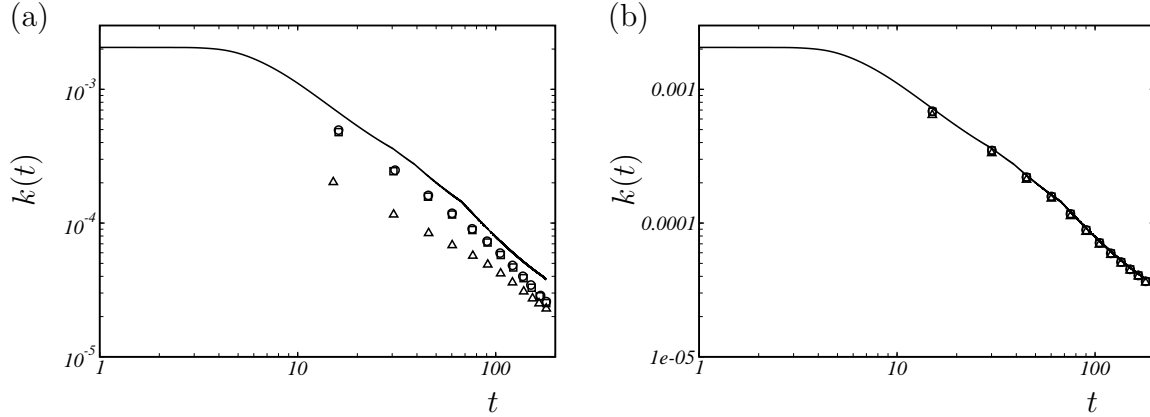
Figure A.9: Temporal decay of total turbulent kinetic energy: (a) $N = 32$, (b) $N = 256$; ———— fully resolved spectral simulation, $\triangle$ implicit SMAGORINSKY model, $\square$ optimal parameters with TV smoothness measure, $\bigcirc$ optimal parameters with WENO smoothness measure.

Also for this test case the results confirm that the optimal models result in a significantly improved prediction compared with the implicit SMAGORINSKY model. For illustration a snapshot of the instantaneous solutions for the fully resolved simulation and the different LES at two different resolutions is shown in Figure A.10.
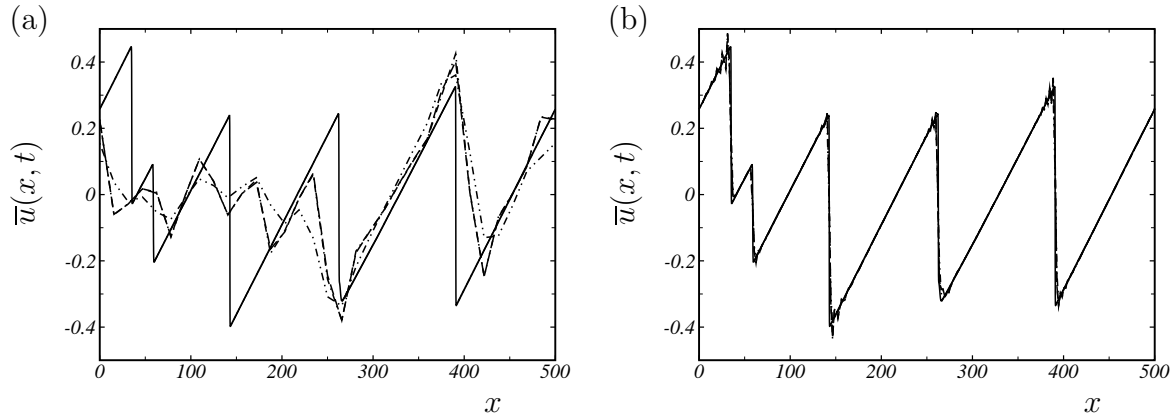

Figure A.10: Instantaneous solution for the fully resolved simulation and for the LES of decaying BURGERS turbulence at time $t = 180$: (a) LES with $N = 32$, (b) LES with $N = 256$; ———— fully resolved spectral simulation, —··—··— implicit SMAGORINSKY model, ———— optimal parameters with TV smoothness measure, ·—·—·— optimal parameters with WENO smoothness measure.

A.4 Summary

Prior to the development of ALDM for the NAVIER-STOKES equations, tools for systematic implicit subgrid-scale modeling have been tested for a one-dimensional transport equation. The viscous BURGERS equation is considered as a relevant model for NAVIER-STOKES turbulence. In particular this holds for the case of a stochastically forced BURGERS equation where the forcing spans the entire wavenumber range. We have studied approaches for driving discretizations of the BURGERS equation towards an optimized or otherwise designed truncation error. It is argued that the truncation error has the same functionality as an explicit subgrid-scale model in flow regions of developed turbulence. On the example of the SMAGORINSKY model it is demonstrated that a given explicit SGS model can be matched by an implicit one. In this case the only benefit of the implicit SGS model is that no explicit computation of model terms is necessary. Implicit model parameters can, however, also be subjected to systematic optimal selection. Optimization target is a generic reference flow configuration which represents the essential properties of flow configurations to which the implicit model will be applied. We have demonstrated that a set of optimal parameters for the case of the large-scale forced BURGERS equation delivers also good results for other forcings and for decaying turbulence.

SIMPLIFIED ADAPTIVE LOCAL DECONVOLUTION (SALD) METHOD

B.1 Simplified Algorithm

The original formulation of ALDM [69] can be further simplified to accelerate computation. In the following, the differences between the original ALDM and the simplified adaptive local deconvolution (SALD) method [63, 66] are briefly described.

ALDM is formulated for the incompressible NAVIER-STOKES equations and applies to the convective flux $\boldsymbol{F} = \boldsymbol{u}\boldsymbol{u}$, where $\boldsymbol{u}$ is the velocity vector. In the framework of a finite-volume discretization, filtering $\overline{\boldsymbol{u}} = \boldsymbol{G} * \boldsymbol{u}$ with kernel $\boldsymbol{G}(\boldsymbol{x}) = \boldsymbol{G}_x(x) \cdot \boldsymbol{G}_y(y) \cdot \boldsymbol{G}_z(z)$ applied to the flux divergence $\boldsymbol{\nabla} \cdot \boldsymbol{F}(\boldsymbol{u})$ returns the flux through the surfaces of cell $\Omega_{i,j,k}$. By GAUSS' theorem we obtain

$$
\left[\boldsymbol{G} * \boldsymbol{\nabla} \cdot \boldsymbol{F}\left(\boldsymbol{G}^{-1} * \overline{\boldsymbol{u}}\right)\right]_{i,j,k}
$$

$$
= \; \frac{1}{hx_i} \, \boldsymbol{G}_y * \boldsymbol{G}_z * \left(\overset{1}{\boldsymbol{f}}(\boldsymbol{G}^{-1} * \overline{\boldsymbol{u}})_{i+\frac{1}{2},j,k} - \overset{1}{\boldsymbol{f}}(\boldsymbol{G}^{-1} * \overline{\boldsymbol{u}})_{i-\frac{1}{2},j,k} \right)
$$

$$
+ \; \frac{1}{hy_j} \, \boldsymbol{G}_z * \boldsymbol{G}_x * \left(\overset{2}{\boldsymbol{f}}(\boldsymbol{G}^{-1} * \overline{\boldsymbol{u}})_{i,j+\frac{1}{2},k} - \overset{2}{\boldsymbol{f}}(\boldsymbol{G}^{-1} * \overline{\boldsymbol{u}})_{i,j-\frac{1}{2},k} \right)
$$

$$
+ \; \frac{1}{hz_k} \, \boldsymbol{G}_x * \boldsymbol{G}_y * \left(\overset{3}{\boldsymbol{f}}(\boldsymbol{G}^{-1} * \overline{\boldsymbol{u}})_{i,j,k+\frac{1}{2}} - \overset{3}{\boldsymbol{f}}(\boldsymbol{G}^{-1} * \overline{\boldsymbol{u}})_{i,j,k-\frac{1}{2}} \right) \qquad \text{(B.1)}
$$

where the flux vector $\overset{l}{\boldsymbol{f}} = u_l\boldsymbol{u}$ denotes the l-direction component of $\boldsymbol{F}$. As a consequence of this identity finite-volume schemes require a reconstruction of data at the faces of the computational volumes.

Numerical experiments [63] show that the implementation of ALDM can be simplified significantly without affecting the prediction capability of the implicit SGS model. The

SALD method is based on the simplification

$$
\begin{aligned}
\left[\boldsymbol{G} * \boldsymbol{\nabla} \cdot \boldsymbol{F} \left(\boldsymbol{G}^{-1} * \overline{\boldsymbol{u}} \right) \right]_{i,j,k} & \\
\approx \quad & \frac{1}{hx_i} \left(\overset{1}{\boldsymbol{f}}(\boldsymbol{G}_x^{-1} * \overline{\boldsymbol{u}})_{i+\frac{1}{2},j,k} - \overset{1}{\boldsymbol{f}}(\boldsymbol{G}_x^{-1} * \overline{\boldsymbol{u}})_{i-\frac{1}{2},j,k} \right) \\
+ \quad & \frac{1}{hy_j} \left(\overset{2}{\boldsymbol{f}}(\boldsymbol{G}_y^{-1} * \overline{\boldsymbol{u}})_{i,j+\frac{1}{2},k} - \overset{2}{\boldsymbol{f}}(\boldsymbol{G}_y^{-1} * \overline{\boldsymbol{u}})_{i,j-\frac{1}{2},k} \right) \\
+ \quad & \frac{1}{hz_k} \left(\overset{3}{\boldsymbol{f}}(\boldsymbol{G}_z^{-1} * \overline{\boldsymbol{u}})_{i,j,k+\frac{1}{2}} - \overset{3}{\boldsymbol{f}}(\boldsymbol{G}_z^{-1} * \overline{\boldsymbol{u}})_{i,j,k-\frac{1}{2}} \right).
\end{aligned}
$$

$$(B.2)$$

The original formulation of ALDM [69] employs a standard GAUSSian quadrature rule with kernel $\boldsymbol{C}_k$ to approximate the filter operation $\boldsymbol{G}_l * \boldsymbol{G}_m$ over the cell faces and a solution adaptive deconvolution scheme to approximate $\boldsymbol{G}^{-1}$. The SALD method uses a simple second-order accurate approximation of $\boldsymbol{G}_l * \boldsymbol{G}_m$, i.e., no explicit filtering over the faces of the computational cells is applied. The benefits of higher-order schemes were found to be negligible since second-order accurate interpolants contribute to the deconvolution operator. Furthermore, approximate deconvolution $\boldsymbol{G}^{-1}$ is applied only in those directions for which interpolation at cell faces is necessary. With the SALD method, the fully 3-D scheme of the original ALDM is replaced by a single 1-D step at the target cell-face. Deconvolution is not performed in the transverse directions.

B.2 Numerical Results

B.2.1 Homogeneous Isotropic Turbulence

As a first test case the numerical schemes are applied to decaying grid-generated turbulence. The computations are initialized with energy spectrum and Reynolds numbers adapted to the wind-tunnel experiments of COMTE-BELLOT and CORRSIN [27], see Section 4.4 for a detailed description.

We present numerical results for implicit LES with the original ALDM scheme and with successively simplified formulations. Figure B.1a compares results obtained by 4th-order ($\boldsymbol{C}_4$ of Eq. 2.18) with those obtained by a second order ($\boldsymbol{C}_2$ of Eq. 2.18) GAUSSian quadrature rule for the approximation of the filter operation $\boldsymbol{G}_l * \boldsymbol{G}_m$. It is found that the choice of the integration kernel has marginal effects on the computed energy spectra. The effect of omitting deconvolution in the transverse directions, i.e., the difference between full and simplified ALDM, is negligible, see Fig. B.1b.
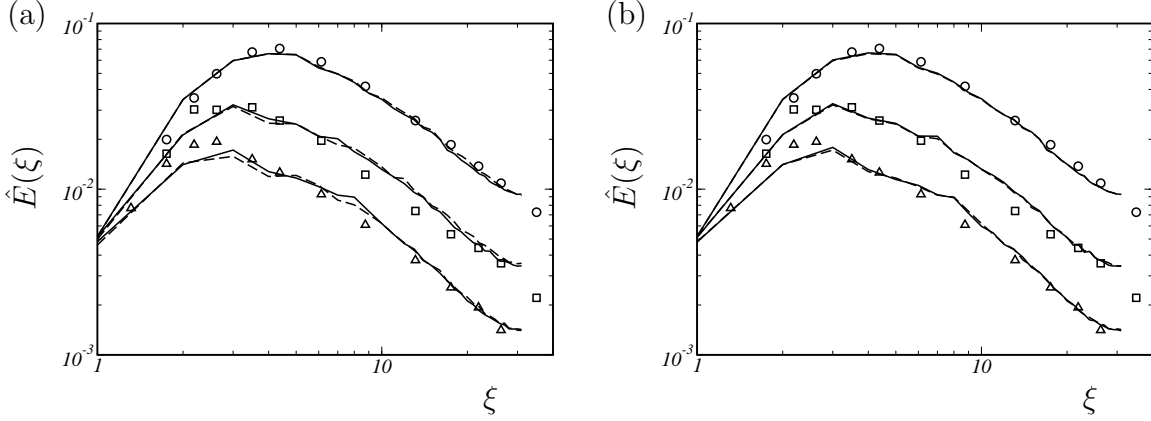
(a)

(b)

Figure B.1: Instantaneous 3-D energy spectra for LES with 64^3 cells of the Comte-Bellot – Corrsin experiment. (a) ——— ALDM with full deconvolution and C_2, — — — — ALDM with full deconvolution and C_4. (b) ——— SALD, — — — — ALDM with full deconvolution and C_2. Symbols represent experimental data of Comte-Bellot and Corrsin [27].

B.2.2 Turbulent Channel Flow

As an example for anisotropic wall bounded turbulence, we simulate channel flow at $\mathrm{Re}_{bulk} = 6875$ ($\mathrm{Re}_\tau = 395$). Reference DNS data is provided by Moser *et al.* [121]. The computational domain measures $2\pi h \times 2h \times \pi h$ (streamwise × wall-normal × spanwise), where h is the channel half width. The spectral DNS of Moser *et al.* required $256 \times 193 \times 192$ grid points. The computational grid of the present LES consists of $64 \times 68 \times 64$ cells with grid stretching applied in the wall-normal direction.

Figures B.2 and B.3 show profiles of mean velocity and Reynolds stresses from LES with the original and the simplified scheme. The differences between the original and the simplified model are marginal. This holds even for the pressure fluctuation, see Fig. B.4, for which differences between DNS and LES are most clearly manifested. Both LES agree well with the reference DNS data. Note the correct wall-asymptotic behavior of the Reynolds stresses of both LES, see Fig. B.3.

B.3 Efficient Implementation

B.3.1 Weight Functionals

It is interesting to note that the evolutionary optimization finally selected $\gamma_{2,0}^{+1/2} = 1$ and $\gamma_{2,1}^{+1/2} = 0$. Consequently, solution adaptivity is ruled out for all but the third-order stencils. It is therefore not necessary to compute the weight functionals $\omega_{1,r}$ and $\omega_{2,r}$.
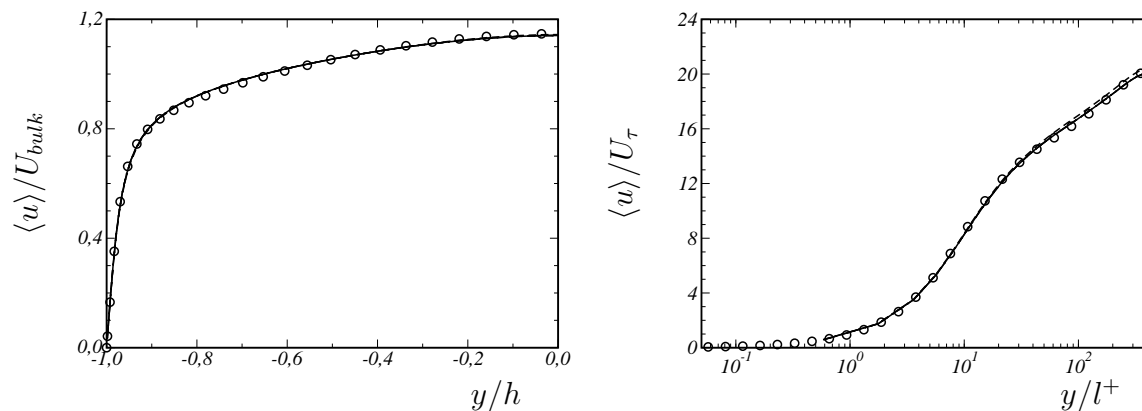
Figure B.2: Mean profiles of velocity for LES of turbulent channel flow at $\text{Re}_\tau = 395$. ——— SALD, −−−− ALDM with full deconvolution and $\boldsymbol{C}_2$, ○ DNS [121].

The advantage of the total-variation smoothness measure, definition (2.33), over smoothness measures proposed by LIU *et al.* [102] and by JIANG and SHU [80], see, e.g., definition (A.18), is that

$$\beta_{k,r}\left(\overline{\varphi}_N, x_i\right) = \beta_{k,r-1}\left(\overline{\varphi}_N, x_{i-1}\right) \tag{B.3}$$

can be exploited to improve computational efficiency.

B.3.2 Vectorization

Although LES does not aim at resolving all spatial scales of turbulent fluid motion, it often requires large computational grids with tens of millions of grid points. On each grid point, however, only few operations have to be performed in one time step. This implies, to our experience, a poor ratio of usable to peak performance on scalar machines, where frequent cache use is the key to high efficiency. Applying the identical operation to vast data fields is much better suited to vector machines.

During the course of this work a flow solver has been written that is optimized for parallel high-performance vector computers [63]. In the following we discuss the special requirements concerning the efficient implementation of ALDM on vector computers, particularly with regard to the NEC SX-8 cluster at the Stuttgart High-Performance Computing Center (HLRS).

On inhomogeneous grids spatially varying coefficients are needed for deconvolution, interpolation, and differencing. These coefficients are usually computed in advance of the actual simulation. Due to memory limitations one tries to avoid to store 3-D coefficient arrays whenever possible. Orthogonal CARTESian grids allow for a reduction of these
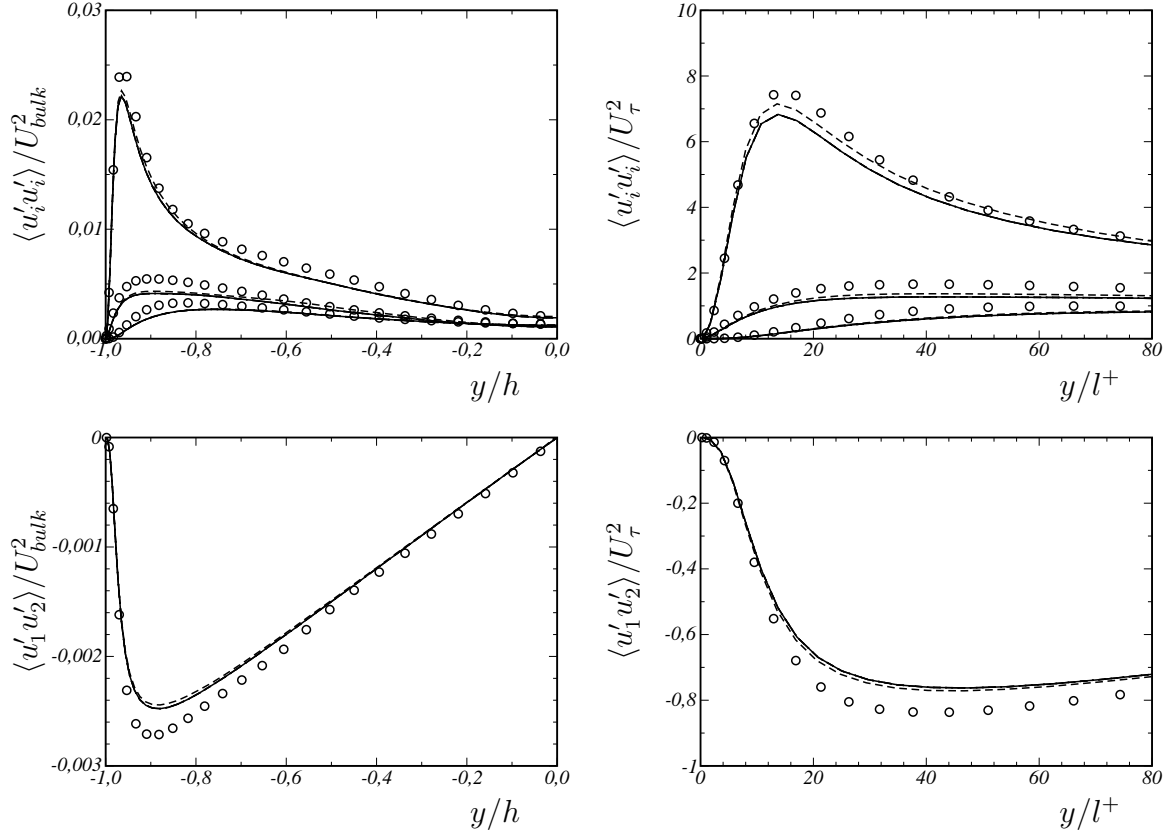
Figure B.3: Mean profiles of REYNOLDS stresses for LES of turbulent channel flow at $\mathrm{Re}_\tau = 395$.
———— SALD, − − − − ALDM with full deconvolution and $\boldsymbol{C}_2$, ∘ DNS [121].

memory requirements from $\sim (N_x \times N_y \times N_z)$ to $\sim (N_x + N_y + N_z)/3$, since a coefficient varies only in one spatial direction. The drawback associated with such an implementation is that the average computational loop length is reduced by the same amount. With typical LES, the respective lengths are of the order of the machine vector length, resulting in a significant number of unused vector elements during computation. In order to avoid this problem, we perform an explicit vectorization, where the physical 3-D arrays are projected onto a 2-D computational space. In computational space, an array has at most two dimensions ξ and η, where the number of cells in the first direction N_ξ is the lowest common multiple of the machine-vector length and the respective physical vector length. To limit the required expansion, we allow 2 vector elements to be unused. The transformation does not require any additional operations at runtime because it only affects pre-computed coefficient arrays and loop-length parameters.

The explicit vectorization method is combined with a re-sorting algorithm. That is, before and after performing expensive operations, all arrays are re-sorted in such a way that the operation is then performed on the first index. The re-sorting routine consumes
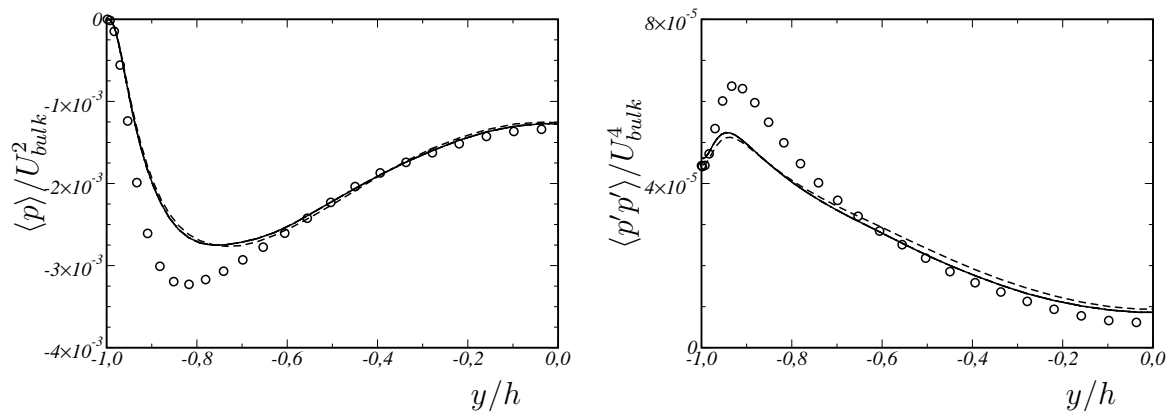
Figure B.4: Mean profiles of pressure and pressure fluctuations for LES of turbulent channel flow at $Re_\tau = 395$. ———— SALD, − − − − ALDM with full deconvolution and C_2, ∘ DNS [121].

less then 1% of the overall computational time but accelerates in particular the deconvolution procedure significantly. As side effect, all operations need to be implemented only for one spatial direction when re-sorting is employed.

B.3.3 Parallelization

Parallelization of our flow solver is generally achieved by domain decomposition. The effective stencil of deconvolution operator and numerical flux function covers 7 cells, requiring knowledge of the solution in three neighbor-cells to each side. The discretization stencils are not modified at flow boundaries or sub-domain interfaces. Rather, the computational sub-domains are covered by three layers of ghost cells for coupling of the solution with neighboring sub-domains. We follow a dual strategy for filling these ghost cells. A shared-memory *openMP* parallelization is employed for sub-domains on the same computer node, whereas information between different nodes is exchanged using *MPI*. Compared to the fully *MPI* parallelized implementation, the computational overhead of the shared-memory parallelization with *openMP* is small.

B.3.4 Performance

The present simulations were performed on a NEC SX-8 cluster, where the computational performance of our implementation could be measured with *ftrace*. The strategy based on transformation and re-sorting results in efficient vectorization and memory access. Typically the average vector length is 255.2 out of possible 256. The vector operation ratio is 99.6 percent. For the LES presented in Chapter 7 the CPU-time

consumption was divided as follows: $\approx 85\%$ iterative solver for the pressure Poisson equation, $\approx 6\%$ per cent right-hand side of the Navier-Stokes equations, $\approx 9\%$ concurrent statistical analysis, and $< 1\%$ auxiliary subroutines. Depending on the problem size, the measured number of floating point operations per second (Flops) and CPU for the deconvolution operator and the numerical flux function were $12 - 13$ GFlops and $8 - 10$ GFlops, respectively. The overall performance and the parallel performance are substantially affected by the solver for the pressure Poisson equation. Using a 3-D conjugate-gradient-method based solver for the pressure Poisson equation, the overall performance was ≈ 9 GFlops. Somewhat lower GFlops values were achieved with FFT-based solvers. Despite the favorable problem size, the overall performance of the implementation with spanwise FFT and 2-D BiCGstab was typically 6 GFlops per CPU.

B.4 Summary

Recommendations for the efficient implementation of ALDM for the incompressible 3-D Navier-Stokes are given and a simplification of ALDM is proposed leading to the simplified adaptive local deconvolution (SALD) method. With the SALD method, the fully 3-D reconstruction scheme of the original ALDM is replaced by a single 1-D step at the target cell-face. This allows for considerable savings of computational resources. SALD is about twice as fast as the original ALDM, whereas the prediction power of the implicit model is preserved. The method is computationally more efficient than a second-order central scheme with a dynamic Smagorinsky model.

For incompressible flows a fractional-step approach is pursued where a pressure correction is subsequently computed solving a Poisson equation. Flows in complex geometries with non-periodic directions require the use of iterative Poisson solvers, consuming typically about 60% and sometimes up to 95% of the computational time. It is recommended to use the SALD method whenever the CPU-time consumption of the discretization of the convective term is relevant. This holds in particular for flow configurations where efficient FFT-based solvers for the pressure Poisson equation are available, such as homogeneous turbulence and channel flow.

NEAR-WALL SCALING OF ALDM WEIGHT FUNCTIONS

One reason for the good performance of the implicit model of ALDM might be the solution-adaptivity of the local deconvolution operator. Fig. C.1-C.6 show the profiles of mean values and fluctuations of the weight functions of the deconvolution operator in turbulent channel flow at $\mathrm{Re}_\tau = 395$. We note that ALDM responds to flow anisotropy and grid stretching by becoming anisotropic in the near wall region. The resulting weights prefer the stencil that is closer to the wall as shown, e.g., for the wall-normal velocity component in Fig. C.1. This weight distribution leads to an upwind bias for fluid moving away from the wall (ejections) and to a downwind bias for fluid moving towards the wall (sweeps). A central scheme is reproduced only at the channel centerline and at 1 or 2 other planes within the logarithmic layer.
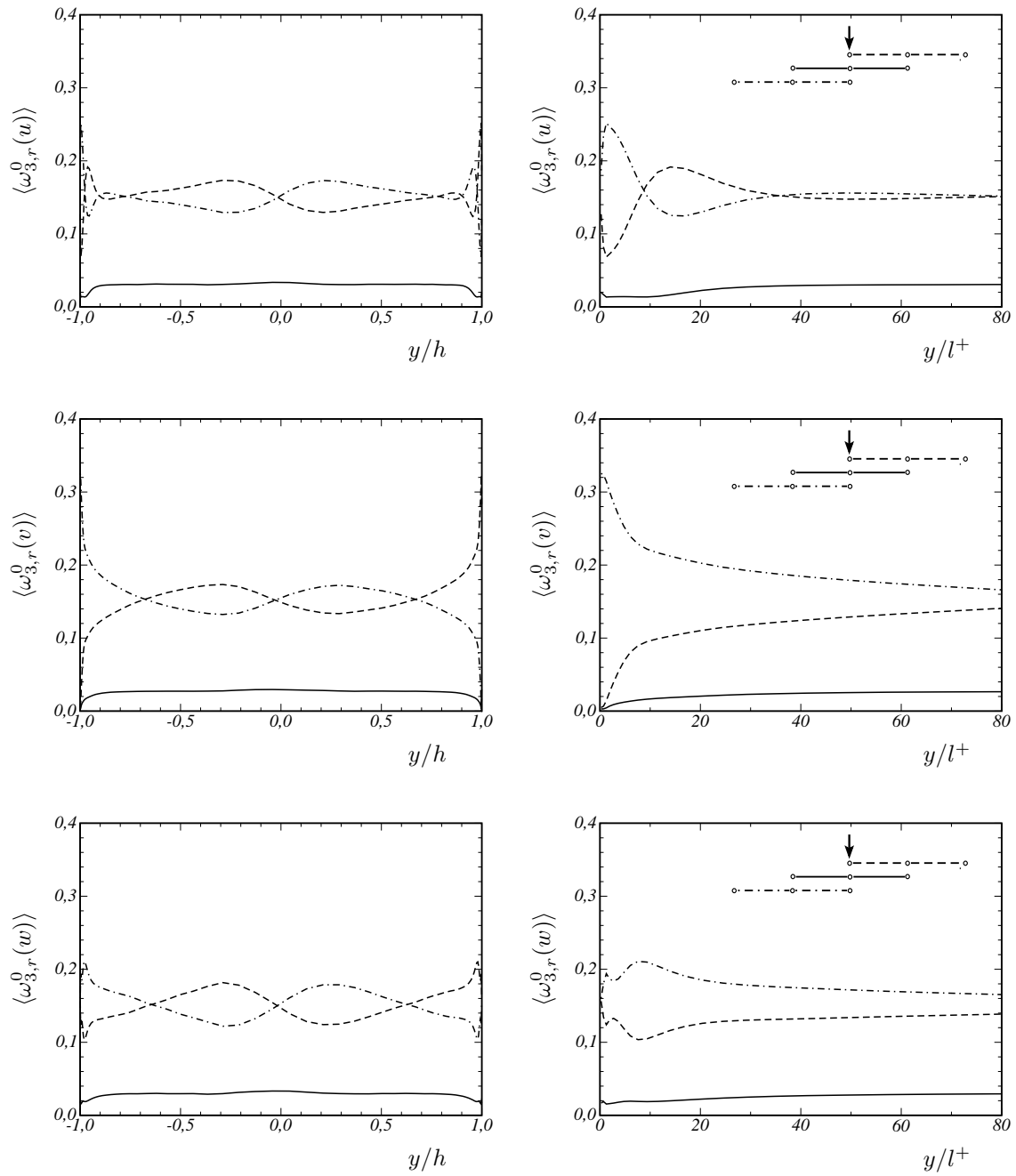
Figure C.1: Time-averaged weight functions of ALDM for the central deconvolution of the streamwise, wall-normal, and spanwise velocity component. Implicit LES of turbulent channel flow at $\mathrm{Re}_\tau = 395$. $----$ $\omega_{3,0}$, $\rule{1cm}{0.4pt}$ $\omega_{3,1}$, $\cdot-\cdot-\cdot-$ $\omega_{3,2}$.
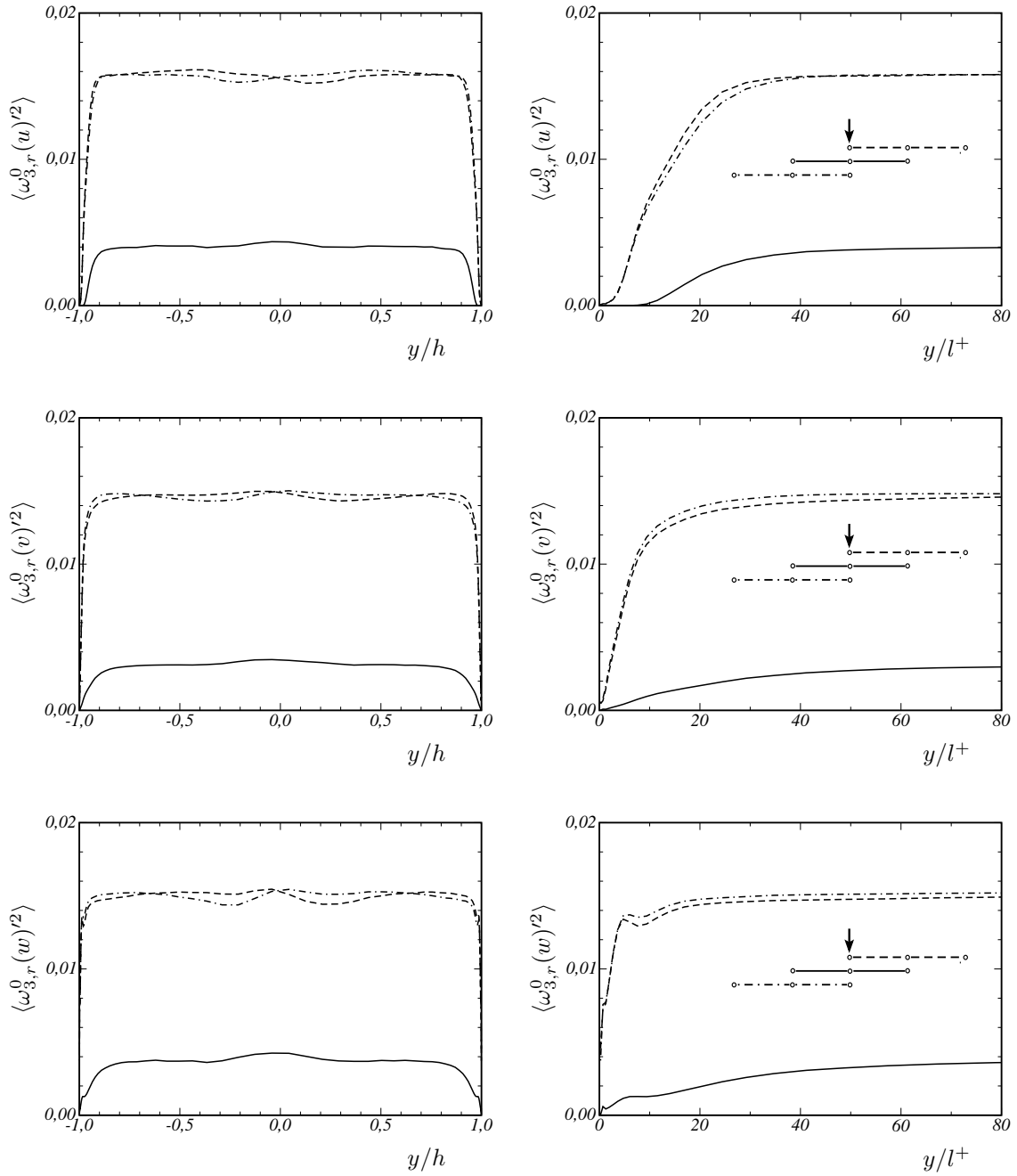
Figure C.2: RMS fluctuations of averaged weight functions of ALDM for the central deconvolution of the streamwise, wall-normal, and spanwise velocity component. Implicit LES of turbulent channel flow at $\mathrm{Re}_\tau = 395$. $----$ $\omega_{3,0}$, $———$ $\omega_{3,1}$, $-\cdot-\cdot-$ $\omega_{3,2}$.

Figure C.3: Time-averaged weight functions of ALDM for the upward deconvolution of the streamwise, wall-normal, and spanwise velocity component. Implicit LES of turbulent channel flow at $\mathrm{Re}_\tau = 395$. $- - - -\ \omega_{3,0}$, $\underline{\hspace{1.2cm}}\ \omega_{3,1}$, $\cdot - \cdot - \cdot -\ \omega_{3,2}$.

Figure C.4: RMS fluctuations of averaged weight functions of ALDM for the upward deconvolution of the streamwise, wall-normal, and spanwise velocity component. Implicit LES of turbulent channel flow at $\mathrm{Re}_\tau = 395$. $----$ $\omega_{3,0}$, $\rule{1cm}{0.4pt}$ $\omega_{3,1}$, $-\cdot-\cdot-$ $\omega_{3,2}$.
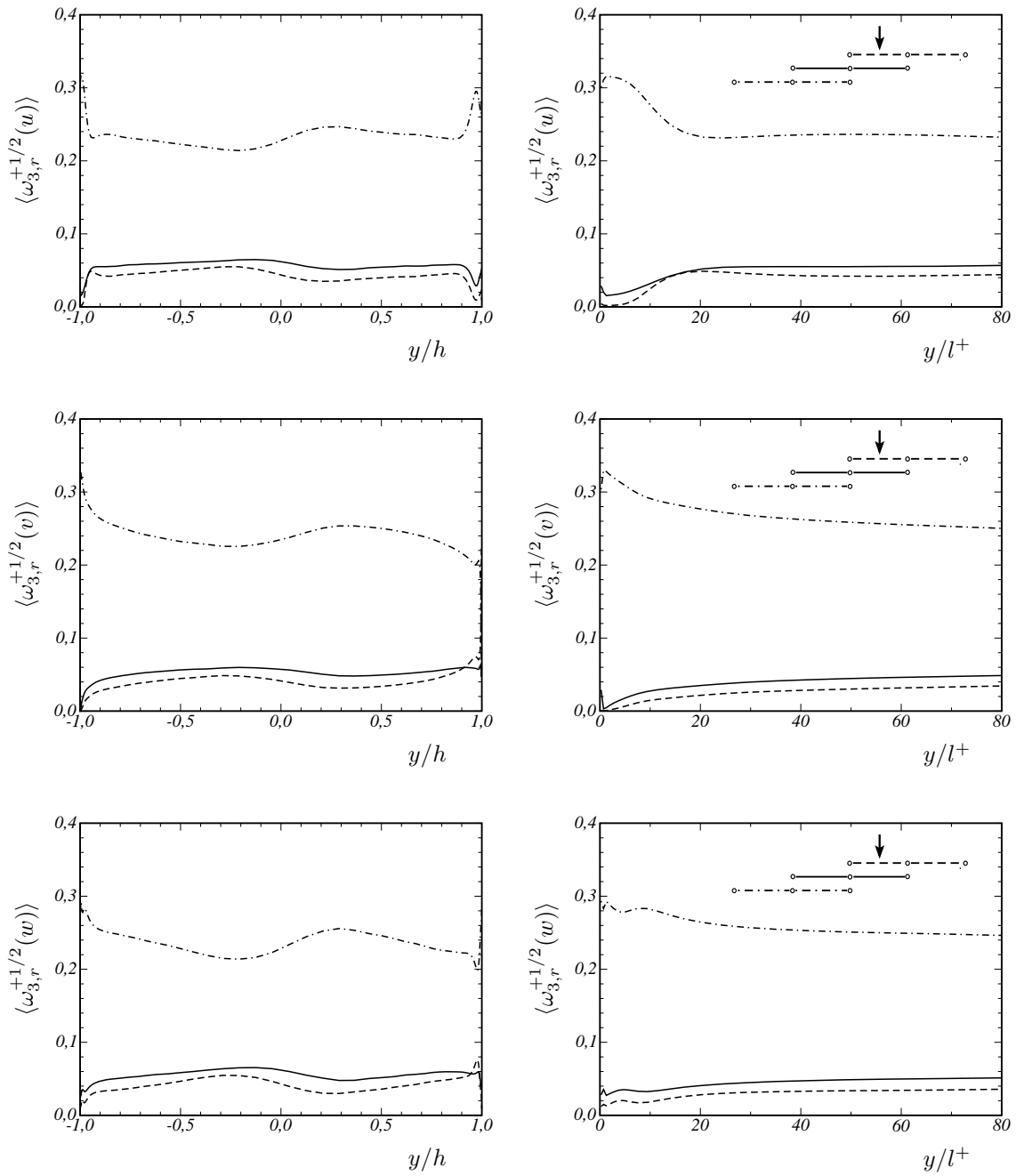
Figure C.5: Time-averaged weight functions of ALDM for the downward deconvolution of the streamwise, wall-normal, and spanwise velocity component. Implicit LES of turbulent channel flow at $Re_\tau = 395$. $----$ $\omega_{3,0}$, $\rule{1cm}{0.5pt}$ $\omega_{3,1}$, $-\cdot-\cdot-$ $\omega_{3,2}$.
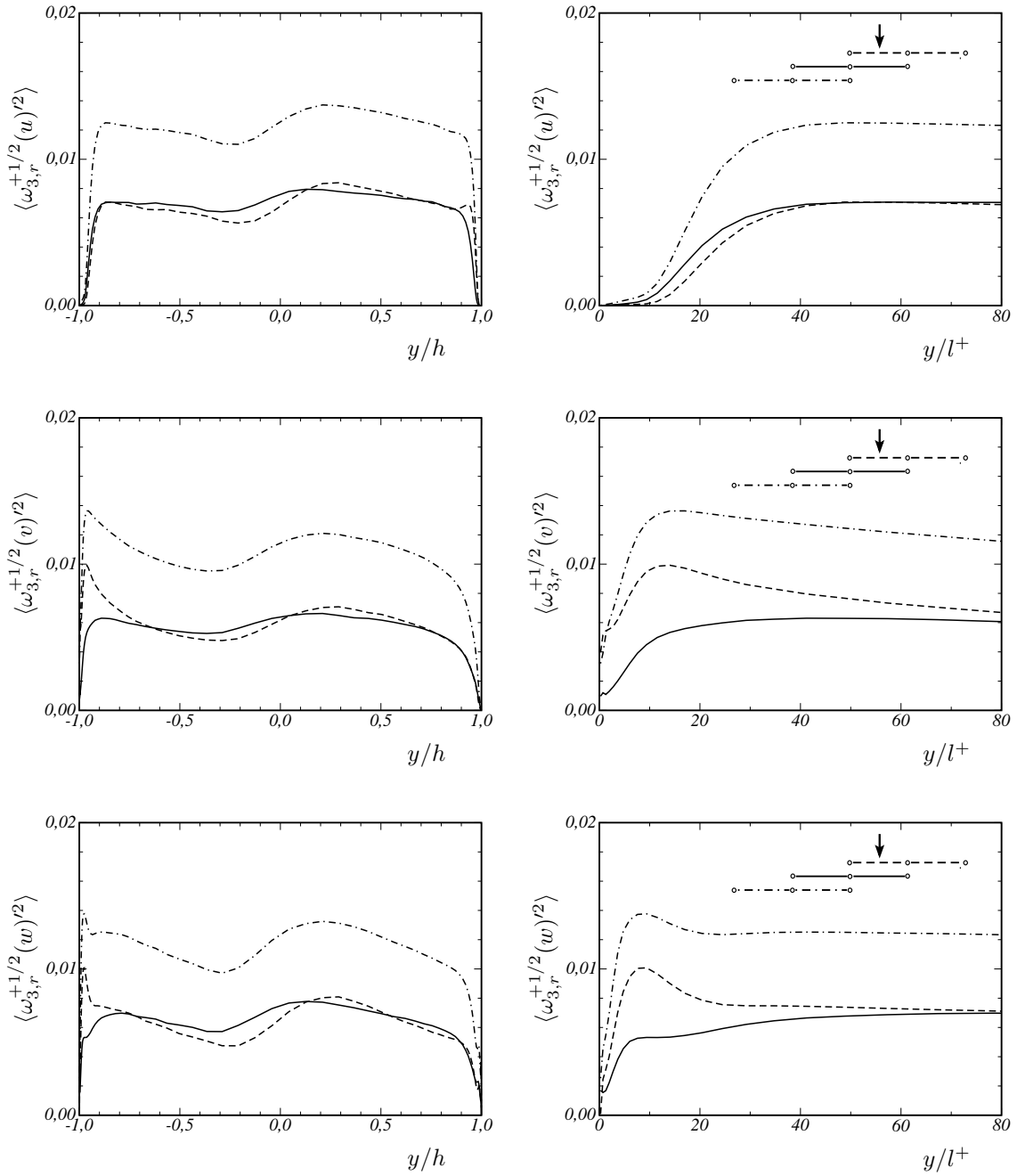
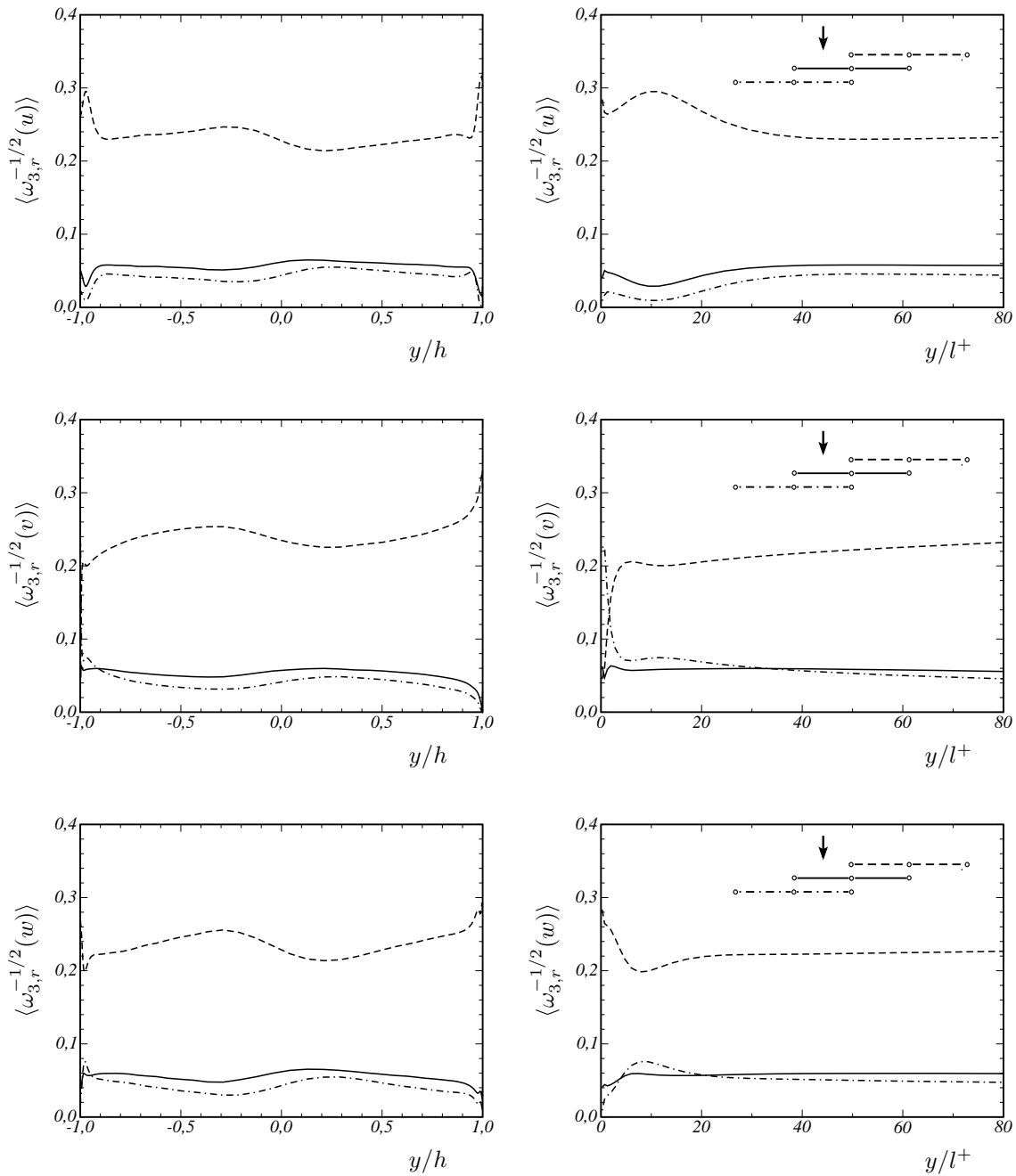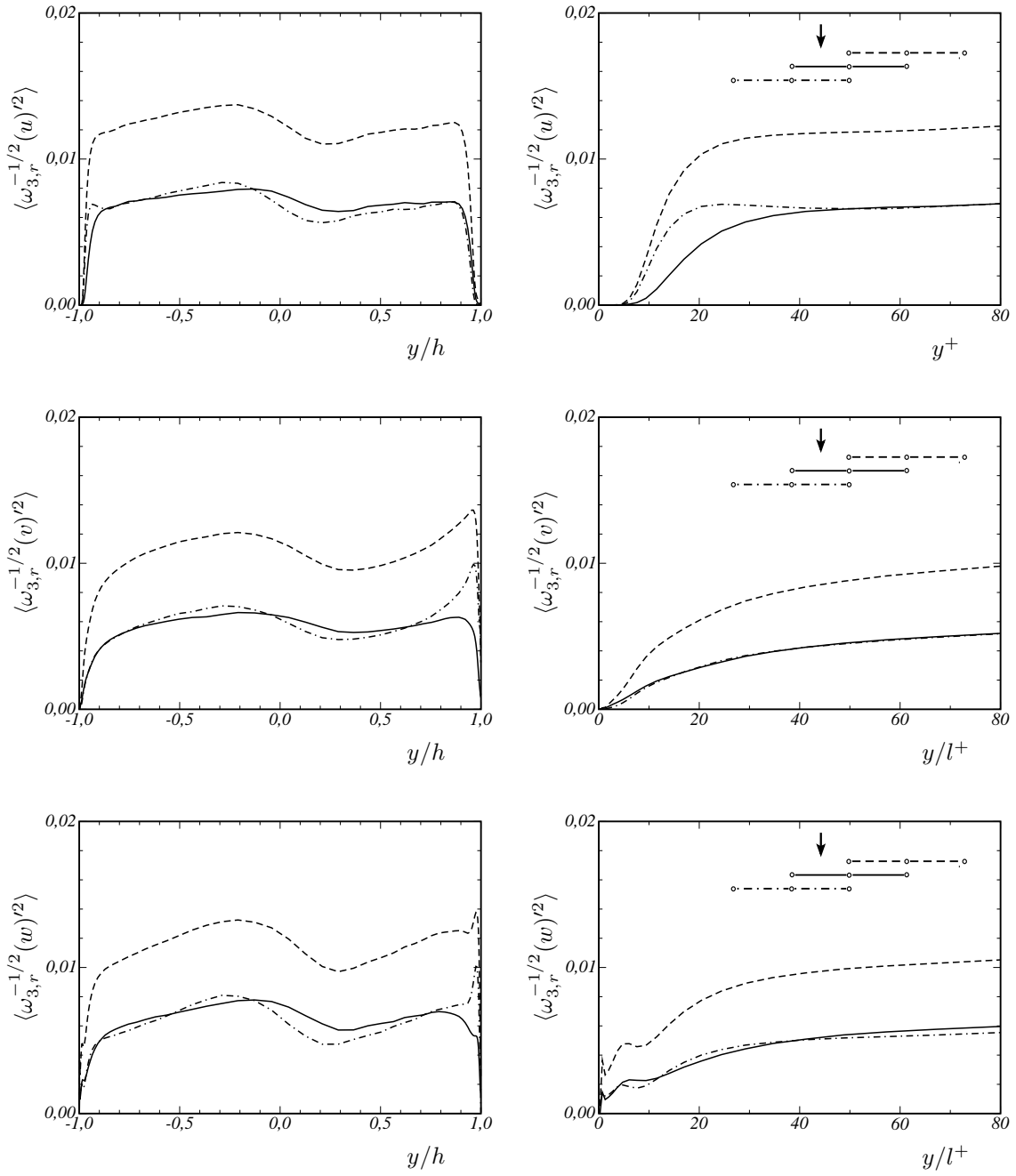**Figure C.6:** RMS fluctuations of averaged weight functions of ALDM for the downward deconvolution of the streamwise, wall-normal, and spanwise velocity component. Implicit LES of turbulent channel flow at $\mathrm{Re}_\tau = 395$. $----$ $\omega_{3,0}$, ——— $\omega_{3,1}$, $-\cdot-\cdot-$ $\omega_{3,2}$.

SUPPLEMENTARY
APG BOUNDARY-LAYER DATA

As supplement to Chapter 7, additional results from the large-eddy simulation of turbulent boundary-layer separation are given in the following. These data are presented here in order to maintain the main part's concise form.

D.1 Instantaneous Wall-Shear Stress

Contours of the instantaneous wall friction are shown in Figs. D.1–D.4. Typical streaky structures dominate the boundary layer at the inflow. As the flow experiences the adverse pressure gradient, the average width of the streaks grows and their relative length decreases. Intermittent backflow is observed from $x = 0.1$ onwards. There is no well-defined separation line, instead the fraction of separated flow zones increases gradually. Within the separated region eddies with large spanwise extents are dominating. Secondary flow reversal occurs in several regions. Streaky structures are found again shortly before the reattachment. Generally, the flow structures observed at and after reattachment are one order of magnitude larger than those of the attached boundary layer before separation.

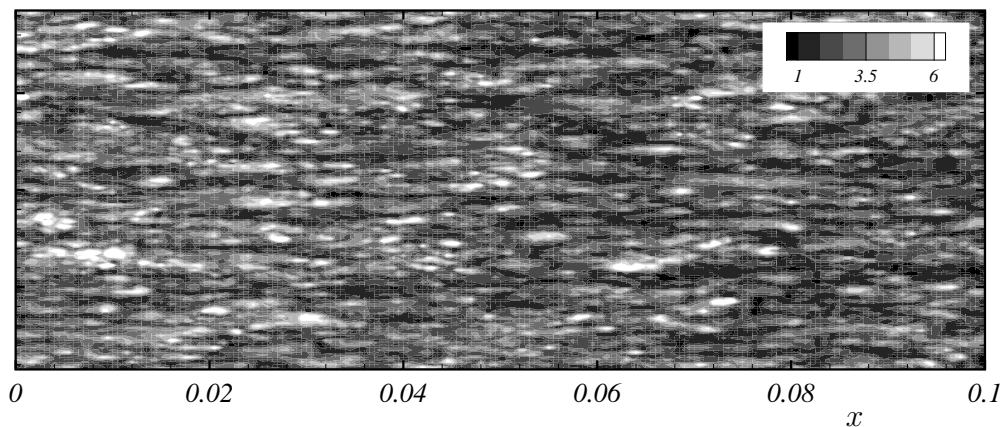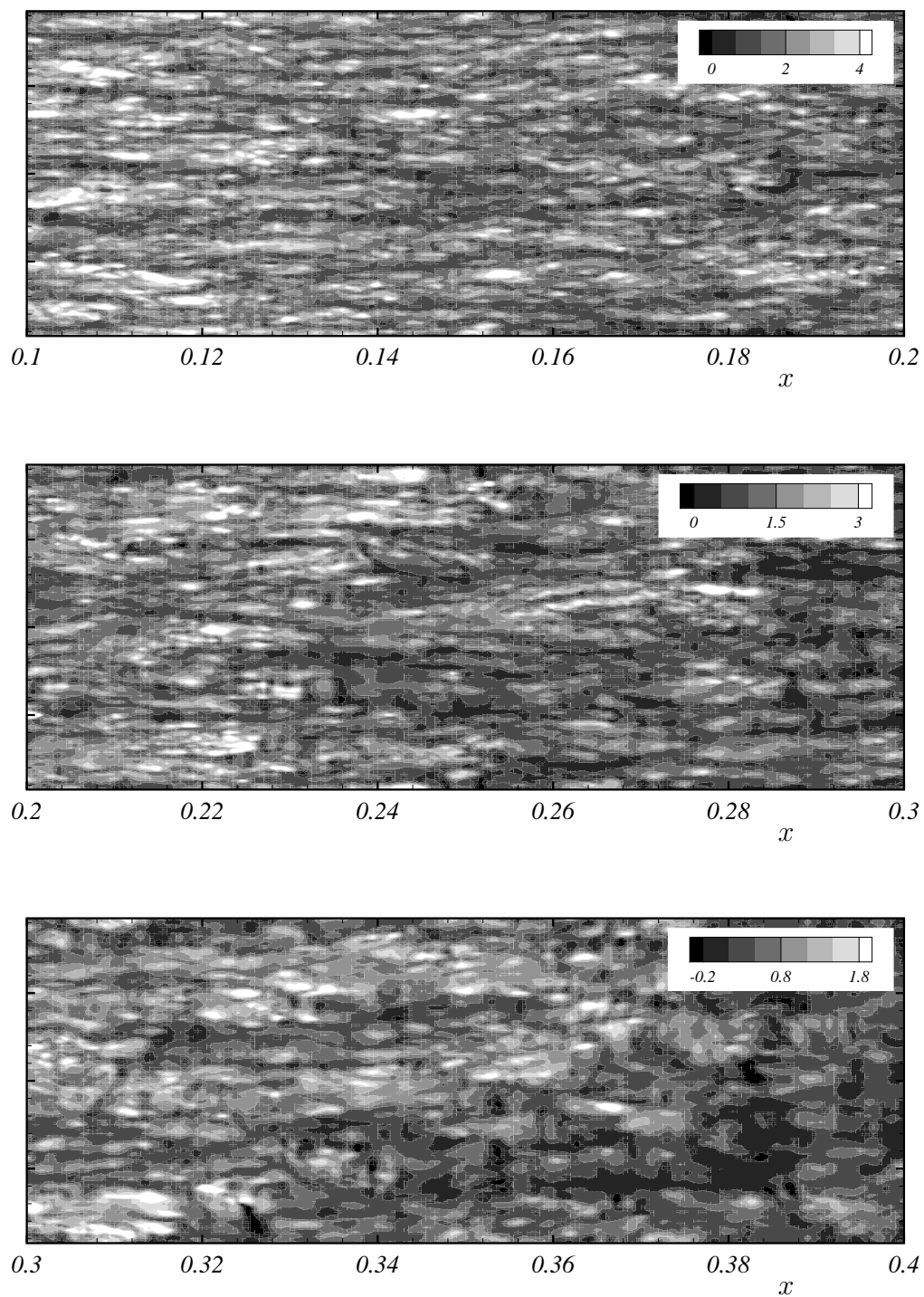**Figure D.1:** Instantaneous contours of the wall-shear stress.

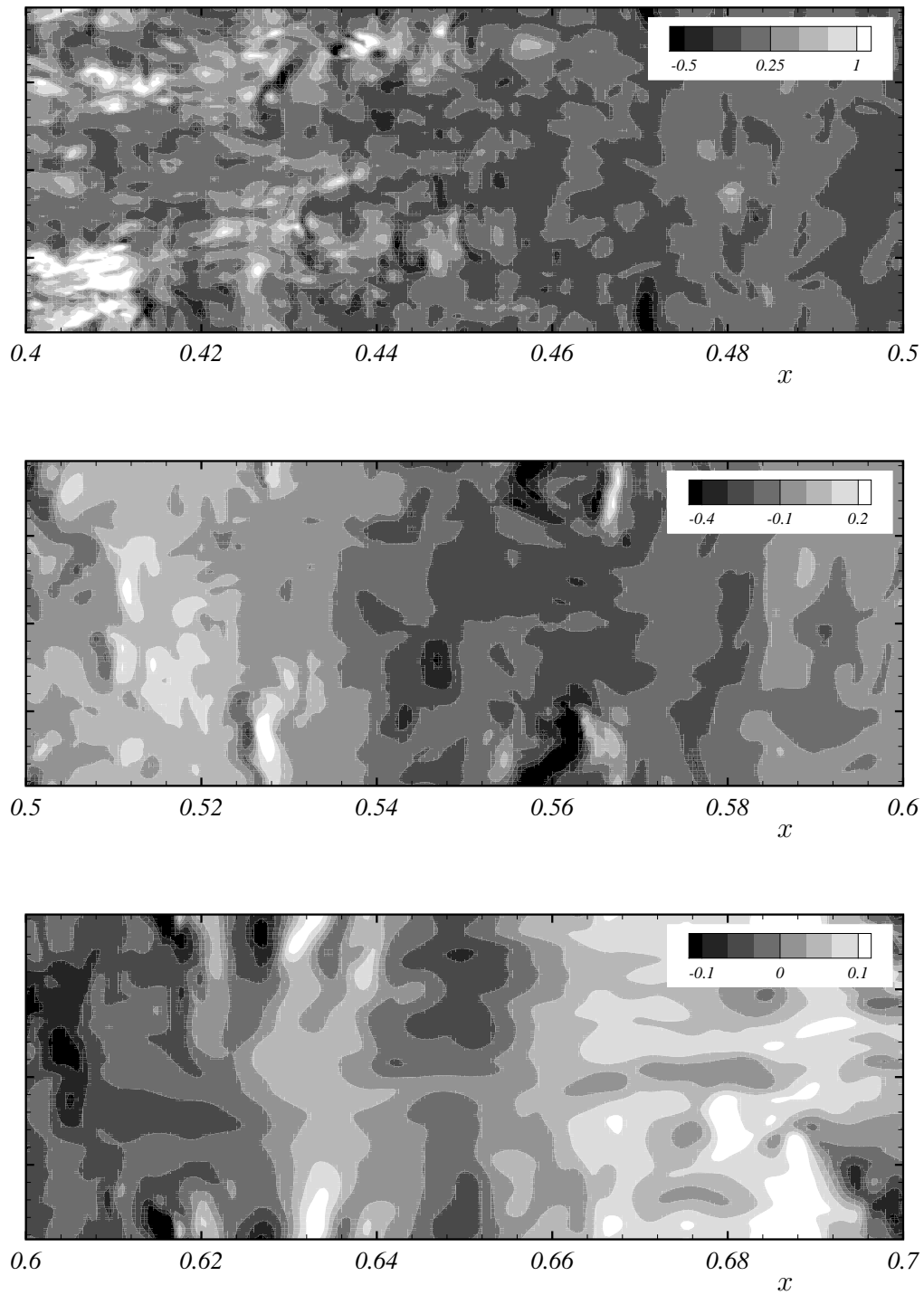**Figure D.2:** Instantaneous contours of the wall-shear stress.

Figure D.3: Instantaneous contours of the wall-shear stress.
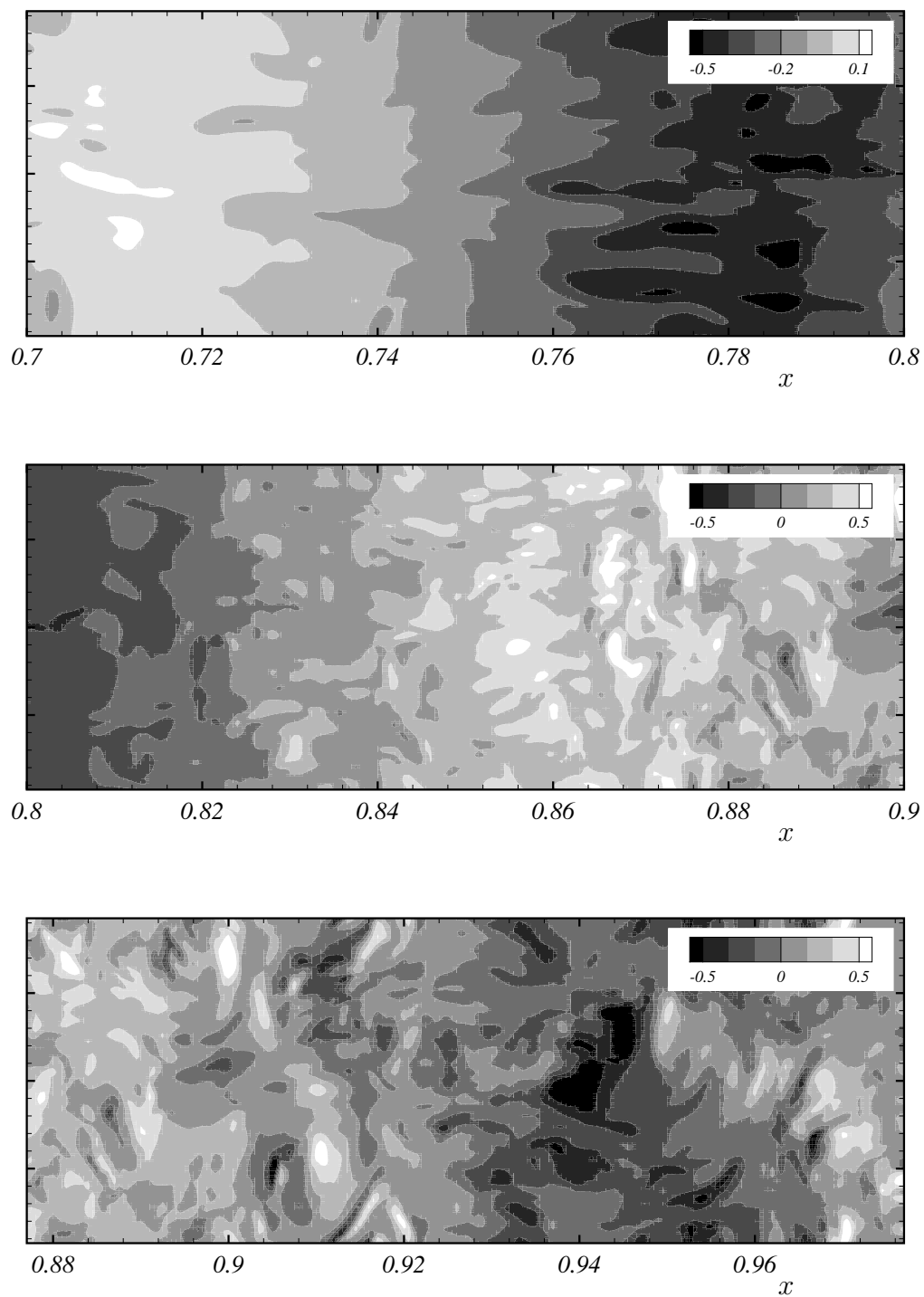
Figure D.4: Instantaneous contours of the wall-shear stress.

D.2 Momentum Balance

The streamwise momentum balance is

$$
\begin{aligned}
0 = \ & -\partial_x \langle u \rangle \langle u \rangle - \partial_y \langle u \rangle \langle v \rangle - \partial_z \langle u \rangle \langle w \rangle && \text{(convection)} \\
& -\partial_x \langle p \rangle && \text{(pressure normal stress)} \\
& +\nu \, \partial_x^2 \langle u \rangle + \nu \, \partial_y^2 \langle u \rangle + \nu \, \partial_z^2 \langle u \rangle && \text{(viscous shear stress)} \\
& -\partial_x \langle u'u' \rangle - \partial_y \langle u'v' \rangle - \partial_z \langle u'w' \rangle && \text{(\textsc{Reynolds} stress)}
\end{aligned}
\tag{D.1}
$$

The individual contributions to the stress balance are shown in Figures D.5 and D.6. We note that the above listed stresses do not balance completely in LES since the SGS model results in another stress contribution. The incoming flow shows essentially the same characteristics as zero-pressure-gradient turbulent boundary layers. The dominant stresses are the viscous stress and the Reynolds stress, which balance each other. The influence of the pressure gradient is relatively small. It is balanced by convection in the outer part and by the Reynolds stress near the wall. Since the flow is decelerated by a constant pressure gradient, the importance of the pressure force and the therewith linked convection increases compared to Reynolds stress and viscous shear stress. The viscous stress becomes progressively smaller with increasing x as the flow approaches separation. At separation, also the contribution of convection vanishes over the largest part of the boundary layer, see Fig. D.6, and the entire pressure force has to be balanced by the Reynolds stress.

The wall-normal momentum balance reads

$$
\begin{aligned}
0 = \ & -\partial_x \langle v \rangle \langle u \rangle - \partial_y \langle v \rangle \langle v \rangle - \partial_z \langle v \rangle \langle w \rangle && \text{(convection)} \\
& -\partial_y \langle p \rangle && \text{(pressure normal stress)} \\
& +\nu \, \partial_x^2 \langle v \rangle + \nu \, \partial_y^2 \langle v \rangle + \nu \, \partial_z^2 \langle v \rangle && \text{(viscous shear stress)} \\
& -\partial_x \langle v'u' \rangle - \partial_y \langle v'v' \rangle - \partial_z \langle v'w' \rangle && \text{(\textsc{Reynolds} stress)}
\end{aligned}
\tag{D.2}
$$

Figures D.7 and D.8 reveal that convection and viscous stress contribute negligibly to the wall-normal stress balance in the attached boundary layer. The wall-normal Reynolds stress $\partial_y \langle v'v' \rangle$ is balanced by a negative pressure gradient $\partial_y \langle p \rangle / \rho$. This changes only close to separation, where the fast growth of the boundary layer results in relevant contributions of the convection. The viscous stress plays no role at all.
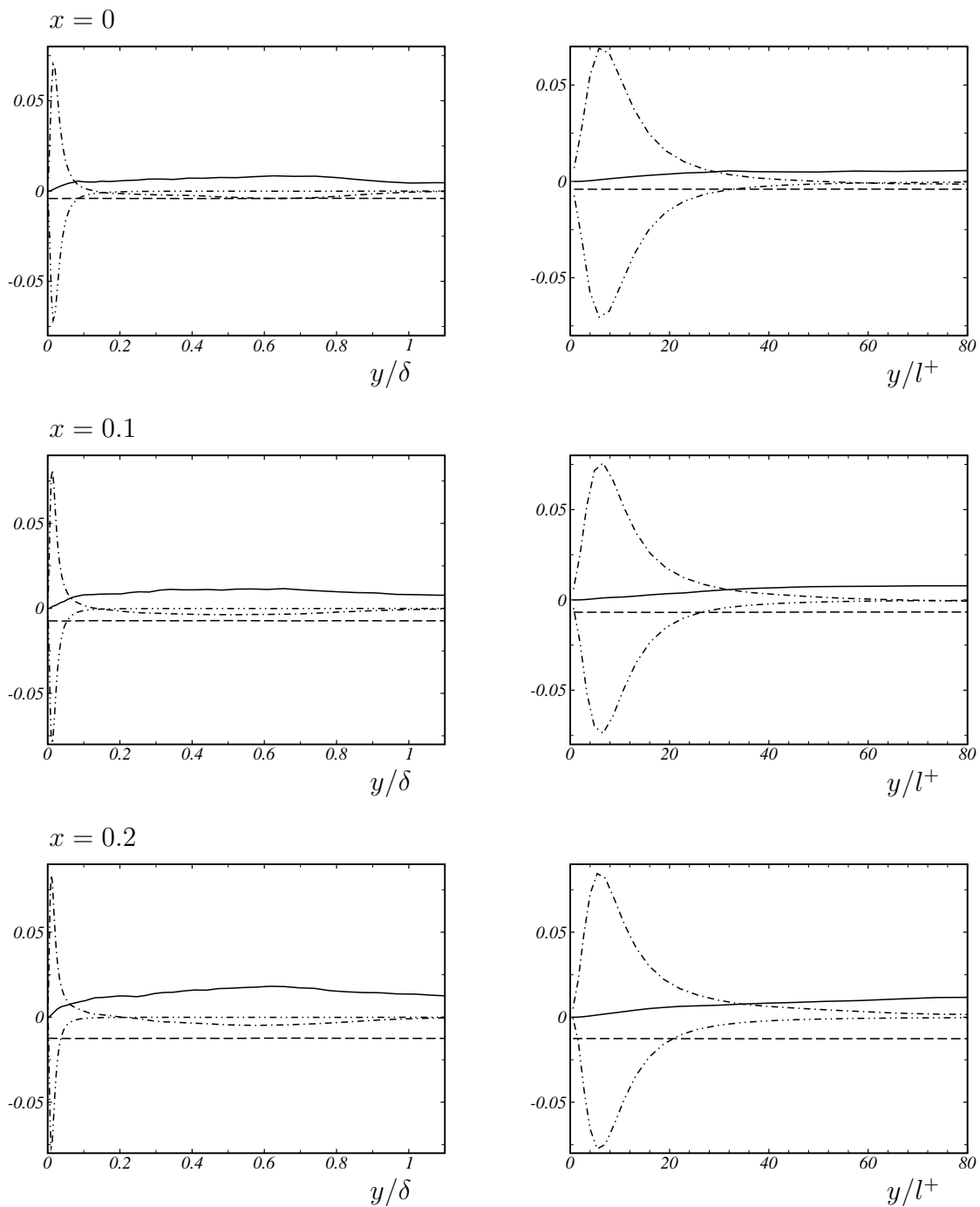
Figure D.5: Streamwise momentum balance in outer and inner scaling: ——— convection — — — — pressure normal stress —··—··— viscous stress ·—·—·— Reynolds stress .

$x = 0.3$

$x = 0.4$

$x = 0.5$

Figure D.6: Streamwise momentum balance in outer and inner scaling: ———— convection — — —
pressure normal stress —··—··— viscous stress ·—·—·— Reynolds stress .

Figure D.7: Wall-normal momentum balance in outer and inner scaling: ——— convection ————
pressure normal-stress —··—··— viscous stress ·—·—·— Reynolds stress .
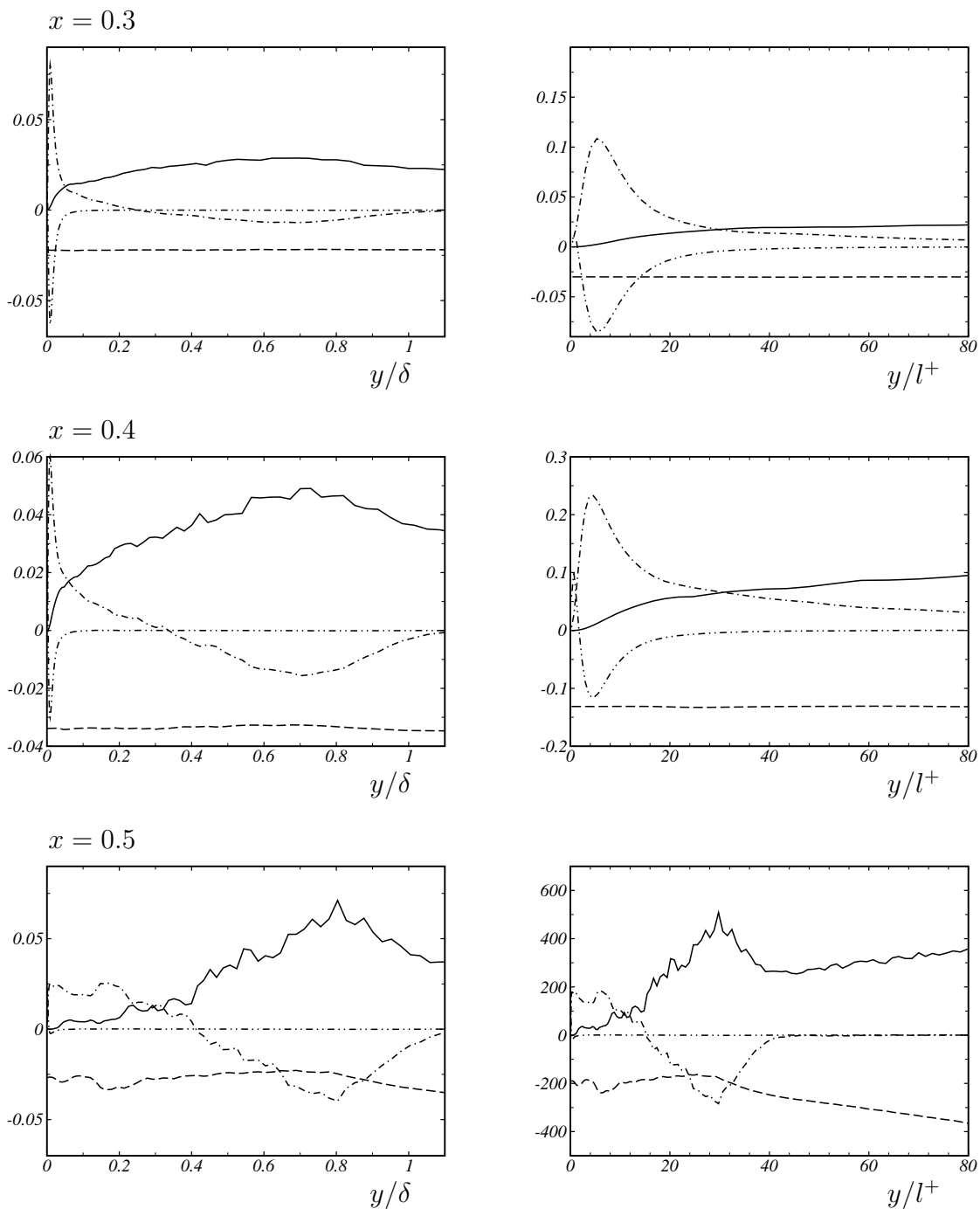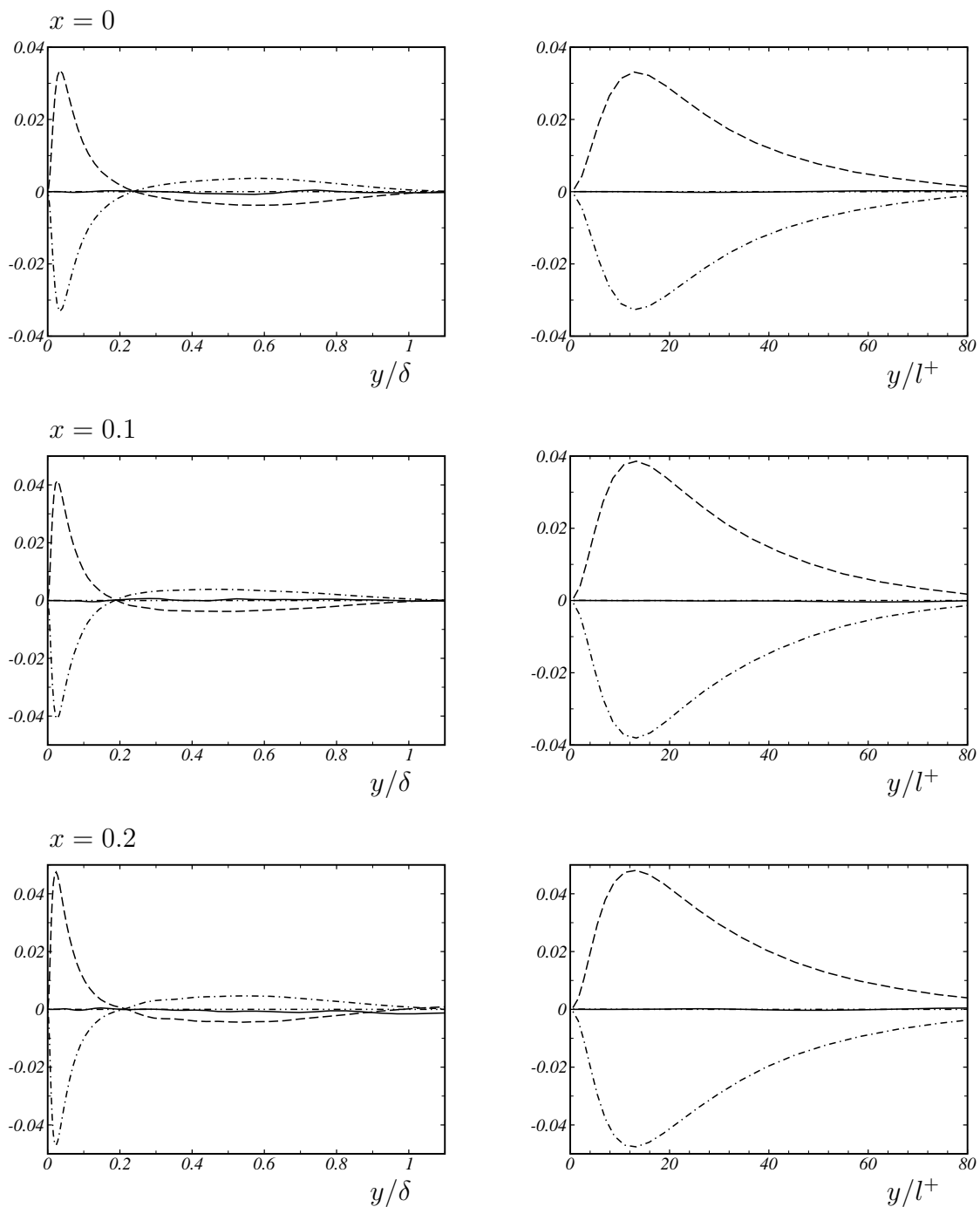
Figure D.8: Wall-normal momentum balance in outer and inner scaling: ———— convection — — —
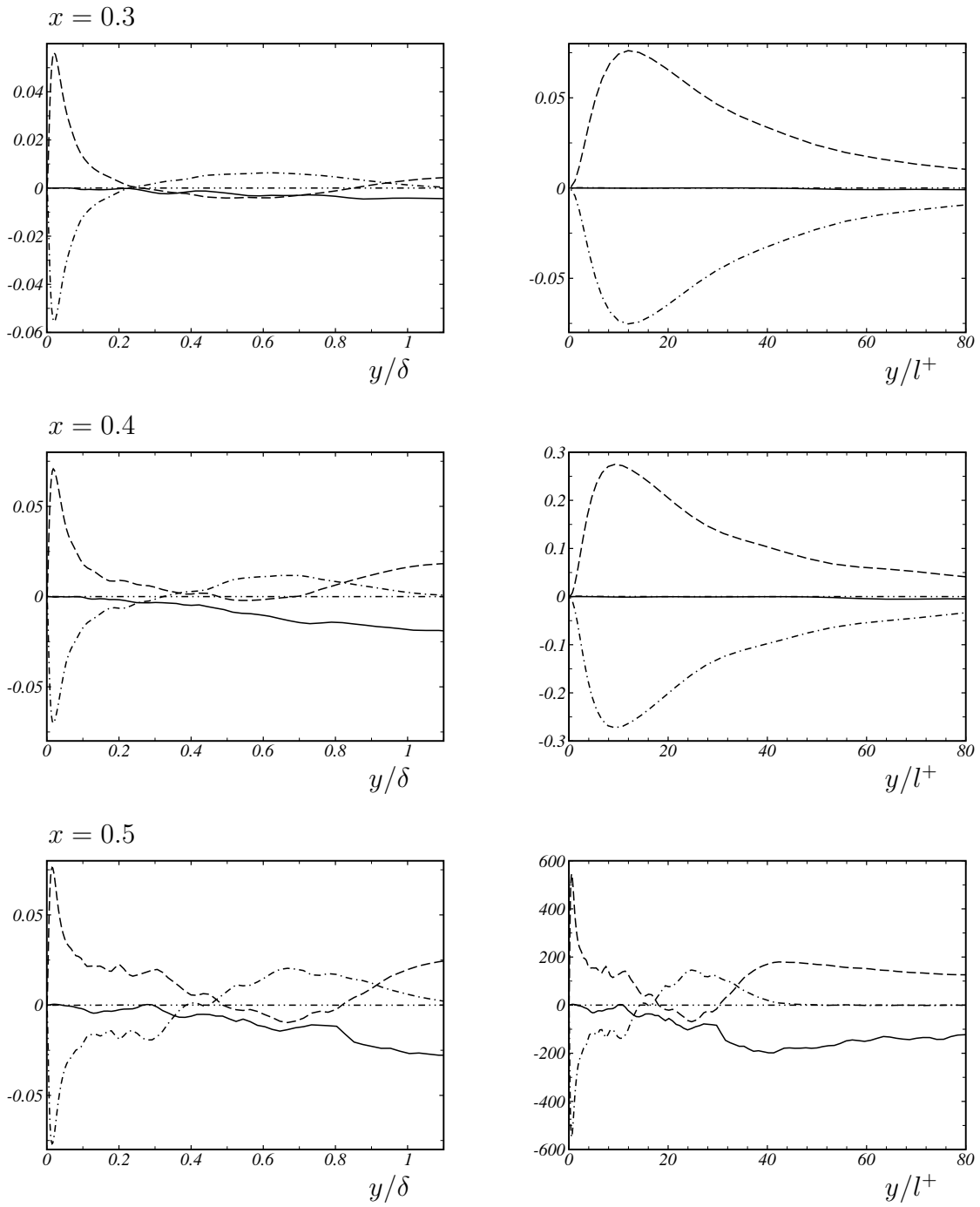pressure normal-stress —··—··— viscous stress ·—·—·— Reynolds stress .

D.3 Budgets of Turbulence Energy

The transport equation for the mean turbulent kinetic energy $k = \frac{1}{2} \langle u'_k u'_k \rangle$ derived from the NAVIER-STOKES equations is

$$
\begin{aligned}
0 = \ & - \ \langle u_k \rangle \, \partial_k \langle u'_j u'_j \rangle && \text{(mean convection)} \\
& - \ \langle u'_j u'_k \rangle \, \partial_k \langle u_j \rangle && \text{(production)} \\
& - \ \nu \frac{1}{2} \left\langle \left(\partial_k u'_j + \partial_j u'_k \right)^2 \right\rangle && \text{(dissipation)} \\
& + \ \nu \frac{1}{2} \, \partial_{kk} \langle u'_i u'_i \rangle + \nu \, \partial_{ij} \langle u'_i u'_j \rangle && \text{(molecular diffusion)} \\
& - \ \frac{1}{2} \, \partial_k \langle u'_j u'_j u'_k \rangle && \text{(turbulent diffusion)} \\
& - \ \partial_k \langle u'_k p' \rangle \ . && \text{(pressure transport)}
\end{aligned}
\tag{D.3}
$$

The individual contributions to the turbulent-kinetic-energy budged indicated in (D.3) are analyzed in Figures D.9 and D.10.

The incoming flow obeys all characteristics of turbulent boundary layers as known from classical textbook presentations, e.g., POPE [136]. The mean-flow convection is negligible. In the viscous sublayer, $y < 4l^+$, the budget is dominated by the viscous diffusion (positive) and the viscous dissipation (negative). In the buffer layer relevant contributions are made by turbulent convection and pressure transport. The largest individual contribution is the turbulence production term. Turbulence energy is generated near the wall, mostly below $y < 50l^+$. The production peak is observed at $y \approx 10l^+$ within the buffer layer. In the logarithmic layer, for $y \geq 40l^+$, the dominant balance is between production and dissipation. Turbulent convection gains importance again at very low magnitudes in the outer part of the boundary layer. This situation changes with increasing x. When the flow approaches separation, more and more turbulence is generated in the wake region. A new production maximum develops around $y = 0.5\delta$, where production is partially balanced by turbulent convection and viscous dissipation. We note that the budget does not sum up to zero, see Fig. D.10. This is due to a coarse grid resolution. The grid points are concentrated near the wall to allow for reliable predictions of the incoming boundary layer flow. At later stations the boundary layer growth into coarser grid regions. This results in an increased proportion of non-represented viscous diffusion and dissipation. These unresolved contributions are represented by the SGS model.

Figure D.9: Resolved budget of turbulent kinetic energy in outer and inner scaling: ——— production ·—·—· viscous diffusion ———— viscous dissipation —··—··— pressure transport ·········· turbulent convection ·——·—— mean convection .
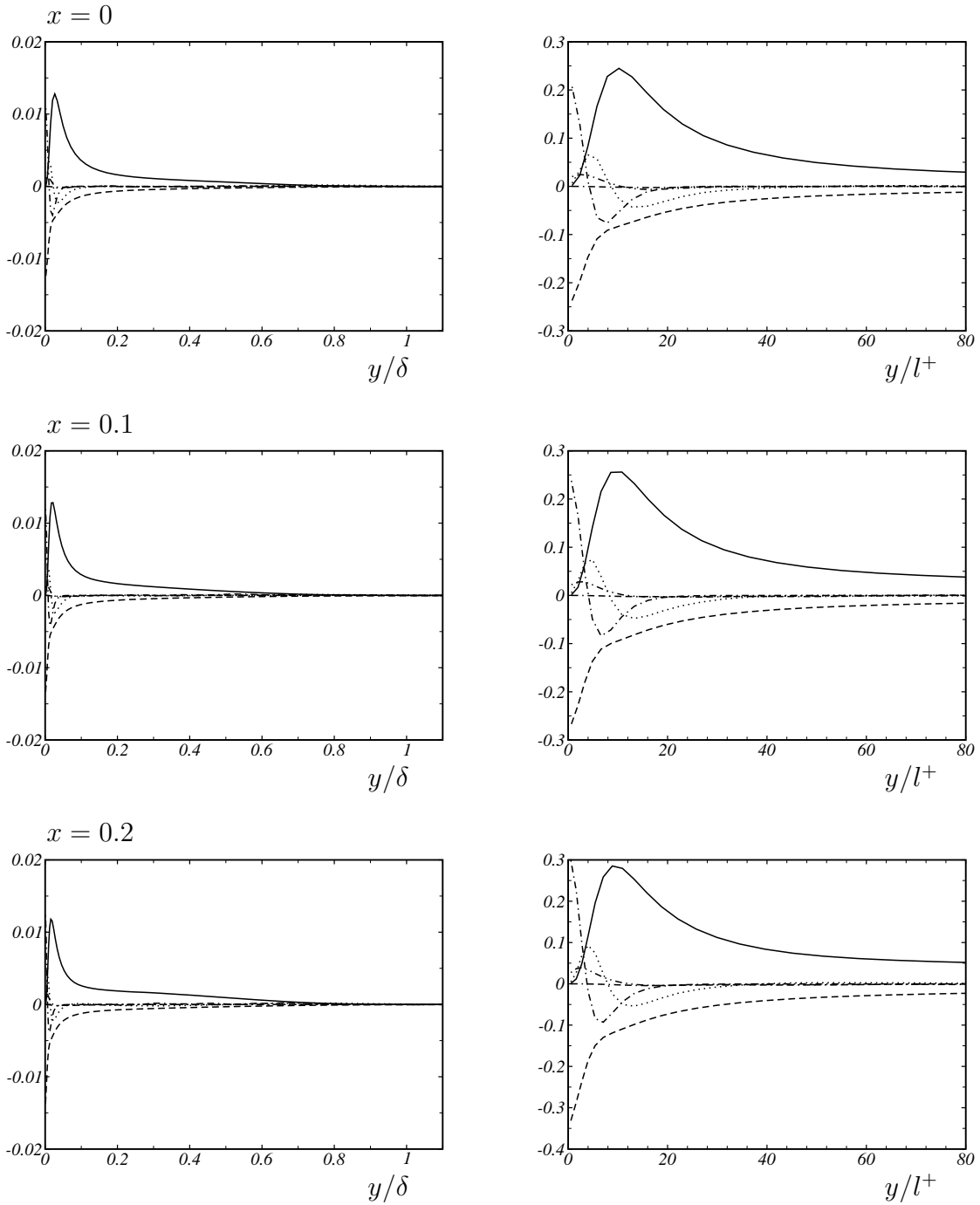
$x = 0.3$

$x = 0.4$

$x = 0.5$
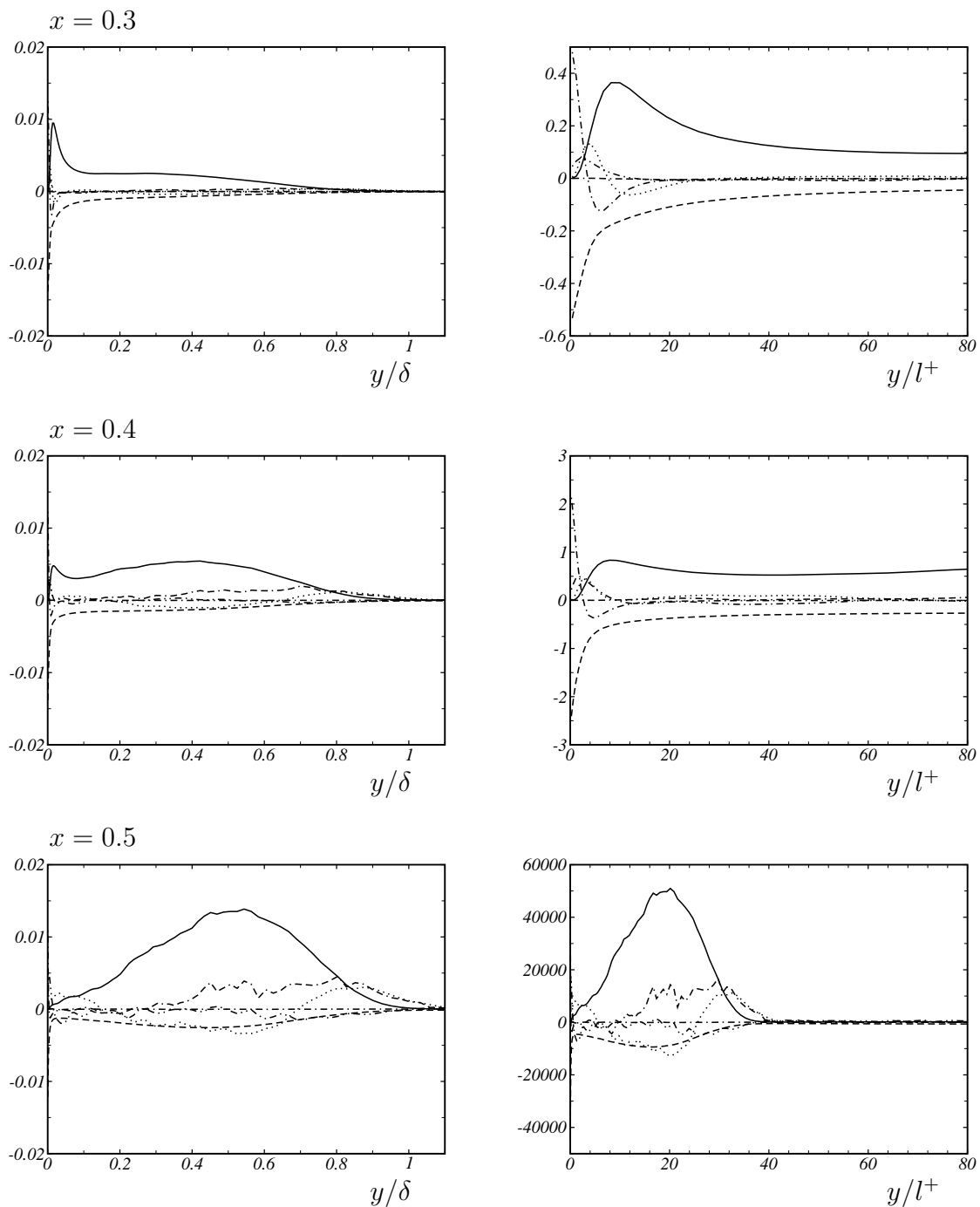
Figure D.10: Resolved budget of turbulent kinetic energy in outer and inner scaling: ———— produc-
tion ·—·—·— viscous diffusion —————— viscous dissipation —·—··—·— pressure transport
·········· turbulent convection ·——·—— mean convection .

D.4 Passive Scalar Mixing

In addition to the experimental setup, transport equations were solved for a passive scalar with SCHMIDT number Sc = 1. The scalar c is transported from an isothermal wall with $C_W = c(y = 0) = 1$ to a fluid with $C_\infty = c(y \gg \delta) = 0$ in the free stream. In this section, a brief description of selected results will be given. A deeper analysis of passive scalar mixing in this APG turbulent boundary layer will be the subject of future work. Figure D.11 gives an overview of mean concentration and scalar variance.
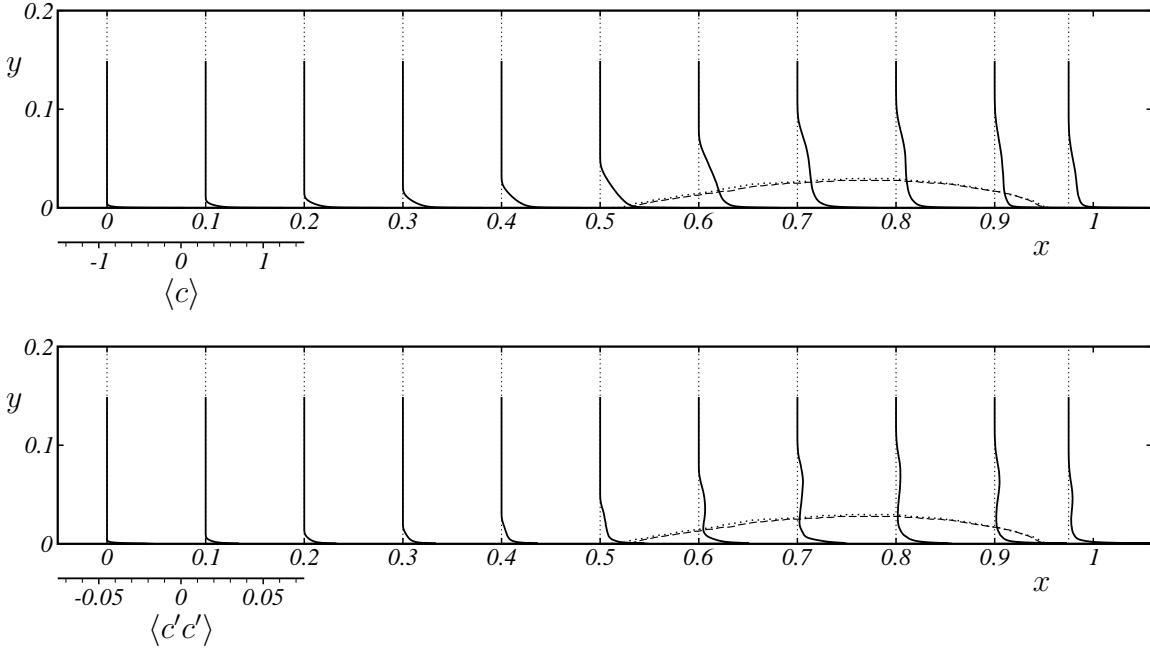
Figure D.11: Mean scalar concentration and scalar variance for LES of adverse-pressure-gradient turbulent-boundary-layer flow.

Mean scalar profiles are presented also in Fig. D.12 in a larger scale. Fig. D.13 shows profiles for the scalar variance and the turbulent transport. Individual terms of the scalar-variance budget

$$
\begin{aligned}
0 = \quad &- \langle u_k \rangle \partial_k \langle c'c' \rangle && \text{(mean convection)} \\
&- 2 \langle c'u'_k \rangle \partial_k \langle c \rangle && \text{(production)} \\
&- 2\kappa \langle \partial_k c' \partial_k c' \rangle && \text{(dissipation)} \\
&+ \kappa \, \partial_{kk} \langle c'c' \rangle && \text{(molecular diffusion)} \\
&- \partial_k \langle u'_k c'c' \rangle && \text{(turbulent diffusion)}
\end{aligned}
\tag{D.4}
$$

are presented in Figures D.14 and D.15.
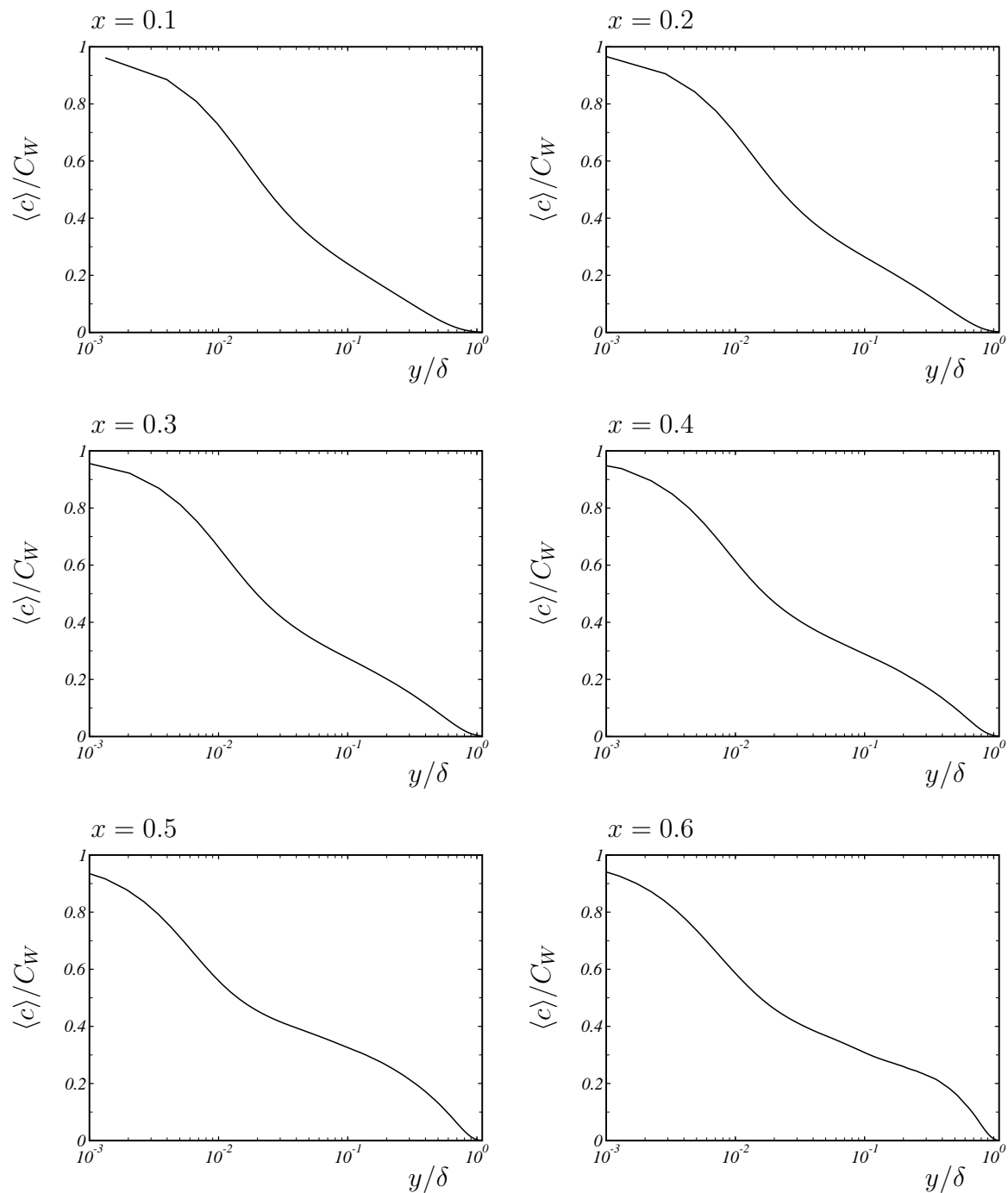
Figure D.12: Mean scalar concentration profiles in outer coordinates.
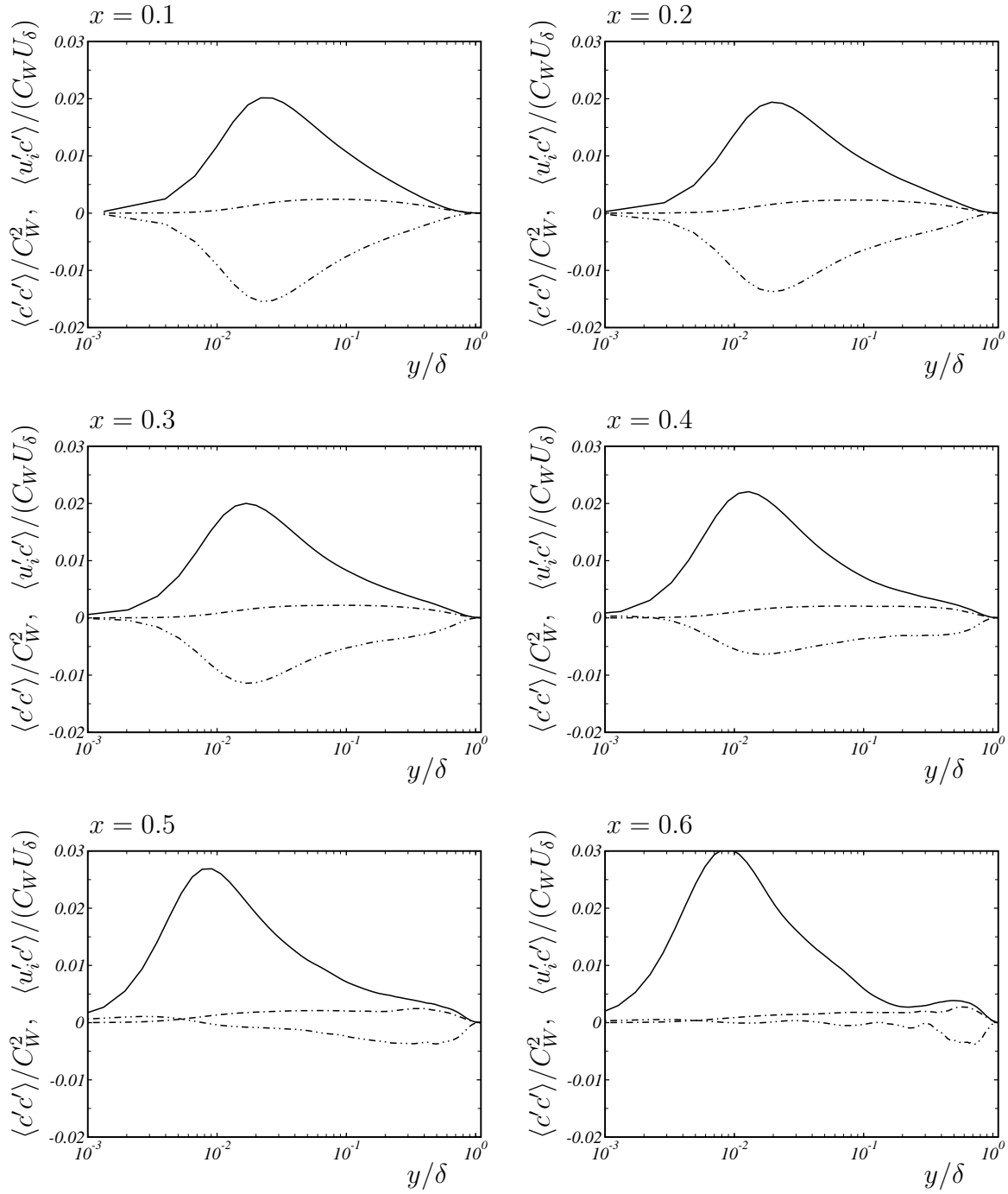
Figure D.13: Scalar variance and turbulent scalar transport.
——— $\langle c'c' \rangle / C_W^2$, —·—··— $\langle u'c' \rangle / (C_W U_\delta)$, ·—·—·— $\langle v'c' \rangle / (C_W U_\delta)$.

Figure D.14: Budget of scalar variance in outer and inner scaling: ———— production – – – – dissipation ·—·—·— molecular diffusion ·········· turbulent diffusion ·—·—·—· mean convection .
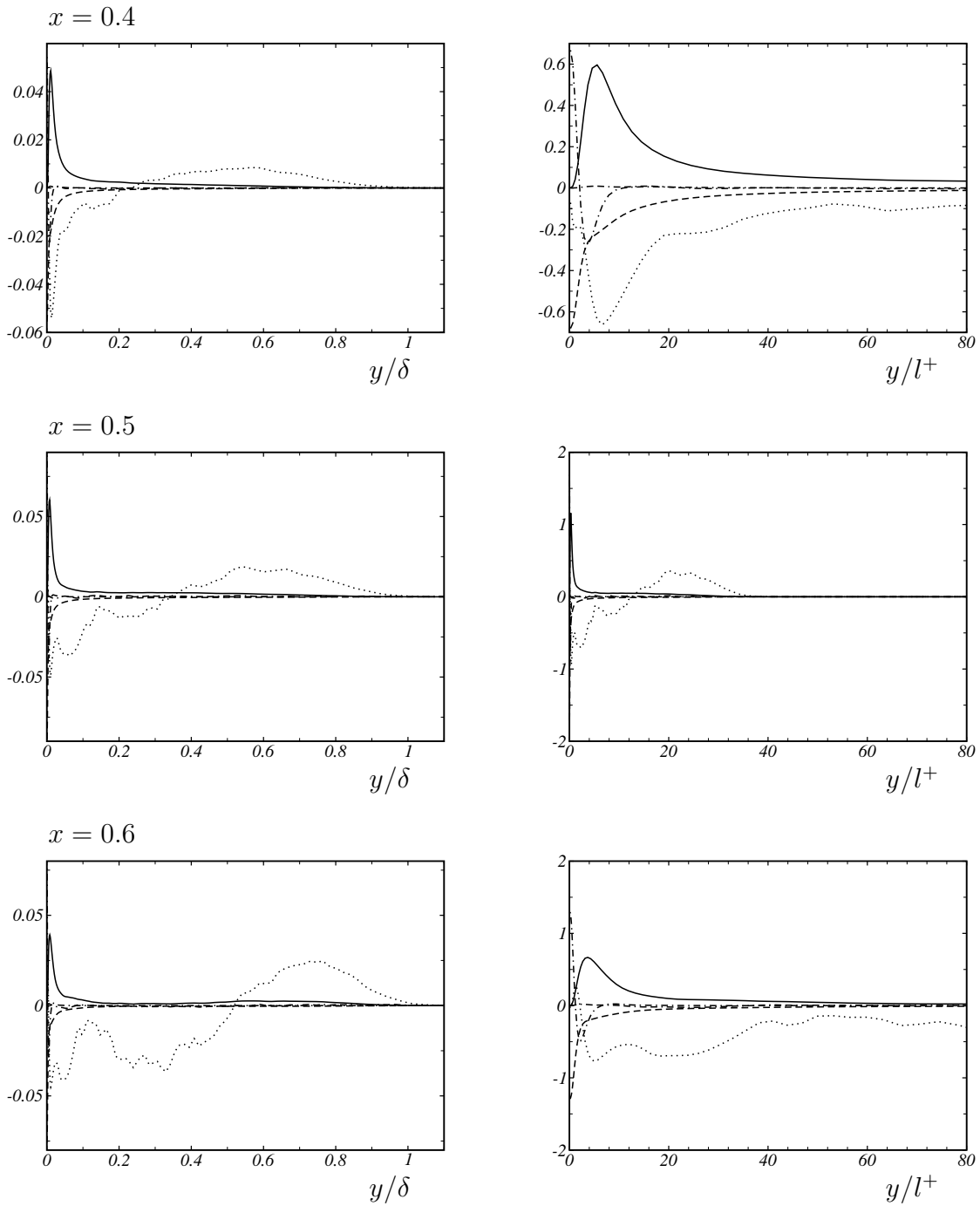
Figure D.15: Budget of scalar variance in outer and inner scaling: ——— production ———— dissipation ·—·—·— molecular diffusion ·········· turbulent diffusion ·—·—·— mean convection
.

D.5 Tabulated Data

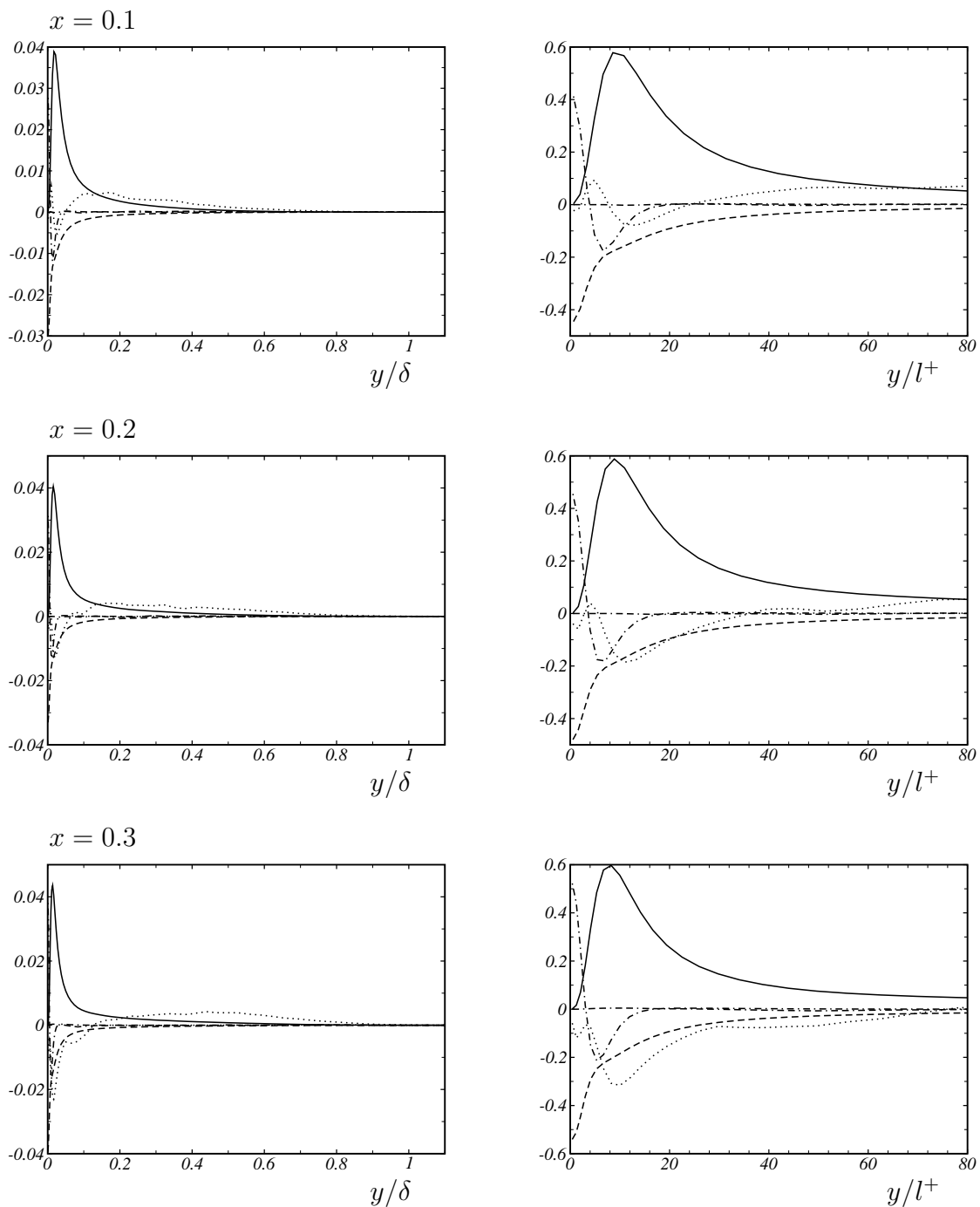| x	U_∞	$\frac{1}{\rho}\langle\partial_x p\rangle_w$	$\frac{1}{\rho}\langle\partial_x p\rangle_\delta$	β	Δ_P	Λ_{δ_2}	$K \cdot 10^6$
0.000	1.08291	0.79704	0.80273	0.21147	0.00402	0.11883	-0.55130
0.025	1.06389	0.80311	0.80892	0.26891	0.00459	0.15843	-0.57432
0.050	1.04442	0.80752	0.81048	0.33786	0.00523	0.19263	-0.61607
0.075	1.02471	0.80391	0.80884	0.42120	0.00596	0.19936	-0.64948
0.100	1.00451	0.80587	0.80886	0.52406	0.00681	0.24510	-0.69847
0.125	0.98385	0.80912	0.81062	0.65241	0.00783	0.24609	-0.73679
0.150	0.96274	0.81782	0.81494	0.81586	0.00906	0.28928	-0.79628
0.175	0.94107	0.82474	0.81944	1.02652	0.01059	0.26931	-0.83023
0.200	0.91887	0.83119	0.82675	1.30804	0.01255	0.33134	-0.92305
0.225	0.89609	0.83582	0.82997	1.67371	0.01493	0.28855	-0.96947
0.250	0.87257	0.84330	0.83410	2.19344	0.01824	0.32845	-1.07840
0.275	0.84825	0.84761	0.83486	2.93184	0.02275	0.36080	-1.18242
0.300	0.82330	0.84815	0.82682	4.03893	0.02933	0.33653	-1.28200
0.325	0.79800	0.82933	0.80429	5.74363	0.03915	0.30300	-1.34920
0.350	0.77263	0.80239	0.76987	8.43214	0.05399	0.30139	-1.46339
0.375	0.74779	0.73644	0.70056	12.9488	0.07963	0.26313	-1.46390
0.400	0.72474	0.64549	0.61454	20.8566	0.12517	0.23709	-1.44083
0.425	0.70352	0.54465	0.51373	35.5964	0.21712	0.20034	-1.39420
0.450	0.68484	0.38556	0.40634	65.8372	0.43552	0.16506	-1.24816
0.475	0.66911	0.29530	0.32513	146.976	1.16080	0.14100	-1.12488
0.500	0.65521	0.24531	0.26163	3456.13	107.717	0.12193	-1.03131
0.525	0.64345	0.13132	0.20864	500.266	4.97482	0.10877	-0.88769
0.550	0.63338	0.16326	0.19328	145.313	0.62344	0.11153	-0.81419
0.575	0.62421	0.09033	0.17879	169.465	0.64971	0.12165	-0.78046
0.600	0.61558	0.04861	0.16615	226.380	0.85531	0.13327	-0.70608

Table D.2: Pressure gradient and pressure-gradient parameters.

x	h_x/l^+	h_y/l^+	h_z/l^+	$t_{ave}U_\delta/\delta_1$	$t_{ave}U_\tau/l^+$
0.000	32.58	1.56 − 65.2	16.29	31755.6	85538.7
0.025	31.24	1.50 − 62.5	15.62	26888.5	78649.0
0.050	29.92	1.44 − 59.8	14.96	22944.1	72158.3
0.075	28.63	1.37 − 57.3	14.32	19680.3	66072.2
0.100	27.39	1.31 − 54.8	13.69	16950.9	60440.2
0.125	26.16	1.26 − 52.3	13.08	14643.3	55164.5
0.150	24.97	1.20 − 49.9	12.48	12652.9	50223.4
0.175	23.74	1.14 − 47.5	11.87	10926.9	45431.1
0.200	22.50	1.08 − 45.0	11.25	9404.9	40806.2
0.225	21.27	1.02 − 42.5	10.63	8056.4	36447.5
0.250	19.93	0.96 − 39.9	9.96	6852.3	31998.2
0.275	18.52	0.89 − 37.0	9.26	5776.8	27629.8
0.300	16.96	0.81 − 33.9	8.48	4806.4	23171.0
0.325	15.26	0.73 − 30.5	7.63	3934.7	18766.1
0.350	13.51	0.65 − 27.0	6.76	3168.6	14710.2
0.375	11.50	0.55 − 23.0	5.75	2507.3	10661.2
0.400	9.47	0.45 − 18.9	4.73	1952.5	7225.7
0.425	7.42	0.36 − 14.8	3.71	1510.3	4441.2
0.450	5.44	0.26 − 10.9	2.72	1169.2	2387.4
0.475	3.64	0.17 − 7.3	1.82	913.2	1069.9
0.500	0.50	0.02 − 1.0	0.25	725.0	30.4
0.525	1.92	0.09 − 3.8	0.96	587.2	299.9
0.550	3.77	0.18 − 7.5	1.89	485.8	1145.8
0.575	3.62	0.17 − 7.2	1.81	411.1	1058.1
0.600	3.23	0.15 − 6.5	1.61	355.8	839.2

Table D.1: Grid parameters and averaging time in outer and inner time units.

x	δ	δ_1	δ_2	δ_3	H_{12}	H_{32}
0.000	0.00590	0.00081	0.00054	0.00095	1.49	1.76
0.025	0.00674	0.00094	0.00063	0.00111	1.48	1.76
0.050	0.00752	0.00108	0.00073	0.00128	1.48	1.75
0.075	0.00828	0.00123	0.00083	0.00145	1.48	1.75
0.100	0.00905	0.00140	0.00094	0.00164	1.49	1.74
0.125	0.00983	0.00159	0.00106	0.00185	1.50	1.74
0.150	0.01068	0.00180	0.00120	0.00207	1.51	1.73
0.175	0.01155	0.00204	0.00134	0.00231	1.52	1.72
0.200	0.01254	0.00232	0.00150	0.00258	1.54	1.71
0.225	0.01360	0.00264	0.00169	0.00288	1.56	1.70
0.250	0.01475	0.00302	0.00190	0.00323	1.58	1.69
0.275	0.01605	0.00348	0.00215	0.00361	1.62	1.68
0.300	0.01758	0.00406	0.00244	0.00407	1.66	1.67
0.325	0.01938	0.00481	0.00279	0.00460	1.72	1.65
0.350	0.02150	0.00578	0.00321	0.00522	1.80	1.63
0.375	0.02414	0.00707	0.00370	0.00594	1.91	1.60
0.400	0.02729	0.00880	0.00428	0.00674	2.06	1.58
0.425	0.03102	0.01104	0.00489	0.00758	2.26	1.55
0.450	0.03542	0.01388	0.00551	0.00841	2.52	1.53
0.475	0.04041	0.01736	0.00610	0.00920	2.85	1.51
0.500	0.04591	0.02142	0.00667	0.00998	3.21	1.50
0.525	0.05184	0.02597	0.00715	0.01067	3.63	1.49
0.550	0.05804	0.03090	0.00749	0.01124	4.13	1.50
0.575	0.06433	0.03598	0.00777	0.01178	4.63	1.51
0.600	0.07031	0.04101	0.00791	0.01215	5.18	1.54

Table D.3: Boundary-layer thickness and shape parameters.

x	Re_δ	Re_{δ_1}	Re_{δ_2}	Re_τ	$C_f \cdot 10^3$	χ_{wall}
0.000	7478	1025	686.9	384.39	5.285	0.000
0.025	8389	1168	787.1	420.88	5.035	0.000
0.050	9194	1319	890.1	450.08	4.793	0.000
0.075	9926	1480	997.3	473.93	4.559	0.000
0.100	10641	1651	1108.5	495.70	4.340	0.000
0.125	11325	1834	1224.8	514.59	4.129	0.001
0.150	12032	2032	1347.2	533.09	3.926	0.001
0.175	12728	2249	1477.3	548.71	3.717	0.001
0.200	13487	2491	1618.7	564.34	3.502	0.002
0.225	14265	2765	1774.7	578.45	3.289	0.003
0.250	15065	3083	1945.7	587.82	3.045	0.004
0.275	15935	3456	2135.8	594.34	2.782	0.007
0.300	16944	3912	2354.6	596.28	2.477	0.013
0.325	18099	4490	2608.6	591.39	2.135	0.025
0.350	19448	5227	2903.2	581.10	1.786	0.050
0.375	21127	6187	3242.5	555.26	1.382	0.097
0.400	23156	7463	3628.8	516.98	0.997	0.169
0.425	25548	9092	4030.1	460.69	0.651	0.262
0.450	28391	11129	4418.8	385.66	0.369	0.351
0.475	31649	13601	4777.9	294.63	0.174	0.432
0.500	35212	16427	5115.5	68.77	0.009	0.503
0.525	39044	19562	5382.5	200.71	-0.053	0.532
0.550	43030	22912	5551.6	437.75	-0.207	0.617
0.575	47003	26293	5680.8	466.29	-0.197	0.611
0.600	50668	29550	5699.2	453.83	-0.160	0.593

Table D.4: REYNOLDS numbers, friction coefficient, and reverse-flow parameter.

BIBLIOGRAPHY

[1] ADAMS, N. A., HICKEL, S. & FRANZ, S. 2004 Implicit subgrid-scale modeling by adaptive deconvolution. *J. Comp. Phys.* **200**, 412–431.

[2] AGARD, ed. 1998 *A Selection of Test Cases for the Validation of Large-Eddy Simulations of Turbulent Flows. Technical Report AGARD-AR-345* AGARD-AR-345. NATO.

[3] ALDAMA, A. A. 1990 *Filtering techniques for turbulent flow simulation*, *Lecture Notes in Engineering*, vol. 56. Berlin: Springer.

[4] BACK, T., FOGEL, D. & MICHALEWICZ, Z. 1997 *Handbook of Evolutionary Computation*. University Oxford Press.

[5] BARDINA, J., FERZIGER, J. H. & REYNOLDS, W. C. 1980 Improved subgrid-scale models for large-eddy simulation. *AIAA paper* pp. No. 80–1357.

[6] BATCHELOR, G. 1953 *The Theory of Homogenous Turbulence*. Cambridge University Press.

[7] BATCHELOR, G., HOWELLS, I. & TOWNSEND, A. 1959 Small-scale variation of convected quantities like temperature in turbulent fluid. Part 2. The case of large conductivity. *J. Fluid Mech.* **5**, 134–139.

[8] BATCHELOR, G. K. 1959 Small-scale variation of convected quantities like temperature in turbulent fluid. Part 1. General discussion and the case of small conductivity. *J. Fluid Mech.* **5**, 113–133.

[9] BEASLEY, D., BULL, D. R. & MARTIN, R. R. 1993 An overview of genetic algorithms: Part 1, fundamentals. *University Computing* **15**, 58–69.

[10] BEASLEY, D., BULL, D. R. & MARTIN, R. R. 1993 An overview of genetic algorithms: Part 2, research topics. *University Computing* **15**, 170–181.

[11] BERNARD, A., FOUCAUT, J. M., DUPONT, P. & STANISLAS, M. 2003 Decelerating boundary layer: A new scaling and mixing length model. *AIAA Journal* **41** (2), 248–255.

[12] BOGUCKI, D., DOMARADZKI, J. & YEUNG, P. 1997 Direct numerical simulations of passive scalars with Pr > 1 advected by turbulent flow. *Journal of Fluid Mechanics* **343**, 111–130.

[13] BORIS, J. & BROOK, D. 1973 Flux corrected transport. I. SHASTA, a fluid transport algorithm that works. *J. Comput. Phys.* **11**, 38–69.

[14] BORIS, J. P., GRINSTEIN, F. F., ORAN, E. S. & KOLBE, R. L. 1992 New insights into large eddy simulation. In *Fluid Dynamics Research*, , vol. 10, pp. 199–228. North Holland.

[15] BRACHET, M. E., MEIRON, D. I., ORSZAG, S. A., NICKEL, B. G., MORF, R. H. & FRISCH, U. 1983 Small-scale structure of the Taylor-Green vortex. *J. Fluid. Mech.* **130**, 411–452.

[16] BRACHET, M. E., MENEGUZZI, M., VINCENT, A., POLITANO, H. & SULEM, P.-L. 1992 Numerical evidence of smooth self-similar dynamics and possibility of subsequent collapse for three-dimensional ideal flow. *Phys. Fluids* **4**, 2845–2854.

[17] CALMET, I. & MAGNAUDET, J. 1996 Large-eddy simulation of high-schmidt number mass transfer in a turbulent channel flow. *Phys. Fluids* **9**, 438–455.

[18] CARATI, D., GHOSAL, S. & MOIN, P. 1995 On the representation of backscatter in dynamic localization models. *Physics of Fluids* **7**, 606–616.

[19] CASTILLO, L. & GEORGE, W. K. 2001 Similarity analysis for turbulent boundary layer with pressure gradient : Outerflow. *AIAA Journal* **39** (1), 41–47.

[20] CASTILLO, L., XIAWANG & GEORGE, W. K. 2004 Separation criterion for turbulent boundary layers via similarity analysis. *Journal of Fluids Engineering* **126** (1), 297–303.

[21] CHAPMAN, D. R. 1979 Computational aerodynamics, development and outlook. *AIAA Journal* **17**, 1293–1313.

[22] CHEKHLOV, A. & YAKHOT, V. 1995 Kolmogorov turbulence in a random-force driven Burgers equation: anomaleous scaling and probability density function. *Phys. Rev. E* **52**, 5681–5684.

[23] CHOLLET, J.-P. 1984 Two-point closures as a subgrid-scale modeling tool for large-eddy simulations. In *Turbulent Shear Flows IV* (ed. F.Durst & B. Launder), pp. 62–72. Heidelberg: Springer.

[24] CHOLLET, J.-P. & LESIEUR, M. 1981 Parametrization of small scales of three-dimensional isotropic turbulence utilizing spectral closures. *J. Atmos. Sci.* **38**, 2747–2757.

[25] CLAUSER, F. H. 1954 Turbulent boundary layers in adverse pressure gradient. *J. Aeronaut. Sci.* **21**, 91–108.

[26] COLELLA, P. & WOODWARD, P. R. 1984 The piecewise parabolic method (PPM) for gas-dynamical simulations. *J. Comput. Phys.* **54**, 174–201.

[27] COMTE-BELLOT, G. & CORRSIN, S. 1971 Simple Eulerian time correlation of full and narrow-band velocity signals in grid-generated 'isotropic' turbulence. *J. Fluid Mech.* **48**, 273–337.

[28] CORRSIN, S. 1951 On the spectrum of isotropic temperature fluctuations in an isotropic turbulence. *Journal of Applied Physics* **22** (4), 469–473.

[29] COURANT, R., FRIEDRICHS, K. O. & LEWY, H. 1928 Über die partiellen Differenzengleichungen der mathematischen Physik. *Mathematische Annalen* **100**, 32–74.

[30] DAKHOUL, V. M. & BEDFORD, K. W. 1986 Improved averaging method for turbulent flow simulation. I - Theoretical development and application to Burgers' transport equation. *International Journal for Numerical Methods in Fluids* **6**, 49–64.

[31] DEARDORFF, J. W. 1970 Numerical study on turbulent channel flow. *J. Fluid Mech.* **41**, 453–480.

[32] DEL ÁLAMO, J., JIMÉNEZ, J., ZANDONADE, P. & MOSER, R. 2004 Scaling of the energy spectra of turbulent channels. *J. Fluid Mech.* **500**, 135–144.

[33] DENGEL, P. & FERNHOLZ, H. H. 1990 An experimental investigation of an incompressible turbulent boundary layer in the vicinity of separation. *Journal of Fluid Mechanics* **212**, 615–636.

[34] DOMARADZKI, J. A. & ADAMS, N. A. 2002 Direct modeling of subgrid scales of turbulence in large-eddy simulations. *J. Turb.* **3**, 24.

[35] DOMARADZKI, J. A., METCALFE, R. W., ROGALLO, R. S. & RILEY, J. J. 1987 Analysis of subgrid-scale eddy viscosity with use of results from direct numerical simulations. *Phys. Rev. Lett.* **58** (6), 547–550.

[36] DOMARADZKI, J. A. & RADHAKRISHNAN, S. 2005 Eddy viscosities in implicit large eddy simulations of decaying high Reynolds number turbulence with and without rotation. *Fluid Dynamics Research* **36**, 385–406.

[37] DOMARADZKI, J. A. & SAIKI, E. M. 1997 Backscatter models for large-eddy simulation. *Theoret. Comput. Fluid Dynamics* **9**, 75–83.

[38] DOMARADZKI, J. A., XIAO, Z. & SMOLARKIEWICZ, P. K. 2003 Effective eddy viscosities in implicit large eddy simulations of turbulent flows. *Phys. Fluids* **15**, 3890–3893.

[39] FERNHOLZ, H.-H. 1964 Halbempirische Gesetze zur Berechnung turbulenter Grenzschichten nach der Methode der Integralbedingungen. *Ingenieur-Archiv* **33** (6), 384–395.

[40] FERZIGER, J. H. & PERIC, M. 1999 *Computational Methods for Fluid Dynamics*. Springer.

[41] FRISCH, U. 1995 *Turbulence*. Cambridge University Press.

[42] FUREBY, C. & GRINSTEIN, F. F. 2002 Large eddy simulation of high-Reynolds-number free and wall-bounded flows. *J. Comput. Phys.* **181**, 68–97.

[43] FUREBY, C., TABOR, G., WELLER, H. G. & GOSMAN, A. D. 1997 A comparative study of subgrid scale models in homogeneous isotropic turbulence. *Phys. Fluids* **9**, 1416–1429.

[44] GARNIER, E., MOSSI, M., SAGAUT, P., COMTE, P. & DEVILLE, M. 1999 On the use of shock-capturing schemes for large-eddy simulation. *J. Comput. Phys.* **153**, 273–311.

[45] GEORGE, W. K. 2006 Recent advancements toward the understanding of turbulent boundary layers. *AIAA Journal* **44** (11), 2435–2449.

[46] GERMANO, M., PIOMELLI, U., MOIN, P. & CABOT, W. H. 1991 A dynamic subgrid-scale eddy viscosity model. *Phys. Fluids* **A 3**, 1760–1765.

[47] GEURTS, B. J. & FRÖHLICH, J. 2002 A framework for prediction accuracy limitations in large-eddy simulation. *Phys. Fluids* **14** (6), L41–L44.

[48] GHOSAL, S. 1996 An analysis of numerical errors in large-eddy simulations of turbulence. *J. Comput. Phys.* **125**, 187–206.

[49] GHOSAL, S., LUND, T. S., MOIN, P. & AKSELVOLL, K. 1995 A dynamic localization model for large-eddy simulation of turbulent flows. *J. Fluid Mech.* **286**, 229–255.

[50] GOTTLIEB, S. & SHU, C.-W. 1998 Total variation diminishing Runge-Kutta schemes. *Math. Comput.* **67**, 73–85.

[51] GRINSTEIN, F., MARGOLIN, L. & RIDER, W., ed. 2007 *Implicit Large Eddy Simulation: Computing Turbulent Flow Dynamics*. Cambridge, UK: Cambridge University Press.

[52] GRINSTEIN, F. F. & FUREBY, C. 2004 From canonical to complex flows: Recent progress on monotonically integrated LES. *Comp. Sci. Eng.* **6**, 36–49.

[53] GRÖTZBACH, G. 1977 Direkte numerische Simulation turbulenter Geschwindigkeits-, Druck- und Temperaturfelder bei Kanalströmungen. PhD thesis, Universität Karlsruhe.

[54] GRÖTZBACH, G. 1987 Direct numerical and large eddy simulation of turbulent channel flows. In *Encyclopaedia of Fluid Mechachnics* (ed. N. Cheremisino), pp. 1337–1391. Houston: Gulf Publication.

[55] GRÖTZBACH, G. & SCHUMANN, U. 1977 Direct numerical simulation of turbulent velocity-, pressure-, and temperature-fields in channel flows. In *First Symposium on Turbulent Shear Flows*, pp. 370–385. Berlin: Springer.

[56] GULLBRAND, J. & CHOW, F. K. 2003 The effect of numerical errors and turbulence models in large-eddy simulations of channel flow, with and without explicit filtering. *J. Fluid Mech.* **495**, 323–341.

[57] HARTEN, A., ENGQUIST, B., OSHER, S. & CHAKRAVARTHY, S. 1987 Uniformly high order accurate essentially non-oscillatory schemes, III. *J. Comp. Phys.* **71**, 231–303.

[58] HARTEN, A., LAX, P. D. & VAN LEER, B. 1983 On upstream differencing and Godunov-type schemes for hyperbolic conservation laws. *SIAM Review* **25** (1), 35–61.

[59] HEAD, M. R. & RAM, V. V. 1971 Improved presentation of preston tube calibration. *Aeronautical Quaterly* **22**, 295–300.

[60] HEISENBERG, W. 1948 Zur statistischen Theorie der Turbulenz. *Z. Phys. A* **124**, 628–657.

[61] HICKEL, S. & ADAMS, N. A. 2004 Implicit subgrid-scale modeling by adaptive local deconvolution. *Proc. Appl. Math. Mech.* **4**, 460–461.

[62] HICKEL, S. & ADAMS, N. A. 2006 ALDM - A modeling environment for ILES. In *Proceedings of the European Conference on Computational Fluid Dynamics EC-COMAS CFD 2006* (ed. P. Wesseling, E. Onate & J. Périaux). TU Delft.

[63] HICKEL, S. & ADAMS, N. A. 2006 Efficient implementation of nonlinear deconvolution methods for implicit large-eddy simulation. In *High Performance Computing in Science and Engineering. Transactions of the High Performance Computing Center, Stuttgart (HLRS)* (ed. W. Nagel, W. Jäger & M. Resch), pp. 293–306. Springer.

[64] HICKEL, S. & ADAMS, N. A. 2007 LES of turbulent boundary-layer separation. In *Proceedings of the 5th International Symposium on Turbulence and Shear Flow Phenomena (TSFP5)* (ed. R. Friedrich, N. A. Adams, J. K. . Eaton, J. A. C. Humphrey, N. Kasagi & M. A. Leschziner), pp. 321–326.

[65] HICKEL, S. & ADAMS, N. A. 2007 On implicit subgrid-scale modeling in wall-bounded flows. *Phys. Fluids* **19**, 105106.

[66] HICKEL, S. & ADAMS, N. A. 2007 A proposed simplification of the adaptive local deconvolution method. *ESAIM: Proceedings* **16**, 66–76, special issue for the proceedings of the Centre d'été Mathématique de Recherche Avancée en Calcul scientifique (CEMRACS) 2005, Marseille, France.

[67] HICKEL, S. & ADAMS, N. A. 2008 Implicit LES applied to zero-pressure-gradient and adverse-pressure-gradient boundary-layer turbulence. *Int. J. Heat and Fluid Flow* **29**, 626–639.

[68] HICKEL, S., ADAMS, N. A. & DOMARADZKI, J. A. 2004 Physically optimized implicit LES. *Bulletin of the American Physical Society* **49**, .

[69] HICKEL, S., ADAMS, N. A. & DOMARADZKI, J. A. 2006 An adaptive local deconvolution method for implicit LES. *J. Comp. Phys.* **213**, 413–436.

[70] HICKEL, S., ADAMS, N. A. & MANSOUR, N. N. 2006 Implicit subgrid-scale modeling for large-eddy simulation of passive-scalar mixing. In *Proceedings of the 2006 Summer Program*, pp. 123–138. Center for Turbulence Research, Stanford University.

[71] HICKEL, S., ADAMS, N. A. & MANSOUR, N. N. 2007 Implicit subgrid-scale modeling for large-eddy simulation of passive-scalar mixing. *Phys. Fluids* **19**, 095102.

[72] HICKEL, S., FRANZ, S., ADAMS, N. A. & KOUMOUTSAKOS, P. D. 2004 Optimization of an implicit subgrid-scale model for LES. In *Proceedings of the 21st International Congress of Theoretical and Applied Mechanics (ICTAM)*. Warsaw, Poland.

[73] HICKEL, S., KEMPE, T. & ADAMS, N. A. 2005 On implicit subgrid-scale modeling in wall-bounded flows. In *Proceedings of the EUROMECH Colloquium 469*, pp. 36–37. Dresden, Germany.

[74] HICKEL, S., KEMPE, T. & ADAMS, N. A. 2008 Implicit large-eddy simulation applied to turbulent channel flow with periodic constrictions. *Theoret. Comput. Fluid Dynamics* **22**, 227–242.

[75] HICKEL, S., WEYNANS, L., ADAMS, N. A. & COTTET, G.-H. 2007 Towards implicit subgrid-scale modeling by particle methods. *ESAIM: Proceedings* **16**, 77–88, special issue for the proceedings of the Centre d'été Mathématique de Recherche Avancée en Calcul scientifique (CEMRACS) 2005, Marseille, France.

[76] INDINGER, T. 2005 Einfluss eines positiven Druckgradienten auf turbulente Grenzschichten an glatten und gerillten Oberflächen. PhD thesis, TU München.

[77] INDINGER, T., BUSCHMANN, M. H. & GAD-EL-HAK, M. 2006 Mean-velocity profile of turbulent boundary layers approaching separation. *AIAA Journal* **44** (11), 2465–2474.

[78] INDINGER, T., HICKEL, S. & ADAMS, N. 2004 3D-measurements in an adverse-pressure-gradient turbulent boundary layer over smooth and ribbed surfaces. In *Proceedings of the 21st International Congress of Theoretical and Applied Mechanics (ICTAM)*. Warsaw, Poland.

[79] JEONG, J. & HUSSAIN, F. 1995 On the identification of a vortex. *J. Fluid Mech.* **285**, 69–94.

[80] JIANG, G.-S. & SHU, C.-W. 1996 Efficient implementation of weighted ENO schemes. *J. Comput. Phys.* **126**, 202–228.

[81] KADER, B. A. & YAGLOM, A. M. 1972 Heat and mass transfer laws for fully turbulent wall flows. *Int. J. Heat Mass Transfer* **15**, 2329–2353.

[82] KALTER, M. & FERNHOLZ, H. H. 2001 The reduction and elimination of a closed separation region by free-stream turbulence. *J. Fluid Mech.* **446**, 271–308.

[83] KANG, H., CHESTER, S. & MENEVEAU, C. 2003 Decaying turbulence in an active-grid-generated flow and large-eddy simulation. *J. Fluid Mech.* **480**, 129–160.

[84] KARAMANOS, G.-S. & KARNIADAKIS, G. 2000 A spectral vanishing viscosity method for large-eddy simulations. *J. Comput. Phys.* **163**, 22–50.

[85] KAWAMURA, T. & KUWAHARA, K. 1984 Computation of high Reynolds number flow around a circular cylinder with surface roughness. *AIAA paper* **84-0340**.

[86] KEMPE, T. 2003 LES of turbulent channel flow using the dynamic Smagorinsky model. Personal communication.

[87] KIM, J., MOIN, P. & MOSER, R. 1987 Turbulence statistics in fully developed channel flow at low Reynolds number. *J. Fluid Mech.* **177**, 133–166.

[88] KRAICHNAN, R. 1968 Small-scale structure of a scalar field convected by turbulence. *Phys. Fluids* **11**, 945–953.

[89] KRAVCHENKO, A. G. & MOIN, P. 1997 On the effect of numerical errors in large-eddy simulation of turbulent flows. *J. Comp. Phys.* **130**, 310–322.

[90] LANGFORD, J. A. & MOSER, R. D. 2001 Breakdown of continuity in large-eddy simulation. *Phys. Fluids* **13**, 1524–1527.

[91] LELE, S. K. 1992 Compact finite difference schemes with spectral-like resolution. *Journal of Computational Physics* **103** (1), 16–42.

[92] LEONARD, A. 1974 Energy cascade in large eddy simulations of turbulent fluid flows. *Adv. Geophys.* **18A**, 237–248.

[93] LESIEUR, M. 1997 *Turbulence in Fluids*, 3rd edn. Dordrecht, The Netherlands: Kluwer Academic Publishers.

[94] LESIEUR, M., COMTE, P., DUBIEF, Y., LAMBALLAIS, E., MÉTAIS, O. & OSSIA, S. 1999 From two-point closures of isotropic turbulence to LES of shear flows. *Flow, Turbulence and Combustion* **63**, 247–267.

[95] LESIEUR, M. & MÉTAIS, O. 1996 New trends in large-eddy simulations of turbulence. *Annu. Rev. Fluid. Mech.* **28**, 45–82.

[96] LESLIE, D. & QUARINI, G. 1979 The application of turbulence theory to the formulation of subgrid modelling procedures. *Journal of Fluid Mechanics* **91**, 65–91.

[97] LÉVÊQUE, E., TOSCHI, F., SHAO, L. & BERTOGLIO, J.-P. 2007 Shear-improved Smagorinsky model for large-eddy simulation of wall-bounded turbulent flows. *J. Fluid Mech.* **570**, 491–502.

[98] LEVEQUE, R. J. 1992 *Numerical methods for conservation laws*. Basel, Switzerland: Birkhäuser.

[99] LILLY, D. K. 1966 *On the application of the eddy viscosity concept in the inertial subrange of turbulence*. Boulder, Colorado: National Center for Atmospheric Research, nCAR MS 123.

[100] LILLY, D. K. 1967 The representation of small-scale turbulence in numerical simulation experiments. In *Proc. IBM Scientific Computing Symposium on Environmental Sciences* (ed. H. H. Goldstein), pp. 195–201. IBM.

[101] LILLY, D. K. 1992 A proposed modification of the Germano subgrid-scale closure model. *Phys. Fluids A* **4**, 633–635.

[102] LIU, S. W., MENEVEAU, C. & KATZ, J. 1994 On the properties of similarity subgrid-scale models as deduced from measurements in a turbulent jet. *J. Fluid Mech.* **275**, 83–119.

[103] LUDWIEG, H. & TILLMANN, W. 1949 Untersuchungen über die Wandschubspannungen in turbulenten Reibungsschichten. *Ingenieur-Archiv* **17**, 288–299.

[104] LUMLEY, J. L. 1978 Computational modeling of turbulent flows. *Adv. Appl. Mech.* **18**, 123–176.

[105] LUMLEY, J. L. & NEWMAN, G. 1977 The return to isotropy of homogeneous turbulence. *J. Fluid Mech.* **82**, 161–178.

[106] LUND, T., WU, X. & SQUIRES, K. 1998 Generation of turbulent inflow data for spatially-developing boundary layer simulations. *J. Comp. Phys.* **140**, 233–258.

[107] LYONS, S., HANRATTY, T. & MCLAUGHLIN, J. B. 1991 Large-scale computer simulation of fully developed turbulent channel flow with heat transfer. *Int. J. Num. Meth. Fluids* **13**, 999–1028.

[108] MACIEL, Y., ROSSIGNOL, K.-S. & LEMAY, J. 2006 Self-similarity in the outer region of adverse-pressure-gradient turbulent boundary layers. *AIAA Journal* **44**, 2450–2464.

[109] MANHART, M. & FRIEDRICH, R. 2002 DNS of a turbulent boundary layer with separation. *Int. J. Heat and Fluid Flow* **23**, 572–581.

[110] MANHART, M., PELLER, N. & BRUN, C. 2007 Near-wall scaling for turbulent boundary layers with adverse pressure gradient: A priori tests on DNS of channel flow with periodic hill constrictions and DNS of separating boundary layer. *Theoret. Comput. Fluid Dynamics* (in press).

[111] MARGOLIN, L., RIDER, W. & GRINSTEIN, F. 2006 Implicit turbulence modeling for high Reynolds number flows. *Journal of Turbulence* **7** (15), 1–27.

[112] MARGOLIN, L. G. & RIDER, W. J. 2002 A rationale for implicit turbulence modeling. *Int. J. Numer. Meth. Fluids* **39**, 821–841.

[113] MARGOLIN, L. G. & RIDER, W. J. 2005 The design and construction of implicit LES models. *Int. J. Numer. Meth. Fluids* **47**, 1173–1179.

[114] MARGOLIN, L. G., SMOLARKIEWICZ, P. K. & WYSZOGRODZKI, A. A. 2002 Implicit turbulence modeling for high Reynolds number flows. *Journal of Fluids Engineering* **124**, 862–867.

[115] MCCOMB, W. D. 1990 *The Physics of Fluid Turbulence*. Oxford: Clarendon Press.

[116] MENEVEAU, C. & KATZ, J. 2000 Scale-invariance and turbulence models for large-eddy simulation. *Annu. Rev. Fluid. Mech.* **32**, 1–32.

[117] MENEVEAU, C., LUND, T. & CABOT, E. 1996 A Lagrangian dynamic subgrid-scale model of turbulence. *J. Fluid Mech.* **319**, 353–385.

[118] MÉTAIS, O. & LESIEUR, M. 1992 Spectral large-eddy simulations of isotropic and stably-stratified turbulence. *J. Fluid Mech.* **239**, 157–194.

[119] MISRA, A. & LUND, T. S. 1996 Evaluation of a vortex-based subgrid stress model using DNS databases. In *CTR Proc. 1996 Summer Program*, pp. 359–368. Stanford, California: Center for Turbulence Research,Stanford University and NASA Ames Research Center.

[120] MORINISHI, Y., LUND, T., VASILYEV, O. & MOIN, P. 1998 Fully conservative higher order finite difference schemes for incompressible flow. *J. Comput. Phys.* **143**, 90–124.

[121] MOSER, R. D., KIM, J. & MANSOUR, N. 1999 Direct numerical simulation of turbulent channel flow up to $Re_\tau = 590$. *Phys. Fluids* **11**, 943–945.

[122] NA, Y. & MOIN, P. 1998 Direct numerical simulation of a separated turbulent boundary layer. *J. Fluid Mech.* **374**, 379–405.

[123] NA, Y. & MOIN, P. 1998 The structure of wall-pressure fluctuations in turbulent boundary layers with adverse pressure gradient and separation. *J. Fluid Mech.* **377**, 347–373.

[124] NA, Y., PAPAVASSILIOU, D. V. & HANRATTY, T. J. . 1999 Use of direct numerical simulation to study the effect of Prandtl number on temperature fields. *International Journal of Heat and Fluid Flow* **20**, 187–195.

[125] NAGANO, Y., TSUJI, T. & HOURA, T. 1998 Structure of turbulent boundary layer subjected to adverse pressure gradient. *International Journal of Heat and Fluid Flow* **19**, 563–572.

[126] PANTON, R. L. 2005 Review of wall turbulence as described by composite expansions. *Applied Mechanics Reviews* **58** (1), 1–36.

[127] PAPAVASSILIOU, D. V. & HANRATTY, T. J. 1995 The use of Lagrangian methods to describe turbulent transport of heat from a wall. *Industrial & Engineering Chemistry Research* **34**, 3359–3367.

[128] PAPAVASSILIOU, D. V. & HANRATTY, T. J. 1997 Transport of a passive scalar in a turbulent channel flow. *International Journal of Heat and Mass Transfer* **40**, 1303–1311.

[129] PATEL, V. C. 1965 Calibration of the Preston tube and limitations on its use in pressure gradients. *J. Fluid Mech.* **23** (1), 185–208.

[130] PATNAIK, G., BORIS, J. & GRINSTEIN, F. 2006 Large scale urban simulations with miles. In *Proceedings of the European Conference on Computational Fluid Dynamics ECCOMAS CFD 2006*.

[131] PIOMELLI, U. 1988 Models for large eddy simulations of turbulent flow including transpiration. PhD thesis, Stanford University.

[132] PIOMELLI, U. 1993 High Reynolds number calculations using the dynamic subgrid-scale stress model. *Phys. Fluids* **A 5**, 1484–1490.

[133] PIOMELLI, U. 1999 Large-eddy simulation: achievements and challenges. *Progress in Aerospace Sciences* **35**, 335–362.

[134] PIOMELLI, U. & BALARAS, E. 2002 Wall-layer models for large-eddy simulation. *Ann. Rev. Fluid Mech.* **34**, 349–374.

[135] PIOMELLI, U., CABOT, W., MOIN, P. & LEE, S. 1991 Subgrid-scale backscatter in turbulent and transitional flows. *Phys. Fluids* **3**, 1766–1771.

[136] POPE, S. B. 2000 *Turbulent Flows*. Cambridge University Press.

[137] PORTER, D. H., POUQUET, A. & WOODWARD, P. R. 1994 Kolmogorov-like spectra in decaying three-dimensional supersonic flows. *Phys. Fluids* **6**, 2133–2142.

[138] PORTER, D. H., WOODWARD, P. R. & POUQUET, A. 1998 Inertial range structures in decaying compressible turbulent flows. *Phys. Fluids* **10**, 237–245.

[139] PRUETT, C., GATSKI, T., GROSCH, C. & THACKER, W. 2003 The temporally filtered Navier-Stokes equations: Properties of the residual stress. *Phys. Fluids* **15**, 2127–2140.

[140] PRUETT, C. D., THOMAS, B. C., GROSCH, C. E. & GATSKI, T. B. 2005 A temporal approximate deconvolution model for LES. In *Fourth International Symposium on Turbulence and Shear Flow Phenomena* (ed. J. A. C. Humphrey, T. B. Gatski, J. K. Eaton, R. Friedrich, N. Kasagi & M. A. Leschziner), pp. 705–710. Williamsburg, VA USA.

[141] QIAN, J. 1995 Viscous range of turbulent scalar of large prandtl number. *Fluid Dyn. Res.* **15**, 103–112.

[142] REYNOLDS, O. 1895 On the dynamical theory of incompressible viscous fluids and the determination of the criterion. *Philosophical Transactions of the Royal Society of London. A* **186**, 123–164.

[143] RIDER, W. & MARGOLIN, L. 2003 From numerical analysis to implicit turbulence modeling. *AIAA paper* **2003-4101**.

[144] SAGAUT, P. 2005 *Large-Eddy Simulation for Incompressible Flows*, 3rd edn. Springer.

[145] SAGAUT, P., COMTE, P. & DUCROS, F. 2000 Filtered subgrid-scale models. *Phys. Fluids* **12**, 233–236.

[146] SCHLICHTING, H. 1979 *Boundary-Layer Theory*. McGraw-Hill.

[147] SCHUMANN, U. 1973 Ein Verfahren zur direkten numerischen Simulation turbulenter Strömungen in Platten- und Ringspaltkanälen und über seine Anwendung zur Untersuchung von Turbulenzmodellen. PhD thesis, TH Karlsruhe, KFK 1854.

[148] SCHUMANN, U. 1975 Subgrid scale model for finite-difference simulations of turbulence in plane channels and annuli. *J. Comp. Phys.* **18**, 376–404.

[149] SCHWERTFIRM, F. & MANHART, M. 2005 ADM-modelling approach for semi-direct numerical simulation of turbulent mixing and mass transport. In *Proceedings of the 4th International Symposium on Turbulence and Shear Flow Phenomena (TSFP4)*, pp. 823–828. Williamsburg/VA, USA.

[150] SCHWERTFIRM, F. & MANHART, M. 2006 DNS of passive-scalar transport in turbulent channel flow at high Schmidt numbers. In *Proceedings of Turbulence, Heat and Mass Transfer 5*.

[151] SEVERAC, E. & SERRE, E. 2007 A spectral vanishing viscosity for the LES of turbulent flows within rotating cavities. *Journal of Computational Physics* **226**, 1234–1255.

[152] SHAW, D. A. & HANRATTY, T. J. 1977 Turbulent mass transfer rates to a wall for large Schmidt numbers. *A. I. Ch. E. Journal* **23**, 28–37.

[153] SHU, C.-W. 1988 Total-variation-diminishing time discretizations. *SIAM J. Sci. Stat. Comput.* **9** (6), 1073–1084.

[154] SHU, C.-W. 1997 Essentially non-oscillatory and weighted essentially non-oscillatory schemes for hyperbolic conservation laws. *Tech. Rep.* 97-65. ICASE, NASA Langley Research Center, Hampton, Virginia.

[155] SHU, C.-W. & OSHER, S. 1989 Efficient implementation of essentially non-oscillatory shock-capturing schemes, II. *J. Comput. Phys.* **83**, 32–78.

[156] SIMPSON, R. L. 1981 A review of some phenomena in turbulent flow separation. *J. Fluids Eng.* **102**, 520–533.

[157] SIMPSON, R. L. 1983 A model for the backflow mean velocity profile. *AIAA J.* **21**, 142.

[158] SIMPSON, R. L. 1989 Turbulent boundary-layer separation. *Ann. Rev. Fluid Mech.* **21**, 205–234.

[159] SKÅRE, P. E. & KROGSTAD, P.-Å. 1994 A turbulent equilibrium boundary layer near separation. *Journal of Fluid Mechanics* **272**, 319–348.

[160] SLEIJPEN, G. L. G., VAN DER VORST, H. A. & FOKKEMA, D. R. 1994 BiCGstab(l) and other hybrid Bi-CG methods. *Numerical Algorithms* **7**, 75–109.

[161] SMAGORINSKY, J. 1963 General circulation experiments with the primitive equations. *Mon. Weath. Rev.* **91**, 99–164.

[162] SMAGORINSKY, J. 1993 Some historical remarks on the use of nonlinear viscosities. In *Large eddy simulation of complex engineering and geophysical flows* (ed. B. Galperin & S. A. Orszag), pp. 3–36. Cambridge University Press.

[163] SMOLARKIEWICZ, P. K. 1984 A fully multidimensional positive definite advection transport algorithm with small implicit diffusion. *J. Comp. Phys.* **54**, 325–362.

[164] SMOLARKIEWICZ, P. K. & CLARK, T. L. 1986 The multidimensional positive definite advection transport algorithm: Further development and applications. *Journal of Computational Physics* **67**, 396–438.

[165] SMOLARKIEWICZ, P. K. & MARGOLIN, L. G. 1998 MPDATA: A finite-difference solver for geophysical flows. *J. Comput. Phys.* **140**, 459–480.

[166] SPALART, P. R. 1988 Direct simulation of a turbulent boundary layer up to $Re_\theta = 1410$. *J. Fluid Mech.* **187**, 61–98.

[167] SPALART, P. R. & COLEMAN, G. N. 1997 Numerical study of a separation bubble with heat transfer. *European Journal of Mechanics. B, Fluids* **16**, 169–189.

[168] STOLZ, S. & ADAMS, N. A. 1999 An approximate deconvolution procedure for large-eddy simulation. *Phys. Fluids* **11**, 1699–1701.

[169] STOLZ, S., ADAMS, N. A. & KLEISER, L. 2001 The approximate deconvolution model for compressible flows: decaying turbulence and shock-turbulent-boundary-layer interaction. In *Large-Eddy simulation of complex transitional and turbulent flows* (ed. R. Friedrich & W. Rodi). Kluwer.

[170] STOLZ, S., ADAMS, N. A. & KLEISER, L. 2001 An approximate deconvolution model for large-eddy simulation with application to incompressible wall-bounded flows. *Phys. Fluids* **13**, 997–1015.

[171] Stolz, S., Schlatter, P. & Kleiser, L. 2005 High-pass filtered eddy-viscosity models for large-eddy simulations of transitional and turbulent flow. *Phys. Fluids* **17**, 065103.

[172] Tadmor, E. 1989 Convergence of spectral methods for nonlinear conservation laws. *SIAM J. Numer. Anal.* **26**, 30–44.

[173] Tollmien, W. 1929 Über die Entstehung der Turbulenz. 1. Mitteilung. *Nachr. Ges. Wiss. Göttingen, Math. Phys. Klasse* pp. 21 – 44.

[174] van der Vorst, H. 1992 Bi-CGSTAB: A fast and smoothly converging variant of Bi-CG for the solution of nonsymmetric linear systems. *SIAM J. Sci. Statist. Comput.* **13**, 631–644.

[175] van Leer, B. 1979 Towards the ultimate conservative difference scheme. V. A second-order sequel to Godunov's method. *J. Comput. Phys.* **31**, 276–299.

[176] Vichnevetsky, R. & Bowles, J. 1982 *Fourier Analysis of Numerical Approximations of Hyperbolic Equations*. Philadelphia: SIAM.

[177] von Kármán, T. 1930 Mechanische Ähnlichkeit und Turbulenz. *Nachrichten von der Gesellschaft der Wissenschaften zu Göttingen* pp. 58–76.

[178] von Neumann, J. & Richtmyer, R. D. 1950 A method for the numerical calculation of hydrodynamic shocks. *J. Appl. Phys.* **21**, 232–237.

[179] Vreman, A. W. 2003 The filtering analog of the variational multiscale method in large-eddy simulation. *Phys. Fluids* **15**, L61–L64.

[180] Vreman, B., Geurts, B. & Kuerten, H. 1994 Discretization error dominance over subgrid terms in large eddy simulation of compressible shear layers in 2D. *Communications in numerical methods in engineering* **10**, 785–790.

[181] Vreman, B., Geurts, B. & Kuerten, H. 1994 On the formulation of the dynamic mixed subgrid-scale model. *Phys. Fluids* **6**, 4057–4059.

[182] Williamson, J. H. 1980 Low-storage Runge–Kutta schemes. *J. Comp. Phys.* **35**, 48–56.

[183] Xu, C., Zhang, Z., den Toonder, J. & Nieuwstadt, F. 1996 Origin of high kurtosis levels in the viscous sublayer. Direct numerical simulation and experiment. *Phys. Fluids* **8** (7), 1938–1944.

[184] YANG, X. & DOMARADZKI, J. 2004 Large eddy simulations of decaying rotating turbulence. *Phys. Fluids* **16** (11), 4088–4104.

[185] YEUNG, P., XU, S. & SREENIVASAN, K. 2002 Schmidt number effects on turbulent transport with uniform mean scalar gradient. *Phys. Fluids* **14** (12), 4178–4191.

[186] YEUNG, P. & ZHOU, Y. 1997 On the universality of the Kolmogorov constant in numerical simulations of turbulence. *Tech. Rep.* 97-64. ICASE, NASA Langley Research Center, Hampton, Virginia.

[187] ZAGAROLA, M. & SMITS, A. 1998 Mean-flow scaling in turbulent pipe flow. *J. Fluid Mech.* **373**, 33–79.

[188] ZALESAK, S. T. 1979 Fully multidimensional flux-corrected transport algorithms for fluids. *J. Comput. Phys.* **31**, 335–362.

[189] ZANDONADE, P., LANGFORD, J. & MOSER, R. 2004 Finite-volume optimal large-eddy simulation of isotropic turbulence. *Phys. Fluids* **16** (7), 2255–2271.

[190] ZANG, Y., STREET, R. & KOSEFF, J. 1993 A dynamic mixed subgrid-scale model and its application to turbulent recirculating flows. *Phys. Fluids* **A 5**, 3186–3196.